Advanced atomistic models for magnetisation dynamics

Mara Stefania Strungaru

Doctor of Philosophy

University of York
Physics

December 2020

Abstract

The next generation of ultra-high density storage technology will be based on heat-assisted magnetic recording that uses the highly anisotropic $L1_0$ phase of FePt. As the areal density increases, the grain size decreases and finite-size effects are becoming crucial. The damping mechanism controls the magnetisation dynamics and the writing speed of the information, hence its behavior for small FePt grain sizes needs to be studied. Using atomistic spin dynamics simulations, the variation of damping with temperature and system size is systematically analysed by employing ferromagnetic resonance calculations. The damping of FePt grains is enhanced with increased temperatures, but the linewidth of the system can decrease in the presence of size distributions due to the transition of small grains to the paramagnetic state. Switching is investigated within the heated dot limit, assuming the largest areal density possible in recording media and shows that the numerical calculation involving a dynamical switching of the media leads to larger bit-error rates due to thermal transitions over the energy barrier and subsequent smaller areal densities.

Atomistic spin dynamics simulations assume a fixed lattice of atoms, however, as the magnetic material is heated up, both magnetic and mechanical properties will be dynamically affected. To include the lattice contribution during magnetic relaxation (magnon-phonon interactions), a coupled spin-lattice dynamics model has been developed. The fundamental properties of the SLD framework, with application to BCC Fe, have been analysed. The existence of a direct channel of energy and angular momentum transfer between magnons and phonons increases the damping via spin-lattice coupling, which is important for the study of both magnetic insulators and metals. Finally, the magnetisation dynamics is studied under the effect of THz phonon excitation, showing that it is possible to switch the magnetisation via the direct excitation of various phonon modes.

Table of contents

List of tables **ix**

List of figures **xi**

1 Introduction **1**

1.1 Motivation 1

1.1.1 Beyond the magnetic trilemma 2

1.1.2 Magnetic relaxation and intrinsic damping 4

1.1.3 Modelling magnetic materials 5

1.2 Outline of the thesis 6

2 Spin dynamics and the atomistic model approach **9**

2.1 The origin of the magnetic moments 9

Magnetic materials 10

2.2 Exchange interaction 10

Magnetic anisotropy 12

Zeeman interaction 13

2.3 Ferromagnetic resonance 13

2.4 Magnon dispersion 16

2.5 Magnetisation switching 17

Switching at $T = 0$K with an external field 17

Thermally assisted switching - HAMR 18

All-optical switching 19

2.6 Atomistic spin dynamics 19

LLG equation 20

Langevin dynamics 22

2.7 Monte-Carlo methods 24

2.8 Temperature dependence of magnetic parameters 25

2.9 Conclusions 26

3 Atomistic spin-lattice dynamics model 27
3.1 Introduction 27
3.2 Overview of SLD models 29
3.3 Equations of motion 30
3.4 Integration algorithm 32
3.5 Code development 34
3.5.1 Parallelisation 36
3.6 Phenomenological spin-orbit coupling terms 37
3.6.1 Simple coupling - Karakurt *et al.* [54] 37
3.6.2 Anisotropy coupling - Perera *et al.* [55] 38
3.6.3 Pseudo-dipolar coupling - Akhiezer [86] 42
3.6.4 Single site pseudo-dipolar coupling 44
3.7 Magneto-elastic simulations 44
3.8 Thermalisation of the spin and lattice sub-systems 46
3.9 Phonon dispersion 47
3.10 Magnon dispersion 50
3.11 Temporal correlations of the coupling field 53
3.12 Conclusions 55

4 Damping and anisotropy calculations at elevated temperatures 57
4.1 Introduction 57
4.2 First investigations of damping in FePt 58
4.3 Ferromagnetic resonance 59
4.4 High-temperature FMR: damping and anisotropy calculations for FePt . . . 62
4.5 Thermal FMR 68
4.6 Grid-search method 72
4.7 FMR Model including inhomogeneous line broadening 75
4.8 FMR in ECC media 80
4.9 Conclusions 84

5 Spin dynamics under phonon excitation 87
5.1 Equilibrium M(T) 87
5.1.1 Thin film systems 92
5.2 Magnon-phonon damping 95
5.3 Magnetisation switching by THz phonons 99

5.3.1 Introduction: Controlling magnetisation via laser excitation and phonons . . . 99
5.3.2 Switching via THz phonons . . . 101
5.3.3 Switching phase diagram $T \geq 0$K . . . 110
5.3.4 Phase diagram for a Morse Potential . . . 114
5.4 Conclusions . . . 118

6 Advanced recording media applications 121
6.1 Heated dot magnetic recording media . . . 121
6.1.1 Heated Dot Recording Media: FePt and NdFeB . . . 122
6.1.2 Improved switching probability in FePt . . . 126
6.1.3 Maximum areal densities for HDMR . . . 130
6.2 Ultrafast dynamics in FePt/FeRh structures . . . 133
6.2.1 Model of FePt/FeRh structures . . . 134
6.2.2 The two-temperature model . . . 135
6.2.3 Switching in FePt/FeRh bilayers . . . 137
6.3 Conclusions . . . 139

7 Conclusions 141
7.1 Further work . . . 143

Appendix A Conservation properties of the precessional equation 145

Appendix B Fluctuation dissipation theorem 149

References 153

List of tables

3.1 Parameters used in the spin-lattice model to simulate BCC Fe. 32

4.1 Parameters used for FePt. 63

6.1 The Curie temperature of FePt and NdFeB for different grain diameters. . . 125
6.2 Parameters used for the FePt/FeRh simulations, extracted from Ref. [30]. . 135

List of figures

1.1 Magnetic recording trilemma and quadrilemma. 2
1.2 Advanced storage technology consortium - ASTC (currently Advanced storage research consortium - ASRC) Technology Roadmap [5]. 3
1.3 Energy flow in a ferromagnet which arises from the excitation of a uniform mode, $k = 0$. 4
1.4 Length and timescales specific to different magnetic modelling techniques. . 6

2.1 Types of magnetic materials. 10
2.2 Ferromagnetic resonance for a one-dimensional system. 15
2.3 Illustration of magnetisation switching under the application of an antiparallel or perpendicular external field. 17
2.4 Schematics showing the writing process in HAMR media. 18
2.5 All-optical switching in ferrimagnetic GdFe, extracted from Ref. [41]. . . . 19
2.6 Illustration of spin dynamics: precession, damping and thermal fluctuations. 24
2.7 The temperature dependence of different magnetic quantities. 26

3.1 Overview of characteristic timescales in the Spin-Lattice dynamics framework. 28
3.2 Flowchart of the SLD code. 35
3.3 Speedup as function of number of threads for -O2 compilation. 36
3.4 Components of the coupling field and force for a simple spin-lattice coupling. 38
3.5 Components of exchange field and force for a simple spin-lattice coupling. . 39
3.6 Temperature and energy variation for a magnetic system coupled by a simple spin-lattice coupling. 39
3.7 Components of the coupling field and force for a on-site spin-lattice coupling. 41
3.8 Components of the coupling field and force for a pseudo-dipolar spin-lattice coupling. 43
3.9 Temperature and energy variation for a magnetic system coupled by a pseudo-dipolar spin-lattice coupling. 43

3.10 Temperature and energy variation for a magnetic system coupled by a single-site pseudo-dipolar spin-lattice coupling. 44
3.11 Magnetic anisotropy energy as function of strain for different coupling strengths at $T = 0$K. 45
3.12 Thermalisation of spin and lattice sub-systems. 46
3.13 The Brillouin zone for a BCC lattice as extracted from [92]. 47
3.14 Phonon spectrum for a Morse potential. 48
3.15 Phonon spectrum for a Harmonic potential. 49
3.16 Phonon spectra for a Harmonic potential parameterised from the Morse potential coefficients. 50
3.17 Magnon spectrum for a Morse potential. 51
3.18 Magnon spectrum for a Harmonic potential. 52
3.19 Magnon spectrum for different temperatures. 52
3.20 The power density of the auto-correlation function in the frequency domain for magnons, phonons, coupling field for a SLD simulations. 53
3.21 The power density of the auto-correlation function in the frequency domain for the coupling field at different temperatures. 54
3.22 The power density of the auto-correlation function in the frequency domain for the coupling field for fixed and dynamic lattice. 54
3.23 The large frequency domain of the power density of the auto-correlation function in the frequency domain for the coupling field for fixed and dynamic lattice. 55

4.1 Illustration of the setup used for ferromagnetic resonance experiments and corresponding in-plane magnetisation for two frequencies. 60
4.2 Power spectrum of a single FePt grain at $T = 0$K, with an initial damping of 0.01. 60
4.3 Power spectrum of a FePt grain for different temperatures. 61
4.4 Damping and magnetisation curves as a function of normalised temperature for bulk and granular FePt systems. 63
4.5 Resonance frequency and anisotropy field as a function of normalised temperature for bulk and granular FePt. 65
4.6 Damping as a function of temperature for granular and bulk systems. 66
4.7 Temperature dependence of the damping constant for cube diameters of 4nm, 5nm and 6nm. 67
4.8 Layer resolved power spectra for a cube of size 4nm at $T = 600$K. 67
4.9 Experimental thermal FMR measurements extracted from [104]. 69

4.10 Magnetisation dynamics under the application of a laser pulse of fluence 1 mJ/cm^2 for two magnitudes of the applied field. 70
4.11 Resonance frequencies for two values of the applied field and a laser pulse of fluence 1 J/cm^2. 71
4.12 Illustration of the grid-search method. 72
4.13 χ^2 map at $T = 550.1$K and the variation of χ^2 as a function of damping for the corresponding anisotropy. 73
4.14 Relative error in the determination of the damping and anisotropy via the grid search method. 74
4.15 Comparison of damping and anisotropy for FMR and grid-search fitting. . . 75
4.16 Schematics of the inhomogeneous line broadening in the presence of distribution of properties. 76
4.17 Field swept FMR measurements for granular systems of FePt, extracted from Richardson *et al.* [103]. 78
4.18 Field swept FMR for a lognormal distribution of grains of average diameter $D = 7$ nm and $\sigma_D = 0.17$. 79
4.19 Temperature dependence of the FMR linewidth for different system sizes. . 79
4.20 FMR spectra for hard/soft bilayers with a coupling constant of $C = 5\%$. . . 82
4.21 Damping and resonance frequency for a soft/hard system as a function of the coupling strength for different choices of input damping for the soft layer. . 82
4.22 FMR spectra for hard/hard bilayers with a coupling constant of $C = 5\%$. . . 83
4.23 Damping and resonance frequency for a hard/hard system as a function of the coupling strength for different choices of damping for one of the macrospins. 84

5.1 Magnetisation versus temperature curves for the SLD model with different choices of lattice potential and fixed lattice calculations. 88
5.2 Average exchange coupling versus temperature for the SLD model with different choices of lattice potential. 89
5.3 Effective exchange coupling energy calculated during the simulation time for a $10 \times 10 \times 10$ BCC Fe unit cell periodic system. 90
5.4 Normalised effective exchange coupling energy as a function of distribution width. 91
5.5 Gaussian distribution of relative distances for nearest-neighbours pairs of atoms for two temperatures. 92
5.6 Magnetisation versus temperature curves for a $10 \times 10 \times 10$ BCC Fe unit cell thin film. 93

5.7 Magnetisation versus temperature curves for fixed and dynamic lattice simulations. 93
5.8 Relative distance profile for nearest neighbours interaction for a thin film system of $z = 10$ layers at two different temperatures. 94
5.9 Relative distance distributions for nearest neighbours interaction for the top and middle layer of a thin film system of $z = 10$ layers at a temperature of $T = 800$K. 94
5.10 Effective exchange coupling energy calculated during the simulation time for a thin film system. 95
5.11 Temperature dependence of the damping parameter for two choices of atomic potential. 96
5.12 Damping parameter for different coupling strengths and two choices of atomic potential. 97
5.13 Temperature variation of the damping for Néel-like on-site coupling. 98
5.14 Modulation of exchange under the application of a laser pulse between two sub-lattices in YIG and between surface and sub-surface atoms in Gd. Extracted from [68], [69]. 100
5.15 Schematics of light induced FMR and lattice-mediated oscillations of magnetic anisotropy, extracted from [137]. 100
5.16 Generation of acoustic pulses that can potentially switch the magnetisation. 101
5.17 Schematics of THz excitation 102
5.18 Temporal evolution and the Fourier Transform of the x coordinate of the atom at position (0,0,0) for a Harmonic and Morse Potential and the FFT of the signal. 103
5.19 Phonon spectra of the x component of velocities at $T = 10$K for a Harmonic potential. 103
5.20 Magnetisation behaviour under the application of different THz pulse widths ranging from 5ps to 125ps at $T = 0$K. 104
5.21 Magnetisation dynamics during the application of a THz pulse of frequency 8.3THz for 115ps. 105
5.22 Average velocities and displacements during the application of a THz pulse of frequency 8.3THz for 115ps. 106
5.23 Average forces produced by the magnetic subsystem during the application of a THz pulse of frequency 8.3THz for 115ps. 106
5.24 Histogram of average forces produced by the magnetic subsystem during the application of a THz pulse of frequency 8.3THz for 115ps. 107

5.25 Average magnetic fields during the application of a THz pulse of frequency 8.3THz for 115ps. 107
5.26 Average coupling and anisotropy fields during the application of a THz pulse of frequency 8.3THz for 115ps. 108
5.27 Effective exchange and pseudo-dipolar couplings under the effect of a THz pulse of frequency 8.3THz for 115ps. 109
5.28 Magnetisation and effective pseudo-dipolar couplings under the effect of a THz pulse of frequency 8.4THz for 125ps. 110
5.29 Switching phase diagram at $T = 0$K for two coupling values: $C = 0.3$ and $C = 0.5$. 110
5.30 Simplified switching phase diagram at $T = 0$K for two coupling values: $C = 0.3$ and $C = 0.5$. 111
5.31 Behaviour of magnetisation and coupling field for different pulse widths of frequency 8.4THz. 112
5.32 Behaviour of magnetisation and coupling field for different pulse widths of frequency 8.3THz. 113
5.33 Simplified switching phase diagram at $T = 10$K for a single realisation and averaged over 4 realisations. 113
5.34 Switching phase diagram at $T = 0$K for a Morse Potential. 114
5.35 Temporal evolution and the Fourier Transform of the x coordinate of the atom at position (0,0,0) for a Morse Potential for a frequency of 8.6THz. . . 115
5.36 Switching dynamics for a pulse width of 145ps and a frequency of 8.6THz for a Morse potential. 116
5.37 Behaviour of magnetisation and coupling field for a Morse Potential for different pulse widths of frequency 8.6THz. 117
5.38 Lattice and spin dynamics for a continuous THz pulse of frequency of 10.6THz for a Morse potential. 117

6.1 Example of heated dot magnetic simulations. 122
6.2 Schematics of energy barrier. 123
6.3 Switching probability calculations for FePt and NdFeB grains. 124
6.4 Curie temperature as a function of grain diameter. 125
6.5 BER calculation for FePt and NdFeB. 126
6.6 Bit error rate calculations of FePt grains for varying magnetic moment. . . . 128
6.7 Bit error rate calculations of FePt grains for varying Curie temperature. . . 128
6.8 BER as function of grain diameter calculated for varying damping and temperature pulse widths. 129

6.9 Bit error rate calculations of FePt grains for varying applied field. 130
6.10 Blocking temperature calculations for FePt grains of 3 nm diameter. 132
6.11 Analytical and numerical areal density calculations for HDMR. 132
6.12 Equilibrium magnetisation and spin configuration for different coupling strengths between FePt and FeRh bilayers. 135
6.13 Diagram of energy flow in the two temperature model and evolution of the electron and phonon temperatures. 136
6.14 Example of ultrafast switching in FePt/FeRh bilayers 137
6.15 Switching probability of FePt as function of coupling strength in FePt/FeRh grains. 139

To my husband, Sergiu

And in memory of my loving brother, ecotoxicologist Dr. Stefan-Adrian Strungaru
who left this world suddenly on April 2021, at only 31 years old.
Throughout his infinite kindness, love for science, optimism and professionalism, Stefan has inspired many students, including myself.
I wish there was a happier way to thank again to the best brother I could have.
Your little sister loves you throughout eternity. Rest in peace, Stefan.

Acknowledgements

I would like to express my appreciation to my supervisors, Prof. Roy Chantrell and Dr. Richard Evans for their endless support, positive attitudes and optimism. Thank you Roy for all the opportunities you have offered me and for all the trust, encouragements and patience. Your constant feedback and ideas would keep the research going when times were hard and the laughs and beautiful stories you shared with us have reached my heart. I am grateful to Dr. Richard Evans for making me part of the VAMPIRE family, for all the scientific and programming advice and inspiring morning coffee discussions.

I am grateful to Matthew Ellis for guiding me in the world of spin-lattice dynamics, for his patience and kind support which helped part of this work thrive. I am grateful to Oksana Chubykalo-Fesenko for being my model of a female scientist, for her professional feedback which has influenced the work presented here, for her friendship and encouragements that inspired me in tough moments. I would also like to thank Noi and Jay for their research input and for accepting me to visit their group in Thailand and to Oksana to visit her in Madrid.

I would like to thank ASTC (Advance Storage Technology Consortium) for funding this project. I would like to address special thanks to Sergiu and Andrea for their continuous kind scientific advice and to my past and present office colleagues Ewan, Paul, Razvan, Tim, Daniel, Luke, Alejandro for their support. I would like to thank to Thomas Ostler, Joseph Barker, Pui-wa Ma, Matt Probert, Jamie Massey for fruitful discussions and to Liliana Alexandru, Alexandru Stancu and Cristian Enachescu for their guidance in the past years. I am grateful to Natty, Tong, Zuwei and Cristina, who become my very good friends during their visit to York and to the MINT group in Thailand for their friendship.

Last but not the least, I would like to thank my parents, Maria and Maricel, my extended family, Paulina and Vasile and my friends for their sincere support, to Roxana and Stefan for inspiring me in all these years and to Vlad for the giggles and joy he brought in our lives. Nothing would have been possible without the endless love and support from my husband Sergiu, who made this PhD and life journey more beautiful and who will constantly impress me with his smart jokes and tasty recipes.

Declaration

I hereby declare that except where specific reference is made to the work of others, the contents of this dissertation are original and have not been submitted in whole or in part for consideration for any other degree or qualification in this, or any other university. The atomistic spin dynamics simulations have been performed via the software package VAMPIRE. The spin-lattice dynamics have been performed via an in-house developed code, inherited from Dr. Matthew Ellis and further developed by the candidate during this work. The majority of this thesis has been presented at various conferences by the author, some chapters being based on the following publications:

- **Strungaru, M.**, Ruta, S., Evans, R. F., Chantrell, R. W. (2020). Model of magnetic damping and anisotropy at elevated temperatures: Application to granular FePt films. Physical Review Applied, 14(1), 014077.
- **Strungaru, M.**, Ellis, M. O., Ruta, S., Chubykalo-Fesenko, O., Evans, R. F., Chantrell, R. W. (2020). Modeling coupled spin and lattice dynamics. arXiv preprint arXiv:2010.00642 (in Review for Physical Review B with the updated title: Spin-lattice dynamics model with angular momentum transfer for canonical and microcanonical ensembles)

1

Introduction

1.1 Motivation

Magnetic materials maintained huge interests for technological applications such as magnetic recording media (initially on magnetic tapes, now on nm-sized granular media). With the increased necessity to store more and more data, it is important to constantly improve/renew the current technologies or seek for other magnetic entities (such as domain walls, skyrmions) to act as a bit of information. Novel research fields in magnetism such as spin-electronics (spintronics), opto-magnetism, magnetism in 2D, neuromorphic and reservoir computing [1] promise to bring more advanced technologies in our daily life, and the usage of magnetic nano-particles in bio-medicine to even cure some types of cancer. In this thesis we tackle the possibilities of improving recording media applications via simulations of nano-magnets.

The current recording media is based on Heat-Assisted Magnetic Recording (HAMR), where nm-sized grains of $L1_0$ FePt are heated during the writing process. There are multiple investigations of the temperature dependence of the magnetisation and anisotropy for HAMR systems, however, also the temperature dependence of the damping that controls the writing speed and magnetisation dynamics has been recently brought to the attention. Future recording media technologies such as Heated Dot Recording Media require an understanding and control of the bit error rate which can limit the maximum areal density possible to achieve. With the discovery of ultrafast magnetisation dynamics and all-optical switching, the interplay between electrons, phonons and spins is more and more studied fundamentally and from applications point of views, since it can lead to non-dissipative switching technologies. To improve the current recording media systems and develop novel applications, it is important to have advanced modelling techniques able to deal with the diverse aspects in nanomagnetism.

1.1.1 Beyond the magnetic trilemma

The design of new magnetic recording media devices needs to consider the fundamental limitations given by the magnetic recording trilemma and quadrilemma - Fig. 1.1. The trilemma [2] shows the interplay between the thermal stability, writability and the areal density in the development of current technologies. In addition, the quadrilemma highlights the importance of the thermal fluctuation for small system sizes which can lead to considerable bit error rates that need to be minimised for optimum design of the recording media technology. In order to increase the areal density two paths can be followed: *a)* keeping the number of grains per bit as large as possible for good statistics and large signal to noise ratio (SNR) and reduce the diameter of the grains or *b)* reduce the number of grains per bit until a single grain corresponds to a single bit (Bit Patterned Media - BPM). Following path *a)*, a decrease in the grain size leads to a decrease in the energy barrier KV/k_BT, which needs to be kept around the value 60 [3] to preserve the thermal stability of the grains. Hence, in order to keep the ratio $KV/k_BT = 60$, materials with large anisotropy need to be used. Since the writing field has typical values of 10kOe, this is not sufficient to reverse the bit due to its large coercivity. Hence it is necessary to firstly reduce the coercivity of the system, either by heating up the system such as in Heat Assisted Magnetic Recording (HAMR) or by the exchange spring mechanism in Exchange Coupled Composite (ECC) media.

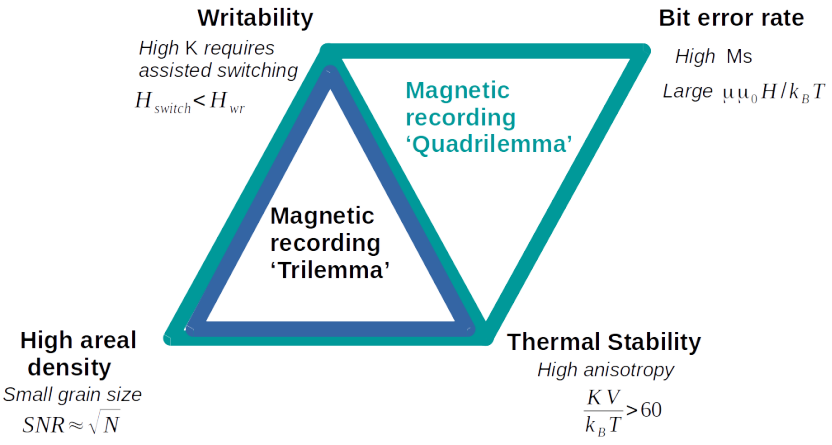

Fig. 1.1 Magnetic recording trilemma and quadrilemma. Adapted from Ref. [2] (trilemma) and Ref. [4] (quadrilemma).

The ASTC Roadmap (currently ASRC) - Fig. 1.2 shows the current and future technologies: HAMR and BPM [5]. HAMR media promises high areal density (above 1Tb/in^2) by employing highly anisotropic materials such as FePt $L1_0$ [6]. HAMR recording uses a

small laser diode attached to each writing head and the light from this laser is focused onto a near field transducer (NFT) which heats the media and decreases its coercive field enough to write data with the available field [7]. The performance of HAMR media is limited by a number of factors, among those the noise due to the distribution of Curie temperature (T_C) that arises from the grain size dispersion [6]. Small grains with narrow size distribution and high temperature dependence of the switching field is also critical for HAMR [8].

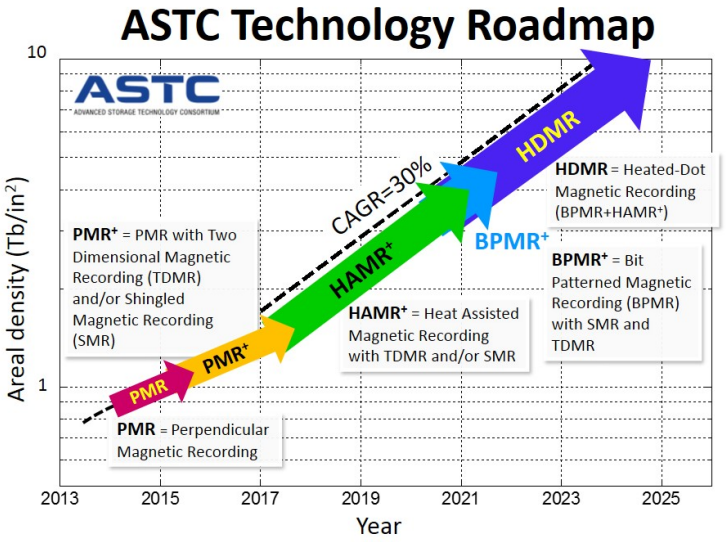

Fig. 1.2 Advanced storage technology consortium - ASTC (currently Advanced storage research consortium - ASRC) Technology Roadmap [5].

Alternatives to the single magnetic layer technologies have been proposed to lower the coercive field by the exchange coupling mechanism in multilayered systems. For example, via the soft ferromagetic phase of the FeRh metamagnet, the coercive field can be lowered in FePt/FeRh bilayer systems [9]. Another promising type of multilayered media is the exchange coupled composite (ECC) [10–12] that uses low-high T_C materials, for example Fe/FePt to obtain lower switching fields than in the case of FePt systems. Bit-Patterned Media - BPM and Heated Dot Recording Media (HDMR) is the next recording media technology to follow, according to the ASTC Roadmap - Fig. 1.2. BPM consists of lithographically defined magnetic grains, however fabrication of BPM with good magnetic properties and tight fabrication tolerances is very challenging [13]. Heated Dot Magnetic Recording (HDMR) represents the ultimate recording media, a combination between HAMR and BPM, that uses single grains of high anisotropy materials for thermal stability and a laser pulse for writing. This technology is limited by the bit error rate, as shown in the quadrilemma - Fig. 1.1, which suggests that thermal fluctuations in the system can lead to write errors, which are significant

with decreasing system size [4]. For equilibrium considerations, Evans *et al.* show that the ratio $\mu\mu_0 H/k_B T$ ($\mu = M_S V$) needs to be kept large for small bit error rates, suggesting that with decreasing system size (V) the saturation magnetisation (M_S) and writing field (H) need to be kept as large as possible.

1.1.2 Magnetic relaxation and intrinsic damping

The timescale of magnetisation dynamics is governed by the damping mechanism which has been introduced phenomenologically in the Landau-Lifshitz-Gilbert model to reflect the energy dissipation channels in the system. In general, it is understood as the coupling of the magnetic modes (primarily the electron spins) to the non-magnetic modes (lattice vibrations) and electronic orbital moments in the magnetic system. The magnetic damping parameter is important from both a fundamental and applications point of view, as it controls the dynamic properties of the system, such as magnetic relaxation, spin waves, domain-wall propagation, and magnetisation reversal processes. In information technologies, damping plays a crucial role, as it can influence the operating parameters, such as the switching current in spin-transfer torque magnetic random access memories (STT-MRAM) [14], the fluence of the ultrafast laser pulse necessary for demagnetizing and switching of the sample [15] or the domain-wall propagation velocity in nano-wires for racetrack memories application [16]. Understanding various coupling mechanisms, including them in magnetic models and quantifying their contributions to damping is crucial for the development of future technologies.

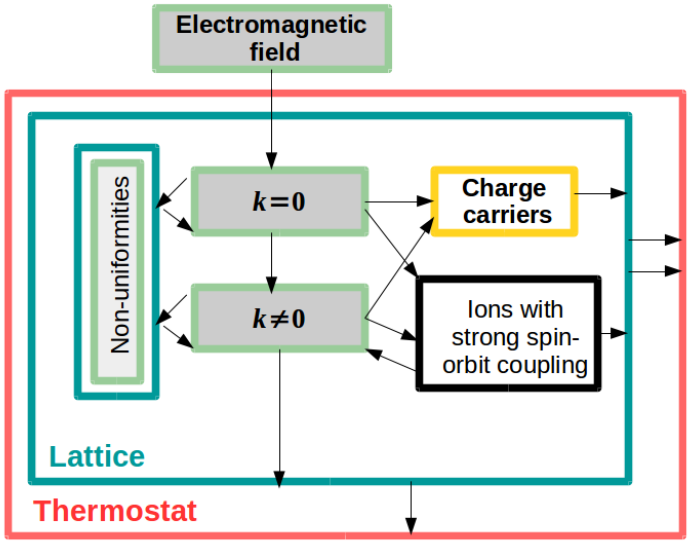

Fig. 1.3 Energy flow in a ferromagnet which arises from the excitation of a uniform mode, $k = 0$, by an electromagnetic field. Adapted from Ref. [17].

Fig. 1.3 (adapted from Ref. [17]) shows the main mechanisms of damping. Generally, the damping can be divided into two contributions: intrinsic and extrinsic. The intrinsic damping originates primarily from the interaction of the spins with the electron orbits, and includes generation of eddy currents and spin–orbit coupling. Another intrinsic contribution to damping occurs through direct magnon–phonon scattering. Other contributions to damping involve magnon-scattering events where the uniform precessional mode ($k = 0$) scatters into a non-uniform precessional mode ($k \neq 0$) and this contributes to extrinsic Gilbert damping. In most cases the energy is transferred finally to the lattice which results in the creation of phonons and consequently heating. The spin-lattice relaxation can be either a direct mechanism (magnons are destroyed and phonons created) or indirect, where energy is transferred to the lattice through some other systems [17]. Besides magnon scattering, other contribution to the extrinsic Gilbert damping is the spin pumping mechanism that enhances the damping in Ferromagnetic/Non-magnetic/Ferromagnetic trilayer systems [18]. The sample inhomogeneities, which lead to a distribution of local resonance fields across the sample lead to a contribution to the FMR linewidth.

1.1.3 Modelling magnetic materials

Magnetism is a multiscale problem, as the spin is a quantum phenomenon and the measured quantities such as magnetisation are at a macroscopic level [1]. The properties of the magnetic materials are influenced by both microscopic/atomic defects as well as their macroscopic shape [1], with magnetic phenomena being present over time-scales ranging from femtoseconds to years. In order to develop competitive magnetic nano-devices, advanced experimental and theoretical frameworks are needed, with the theoretical framework treated as a multiscale problem. Atomistic simulations of magnetic materials can act as a bridge between the *ab initio* (first principles) methods and the continuum approach of micromagnetism, leading towards a multi-scale approach - Fig. 1.4. First principles methods are generally computationally expensive and cannot model more than hundreds of atoms, while micromagnetic modelling cannot deal with effects at the atomistic level.

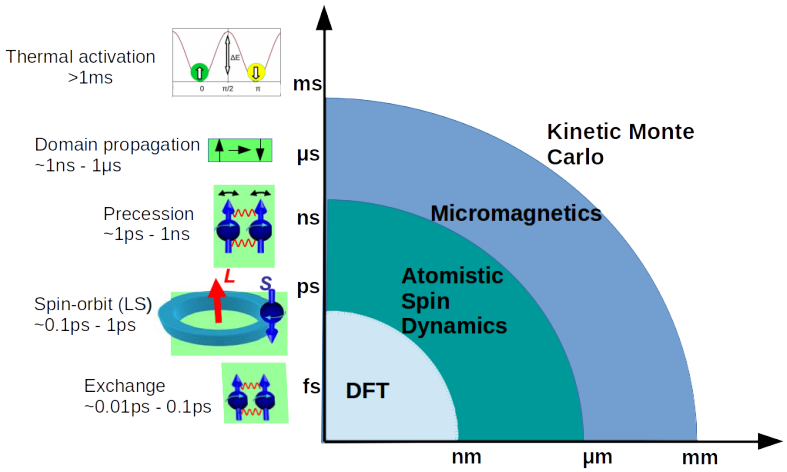

Fig. 1.4 Length and timescales specific to different magnetic modelling techniques together with the fundamental mechanisms specific to each timescale. The exchange, spin-orbit and precession figures are extracted from Ref. [19] and the schematics was adapted from Ref. [20].

The Atomistic Spin Dynamics (ASD) model considers in general only the spin degrees of freedom. A complete description of magnetic systems involves however the interaction between several degrees of freedom, such as lattice, spins and electrons, modelled in a self-consistent simulation framework. The characteristic relaxation timescales of electrons are much smaller (fs) in comparison to spin and lattice (ps), hence magnetisation relaxation processes can be described via coupled dynamics of spin and lattice, framework called Spin-Lattice dynamics (SLD).

1.2 Outline of the thesis

The thesis focuses on the investigation of current and future recording media technologies based on FePt. Although FePt or FePt-based materials have been used throughout the thesis, most of the techniques presented here can be applied for any other ferromagnetic materials. Complementary, the thesis tackles the lack of phonons in the general atomistic spin dynamics simulations, hence a spin-lattice dynamics framework is developed here.

Chapter 2 introduces general concepts in magnetism and describes important spin dynamics phenomena such as ferromagnetic resonance and switching, which motivates the usage of the atomistic model. The theoretical basis of the Atomistic Spin Dynamics model (ASD) is then presented in this Chapter, together with the Landau-Lifsitz-Gilbert (LLG) equation, the inclusion of temperature effects via Langevin dynamics or the Monte-Carlo method. The atomistic spin dynamics model is implemented in the software package

VAMPIRE [21] developed at the University of York and has been used for the investigations presented in Chapter 4 and Chapter 6.

Chapter 3 describes the theoretical background of the Spin-Lattice dynamics model. SLD models can be crucial to disentangle the interplay between the lattice and spins, that can lead to phenomena such as the Einstein-de-Haas effect or controlling magnetisation via THz phonons. As the spin-lattice coupling term is introduced phenomenologically, we study different forms of the coupling. The model reproduces well the properties of the phonons and magnons observed in BCC Fe. The SLD model developed here has been used in Chapter 5 for the investigation of the influence of phonons onto the spin damping and switching.

Chapter 4 investigates the temperature dependence of the damping within the ASD model. The magnetic damping parameter is important from both a fundamental and applications point of view. As current magnetic technologies are based on nanostructures of smaller and smaller sizes, the finite size effects become more important and can significantly influence the magnetic properties including the damping. We therefore investigate the temperature dependence of damping and anisotropy in finite size systems of FePt, the main candidate of HAMR. Since damping simulations are computationally expensive, new methods to investigate the damping and anisotropy are developed such as the grid-search method and a semi-analytical tool to investigate the inhomogeneous line broadening.

Chapter 5 analyses the influence of the phonons on the spin dynamics within the SLD model. The effect of the dynamic lattice on the equilibrium magnetisation is systematically studied for varying system sizes. The magnon-phonon damping is calculated as a function of temperature and spin-lattice coupling strength, and a quadratic increase of the damping is observed in both cases. The possibility of switching the magnetisation via THz phonons is investigated in this Chapter. We observe that, by exciting the phonons at THz frequencies it is possible to switch the magnetisation at ps time-scales via the development of an in-plane field that appears due to the spin-lattice coupling.

Chapter 6 focuses on advanced recording media applications, such as heated dot magnetic recording (HDMR) or exchange spring systems of FePt/FeRh bilayers. In addition to FePt, the permanent magnet NdFeB is studied for HDMR application, its large saturation magnetisation leading to smaller bit error rates. The bit error rate in FePt will limit the maximum areal density possible to obtain for HDMR. Numerical simulations have shown that smaller areal densities are obtained for finite temperature pulse widths, in comparison with thermal equilibrium analytical calculations from literature. We also investigate the ultrafast switching in the FePt/FeRh bilayers and we observe that the coupling to FeRh leads to better switching properties of FePt due to the reversal via the exchange spring mechanism.

2

Spin dynamics and the atomistic model approach

In this Chapter we introduce the concepts and techniques underlying the investigation presented in this thesis. We start with the basic physics of magnetism and magnetic materials and then go on describing some important spin dynamics phenomena including Ferromagnetic resonance and magnetisation reversal (switching). This motivates the usage of the atomistic model approach (atomistic spin and spin-lattice dynamics) which is central to the work presented here and described in the following sections. The atomistic spin dynamics model (ASD) is based on the Heisenberg Hamiltonian, with the spin dynamics being given by a numerical integration of the stochastic Landau-Lifshitz-Gilbert equation. One advantage of the atomistic model is the possibility of calculating the temperature dependence of the magnetic properties (such as anisotropy, magnetisation etc.), which is illustrated in the next sections. Various other investigations can be performed within this model, such as ferromagnetic resonance, magnetisation switching and the interaction of a magnetic material with optical pulses. Atomistic spin models have been reviewed in detail by Evans *et al.* [21] and Skubic *et al.* [22].

2.1 The origin of the magnetic moments

The simplest understanding of magnetic moment involves the rotation of electrons around the nucleus, leading to the appearance of a weak orbital moment. In the case of materials with unpaired electrons, the intrinsic angular momentum (spin) of the electrons on the unoccupied shells leads to the atomic magnetic moment of a system, referred in the atomistic model as spin (**S**), which can be calculated from first principles methods. The term referred to as spin in this work is hence not a quantum mechanical spin, but the expectation value along the spin local quantisation axis, where the quantisation axis then rotates in time, much like a classical

gyroscope. The magnetisation is given by the total magnetic moment per unit volume and gives an insight into the magnetic ordering in the system.

Magnetic materials

The main classes of magnetic materials (according to the classification through the magnetic susceptibility, $\chi = M/H$, which is the response of a material to a magnetic field) are diamagnets, paramagnets, ferromagnets, antiferromagnets and ferrimagnets, the last four classes being schematically represented in Fig. 2.1. Diamagnets have a weak negative susceptibility, while paramagnets have a weak positive susceptibility. In paramagnetic materials the magnetic moments are disordered and the total magnetisation is zero - Fig. 2.1, a). Ferromagnetic materials show a large positive susceptibility. The magnetic moments in ferromagnets are parallel, leading towards a large net magnetisation - Fig. 2.1, b). Antiferromagnets have a weak positive susceptibility. The magnetic moments are antiparallel aligned so they cancel each other, the net magnetisation being zero - Fig. 2.1, c). Ferrimagnets - Fig. 2.1, d) consist of two antiparallel magnetic sublattices, having a non-zero total magnetisation, due to the fact that the moments are not entirely compensated, leading to a macroscopic behaviour similar to ferromagnets - large positive susceptibility.

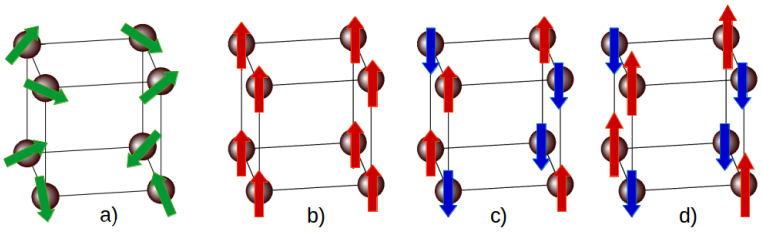

Fig. 2.1 Types of magnetic materials: a) Paramagnet - disordered state, total magnetisation is zero; b) Ferromagnet - ordered state, all spins are parallel; c) Antiferromagnet - ordered state, all spins are antiparallel, total magnetisation is zero; d) Ferrimagnet - ordered state, all spins are antiparallel, non-zero total magnetisation.

2.2 Exchange interaction

The exchange interaction, treated firstly by Heisenberg (1928) [23], is the strong force responsible for the magnetic ordering. The exchange interaction is a quantum phenomenon and arises from the competition between the Coulomb energy and the need to satisfy the Pauli exclusion principle, which implies antiparallel spins of the electrons to occupy the

same orbital, leading to an increase in the Coulomb repulsion which forces the electrons to occupy excited one-electron states. The ordering from the exchange energy can be weakened or even destroyed by thermal excitations, leading to a phase transition from an ordered state to a completely disordered (paramagnetic) state. This critical point is characterised by the Curie temperature, T_C.

The exchange Hamiltonian can be written in terms of a general exchange tensor $\mathscr{J}_{ij}^{\alpha\beta}$:

$$\mathscr{H}_{exch} = -\frac{1}{2}\sum_{i\neq j} \mathbf{S}_i^{\alpha}\ \mathscr{J}_{ij}^{\alpha\beta}\ \mathbf{S}_j^{\beta}\ ,\ \ \alpha,\beta = x,y,z \tag{2.1}$$

The exchange tensor can be decomposed into three terms:

$$\mathscr{J}_{ij} = J_{ij}\mathbf{I} + \mathscr{J}_{ij}^{S} + \mathscr{J}_{ij}^{A} \tag{2.2}$$

The term J_{ij} represents the isotropic part of the exchange tensor ($\mathbf{I}$ represents the unit tensor), $\mathscr{J}_{ij}^{S}$ the symmetric anisotropic exchange and $\mathscr{J}_{ij}^{A}$ is given by the antisymmetric exchange. The isotropic, symmetric and antisymmetric exchange can be easily deduced from the exchange tensor:

$$J_{ij} = \frac{1}{3}Tr(\mathscr{J}_{ij})\ ,\ \ \mathscr{J}_{ij}^{S} = \frac{\mathscr{J}_{ij} + \mathscr{J}_{ij}^{t}}{2} - J_{ij}\mathbf{I}\ ,\ \ \mathscr{J}_{ij}^{A} = \frac{\mathscr{J}_{ij} - \mathscr{J}_{ij}^{t}}{2}, \tag{2.3}$$

where $\mathscr{J}_{ij}^{t}$ is the transpose of the exchange tensor.

The isotropic exchange, also described as the Heisenberg exchange, was introduced to explain the spin ordering at small temperatures. Giving the sign of the exchange, a ferromagnetic ordering (for positive J_{ij}, parallel alignment of spins described in the Heisenberg theory of ferromagnetism) or antiferromagnetic ordering (for negative J_{ij}, antiparallel alignment of spins corresponding to Néel theory of antiferromagnetism) can be found. Due to its electrostatic nature, the Heisenberg exchange is usually stronger relative to other types of interactions.

Dzyaloshinskii-Moriya interaction

The Dzyaloshinskii-Moriya interaction (DMI - suggested by Dzyaloshinskii [24] in 1957 in an attempt to describe the weak ferromagnetism in α-Fe_2O_3 and derived later on by Moriya in 1960 [25]) originates from the antisymmetric part of exchange interaction under the consideration of a strong spin-orbit coupling (SOC) and an inversion-symmetric environment. The energy corresponding to the antisymmetric exchange is given by:

$$\mathscr{H}_{DM} = \mathbf{D}_{ij}\cdot(\mathbf{S}_i \times \mathbf{S}_j) \tag{2.4}$$

The D_{ij} vector can be expressed from the antisymmetric part of the exchange tensor and can be calculated from *ab initio* [26]. From the Moriya symmetry rules, the in-plane DMI vector for a specific atomic layer k can also be expressed as $\mathbf{D}_{ij}^{k} = D^{k} \cdot (\mathbf{z} \times \mathbf{u}_{ij})$, where $\mathbf{z}$ and $\mathbf{u}_{ij}$ are the versors pointing along z direction and from site i and j respectively, and has been used in simulations, for example, of CoPt [26]. The DMI plays an important role as it can produce exotic magnetization textures such as skyrmions [27] that have the potential to be used in magnetic memories.

Higher-order exchange interaction

The Heisenberg Hamiltonian presented above can be extended in order to include higher-order exchange interactions, which have been pointed out by Herring in 1966 [28]. It has been shown that higher-order exchange interactions can be derived from the half-filled Hubbard model by the fourth-order perturbation of the hopping term, the first non-trivial term being the four-spin interaction [29]. The four-spin exchange is given by four electron hopping from one spin configuration to the spin flipped one and can appear between 2 atomic sites - biquadratic exchange, $B_{ij}(\mathbf{S}_i \cdot \mathbf{S}_j)^2$, three atomic sites - $L_{ijk}(\mathbf{S}_i \cdot \mathbf{S}_j)(\mathbf{S}_j \cdot \mathbf{S}_k)$ or four atomic sites - four-spin exchange, $D_{ijkl}(\mathbf{S}_i \cdot \mathbf{S}_j)(\mathbf{S}_k \cdot \mathbf{S}_l)$. The four-spin exchange has been used in order to model the antiferromagnetic to ferromagnetic phase transition in specific materials such as FeRh [30–32].

Magnetic anisotropy

The magnetocrystalline anisotropy gives rise to the preference of the spins to align on a certain lattice direction, termed the easy axis. The anisotropy arises from the interaction of the spin with the crystallographic lattice mediated by spin-orbit coupling. Most of the materials present uniaxial anisotropy (Eq. 2.5) or cubic anisotropy (Eq. 2.6 - for cubic lattices) and are described by the following Hamiltonians:

$$\mathscr{H}_u = \sum_i k_u (\mathbf{S}_i \cdot \mathbf{e})^2 \tag{2.5}$$

$$\mathscr{H}_{cub} = -\sum_i \{k^1 (S_x^2 S_y^2 + S_y^2 S_z^2 + S_x^2 S_z^2) + k^2 (S_x^2 S_y^2 S_z^2) + ...\} \tag{2.6}$$

where k_u represents the first order uniaxial anisotropy constant, $\mathbf{S}_i$ the spin vector and e the easy axis direction (here considered z). In the case of cubic anisotropy, the first two terms of the expansion are presented in Eq. 2.6, S_x, S_y, S_z representing the components of the magnetic moments.

Zeeman interaction

The atomic moments can interact with an external magnetic field, this providing a magnetic torque that can be used to switch the direction of the magnetisation, important for recording media applications. The interaction with an external field is called the Zeeman energy and has the following form:

$$\mathscr{H}_{Zeeman} = -\sum_i \mathbf{S}_i \cdot \mathbf{B}_{ext} \tag{2.7}$$

In order to minimize the energy, the atomic moments will align parallel to the magnetic field.

2.3 Ferromagnetic resonance

Ferromagnetic resonance techniques are generally used to study the magnetisation dynamics, where a large DC magnetic field ($\sim$ 1T) is applied to the system together with a small perturbative AC field ($\sim$ 0.01T) that leads to a precessional motion of the magnetisation in the AC field direction. The investigation of ferromagnetic resonance spectra offers the possibility to estimate many magnetic parameters, such as damping, anisotropy, saturation magnetisation or the magnetic g-factor. The ferromagnetic resonance technique has been used in Chapter 4 to investigate the damping and anisotropy parameters at elevated temperatures via the atomistic model approach. The theory behind the resonance conditions has been established by Kittel [33] and is based on the treatment of the magnetic system as a macrospin.

In this section we determine the FMR resonance conditions starting with the simplest assumptions: a classical macrospin that can precess around an external magnetic field, with the damping and anisotropy term neglected. We follow here the discussion from Ref. [33] and [34]. The effective field will be given by the external out-of-plane static field $\mathbf{B}_0$ and the demagnetisation field $\mathbf{B}_d$. The in-plane oscillating field $\mathbf{b}(t) = b\exp(i\omega t)(\hat{x},0,0)$ is small in comparison to the static field, hence it will induce small deviations of the magnetisation ($\delta\mathbf{m}$) around the equilibrium position. The exchange field is also disregarded, since it does not contribute to the total torque due to the coherent rotation of the spins. The magnetisation can be expressed as following:

$$\mathbf{M}(t) = M_S\hat{z} + \delta\mathbf{m}\exp(i\omega t), \quad \delta\mathbf{m} = \delta m_x\hat{x} + \delta m_y\hat{y} + \delta m_z\hat{z} \tag{2.8}$$

Here it is considered that the oscillating field induces small deviation of the magnetisation around the equilibrium position M_S which is constrained. We next express the demagnetising field in terms of the demagnetising tensor :

$$\mathbf{B}_d = -\mu_0 \begin{bmatrix} N_x & 0 & 0 \\ 0 & N_y & 0 \\ 0 & 0 & N_z \end{bmatrix} \begin{bmatrix} \delta m_x \\ \delta m_y \\ M_S + \delta m_z \end{bmatrix} = -\mu_0 \begin{bmatrix} N_x \delta m_x \\ N_y \delta m_y \\ N_z (M_S + \delta m_z) \end{bmatrix} \tag{2.9}$$

The resonance frequency can be calculated by solving the precession equation:

$$\frac{d\mathbf{M}}{dt} = -\gamma \mathbf{M} \times \mathbf{B}_{eff} = -\gamma (\mathbf{M}_S + \delta \mathbf{m}) \times (\mathbf{B} + \mathbf{B}_d) \tag{2.10}$$

Considering :

$$\mathbf{M}_S \times \mathbf{B} = 0 \tag{2.11}$$

$$\delta \mathbf{m} \times \mathbf{B} = \delta m_y B \hat{x} - \delta m_x B \hat{y} \tag{2.12}$$

$$\mathbf{M}_S \times \mathbf{B}_d = (\mu_0 N_y \delta m_y M_S) \hat{x} - (\mu_0 N_x \delta m_x M_S) \hat{y} \tag{2.13}$$

$$\delta \mathbf{m} \times \mathbf{B}_d \approx -(\mu_0 N_z \delta m_y M_S) \hat{x} - (\mu_0 N_z \delta m_x M_S) \hat{y} \tag{2.14}$$

this leads to the following equations:

$$\frac{dM_x}{dt} = -i\omega t \, \delta m_x = -\gamma (\delta m_y B_0 + \mu_0 (N_y - N_z) \delta m_y M_S) \tag{2.15}$$

$$\frac{dM_y}{dt} = -i\omega t \, \delta m_y = -\gamma (-\delta m_x B_0 + \mu_0 (N_z - N_x) \delta m_x M_S) \tag{2.16}$$

The resonance FMR conditions will be given by:

$$\omega_0 = \gamma \sqrt{[B + \mu_0 (N_x - N_z) M_S][B + \mu_0 (N_y - N_z) M_S]} \tag{2.17}$$

For a sphere, where the diagonal components of the demagnetisation matrix are equal leads to:

$$\omega_0^{sphere} = \gamma B \tag{2.18}$$

For a thin film system, with its surface normal parallel to the z axis, the resonance frequency is:

$$\omega_0^{thinfilm} = \gamma (B - \mu_0 M_S) \tag{2.19}$$

The anisotropy field can be included as well in a tensorial form $\mathbf{B}_k = -\mu_0 \tilde{K} \cdot \mathbf{M}$ and leads to a resonance frequency:

$$\omega_0^{anis} = \gamma \sqrt{[B + \mu_0 [(N_x - N_z) + (K_x - K_z)] M_S][B + \mu_0 [(N_y - N_z) + (K_y - K_z)] M_S]} \tag{2.20}$$

For an uniaxial anisotropy, the anisotropy field can be written as $\mathbf{B}_k = \frac{2K_1}{M_S}\hat{z}$, hence the z only component of the anisotropy tensor is $K_Z = -\frac{2K_1}{\mu_0 M_S^2}$ and the resonance frequency of a sphere with uniaxial anisotropy becomes:

$$\omega_0^{uniaxial} = \gamma(B + \frac{2K_1}{M_S}) \tag{2.21}$$

This formula is also valid for systems where the demagnetisation field is negligible.

Spin-wave resonance

In the presence of pinning effects at the surface, spin waves can be excited within the magnetic system [35], as shown in Fig. 2.2. The quantised spin-waves are called magnons. To determine the magnon dispersion and spin-wave resonance frequencies, an exchange contribution in the form Dk^2 will be added into the resonance frequency calculations, where D represents the spin-wave exchange constant:

$$\omega = \gamma(B + \frac{2K}{Ms}) + D(n\pi/d)^2 \tag{2.22}$$

In order to calculate the spin-wave resonance, the magnetic system cannot be treated anymore as a macrospin. The natural step is hence to discretise the magnetic system to an ensemble of local magnetic moments (or spins) which are associated to individual atoms, a framework called atomistic spin dynamics. The development of atomistic spin dynamics has led to the possibility of treating surface effects at the atomistic model and to include thermal variation of the magnetic properties. The atomistic spin dynamics framework is discussed later on in this Chapter and applied for the study of the magnetic properties at elevated temperature, for nm-sized magnetic systems - Chapter 4.

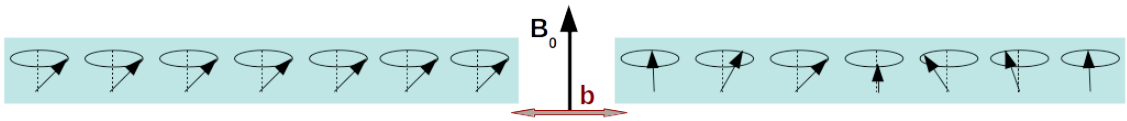

Fig. 2.2 Ferromagnetic resonance for a one-dimensional system. (Left panel) The uniform precession mode ($k = 0$); (Right panel) Non-uniform precessional mode ($k \neq 0$).

2.4 Magnon dispersion

A ferromagnet is perfectly ordered at $T = 0$K, however at non-zero temperature the order will be disturbed by spin-waves, quantised by magnons. The magnon dispersion relation can be deduced following a semi-classical approach, where the magnetic system is discretised in magnetic moments or spins associated to individual atoms. In this Section, the magnon dispersion relation is derived for a ferromagnetic chain with Heisenberg nearest-neighbours exchange interaction, following the approach presented in Blundell [36], Coey [37] and Kittel [33]. The Hamiltonian of spin j can be written as:

$$\mathscr{H}_j = -J\left(\mathbf{S}_j \cdot \mathbf{S}_{j+1} + \mathbf{S}_j \cdot \mathbf{S}_{j-1}\right) \tag{2.23}$$

the effective field being given by:

$$\mathbf{h}_j = J\left(\mathbf{S}_{j+1} + \mathbf{S}_{j-1}\right) \tag{2.24}$$

In the classical approach, the spin angular momentum at site j will equal the torque exerted by the field $\mathbf{h}_j$, the equation of motion being given by:

$$\frac{d\mathbf{S}_j}{dt} = \mathbf{S}_j \times \mathbf{h}_j \tag{2.25}$$

where represents the reduced Planck constant.

The following equations can be easily deduced:

$$\frac{dS_j{}^x}{dt} = S_j^y h_j^z - S_j^z h_j^y, \quad \frac{dS_j{}^y}{dt} = S_j^z h_j^x - S_j^x h_j^z, \quad \frac{dS_j{}^z}{dt} = S_j^x h_j^y - S_j^y h_j^x \tag{2.26}$$

By considering the excitations at each site very small ($S_j^x, S_j^y \ll S_j^z = S$) an approximate set of linear equations can be obtained:

$$\begin{cases} \frac{dS_j{}^x}{dt} = \frac{JS}{}(2S_j^y - S_{j-1}^y - S_{j+1}^y) \\ \frac{dS_j{}^y}{dt} = -\frac{JS}{}(2S_j^x - S_{j-1}^x - S_{j+1}^x) \\ \frac{dS_j{}^z}{dt} = 0 \end{cases} \tag{2.27}$$

By analogy with phonons, we next consider normal mode solutions, $S_j^x = u\,e^{i(jka-\omega t)}$, $S_j^y = v\,e^{i(jka-\omega t)}$, where (u, v) are constants, a is the lattice constant, i the imaginary number and j the atomic site in the chain. In order to have a solution for (u, v), the determinant associated to Eq. 2.27 is required to be zero, this leading to the following equation that needs to be satisfied:

$$\omega = 2JS(1 - cos(ka)) \tag{2.28}$$

For long wavelengths $ka \ll 1$ the dispersion relation can be approximated by $\omega = 2JSa^2k^2$. The coefficient of k^2 is usually referred to as the spin-wave stiffness and can be determined by neutron scattering experiments. Eq. 2.28 represents the magnon dispersion for one-dimensional ferromagnet with isotropic Heisenberg exchange in the nearest-neighbours approximation. Numerically, the spin-wave dispersion can be calculated from the spin-correlation function as shown in Section 3.10.

2.5 Magnetisation switching

For recording media applications, it is necessary to achieve fast and efficient switching of the magnetisation in order to write the information onto the media.

Switching at $T = 0$K with an external field

The simplest way to reverse the dynamics of magnetisation is to apply a magnetic field larger than the anisotropy field, antiparallel to the initial magnetisation orientation - Fig. 2.3, left panel. The switching mechanism can be investigated by approximating the system to a macrospin and solving the LLG equation in the absence of thermal effects.

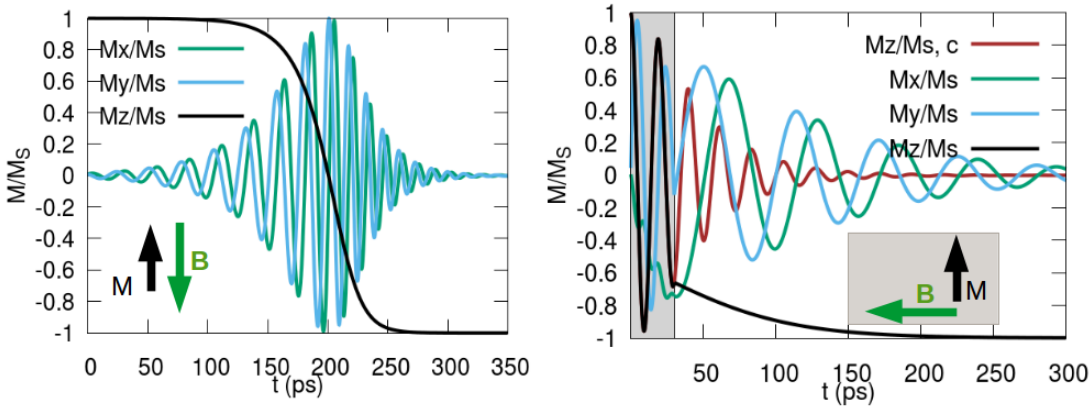

Fig. 2.3 Illustration of magnetisation switching under the application of an antiparallel (left panel) or perpendicular (right panel) external field. In the case of a perpendicular orientation of the external field, a continuous application of the field will trigger a precession of the z component of magnetisation, as shown by the brown line. The grey area shows the region where the field is applied in order to lead to switching.

In the simulations, at $T = 0K$, in the antiparallel orientation of the field and magnetisation there will be no torque and hence no switching. Therefore, usually the magnetisation is initialised with a small angle in order to have a finite torque. For finite temperature simulations and in experiments, there will be always some torque due to the thermal fluctuations that will start the switching.

A more complex way to switch the magnetisation is by applying a field perpendicular to the initial orientation of the magnetisation - Fig. 2.3, right panel, this process being known as precessional switching [38] since the in-plane field triggers a precession of the magnetisation. If the field is applied only for a short time (grey region) in a way that the magnetisation is negative when the field is removed, the system will evolve to a switched state due to the uniaxial anisotropy. This type of switching is usually faster and the field needs to be applied for a shorter time, however it needs a precise control of the pulse time [34]. If the applied field is not stopped at the desired spin orientation, the magnetisation will return to its initial state, in the case of uniaxial anisotropy.

Thermally assisted switching - HAMR

For materials with large anisotropy, such as $L1_0$ FePt, the field necessary for switching cannot be accessible experimentally. In order to lower the anisotropy of the system and record the information, the media is heated by a temperature pulse, technology called Heat Assisted Magnetic Recording (HAMR). The heating process leads to a reduction in the magnetisation and subsequently a reduction in the anisotropy.

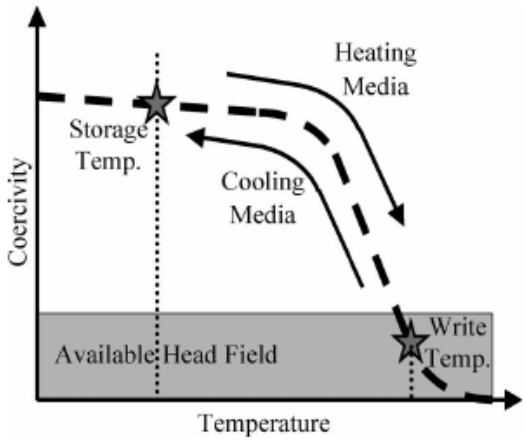

Fig. 2.4 Schematics showing the writing process in HAMR media. Extracted from Ref. [39], ©2008 IEEE.

Fig. 2.4 shows the writing process in HAMR media, that focuses on the variation of the coercivity during the application of the heat pulse. The coercivity of a material is defined based on the magnetic hysteresis as the field where the switching of the magnetisation occurs and depends, in principle, on the anisotropy of the system, the field sweep rate and temperature.

All-optical switching

The heating of a magnetic material can also be done by the application of femtosecond laser pulses at ultrafast time-scales [40]. This allowed the observation of single pulse switching without the necessity of an applied field in ferrimagnets such as GdFe[41]. Fig. 2.5 shows the magnetisation of Gd and Fe sub-lattices during the switching. This switching mechanism appears due to the different demagnetising rates and the antiferromagnetic coupling of the two sub-lattices. Fe demagnetises faster than Gd, and afterwards is magnetised in the Gd direction, leading to the ferromagnetic-like state (around 1.3 ps) [42]. The Fe magnetisation then increases in the switched direction, while Gd is still demagnetising. Due to the antiferromagnetic exchange of the two sub-lattices and the building magnetisation of Fe, Gd reverses after the demagnetisation.

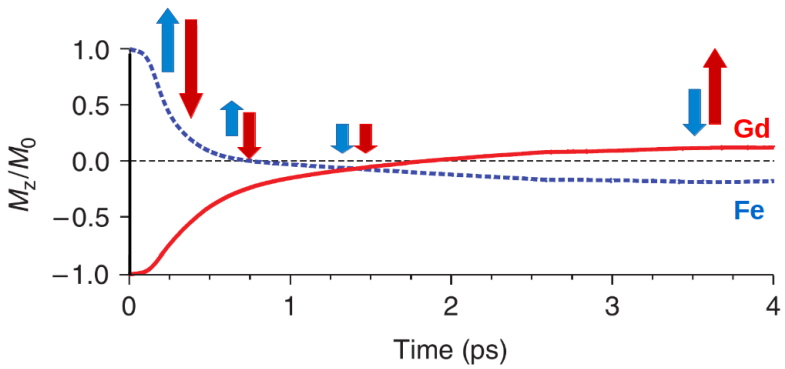

Fig. 2.5 All-optical switching in ferrimagnetic GdFe triggered by the application of a femtosecond laser pulse, extracted from Ref. [41].

2.6 Atomistic spin dynamics

In the atomistic model, the magnetic system is treated as an ensemble of interacting spins, where each spin is associated to a magnetic atom. The reduced magnetisation is used as an

order parameter, for a single material being calculated as :

$$\mathbf{m} = \frac{\mathbf{M}}{M_S} = \frac{1}{N}\sum_{i}^{N}\mathbf{S}_i \tag{2.29}$$

where M_S represents the saturation magnetisation, N represents the total number of spins (atoms) and $\mathbf{S}_i$ the spin vector associated with each atom. The spin vector represents a normalised spin moment (dimensionless) and is given by $\mathbf{S}_i = \mu_i/\mu_s$, where μ_i represents the magnetic moment associated with each atom and μ_s the saturation value of the moment associated with each atom. The reduced magnetisation is equivalent to the ratio between the magnetisation and the saturation magnetisation M_S given by the sum of saturation magnetic moments in the system in the ground state configuration ($M_S V = N\mu_s$ for same-type atoms).

The atomistic Hamiltonian considers only the spins degrees of freedom, and generally can contain the following energy contributions:

$$\mathscr{H} = \mathscr{H}_{exch} + \mathscr{H}_{anis} + \mathscr{H}_{Zeeman} \tag{2.30}$$

where $\mathscr{H}_{exch}$ represents the exchange energy, $\mathscr{H}_{anis}$ the anisotropy energy, usually given by uniaxial anisotropy and $\mathscr{H}_{Zeeman}$ the Zeeman energy due to the interaction with an external applied field. The energy contributions have been described in Section 2.2. The spin-dynamics is given by solving the Landau-Lifshitz-Gilbert equation as described below. The equilibrium magnetic properties such as magnetisation can also be calculated using a Monte-Carlo approach as described in Section 2.7.

LLG equation

Under an external field $\mathbf{H}$ the magnetic moment $\boldsymbol{\mu}$ will precess, the equation describing the dynamics of the magnetic moment being given by:

$$\frac{d\boldsymbol{\mu}}{dt} = -\gamma\,\boldsymbol{\mu} \times (\mu_0 \mathbf{H}) \tag{2.31}$$

where γ represents the gyromagnetic ratio for an electron spin ($\gamma = 1.76 \times 10^{11}$ rad s^{-1}T^{-1}) and $\mu_0 = 4\pi \times 10^{-7}$ Hm^{-1} is the permeability of free space.

In order to add dissipation processes, a damping term needs to be introduced. The damped precession proposed by Landau and Lifshitz [43] has the following form:

$$\frac{\partial \mathbf{M}}{\partial t} = -\gamma \mathbf{M} \times (\mathbf{H} + \alpha(\mathbf{M} \times \mathbf{H})) \tag{2.32}$$

where $\mathbf{M} = \boldsymbol{\mu}/V$ represents the magnetisation and α the damping constant. The LL equation works only in the small damping regime. Gilbert [44] proposed a damping term similar to a viscous force, $\frac{\eta}{M_S}\mathbf{M} \times \frac{\partial \mathbf{M}}{\partial t}$. The equation that describes the evolution of the magnetisation becomes:

$$\frac{\partial \mathbf{M}}{\partial t} = -\gamma \mathbf{M} \times \mathbf{H} + \frac{\eta}{M_S}\mathbf{M} \times \frac{\partial \mathbf{M}}{\partial t} \tag{2.33}$$

The fact that the term $\frac{\partial \mathbf{M}}{\partial t}$ appears in both right and left hand side of the equation, makes it difficult to solve. However, the Gilbert equation can be converted to a Landau-Lifshitz form, an equation known as Landau-Lifshitz-Gilbert (LLG). In the case of atomistic spin dynamics, the LLG equation can be written for each magnetic spin and has the following form:

$$\frac{\partial \mathbf{S}_i}{\partial t} = -\frac{\gamma}{(1+\alpha^2)}\mathbf{S}_i \times (\mathbf{H}_i + \alpha \mathbf{S}_i \times \mathbf{H}_i) \tag{2.34}$$

where $\mathbf{S}_i$ represents the magnetic spin, γ the gyromagnetic ratio, α the phenomenological damping constant and $\mathbf{H}_i$ the effective field acting on spin i. The first term of Eq. 2.34 gives the precession of the magnetic spin around the equilibrium position, while the second term gives the dissipation term, due to the coupling of the spin with the thermal bath. The effective field is deduced from the first derivative of the spin Hamiltonian:

$$\mathbf{H}_i = -\frac{1}{\mu_i \mu_0}\frac{\partial \mathscr{H}}{\partial \mathbf{S}_i} \tag{2.35}$$

Analytical solution of the LLG equation

The LLG equation can be solved analytically in the case when the anisotropy field can be neglected and only an external field H is applied to the system. The solution is given by:

$$S_x(t) = \operatorname{sech}\left(\frac{\alpha\gamma H}{1+\alpha^2}t + A\right)\cos\left(\frac{\gamma H}{1+\alpha^2}t + B\right) \tag{2.36}$$

$$S_y(t) = \operatorname{sech}\left(\frac{\alpha\gamma H}{1+\alpha^2}t + A\right)\sin\left(\frac{\gamma H}{1+\alpha^2}t + B\right) \tag{2.37}$$

$$S_z(t) = \tanh\left(\frac{\alpha\gamma H}{1+\alpha^2}t + A\right) \tag{2.38}$$

where (A, B) are constants of integration and can be deduced from the initial conditions [45]. The above equations can be used for extracting the effective damping for simulated or experimental time-traces of magnetisation. In the case when anisotropy cannot be anymore neglected, there is no universal solution to the LLG equation and obtaining the anisotropy

and effective damping from the time-traces of magnetisation can be done via a grid-search method as presented in Section 4.6.

Langevin dynamics

In order to include the thermal effects, we couple the spin system to a thermostat. There are two key assumptions regarding the thermostat [46]. Firstly, the thermostat has many degrees of freedom, hence the interaction with the spin will dissipate quickly. Also the thermostat remains described by a thermal equilibrium distribution at constant temperature, no matter how much energy and angular momentum is diffusing into the spin system. The second assumption is that the thermostat has no memory.

Numerically the coupling to the thermostat is done by adding a stochastic field $\boldsymbol{\xi}_\mathbf{i}$ to the effective field $\mathbf{H}_\mathbf{i}$, as suggested by Brown [47]:

$$\mathbf{H}_\mathbf{i} = -\frac{1}{\mu_i \mu_0} \frac{\partial \mathscr{H}}{\partial \mathbf{S}_i} + \boldsymbol{\xi}_\mathbf{i} \tag{2.39}$$

The approach is known as Langevin Dynamics and assumes that the thermal fluctuations on each site are given by a Gaussian white noise term, frequency independent, and can be described by the following statistics:

$$\langle \xi_{i\alpha}(t) \rangle = 0 \tag{2.40}$$

$$\langle \xi_{i\alpha}(t) \xi_{j\beta}(s) \rangle = 2D\delta_{\alpha,\beta}\delta_{ij}\delta(t-s) \tag{2.41}$$

where $\langle\rangle$ denotes an average taken over different realisation of the fluctuation field, i, j refer to spin indices, α, β to Cartesian coordinates, t, s to time, δ_{ij} represents the Kroneckers symbol, D refers to the strength of the thermal fluctuations as determined from statistical mechanics considerations. Eq. 2.41 refers to the fact that $\xi_i(t)$ are statistically independent. Eq. 2.41 implies that the stochastic term is local in space and time. The strength of the thermal fluctuations is given by:

$$D = \frac{\alpha k_B T}{\gamma \mu_i} \tag{2.42}$$

where $k_B T$ is the thermal energy and α represents the phenomenological damping.

Numerical integration

For the stochastic LLG equation, one of the simplest integration schemes that can be applied is the Heun method. This is a predictor-corrector scheme, in which the first-step

(predictor) uses an Euler method in order to estimate the initial result, and the next step corresponds to the correction of the initial result.

After each integration step, the spin magnitude needs to be renormalised to unity, as the numerical integration leads to an artificial drift in the magnitude of the spin vector. The LLG equation is solved using the Heun integration scheme which is implemented in the atomistic-spin dynamics software VAMPIRE [21].

Since the spins of individual atoms evolve onto a sphere, geometrical integration can be used, as shown by Depondt-Martens [48]. Semi-implicit schemes such as the ones developed by Mentink *et al.* [49] can allow the increase of the time-step by a factor of 10 compared to the Heun scheme, especially for simple ferromagnetic systems at relatively small temperatures.

Illustration of precession and damping

Fig. 2.6 illustrates the precession of the magnetic moment around the effective field that acts on the spin S_i. The torque ($\mathbf{S}_i \times \mathbf{H}_i$ - blue arrow) induces a precessional motion around the effective field - case a), while the damping term ($\mathbf{S}_i \times (\mathbf{S}_i \times \mathbf{H}_i)$ - green arrow) is perpendicular to the direction of precession and causes the relaxation of the spin towards the equilibrium position given by the direction of the effective field - case b). Below it is plotted the temporal evolution of magnetisation together with the analytical solution given by Eq. 2.36 corresponding to the parameters used in the simulation. In the case of finite temperature simulations, Fig. 2.6, c), the random fluctuations can be observed in the trajectory of the spin and deviation from the analytical solution can be observed.

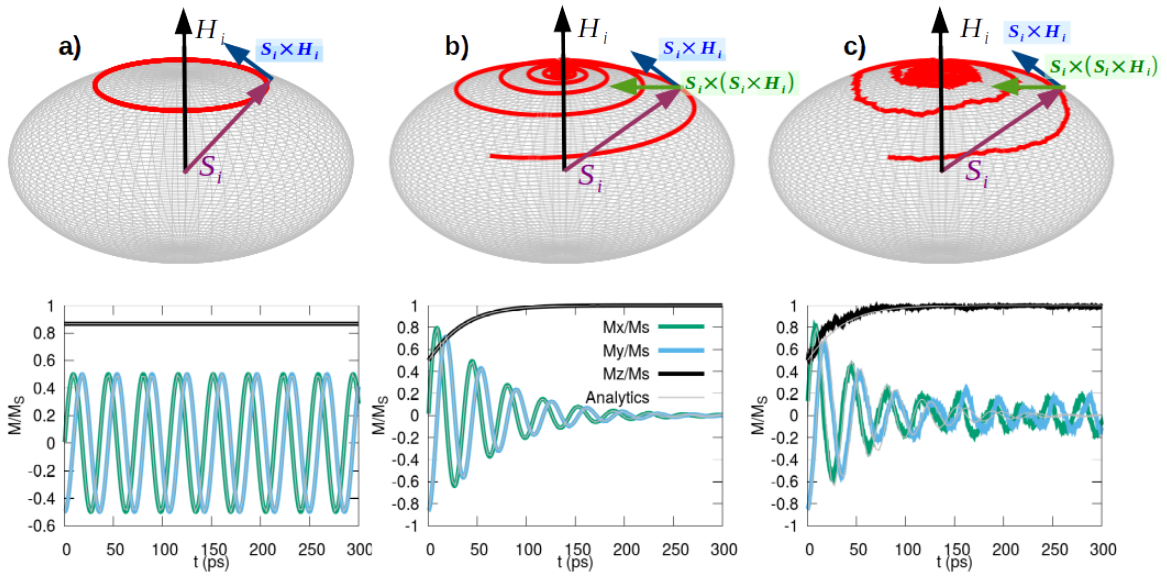

Fig. 2.6 Illustration of spin dynamics for the a) undamped case, b) damped case at $T = 0$K, c) damped case at $T > 0$K. The black arrow illustrates the effective field $\mathbf{H}_i$ that acts on the spin $\mathbf{S}_i$ (purple arrows), together with the precession (blue arrows) and damping (green arrows) energy terms. Below it is plotted the temporal evolution of magnetisation together with the analytical solution given by Eq. 2.36 corresponding to the parameters used in the simulation.

2.7 Monte-Carlo methods

Temperature effects can also be incorporated into the atomistic model by using Monte-Carlo methods. This method is efficient for equilibrium properties, for dynamic properties the stochastic LLG equation needs to be used, since the Monte-Carlo method does not possess an intrinsic time-scale.

Calculations of the properties of a system at thermal equilibrium is based on the calculation of the partition function $Z = \sum_n e^{E_n/k_B T}$ where E_n represents the energy value of a $n-$th state. In practice, the partition function can be calculated only for small systems, as the sum is over all possible states. In order to avoid this problem the equilibrium properties are calculated using the Metropolis algorithm [50]. The Metropolis algorithm samples the energy landscape by going from one state to another with a Boltzmann probability given by the ratio between the difference in total energy between the two states (ΔE) and the thermal contribution ($k_B T$):

$$P = e^{-\Delta E/k_B T} \tag{2.43}$$

Instead of choosing the configurations randomly and weighting them by the Boltzmann factor, the configuration can be chosen with a Boltzmann probability and weighted evenly. After initialising the spin system, the Metropolis algorithm consists in selecting randomly a spin $\mathbf{S}_i$. This spin is then randomly changed to $\mathbf{S}_i'$ and the energy difference between the previous and current state of the same spin is calculated as $\Delta E = E(\mathbf{S}_i') - E(\mathbf{S}_i)$. If $\Delta E < 0$ (lower energy state), the new spin direction $\mathbf{S}_i'$ is accepted. If $\Delta E > 0$, the Boltzmann probability P is calculated via Eq. 2.43. A uniformly distributed random number $r \in [0,1]$ is generated and the probability P is compared with this random number r; if the probability $P > r$, the new spin direction $\mathbf{S}_i'$ is accepted, else the spin state returns to its initial value S_i. This process is repeated until all spins are evaluated. After this, the thermodynamic quantities (e.g. magnetisation, susceptibility) can be calculated for this specific Monte-Carlo step. A more computational efficient method is the one developed by Hinzke and Nowak [51], where the trial move allows the spin to perform either a flip, a random movement within a cone or within a sphere. In the atomistic spin dynamics package VAMPIRE [21], an adaptive algorithm is used, where the cone's width is modified in order to keep an acceptance rate close to 50% [52].

2.8 Temperature dependence of magnetic parameters

The inclusion of the thermal fluctuations of the spins via the stochastic LLG equation at the atomistic level allows the calculation of the temperature dependence of the effective magnetic parameters.

Fig. 2.7 shows the temperature dependence of magnetisation M(T), anisotropy K(T) and susceptibility $\chi(T)$ of the system. The magnetisation and anisotropy curves are calculated via Monte-Carlo integration for a bulk system of FePt and fitted via $M(0)(1-T/T_\mathrm{C})^\beta$ - grey line with the extracted $T_\mathrm{C} = 720$K and $\beta = 0.33$.

At the Curie temperature T_C the system undergoes a phase transition from the ferromagnetic to the paramagnetic state (emphasized by the grey area). The phase transition is marked by a peak in the magnetic susceptibility and no magnetisation or anisotropy. The simulation box is finite, leading to a loss of the criticality associated to the phase transition and a subsequent broadening of the susceptibility divergence. The remanent magnetisation above the Curie temperature is due to the short range correlations that persist above the ordering temperature. The anisotropy decreases faster than the magnetisation at higher temperatures and this can be exploited in thermally assisted switching such as HAMR.

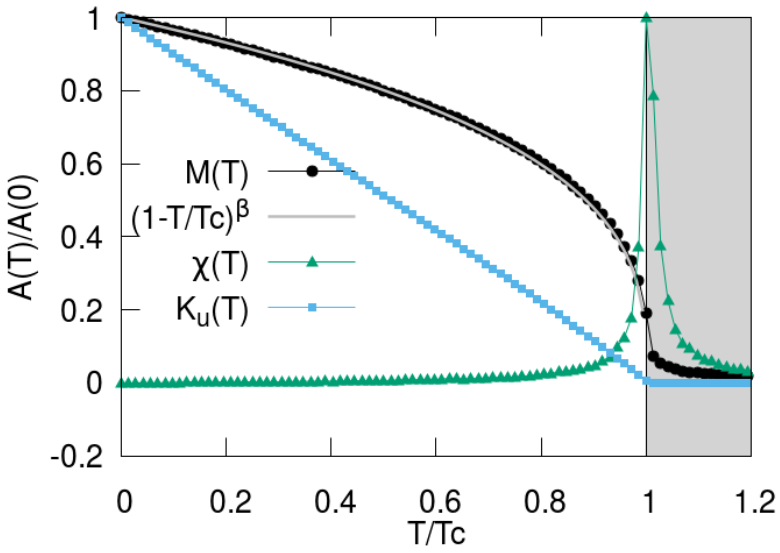

Fig. 2.7 The temperature dependence of different magnetic quantities normalised by their value at $T = 0$K. The temperature dependence of the magnetisation is calculated via Monte-Carlo integration for a bulk system of FePt and fitted via $M(0)(1-T/T_C)^{\beta}$ - grey line with the extracted $T_C = 720$K and $\beta = 0.33$. The scaling law of the anisotropy used for this plot is $K(T) \sim M(T)^3$, exponent corresponding to an uniaxial anisotropy [53]. The susceptibility $\chi(T)$ is calculated during the simulation and shows a peak at $T = T_C$. The grey area emphasizes the region where the system becomes paramagnetic.

2.9 Conclusions

Different magnetic properties are detailed in this Chapter together with the atomistic-spin dynamics framework. We also discuss here additional applications such as ferromagnetic resonance and magnetisation switching which have been investigated via simulations.

3

Atomistic spin-lattice dynamics model

3.1 Introduction

In order to develop competitive magnetic nano-devices, advanced experimental and theoretical frameworks are needed. A complete description of magnetic systems involves the interaction between several degrees of freedom, such as lattice, spins and electrons, modelled in a self-consistent simulation framework. Fig. 3.1 shows the characteristic relaxation and interaction timescales of the degrees of freedom in a magnetic material. Electrons relax very fast ($\approx$ 1 fs) in comparison with spins and phonons, hence the first assumption in a spin-lattice dynamics framework is to consider the electronic degrees of freedom in equilibrium. The fastest experiments in magnetism that probe the magnetisation dynamics via ultrafast laser pulses also consider the electrons in equilibrium during the probe time. As the relaxation time in spin and lattice can be in the same order of magnitude (ps), the two degrees of freedom need to be treated in a self-consistent framework, called spin-lattice dynamics (SLD) [54–61]. Although in Ref. [56] the timescale of spin-lattice coupling is in the order of 100ps, recent experiments that show an ultrafast Einstein-de Haas effect [62] suggest a much faster time-scale of the spin-lattice coupling of under a picosecond. An overview of the current SLD framework is presented in Section 3.2.

With the emergent field of ultrafast magnetisation dynamics [40] the flow of energy and angular momentum between electrons, spins and phonons under the excitation of the ultrashort laser pulses is intensively studied [62–65]. SLD models can be crucial to disentangle the interplay between these sub-systems, being successfully employed for the study of phenomena such as the Einstein-de-Haas effect [66, 60, 67] that appears due to angular momentum conservation. Phonons strongly pumped in the THz regime by laser excitation can modulate the exchange field and manipulate the magnetisation as shown for the magnetic insulator YIG [68] or in Gd [69]. The excitation of THz phonons leads to a magnetic response

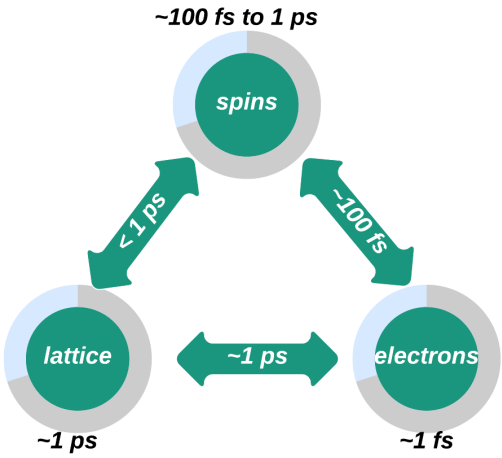

Fig. 3.1 Overview of characteristic timescales in the Spin-Lattice dynamics framework (adapted from Ref. [56]). Recent experiments that show an ultrafast Einstein-de Haas effect [62] suggest a much faster time-scale of the spin-lattice coupling of under a picosecond, in contrast with the 100ps timescale in Ref. [56].

with the same frequency in Gd [69], proving the necessity of considering the dynamics of both lattice and spins. Phonon excitations can modulate both anisotropy and exchange which can successfully manipulate [70–72] or potentially switch the magnetisation [73, 74], ultimately leading to the development of low-power memories. The control of magnetisation via THz phonons has been discussed in detail in Section 5.3.

Magnetisation relaxation is governed by the damping mechanism. Conventional modelling employs a phenomenological description of damping whereby the precession equation of motion is augmented by a friction-like term (LLG equation), which represents the coupling of the magnetic modes (given primarily by the atomic spin) with the non-magnetic modes (phonons) or electron orbital moments, presented in Section 1.1.2. As current models of magnetisation dynamics such as atomistic spin dynamics considers a fixed lattice, the contribution from the magnon-phonon interaction is not explicitly modelled. Via the employment of Spin-Lattice Dynamics we can include magnon-phonon scattering events, which contribute consistently to the effective damping, as shown in Section 5.2. The magnon-phonon damping mechanism is particularly important for modelling magnetic insulators, such as YIG, where it has been shown that magnon-phonon scattering leads to the damping mechanism [75].

3.2 Overview of SLD models

Over the past few years, spin-lattice models have been increasingly used to study magnetic phenomena. Initially the SLD model has been used by Ma *et al.* [57, 76, 58] for BCC Fe, followed by Beaujouan *et al.* [56] who used the framework to model Cobalt nanowires. The employment of SLD models would have not been possible without the development of symplectic integration algorithms based on the Suzuki-Trotter decomposition [77] that conserve the energy and norm of the spin. Further details regarding the integration scheme for spin-lattice models is presented in Section 3.4.

Depending on what research problem is investigated via the SLD model, either a micro-canonical ensemble (NVE) or canonical ensemble (NVT) has been used. The microcanonical ensemble has been used by Assmann *et al.* [60] to investigate the angular momentum transfer between spin and lattice. More precisely, they have used an SLD model to look at the ultrafast Einstein-de-Haas effect that showed a rotation of the system associated with a change in the total magnetisation of the sample, rotation that appears due to the conservation law of angular momentum. To simulate the modelled systems at different temperatures it is necessary to initially deposit different amounts of energy in the system which then will be transferred to spin and lattice sub-systems until reaching thermal equilibrium.

The canonical ensembles (NVT) have been extensively used by Ma *et al.* [78, 57] to investigate BCC Fe. Here two Langevin thermostats are assumed, each connected individually to the lattice and spin degrees of freedom. After sufficient time interacting with a thermostat, the system will reach thermal equilibrium. The dynamics of a degree of freedom cannot affect the properties of the thermostat, which is not true for the SLD dynamics as spins can modify the properties of the phonons that can act as a thermostat for the spin system. This is problematic especially for insulators, where the only dissipation mechanism in the spin system is through phonons. Hence, although the model presented in the current Chapter can include two thermostats, for the above reasoning, we consider a single thermostat that acts on the lattice degrees of freedom only, the spin system being thermalised by spin-lattice coupling only.

One important aspect that differs between different SLD models presented in the literature is the spin-lattice coupling term. The coupling of spins to the lattice and vice versa is assured by the spatial dependence of the magnetic interactions. Some SLD models assume the presence only of exchange interaction in the system [61], which due to its isotropic nature, conserves the total angular momentum of the system as shown in Appendix A. Hence, an additional coupling term is necessary for the transfer between the lattice and spin degrees of

freedom so as to mimic the effect of spin-orbit coupling. For this, several coupling terms have been proposed in the literature [54–56] as discussed in Section 3.6.

Although the SLD models have increased in popularity, there are certain aspects that have not been entirely addressed. Damping due to spin-lattice interaction only, within the canonical ensemble (NVT) has not been addressed, this step being of interest for example in future modelling of magnetic insulators at finite temperature, a systematic investigation being performed in Section 5.2. The magnon and phonon spectra together with the characteristics of the induced spin noise are shown in Sections 3.9, 3.10, 3.11.

3.3 Equations of motion

The lattice and the magnetic system can directly interact with each other via the position and spin dependent Hamiltonian. The total Hamiltonian of the system will consist of a lattice H_{lat} and magnetic component H_{mag}:

$$H_{tot} = H_{lat} + H_{mag} \tag{3.1}$$

The lattice Hamiltonian includes the classical kinetic and potential energies:

$$H_{lat} = \sum_i \frac{\mathbf{p}_i^2}{2m_i} + \sum_{i<j} U(r_{ij}) \tag{3.2}$$

Our model includes a harmonic potential (HP) defined as :

$$U(r_{ij}) = \begin{cases} V_0(r_{ij} - r_{ij}^0)^2/a_0^2 & r_{ij} < r_c \\ 0 & r_{ij} > r_c \end{cases} \tag{3.3}$$

where V_0 has been parameterised for BCC Fe in [60] and $a_0 = 1$Å is a dimension scale factor. To be more specific we consider the equilibrium distances r_{ij}^0 corresponding to a symmetric BCC structure. The interaction cutoff is $r_c = 7.8$ Å. The harmonic potential has been used for simplicity, however it can lead to a rather stiff lattice for a large interaction cutoff.

Another choice of the potential used in our model is a Morse potential (MP) parameterised in [79] for BCC Fe and defined as:

$$U(r_{ij}) = \begin{cases} D[e^{-2\alpha(r_{ij}-r_0)} - 2e^{-\alpha(r_{ij}-r_0)}] & r_{ij} < r_c \\ 0 & r_{ij} > r_c \end{cases} \tag{3.4}$$

The harmonic and Morse potential have been used for simplicity, however other options can be considered such as embedded atom potential [80, 81]. The properties of the phonons given by the two choices of the potential are given in Section 3.9.

The magnetic Hamiltonian (H_{mag}) used in our simulations consists of exchange coupling (H_{exch}) and spin-orbit coupling in the form of pseudo-dipolar coupling (H_c).

$$H_{mag} = H_{exch} + H_c \tag{3.5}$$

$$H_{exch} = -\sum_{i,j} J(r_{ij})(\mathbf{S}_i \cdot \mathbf{S}_j) \tag{3.6}$$

$$H_c = -\sum_{i,j} f(r_{ij}) \left[(\mathbf{S}_i \cdot \hat{\mathbf{r}}_{ij})(\mathbf{S}_j \cdot \hat{\mathbf{r}}_{ij}) - \frac{1}{3}\mathbf{S}_i \cdot \mathbf{S}_j \right] \tag{3.7}$$

The form of exchange $J(r_{ij})$ used in our simulations for BCC Fe was calculated from first principle methods by Ma *et al.* [57] and it follows the dependence:

$$J_{ij} = J_0 \left(1 - \frac{r_{ij}}{r_c}\right)^3 \Theta(r_c - r_{ij}) \tag{3.8}$$

where r_c is the cutoff and $\Theta(r_c - r_{ij})$ is the Heaviside step function. The pseudo-dipolar coupling term is very localised and, for simplicity, it is assumed proportional to the exchange strength: $f(\mathbf{r}_{ij}) = CJ_0(a_0/r_{ij})^4$ as presented in [60] with C the constant of proportionality and $a_0 = 1$Å a dimension scale factor. For testing reasons, other forms of spin-lattice coupling terms have been considered and will be presented in Section 3.6.

The total Hamiltonian will depend on $\mathbf{p}_i = m\mathbf{v}_i$, $\mathbf{r}_i$ and $\mathbf{S}_i$ degrees of freedom. Hence in order to obtain the dynamics of our coupled system, we need to solve the following equations of motion (EOM):

$$\frac{\partial \mathbf{r}_i}{\partial t} = \mathbf{v}_i \tag{3.9}$$

$$\frac{\partial \mathbf{v}_i}{\partial t} = \frac{\mathbf{F}_i}{m_i}, \qquad \mathbf{F}_i = -\frac{\partial H_{tot}}{\partial \mathbf{r}_i} - \eta m_i \mathbf{v}_i + \Gamma_i \tag{3.10}$$

$$\frac{\partial \mathbf{S}_i}{\partial t} = -\gamma \mathbf{S}_i \times \mathbf{H}_i, \quad \mathbf{H}_i = -\frac{\partial H_{tot}}{\partial \mathbf{S}_i} \tag{3.11}$$

where $\mathbf{F}_i$ and $\mathbf{H}_i$ represent the effective force and field, Γ_i represent the fluctuation term (thermal force) and η represents the friction term that controls the dissipation into the lattice. The strength of the fluctuation term can be calculated by converting the dissipation equations

Quantity	Symbol	Value	Units
Exchange [57]	J_0	0.904	eV
	r_c	3.75	Å
Harmonic potential [60]	V_0	0.15	eV
	r_c	7.8	Å
Morse potential [79]	D	0.4174	eV
	α	1.3885	Å
	r_0	2.845	Å
	r_c	7.8	Å
Magnetic moment	μ_s	2.22	μ_B
Coupling constant	C	0.5	
Mass	m	55.845	u
Lattice constant	a	2.87	Å
Lattice damping	η	0.6	s^{-1}

Table 3.1 Parameters used in the spin-lattice model to simulate BCC Fe.

into a Fokker-Planck equation and then calculating the stationary solution. The thermal force will have the form of a Gaussian noise:

$$\langle \Gamma_{i\alpha}(t) \rangle = 0, \quad \langle \Gamma_{i\alpha}(t) \Gamma_{j\beta}(t') \rangle = \frac{2\eta k_B T}{m_i} \delta_{\alpha,\beta} \delta_{ij} \delta(t-t') \tag{3.12}$$

The integration scheme used to solve the EOM is described in Section 3.4. The parameters used in the simulation to model BCC Fe are presented in Table 3.1.

3.4 Integration algorithm

The integration scheme needs to pass the test of the conservation of energy in the micro-canonical ensemble, proven analytically in Appendix A and the conservation of angular momentum, for exchange only magnetic systems. The Heun scheme employed in atomistic spin dynamics fails to conserve the energy of the system due to the fact that the rotation of the spin is approximated by a series of translations, which will result in an artificial addition or subtraction of energy from the system. Hence a symplectic integrator based on Suzuki-Trotter decomposition (STD) needs to be adopted [82] known for its numerical accuracy and stability. The scheme allows it to deal with non-commuting operators, such as in the case of spin-lattice models and conserves the energy and space-phase volume (hence its symplectic nature). Considering the generalized coordinate $\mathbf{X} = \{\mathbf{r}, \mathbf{v}, \mathbf{S}\}$ the equations of motion can be rewritten using the Liouville operators:

$$\frac{\partial \mathbf{X}}{\partial t} = \hat{L}\mathbf{X}(\mathbf{t}) = (\hat{L}_r + \hat{L}_v + \hat{L}_S)\mathbf{X}(t) \tag{3.13}$$

The solution for the Liouville equation is $\mathbf{X}(t+\Delta t) = e^{L\Delta t}\ \mathbf{X}(t)$. Hence, following the form of this solution and applying a Suzuki-Trotter decomposition as in Tsai's work [83, 84], we can write the solution as:

$$\mathbf{X}(t+\Delta t) = e^{\hat{L}_s(\Delta t/2)} e^{\hat{L}_v(\Delta t/2)} e^{\hat{L}_r(\Delta t)} e^{\hat{L}_v(\Delta t/2)} e^{\hat{L}_s(\Delta t/2)} \mathbf{X}(\Delta t) + O(\Delta t^3) \tag{3.14}$$

where L_s, L_v, L_r are the Liouville operators for the spin, velocity and position. This update can be abbreviated as **(s, v, r, v, s)** update. The velocity and position are updated using a first order update, however the spin needs to be updated using a Cayley transform, due to the fact that the norm of each individual spin needs to be conserved.

$$e^{\hat{L}_v \Delta t}\mathbf{v}_i = \mathbf{v}_i + \frac{\Delta t}{m_i}\mathbf{F}_i \tag{3.15}$$

$$e^{\hat{L}_r \Delta t}\mathbf{r}_i = \mathbf{r}_i + \Delta t \mathbf{v}_i \tag{3.16}$$

$$e^{\hat{L}_S \Delta t}\mathbf{S}_i = \frac{\mathbf{S}_i + \Delta t \mathbf{H}_i \times \mathbf{S}_i + \frac{\Delta t^2}{2}((\mathbf{H}_i \cdot \mathbf{S}_i)\mathbf{H}_i - \frac{1}{2}\mathbf{H}_i^2 \mathbf{S}_i)}{1 + \frac{1}{4}\Delta t^2 \mathbf{H}_i^2} \tag{3.17}$$

The spin equations of motion depend directly on the neighbouring spin orientations (through the effective field) hence individual spins do not commute with each other. We need to further decompose the spin system $\hat{L}_s = \sum_i \hat{L}_{s_i}$. The following decomposition will be applied for the spin system:

$$e^{\hat{L}_s(\Delta t/2)} = e^{\hat{L}_{s1}(\Delta t/4)} \ldots e^{\hat{L}_{sN}(\Delta t/2)} \ldots e^{\hat{L}_{s1}(\Delta t/4)} + O(\Delta t^3) \tag{3.18}$$

The rotation of a single spin is analytically solvable hence no numerical dissipation of the total energy is present, which leads to the symplecticity of the method [58]. The accuracy of the integration is assured by testing the conservation laws for energy for the NVE setup for different coupling terms, as shown in Section 3.6.

3.5 Code development

The initial spin-lattice code was inherited from our collaborator, Dr. Matthew Ellis [85]. The code was initially written with GP-GPU acceleration, however the integrator used in his approach was updating the spin simultaneously, this leading to an unstable integration of the spin system for NVE conditions. The results presented by Dr. Matthew Ellis [85] were not affected by this issue, as they were performed always with a Langevin thermostat coupled to the spin sub-system, where total energy conservation was not necessary due to the constant transfer of energy from the system to the thermostat. Since individual spins do not commute with each other, a Suzuki-Trotter decomposition for the spin sub-system is needed. Due to the Suzuki-Trotter algorithm, the integration of the spin system was done in serial with parallelisation of the mechanical part via OpenMP.

The flowchart of the code is presented in 3.2 and shows the main features of the SLD code. There are a couple of simulations that can be performed via the SLD software:

- Magneto-elastic calculations - $stretch\_lattice()$. This program distorts the system into a direction and calculates the anisotropy energy resulting from magneto-elastic effects.
- Damping calculations - $calc\_damping()$. This program rotates coherently the spin system with a certain angle. During the relaxation in a large applied field, the damping can be calculated.
- Temperature pulse - $temp\_pulse()$. This program applies a square temperature pulse to the system between some user-input initial and final time with a maximum constant temperature defined by T_{max}
- THz pulse - $thz\_pulse()$. This program applies to the system a square THz pulse between some user-input initial and final time. The THz pulse is defined by a user-input frequency.
- Correlations - $correlations()$. This program computes the auto-correlation function for specific k points and outputs the magnon and phonon spectra.

For some of the calculations it is needed to start the system as close as possible to thermal equilibrium in order to reduce the computational time, hence a preconditioning algorithm needs to be applied to the system. In order for the system to relax faster to equilibrium, we enable the usage of a spin damping equal to $\lambda_{max} = 0.01$ and a maximum coupling value of $C_{max} = 0.5$ during the first step of preconditioning - Fig. 3.2. The spin damping and coupling value allows the system to reach more quickly thermal equilibrium. The second

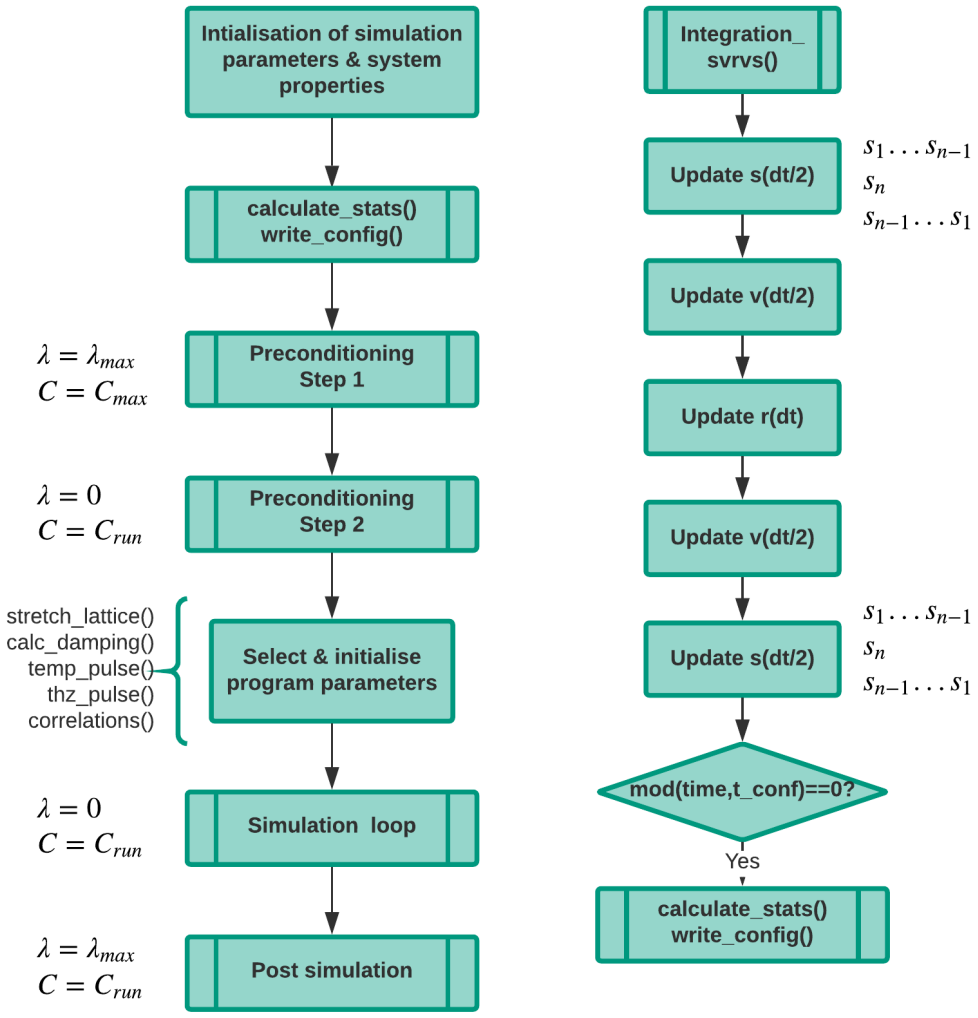

Fig. 3.2 Flowchart of SLD code. The left column shows the main blocks of calculations for an SLD simulation. The preconditioning, simulation and post-simulation blocks loop over a defined number of integration steps. The right column is a representation of the integration algorithm.

step of preconditioning involves integrating the system in the absence of spin damping and for the desired value of the coupling term. In the case of the usage of different coupling strength, this allows the system enough time to evolve in the presence of the new value of the coupling field. After the preconditioning process, the properties of the system are written into a configuration file. The preconditioning is performed only for some particular simulations, for the setups evolved in the testing of the model, no preconditioning is performed. After preconditioning, we start the simulation loop that performs the integration over a specified

number of time-steps. As the dynamics in the presence of spin-lattice damping only is slow due to the small magnon-phonon damping, we then integrate the system after the simulation time in the presence of a large spin damping to make sure that the state reached during the simulation loop is an equilibrium state.

The integration flowchart is presented in Fig. 3.2, right. Before updating the spin, position and velocity, the magnetic fields and mechanical forces are calculated. At the end of the integration, properties such as spin and lattice temperature, energy components and average quantities are calculated and output to a file.

3.5.1 Parallelisation

The parallelisation of the code has been done via OpenMP for the mechanical degrees of freedom. The magnetic degrees of freedom are treated in serial. The speedup is shown in Fig. 3.3 for -O2 compilation flag for 2 system sizes. The enabling of -O2 offers a speedup of almost a factor of 2 compared to -O0. Running on 2 and 4 threads the performance is not very different from the ideal trend. However moving to 8 threads, the speedup is insignificant compared to 4 threads.

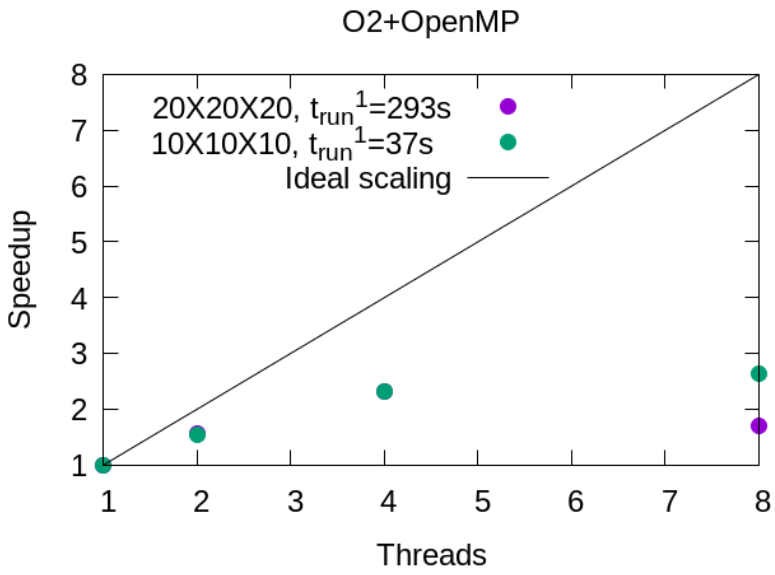

Fig. 3.3 Speedup as function of number of threads for -O2 compilation

The Suzuki-Trotter decomposition implies a serial update of the magnetic degrees of freedom. However, separating the spin system into non-interacting blocks, it is possible to parallelise the algorithm [58]. For a 1D chain of 10 atoms, if we consider the interaction range limited to second nearest neighbours, atom 1 interacts with 2 and 3, however does not

interact with 4. The Suzuki-Trotter update for the spin sub-system can be written as following: 1, 2, 3, 4,... 9, 10, 9, ...4, 3, 2, 1. As atom 1 does not interact with atom 4 and 7, these can be updated at the same time. Hence the update sequence can be split in non-interacting blocks of atoms, where, inside each block, all the atoms are updated simultaneously. For the system sizes modelled in this thesis, the parallelisation of the mechanical integration brings a sufficient speedup to the calculations, however, to model large system sizes more efficiently, parallelisation schemes such as the one presented by Ma *et al.* [58] are necessary.

3.6 Phenomenological spin-orbit coupling terms

First developments of the SLD models suffered from the fact they did not allow angular momentum transfer between lattice and spin. In Appendix A we show that, for a system where the magnetisation dynamics lacks the damping term, for symmetric exchange only Hamiltonian, both energy and angular momentum are conserved. To enable transfer of angular momentum an additional coupling term is necessary in order to mimic the effect of spin-orbit coupling due to symmetry breaking of the local environment. The coupling term needs to obey the physical tests such as conservation of total energy of the system, within the NVE setup. However, several coupling terms suffer from the fact that they induce a collective motion of the atoms in the saturated magnetic state, hence a constant drift in the total energy of the system. This aspect, together with different forms of coupling has been investigated in the next sections.

3.6.1 Simple coupling - Karakurt *et al.* [54]

Karakurt *et al.* [54] has proposed a very simple coupling that will mimic the spin-orbit coupling form $\mathbf{L}\cdot\mathbf{S}$, where $\mathbf{L}$ is the orbital moment. The coupling has the following form:

$$H^i_{anis} = -C\sum_j \mathbf{S}_i \cdot \mathbf{r}_{ji} \tag{3.19}$$

leading to the following dependence of the magnetic fields $\mathbf{h}^i$ and mechanical forces $\mathbf{f}^i$:

$$h^i_x = C/\mu_i \sum_j x_{ij} \quad h^i_y = C/\mu_i \sum_j y_{ij} \quad h^i_z = C/\mu_i \sum_j z_{ij} \tag{3.20}$$

$$f^i_x = C\sum_j Sx^i \quad f^i_y = C\sum_j Sy^i \quad f^i_z = C\sum_j Sz^i \tag{3.21}$$

At $T = 0$K, the magnetic system is saturated. Let's assume the spin configuration is $\mathbf{S} = (0,0,1)$, hence a constant force f_z will act on the atoms as shown in Fig. 3.4(right). This is in contrast with the exchange forces Fig. 3.5 (right) which do not present a net force in a single direction. For the following simulations, the magnetisation is initialised out of plane with $Sz = 0.99$ and small random in-plane components. This leads to an initial spin temperature of about $T_S = 50$K. The lattice is also initialised at a temperature of $T = 300$K. The simulation is set up for an NVE calculation. The constant coupling force that appears on z leads to an uniform translational motion on the z direction, which is non-physical. Although the mechanical forces that appear due to magnetic contributions are usually small, for long time-scale simulations, the uniform displacement will be significant and will lead to a constant pump of energy in the system and a linear increase of the temperature, as shown in Fig. 3.6.

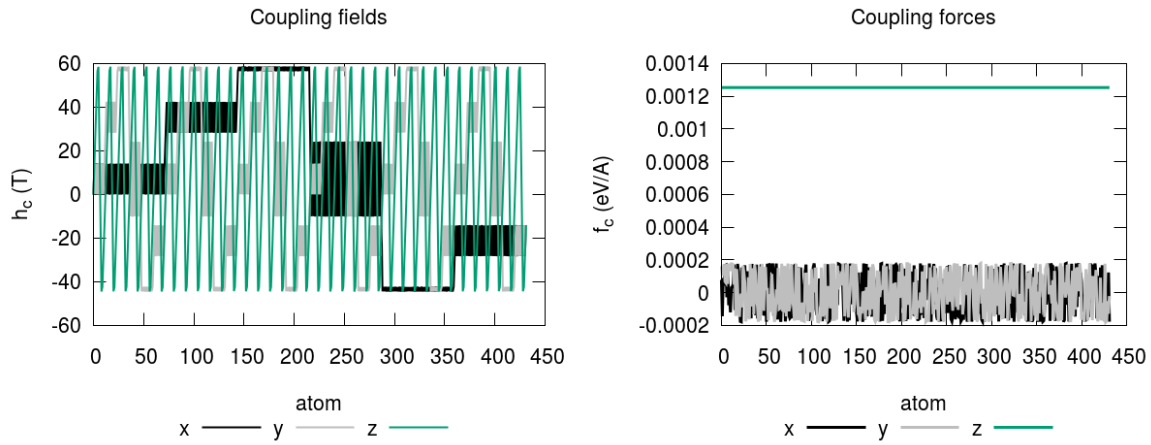

Fig. 3.4 Components of the coupling field and force for a simple spin-lattice coupling (Karakurt *et al.* [54]), $C = 0.0001$, $Sz = 0.99$.

In reality every system is attached to a substrate, which can prevent translational or rotational movements of the system. It is also possible to fix the center of mass of the system or subtract the averaged forces so as to cancel out the translation motion, however this makes the simulation slower. Although these fixes can be added into the code in order to prevent the collective motion of the atoms, we preferred employing a coupling term that does not have any translational artefacts and obeys the physical test of conservation of energy.

3.6.2 Anisotropy coupling - Perera *et al.* [55]

Perera *et al.* [55] have proposed a form of local anisotropy to model the spin-orbit coupling phenomenon due to symmetry breaking of the local environment. Their approach was

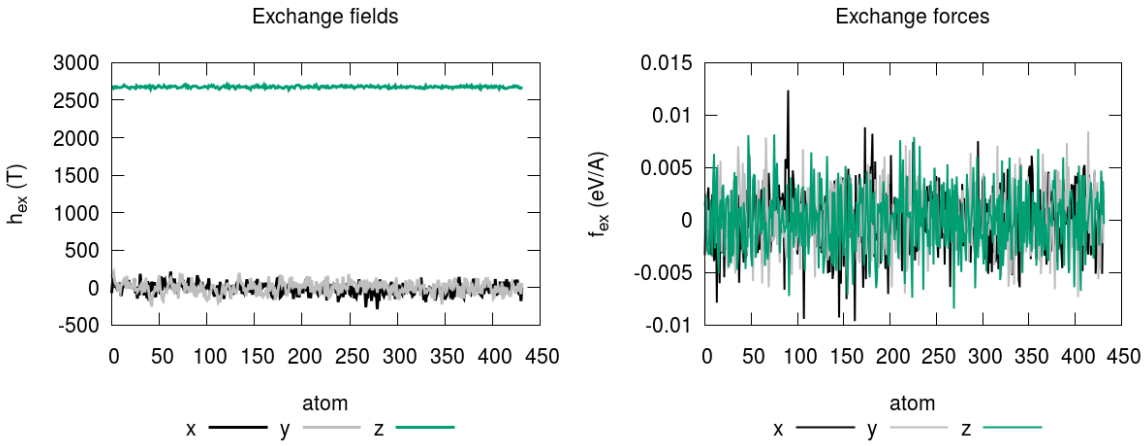

Fig. 3.5 Components of exchange fields and forces for a simple spin-lattice coupling (Karakurt *et al.* [54]), $C = 0.0001$, $Sz = 0.99$.

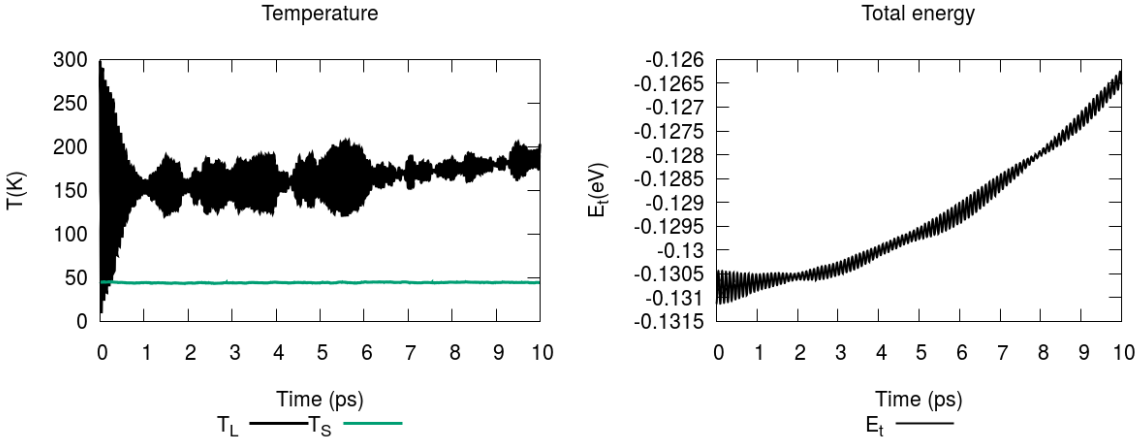

Fig. 3.6 Temperature and energy variation for a magnetic system coupled by a simple spin-lattice coupling (Karakurt *et al.* [54]), $C = 0.0001$, $Sz = 0.99$.

successful in thermalising the subsystems in the absence of a spin thermostat. The coupling energy used in their work is:

$$H_{anis} = -C_1 \sum_{i=1}^{N} \mathbf{K}_i \mathbf{S}_i - C_2 \sum_{i=1}^{N} \mathbf{S}_i^T \Lambda_i \mathbf{S}_i \tag{3.22}$$

where C_1, C_2 are in units of eV. We first analyse the first term of the coupling energy, $-C_1 \sum_{i=1}^{N} \mathbf{K}_i \mathbf{S}_i$ with $\mathbf{K}_i$ defined as:

$$\mathbf{K}_i = \sum_{j,j\neq i} \nabla_{\mathbf{r}_i}\phi = \sum_{j,j\neq i} \nabla_{\mathbf{r}_i}\left[(1-r_{ij}/r_c)^4 \exp(1-r_{ij}/r_c)\right] \tag{3.23}$$

The magnetic forces that act on the lattice are given by:

$$\mathbf{f} = -\frac{\partial H_{anis}}{\partial \mathbf{r}_{ij}} = -\frac{\partial H_{anis}}{\partial |r_{ij}|}\hat{\mathbf{r}_{ij}} \tag{3.24}$$

$$f_i^{\alpha} = \frac{\partial}{\partial \alpha}(K_i^x S_i^x + K_i^y S_i^y + K_i^z S_i^z),\ \alpha = x,y,z \tag{3.25}$$

where:

$$K_i^{\alpha} = \sum_{j,j\neq i}\left[-\frac{\alpha}{r_c r_{ij}}(1-r_{ij}/r_c)^3(5-r_{ij}/r_c)\exp(1-r_{ij}/rc)\right],\ \alpha = x,y,z \tag{3.26}$$

For a particle **i** the forces given by one interaction with a particle **j**:

$$f^{\alpha} = S^x\frac{\partial K^x}{\partial \alpha} + S^y\frac{\partial K^y}{\partial \alpha} + S^z\frac{\partial K^z}{\partial \alpha},\ \alpha = x,y,z \tag{3.27}$$

where K^{α} is given by:

$$K^{\alpha} = \frac{\partial \phi}{\partial \alpha} = \frac{\partial (1-r_{ij}/r_c)^4 \exp(1-r_{ij}/r_c)}{\partial \alpha}, \alpha = x,y,z \tag{3.28}$$

The forces can be re-written in matrix form as:

$$\begin{bmatrix} f^x \\ f^y \\ f^z \end{bmatrix} = \begin{bmatrix} \frac{\partial^2\phi}{\partial x^2} & \frac{\partial^2\phi}{\partial x\partial y} & \frac{\partial^2\phi}{\partial x\partial z} \\ \frac{\partial^2\phi}{\partial y\partial x} & \frac{\partial^2\phi}{\partial y^2} & \frac{\partial^2\phi}{\partial y\partial z} \\ \frac{\partial^2\phi}{\partial z\partial x} & \frac{\partial^2\phi}{\partial z\partial y} & \frac{\partial^2\phi}{\partial z^2} \end{bmatrix} \begin{bmatrix} S^x \\ S^y \\ S^z \end{bmatrix} \tag{3.29}$$

Considering the following substitutions:

$$\begin{aligned} 1 - r_{ij}/r_c &= ra \\ \frac{e^{ra} ra^2}{r_c^2} &= A \\ (ra+6)(ra+2) &= B \\ \frac{r_c}{r_{ij}} ra(ra+4) &= C \\ (x_j - x_i)/r_{ij} &= dx \\ (y_j - y_i)/r_{ij} &= dy \\ (z_j - z_i)/r_{ij} &= dz \end{aligned} \tag{3.30}$$

Finally, the magnetic forces that act on the system are:

$$\begin{aligned} f^x &= S^x A\left[Bdx^2 - C(dy^2 + dz^2)\right] + S^y Adxdy(B+C) + S^z Adxdz(B+C) \\ f^y &= S^x Adydx(B+C) + S^y A\left[Bdy^2 - C(dx^2 + dz^2)\right] + S^z Adydz(B+C) \\ f^z &= S^x Adzdx(B+C) + S^y Adzdy(B+C) + S^z A\left[Bdz^2 - C(dx^2 + dy^2)\right] \end{aligned} \tag{3.31}$$

Similarly, the effective fields that act on the atoms can be written as:

$$\mathbf{h}_i = -\frac{\partial H_s}{\partial \mathbf{S}_i} = C_1 \mathbf{K}_i = C_1 \sum_{j,j\neq i} \nabla_{\mathbf{r}_i} \phi = C_1 \sum_{j,j\neq i} \nabla_{\mathbf{r}_i} \Big((1 - r_{ij}/r_c)^4 \exp(1 - r_{ij}/r_c) \Big) \tag{3.32}$$

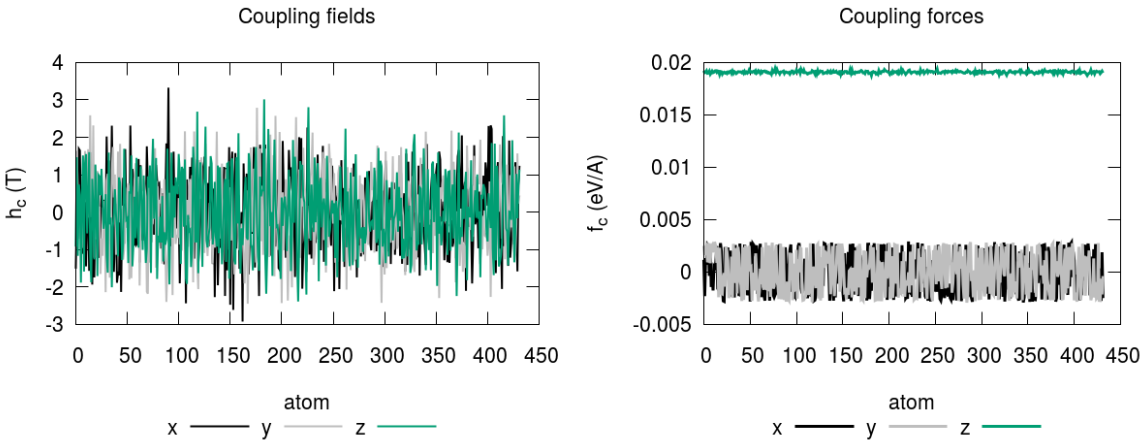

Fig. 3.7 Components of the coupling field and force for a on-site spin-lattice coupling (Perera *et al.* [55]), $C_1 = 0.05$, $Sz = 0.99$.

In a magnetic saturated state, for $\mathbf{S} = (0,0,1)$, a non-zero force appears on all three components of the forces. Considering now a chain of atoms, displacing only in a single direction, such as x direction, while $y = z = 0$, the only remaining force will be on the saturation direction, z. The same happens considering a displacement only on y or z. Hence we expect to have a net force in a magnetised state that will lead to a translation of the system. This can also be observed by calculating for a magnetised system of $Sz = 0.99$ with a small random in-plane magnetisation - Fig. 3.7. The non-zero force on z direction leads to a translational motion of the system and a constant increase of the total energy of the system, hence this form of the coupling term is also unsatisfactory.

3.6.3 Pseudo-dipolar coupling - Akhiezer [86]

In the SLD simulations presented in this work, the spin-lattice coupling used is the pseudo-dipolar coupling:

$$H_c = -\sum_{i,j} f(r_{ij}) \left[(\mathbf{S}_i \cdot \hat{\mathbf{r}}_{ij})(\mathbf{S}_j \cdot \hat{\mathbf{r}}_{ij}) - \frac{1}{3}\mathbf{S}_i \cdot \mathbf{S}_j \right] \tag{3.33}$$

The origin of the term still lies in spin-orbit interaction, appearing from the dynamical crystal field that affects the electronic orbitals and spin states and it has been employed previously in SLD simulations [56, 60]. It was initially proposed by Van Vleck [87] and Akhiezer [86], having the same structure of a dipolar interaction, however having a proportionality function $f(\mathbf{r}_{ij}) = CJ_0{a_0}^4/r_{ij}^4$ that falls off more rapidly with the distance, hence the name pseudo-dipolar interaction. The exchange-like term $-\frac{1}{3}\mathbf{S}_i\mathbf{S}_j$ is necessary in order to conserve the Curie temperature of the system under different coupling strengths.

$$H_c = -\sum_{j,j\neq i} \frac{CJ_0 a_0^4}{r_{ij}^4} \left[\frac{1}{r_{ij}^2}(\mathbf{S}_i \cdot \mathbf{r}_{ij})(\mathbf{S}_j \cdot \mathbf{r}_{ij}) - \frac{1}{3}\mathbf{S}_i \cdot \mathbf{S}_j \right] \tag{3.34}$$

The magnetic field components and forces have the following form:

$$h_i^\alpha = \sum_{j,j\neq i} \frac{CJ_0 {a_0}^4}{r_{ij}^4} \left[\frac{\alpha}{r_{ij}^2}(\mathbf{S}_j \cdot \mathbf{r}_{ij}) - \frac{1}{3}S_j^\alpha \right],\ \alpha = x,y,z \tag{3.35}$$

$$f_i^\alpha = \sum_{j,j\neq i} \frac{CJ_0 a_0^6}{r_{ij}^6} \left[(\mathbf{S}_j \cdot \mathbf{r}_{ij})S_i^\alpha + (\mathbf{S}_i \cdot \mathbf{r}_{ij})S_j^\alpha - \frac{6\alpha}{r_{ij}^2}(\mathbf{S}_j \cdot \mathbf{r}_{ij})(\mathbf{S}_i \cdot \mathbf{r}_{ij}) + 4\alpha\frac{1}{3}\mathbf{S}_i \cdot \mathbf{S}_j \right],\ \alpha = x,y,z \tag{3.36}$$

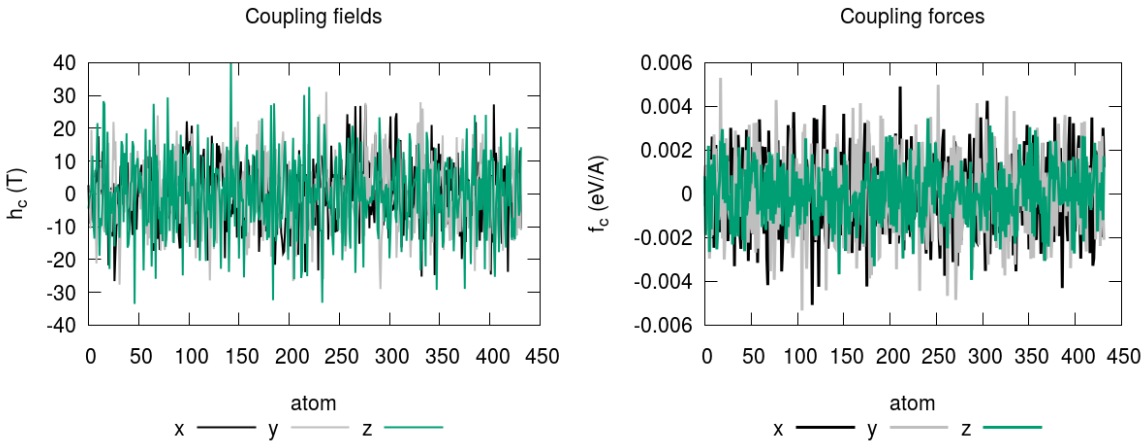

Fig. 3.8 Components of the coupling field and force for a pseudo-dipolar spin-lattice coupling [86, 60], $C = 0.5, Sz = 0.99$.

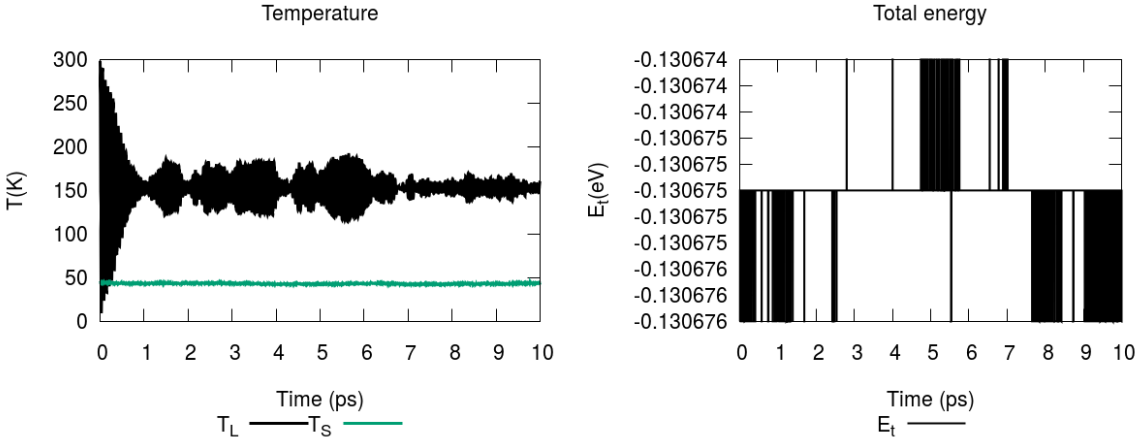

Fig. 3.9 Temperature and energy variation for a magnetic system coupled by a pseudo-dipolar spin-lattice coupling [86, 60], $C = 0.5, Sz = 0.99$.

In a magnetically saturated state, for $\mathbf{S} = (0,0,1)$, a non-zero force appears on all three components of the forces. As the forces are linear in displacement, all three components of the forces will have a non-zero value, hence no evident translation of the lattice. This can be observed by looking at the coupling force plots in Fig. 3.8. No net force can be observed created by this coupling term. The total energy is conserved within the machine precision as shown in Fig. 3.9.

3.6.4 Single site pseudo-dipolar coupling

A variation of the pseudo-dipolar coupling can be written in a single site form, similar to a a Néel anisotropy:

$$H_c = -\sum_{i,j} f(r_{ij}) \left[(\mathbf{S}_i \cdot \hat{\mathbf{r}}_{ij})(\mathbf{S}_i \cdot \hat{\mathbf{r}}_{ij}) - \frac{1}{3}\mathbf{S}_i\mathbf{S}_i \right] \tag{3.37}$$

Similarly to the pseudo-dipolar coupling presented in Section 3.6.3, in the magnetised state the coupling force averages to zero for each component, hence no collective motion of the atoms will be present. The total energy however shows some small variations in the order of 10^{-5}, however no drift in energy is observed in ps timescales - Fig. 3.10. The small fluctuations in energy in the order of 10^{-5} can be associated to the precision of the calculation and are similar to the values observed in [57].

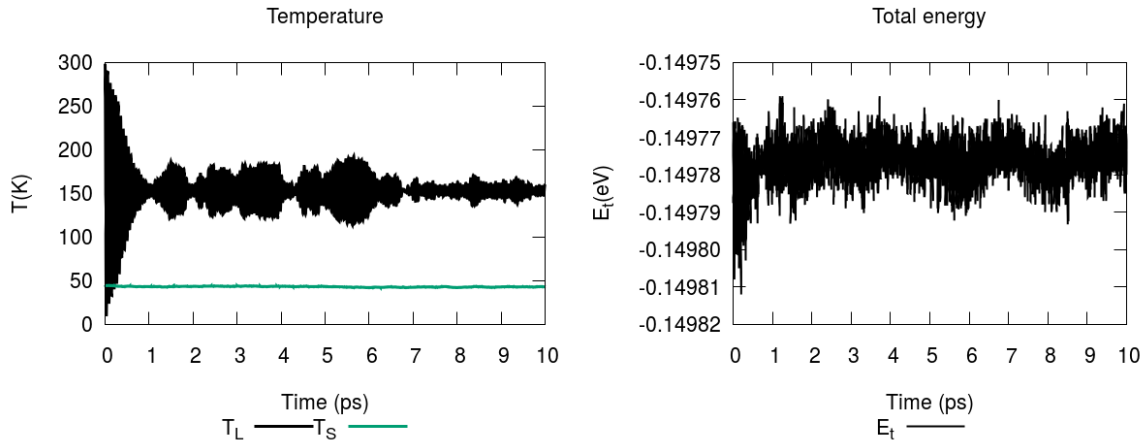

Fig. 3.10 Temperature and energy variation for a magnetic system coupled by a single-site pseudo-dipolar spin-lattice coupling, $C = 0.5$, $Sz = 0.99$.

3.7 Magneto-elastic simulations

In the absence of a spin thermostat, the thermalisation process of the spin system happens via the spin-lattice coupling term that acts as a local anisotropy under thermal distortions. As the thermal displacements in a system average to zero, no global effective anisotropy is induced. To induce some effective anisotropy, the cubic symmetry of the lattice needs to be broken. By stretching the system into a particular direction, the coupling term leads to the appearance of a uniaxial anisotropy, which then can be calculated to parametrise the pseudo-dipolar coupling constant C via magneto-elastic simulations.

The magneto-elastic Hamiltonian can be written for a continuous magnetisation **M** and elastic strain tensor **e** as [88][89]:

$$H_{m-e} = \frac{B_1}{M_s^2}\sum_i M_i^2 e_{ii} + \frac{B_2}{M_s^2}\sum_i M_i M_j e_{ij} \tag{3.38}$$

where (i, j) are coefficients representing the (x, y, z) directions and (B_1, B_2) can be measured experimentally [90]. Under strain effects, an effective anisotropy will arise due to the pseudo-dipolar coupling. To calculate the magnetic anisotropy energy in our simulations, the BCC lattice is strained along the z direction whilst fixed in the xy plane. The sample is then uniformly rotated and the energy barrier can be calculated.

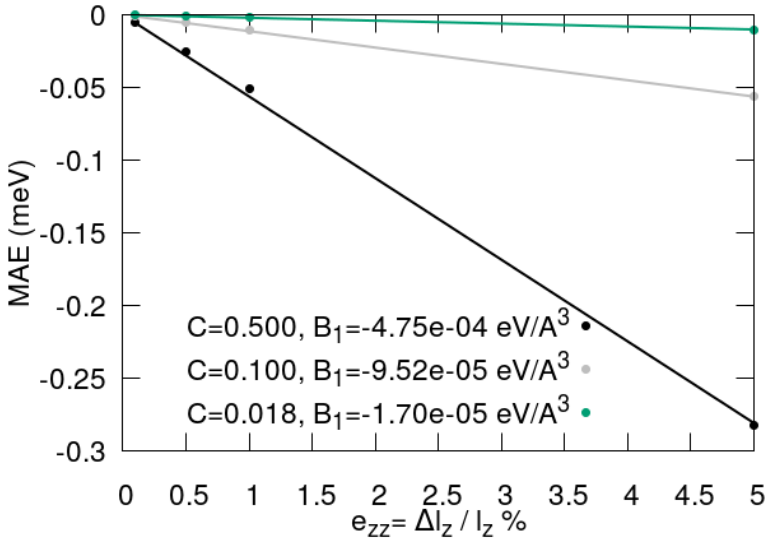

Fig. 3.11 Magnetic anisotropy energy as function of strain for different coupling strengths at $T = 0$K.

Fig. 3.11 shows the magnetic anisotropy energy (MAE) for different strain values and coupling strengths, with the magneto-elastic energy density constants B_1 obtained from the linear fit. For the coupling value of $C = 0.5$, the magneto-elastic coupling obtained from the fit is $B_1 = -4.75 \times 10^{-4}\text{A}^{-3}$ which is larger than values obtained for BCC Fe $B_1 = -3.43$ MJ m^{-3} $= -2.14 \times 10^{-5}$ eV A^{-3}[90] measured at $T = 300$K. Although the magneto-elastic coupling we obtain for BCC Fe for $C = 0.5$ is larger than experimental values, it is important to stress that the large coupling is needed in order to obtain a damping value that compares to that of magnetic insulators where the contribution to the damping appears from magnon-phonon scattering predominantly. In reality, in BCC Fe there is a contribution to the effective damping from electronic sources, which if considered, can lead

to the usage of smaller coupling strengths which are consistent in magnitude with magneto-elastic parameters. Indeed, by calculating the magneto-elastic parameter for smaller coupling strengths ($C = 0.018$), the experimental values observed in BCC Fe can be recovered.

3.8 Thermalisation of the spin and lattice sub-systems

To check if the two sub-systems have reached equilibrium, we need to calculate both the lattice (T_L - from the Equipartition Theorem) and spin temperatures (T_S - from Ref. [91]. These are defined as:

$$T_L = \frac{2}{3Nk_B}\sum_i \frac{\mathbf{p}_i^2}{2m}, \quad T_S = \frac{\sum_i (\mathbf{S}_i \times \mathbf{H}_i)^2}{2k_B \sum_i \mathbf{S}_i \cdot \mathbf{H}_i} \tag{3.39}$$

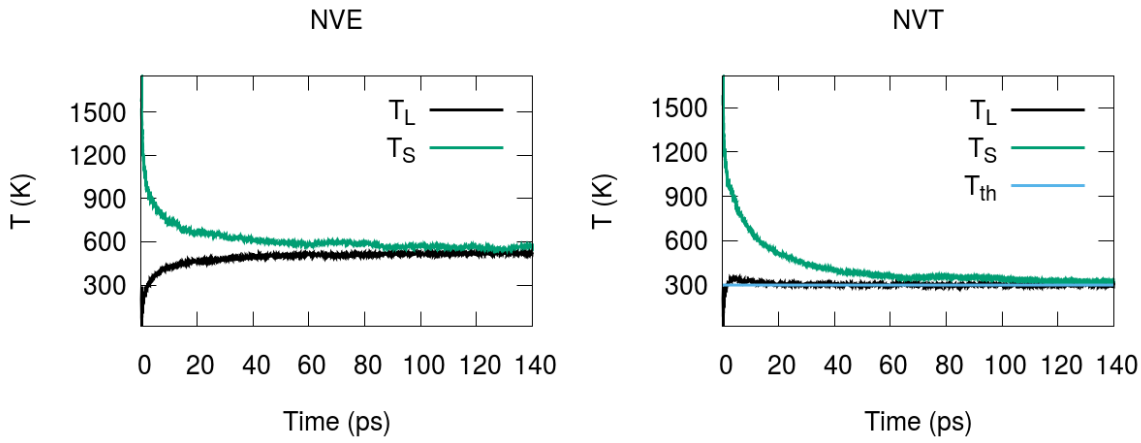

Fig. 3.12 NVE (left) and NVT (right) simulations for a $10 \times 10 \times 10$ unit cell BCC Fe system with a pseudo-dipolar coupling term of strength $C = 0.5$. The spin system is randomly initialised with a temperature of 1900K, while the lattice velocities are initialised by a Boltzmann distribution at $T = 300$K. In both cases we obtain equilibration of the two subsystems on the ps timescale.

As an initial test of our model we check the thermalisation process of the magnetisation performed using NVE (micro-canonical) and NVT (canonical) simulations for a periodic BCC Fe system of $10 \times 10 \times 10$ unit cells. In the case of the NVE simulations, the energy is deposited into the lattice by randomly displacing the atoms from an equilibrium BCC structure within a 0.01 Å radius sphere and by initialising their velocity with a Boltzmann distribution at $T = 300$K. The spin system is initialised randomly in the x-y plane with a

constant component of magnetisation of 0.5 in the out of plane direction. In the case of NVT simulations, the lattice is connected to a thermostat at a temperature of $T = 300$K. The parameters used in the simulations are presented in Table 3.1.

Fig. 3.12 shows the thermalisation process for the two types of simulation. In both cases the spin system has an initial temperature of $T = 1900$K due to the random initialisation of the spins. For the NVE simulations, the two subsystems are seen to equilibrate at a temperature of $T = 600$K, this temperature being dependent on the energy we deposit initially into the system. In the NVT simulations, the lattice is thermalised at 300K followed by the relaxation of the spin towards the same temperature. In both cases we observe that the relaxation of the spin system happens on a 100 ps timescale, corresponding to typical values for spin-orbit relaxation.

3.9 Phonon dispersion

The magnon and phonon dispersion is calculated for the high symmetry path of a BCC crystal structure. The high symmetry points of a BCC Brillouin zone are shown in Fig. 3.13, the figure being extracted from Ref. [92].

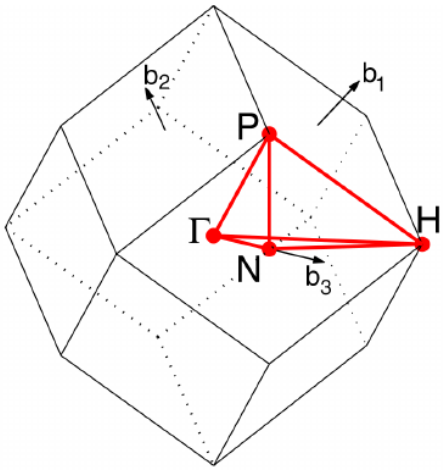

Fig. 3.13 The Brillouin zone for a BCC lattice as extracted from [92], emphasizing the high symmetry points.

The phonon spectrum is calculated from the velocity auto-correlation function defined in the Fourier space as [93, 85]:

$$A^p(k,\omega) = \int_0^{t_f} \langle v_k^p(t') v_k^p(t) \rangle e^{-i\omega t} dt \tag{3.40}$$

where $p = x, y, z$, t_f is the total time and $v_k^p(t)$ is the spatial Fourier Transform calculated numerically as a discrete Fourier Transform:

$$v_k^p(t) = \sum_i v_i^p e^{-i\mathbf{k}\cdot\mathbf{r_i}} \tag{3.41}$$

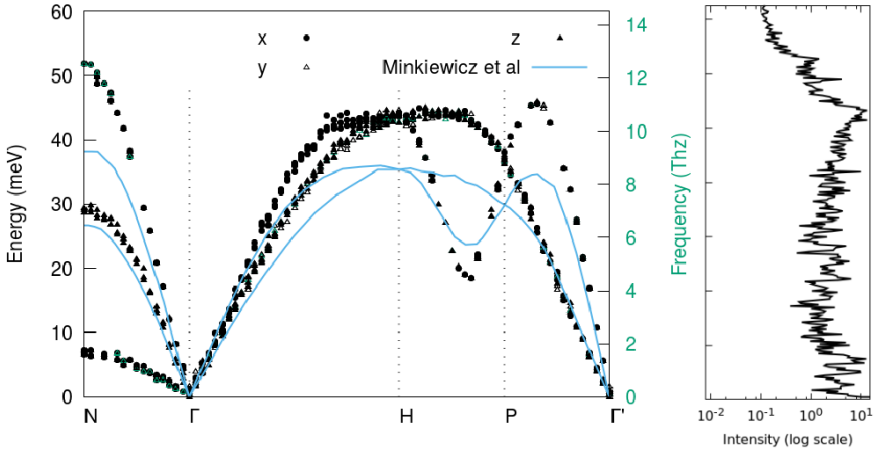

Fig. 3.14 Phonon spectrum calculated for a $32 \times 32 \times 32$ unit cell system at $T = 300$K, $C = 0.5$ for a Morse potential. Right figure includes the projection of the intensity of the spectra onto the frequency space. Solid lines are the experimental data of Minkiewicz *et al.* [94]. For the Minkiewicz *et al.* data there is only one datapoint for the N-Γ path for the second transverse mode which does not show up on the line plots.

Fig.3.14 shows the phonon spectrum for a SLD simulations at $T = 300$K, $C = 0.5$ for a Morse Potential calculated for the high symmetry path of a BCC system with respect to both energy and frequency units. The phonon spectrum reproduces well the spectrum observed experimentally [94] in agreement with the results from [85]. The projection of the spectrum onto the frequency space is shown on the right panel and it is proportional to the density of states (DOS). The projection of the intensity is plotted on a logscale to be able to graphically represent the extreme values. The peak close to 10.5THz in the projection of intensity appears due to the overlap of multiple phonon branches at that frequency. Moving now to a harmonic potential, Fig. 3.15, considering the potential coefficient parameterised by [60], we observe that some of the phonon branches overlap. Around Γ the slope of the harmonic potential is larger, leading to a more stiff lattice. The projection of intensity shows a peak at 8.6THz, due to a flat region in the phonon spectrum. The interaction cutoff for both Morse and Harmonic potential is $r_c = 7.8$Å. The large cutoff makes the Harmonic potential more stiff, as all the interactions are defined by the same energy V_0 and

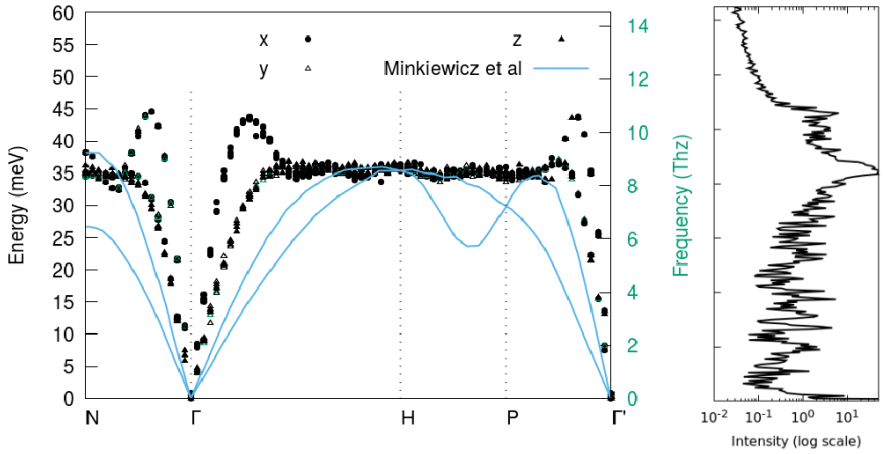

Fig. 3.15 Phonon spectrum calculated for a $32 \times 32 \times 32$ unit cell system at $T = 300$K, $C = 0.5$ for a Harmonic potential. Right figure includes the projection of the intensity of the spectra onto the frequency space. Solid lines are the experimental data of Minkiewicz *et al.* [94].

the difference with respect to the initial displacements of the atomic pairs. This leads to large mechanical forces even near the interaction cutoff. The Morse potential however has an exponential dependence on the difference between the interatomic relative distance and a constant equilibrium parameter r_0 which, for interactions close to the cutoff region results in a lower mechanical force. Although the full symmetry of the BCC Fe phonon spectrum is not reproduced by the harmonic potential parameterised in [60], the phonon energies/frequencies are comparable to the values obtained by the Morse potential.

Better parameterisation of the harmonic potential is possible by decreasing the interaction cutoff and calculating the harmonic potential coefficient from the second derivative of the Morse potential. The Morse potential can be written as $U(x) = D[e^{-2\alpha(x-r_0)} - 2e^{-\alpha(x-r_0)}]$, where $x = r_{ij}$. The second order derivative of the potential is given by:

$$\frac{\partial^2 U}{\partial x^2} = 2D\alpha^2 e^{-\alpha(x-r_0)}(2e^{-\alpha(x-r_0)} - 1) \tag{3.42}$$

which for the atoms placed at $x = a$, where a is the lattice constant results in:

$$\frac{\partial^2 U}{\partial x^2} = 1.416eV/A^2 \tag{3.43}$$

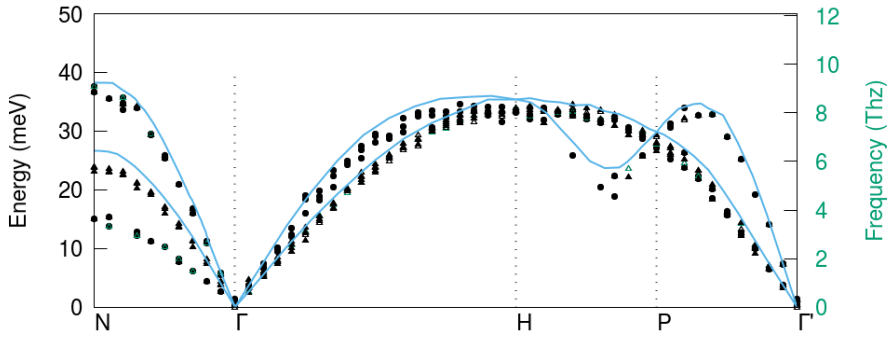

Fig. 3.16 Phonon spectra calculated for a $20\times20\times20$ unit cell system at $T = 300$K, $C = 0.5$ for a Harmonic potential parameterised from the Morse potential coefficients ($V_0 = 1.44$eV). The interaction cutoff is restricted to the nearest and next-nearest neighbours interactions - $r_c = 2.875$Å. Solid lines are the experimental data of Minkiewicz *et al.* [94].

Fig. 3.16 shows the phonon spectrum for a small cutoff distance (first and second nearest neighbours, $r_c = 2.875A$) and a value of the harmonic coefficient close to the analytical calculations ($V_0 = 1.44$eV). The calculated phonon spectrum gives much better agreement to the experimental data of Minkiewicz *et al.* [94], the symmetry of the phonon branches being recovered.

3.10 Magnon dispersion

The magnon spectra can be constructed by using the dynamical spin structure factor, which is given by the space-time Fourier transform of the spin-spin correlation function defined as $C^{\alpha\beta}(r-r',t) = \langle S^{\alpha}(r,t)S^{\beta}(r',0)\rangle$ [95]:

$$S^{\alpha\beta}(\mathbf{k},\omega) = \sum_{r,r'} e^{i\mathbf{k}\cdot(\mathbf{r}-\mathbf{r}')} \int_0^{t_f} C^{\alpha\beta}(r-r',t)e^{-i\omega t}dt \tag{3.44}$$

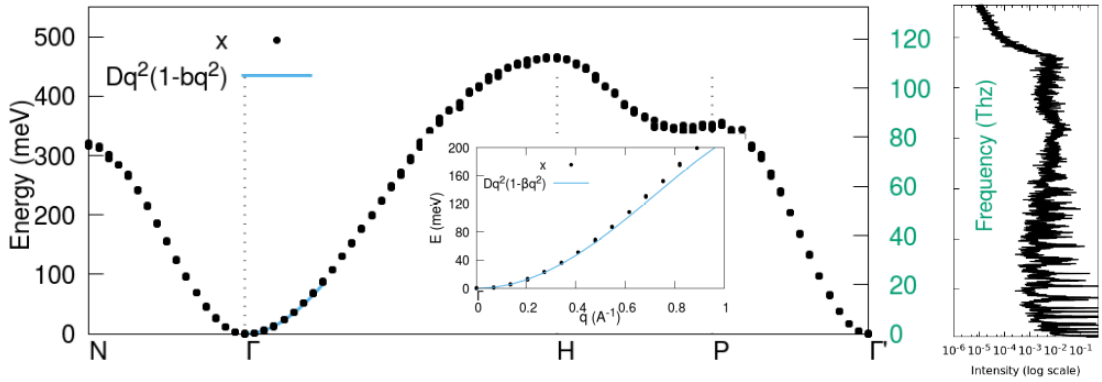

Fig. 3.17 Magnon spectrum (x component) calculated for a $32 \times 32 \times 32$ unit cell system at $T = 300$K, $C = 0.5$ for a Morse potential. Right figure includes the projection of the intensity of the spectra onto the frequency space. The blue line is given by the dispersion equation $Dq^2(1-\beta q^2)$, where the parameters $D = 307$meV, $\beta = 0.32$meVÅ^2 have been extracted from experimental measurements by Loong et al. [96]. The inset shows the behavior of the dispersion for low-q values.

Fig. 3.17 shows the magnon spectrum (x component) obtained within the SLD for a Morse potential, together with its projection onto the frequency space. The results agree very well with previous calculations of magnon spectra [97, 61] and with the experimental magnon dispersion measured by Loong et al. [96]. For the comparison against experiments, we have used the analytical dispersion equation $Dq^2(1-\beta q^2)$, where the parameters D, β have been extracted from experimental measurements. The inset of Fig. 3.17 shows the behavior of the dispersion for low-q values. For the harmonic potential the magnon spectrum is found to be identical to that for the Morse potential with only very small changes regarding the projection of intensity onto the frequency domain - Fig. 3.18. This is in line with our discussion in the previous section where the choice of inter-atomic potential had little effect on the Curie temperature, which is closely linked to the magnonic properties.

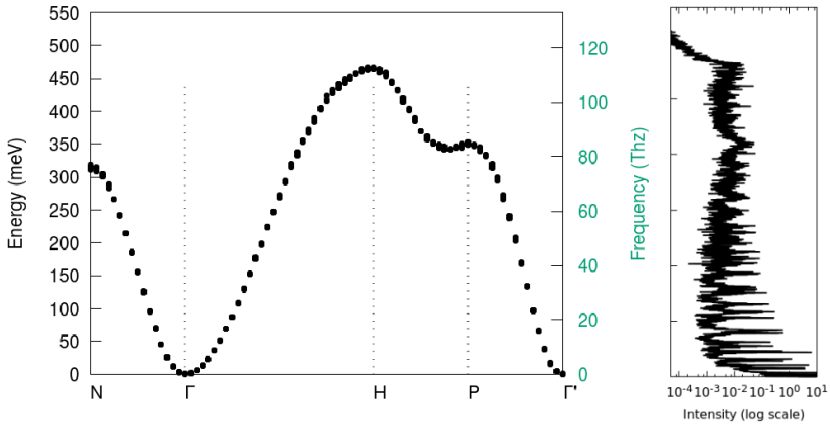

Fig. 3.18 Magnon spectrum (x component) calculated for a $32 \times 32 \times 32$ unit cell system at $T = 300$K, $C = 0.5$ for a Harmonic potential parameterised in [60]. Right figure includes the projection of the intensity of the spectra onto the frequency space.

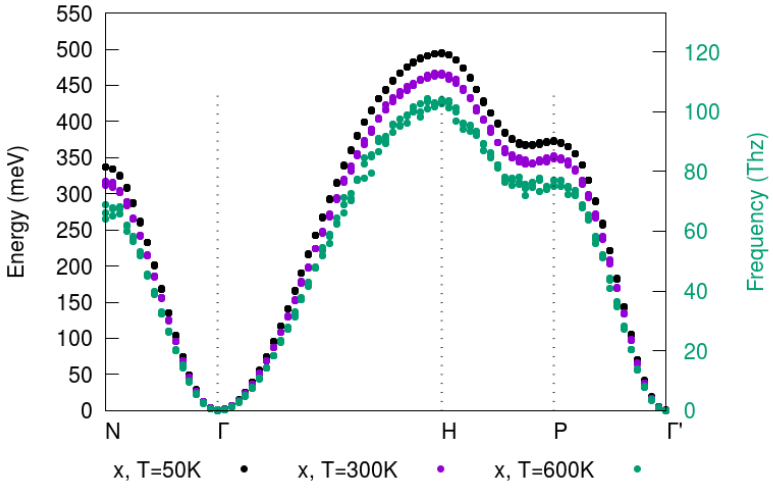

Fig. 3.19 Magnon spectrum (x component) calculated for a $32 \times 32 \times 32$ unit cell system at different temperatures, $C = 0.5$ for a Harmonic potential parameterised in [60].

The temperature dependence of the magnon spectra is shown in Fig. 3.19. We observe that with increasing temperature the magnon modes shift to smaller frequencies. This is a typical situation known as a softening of low-frequency magnon modes, as shown in Ref. [98].

3.11 Temporal correlations of the coupling field

Another method to investigate the properties of the system involves calculating the temporal Fourier transform of individual atoms datasets, and averaging the Fourier response over multiple atoms of the system. This response represents a projection of the properties of the system onto the frequency space. Hence the projection of intensities on the frequency space presented in Section 3.10 has similar features as the spectrum presented in this section. For the results presented in Fig. 3.20- 3.23, a system of $10 \times 10 \times 10$ BCC unit cells have been chosen. The system has been equilibrated for a total of 20ps and the Fast Fourier transform (FFT) is computed for the following 100ps.

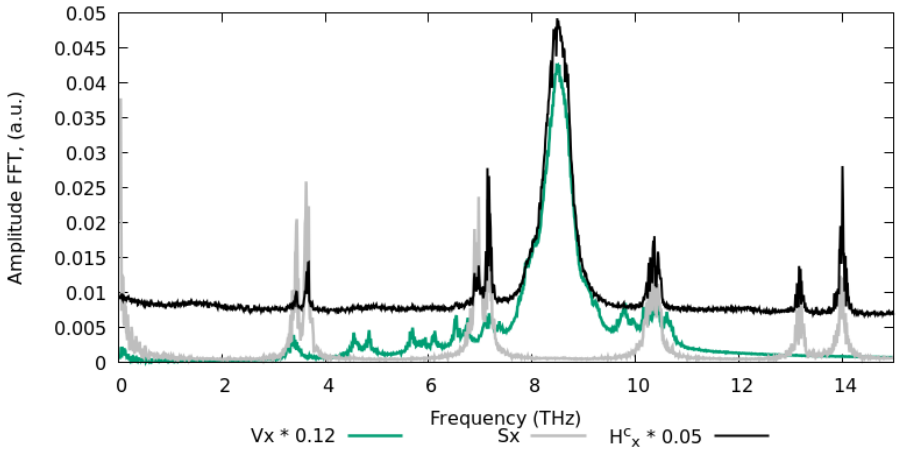

Fig. 3.20 The power density of the auto-correlation function in the frequency domain for magnons, phonons, coupling field for a SLD simulations at $T = 300$K, $C = 0.5$.

The correlations of the magnon, phonons and coupling field are investigated within the SLD model. This is done by calculating the Fast Fourier Transform (FFT) of the x component of velocity v_x, spin S_x and coupling field H_x^c of each atom and averaging over 1000 atom datasets. The FFT is calculated at $T = 300$K after an initial preconditioning at this temperature. The amplitude of the FFT spectra of velocities and coupling fields is multiplied by some scaling values to allow an easy comparison between these quantities. As shown in Fig. 3.20, the coupling term presents both characteristics of magnons and phonons, coupling efficiently the two sub-systems. The large phonon peak in Fig. 3.20 observed at a frequency of 8.6THz appears as a consequence of a flat phonon spectrum for a Harmonic potential, as observed in the phonon spectrum and its projection onto frequency space in Fig. 3.15. Additionally, Fig. 3.20 can give us an insight on the induced spin noise within the SLD framework. The background of the FFT of the coupling field is flat for the frequencies plotted here, showing that the noise that acts on the spin is uncorrelated.

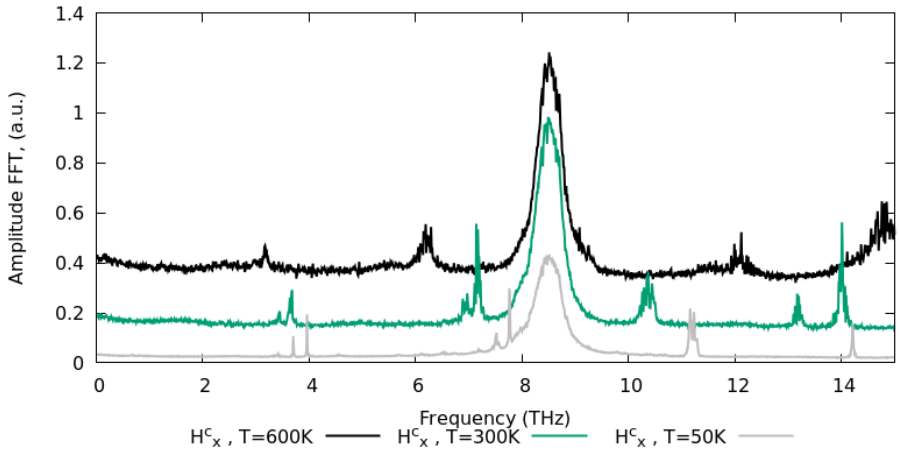

Fig. 3.21 The power density of the auto-correlation function in the frequency domain for the coupling field for a SLD simulation at $C = 0.5$ and different temperatures.

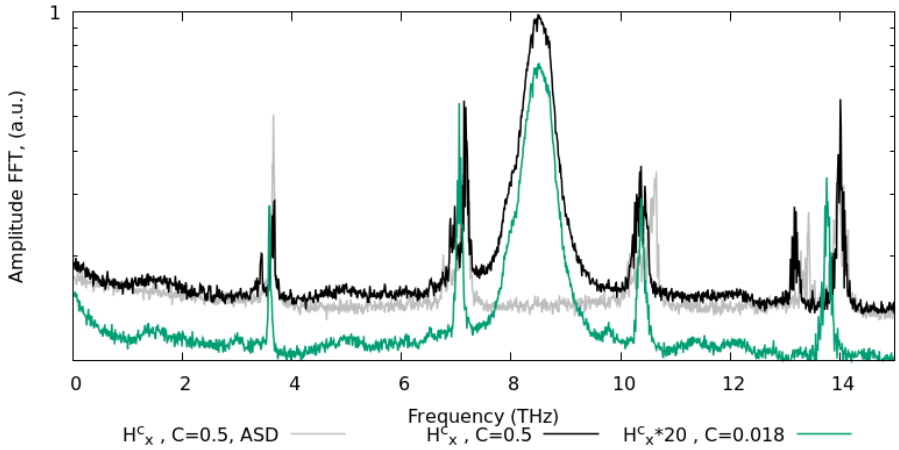

Fig. 3.22 The power density of the auto-correlation function in the frequency domain for the coupling field for fixed lattice (ASD) and dynamic lattice.

Fig. 3.21 shows the characteristics of the pseudo-dipolar coupling field for different temperatures. With increasing temperature, the peaks corresponding to magnons shift to smaller frequencies due to the reduction of exchange in the system, as observed in Section 3.10. The peak corresponding to phonons remains at the same frequency of about 8.6THz, as for this temperature range the phonon spectra is not largely affected.

The characteristics of the coupling term with respect to the coupling strength and for a fixed lattice simulations (ASD) is presented in Fig. 3.22. For the ASD simulations, the phonon peak is not present due to the lack of lattice vibrations. With increasing coupling, we observe an increase in the width of the peaks, suggesting that the magnon-phonon damping could be affected by the coupling strength. We investigate this aspect in detail in Section 5.2.

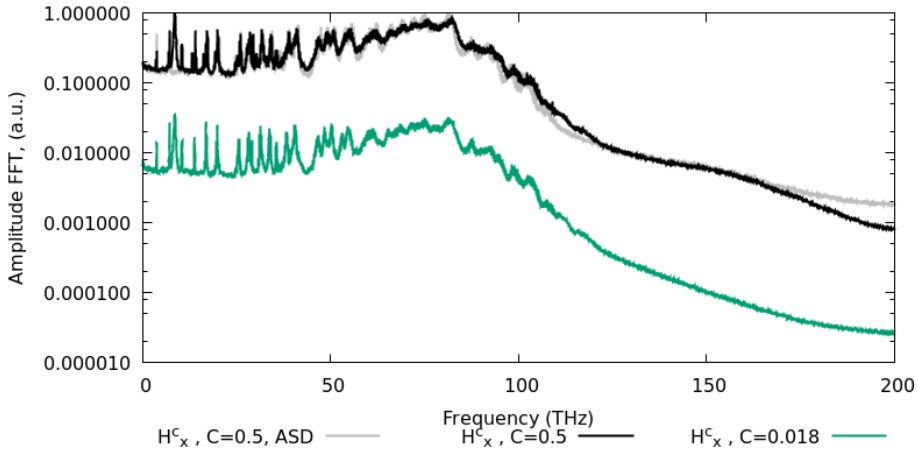

Fig. 3.23 The large frequency domain of the power density of the auto-correlation function in the frequency domain for the coupling field for fixed lattice (ASD) and dynamic lattice.

Moving towards larger frequency regimes, Fig. 3.23 we observe that the enabling of a large coupling gives rise to a plateau in the spectra at around 150THz which is present as well for the fixed-lattice simulations (ASD). The plateau is given by a weak antiferromagnetic exchange that appears at large distances due to the competition between the ferromagnetic exchange and the antiferromagnetic exchange-like term in the pseudo-dipolar coupling. As this behaviour appears at very large frequencies and for large coupling strength, we expect that the dynamics of the spin won't be affected by this plateau zone.

3.12 Conclusions

In this Chapter the spin-lattice dynamics framework is presented. We start with the theoretical background of the model and the numerical scheme used for the integration of the equation of motion and the parallelisation of the algorithm. By performing several physical tests of the model (such as the conservation of energy for NVE simulations) we conclude that one important aspect of the spin-lattice dynamics framework is the coupling term which needs to be formulated in such a way that it does not induce an additional energy drift in the system. We propose a method to calculate the spin-lattice coupling energy by performing magneto-elastic simulation for different strains of the system. The magnon and phonon dispersion curves are presented and compared against BCC Fe, as we have used the properties of this system to parametrise our model. We conclude that the coupling field is responsible for the thermalisation of the spin system and it is able to efficiently transfer both energy and angular momentum between lattice and spin due to the presence of both magnon and phonon modes in the power density spectra.

4

Damping and anisotropy calculations at elevated temperatures

4.1 Introduction

The magnetic damping parameter is important from both a fundamental and applications point of view as it controls the dynamic properties of the system such as magnetic relaxation, spin waves, domain wall propagation and magnetic reversal processes. The damping mechanism also plays a crucial role in magnetic systems as it controls the timescale of the magnetisation dynamics and the coupling of the magnetic system to the energy reservoir. The damping can control, for example, the switching current [14] necessary in spin-transfer torque magnetic random access memories (STT-MRAM) or can influence the fluence of the laser pulse necessary for demagnetising and switching of the sample in ultrafast experiments [15]. Spintronic devices such as race-track memories which are based on domain wall propagation in magnetic nanowires are also influenced by damping [16]. As current magnetic technologies are based on nanostructures of smaller and smaller sizes, finite size effects become more important and can significantly influence the magnetic properties including the damping. Heating the magnetic system can lead to better switching conditions and devices (such as in the current Heat Assisted Magnetic Recording or ultrafast magnetic switching in ferrimagnets - see Section 2.5), therefore understanding the dependence of damping on temperature in finite size systems is a critical step in the development of magnetic nano-technologies.

One of the technologies that is strongly influenced by damping is magnetic recording, where the damping constant of the storage medium controls the writing speeds and bit error rates [99, 100]. The next generation of ultra-high density storage technology is likely to be based on heat-assisted magnetic recording (HAMR) [8, 6, 101, 39] and the main candidate for HAMR media is $L1_0$ ordered FePt [101, 102] due to its increased uniaxial

anisotropy and relative low Curie temperature ($\approx$ 700K). Since HAMR uses small grains for an increased areal density and the properties of the material need to be investigated over a large temperature range (room temperature for the storage of the information and close to the Curie temperature for the writing process), FePt is an ideal candidate for studying the temperature and finite size effects on the damping.

We start the Chapter with a literature review of the first experimental and theoretical investigation of damping in FePt. Then, multiple techniques to measure the damping in magnetic systems are described and used, such as frequency swept ferromagnetic resonance, thermal ferromagnetic resonance via optical pump-probe techniques and calculation of damping via a grid-search method. Since we want to study the damping for small grain sizes, we use atomistic spin dynamics simulation in order to model nanometer grains. Motivated by recent experimental results (Richardson *et al.* [103]) we investigate the damping at elevated temperature via the above methods. This Chapter also presents an analytical model that considers the presence of distribution of properties of grains which corresponds to more realistic conditions of HAMR media and perspectives regarding the behaviour of damping for exchange coupled composite media (ECC media).

4.2 First investigations of damping in FePt

First investigations of the Gilbert damping for FePt involved experimental measurements via optical pump-probe techniques as will be described and used in Section 4.5. However, the damping measured at room temperature varies widely from one study to another: Becker *et al.* [104] reported an effective damping of 0.1, and an even larger value (0.21) was found by Lee *et al.* [105], while the measurements of Mizukami *et al.* [106] gave a value of 0.055. It is important to note that these values include both intrinsic and extrinsic contributions, the purely intrinsic damping being even smaller than the reported values [106, 107].

Using theoretical models, Ostler *et al.* [108] have successfully calculated the temperature dependence of damping in FePt bulk and thin-film systems based on the Landau-Lifshitz-Bloch (LLB) equation [109], showing an increased damping for thin-film systems, in comparison with the bulk case. The LLB equation is derived for a bulk material. It is important to note that a major contribution to damping, especially at elevated temperatures, arises from magnon scattering. On the bulk scale these processes are reproduced by the LLB equation, but with decreasing linear dimension, finite size and surface effects become important. Since these are not accounted for by the LLB equation it is necessary to use atomistic spin dynamics (ASD) simulations [21] for nanoscale grains, since ASD calculations can include magnon scattering processes. Using atomistic spin dynamics, we are able to calculate the FMR

spectra for small system sizes at elevated temperatures and compare against the analytical LLB results, as shown in Section 4.4.

Recently, Richardson *et al.* [103] reported experimental measurements of damping at elevated temperatures showing an unexpected decrease of damping with temperature. A decrease in the effective damping can be crucial in HAMR, as this can increase the switching time, affect the signal to noise ratio and negatively impact the performance of HAMR. In Ref. [103], a proposed mechanism behind the decreasing of damping is via two-magnon scattering, mechanism that should be present within the atomistic spin dynamics framework. A theoretical study on how the damping varies at elevated temperatures and for finite sized systems is therefore a critically important problem for HAMR and it is important to elucidate the mechanism behind the decreased damping observed experimentally.

4.3 Ferromagnetic resonance

To calculate the damping using atomistic spin dynamics we apply an out-of-plane magnetic field (B) to the sample with an additional in-plane oscillating field, $B_{\text{rf}} = B_0 \sin(2\pi\nu t)$, which is the default setup for ferromagnetic resonance experiments - Fig. 4.1. The magnetic Hamiltonian is given by:

$$\mathscr{H} = -\frac{1}{2}\sum_{i,j} J_{ij}\,(\mathbf{S}_i \cdot \mathbf{S}_j\,) - k_u \sum_i (\mathbf{S}_i \cdot \mathbf{e})^2 - \sum_i \mu_i\,[\mathbf{S}_i \cdot (\mathbf{B} + \mathbf{B_{rf}})] \tag{4.1}$$

The oscillating field will induce a coherent precession of the spins of the system which will result in an oscillatory behaviour of the in-plane magnetisation. By sweeping the frequency of the in-plane field, the amplitude of the oscillations of magnetisation will change, with a maximum corresponding to the resonance frequency - Fig. 4.1, b). By Fourier transformation of the in-plane magnetisation, the power spectrum as a function of frequency is obtained. Fig. 4.2 shows the FMR spectrum for a single grain of FePt at 0K. The spectrum can be fitted by a Lorentzian curve (Eq. 4.2) where w represents the width of the curve (the FWHM - the full width at half maximum) and A its amplitude. By fitting to Eq. 4.2, the effective Gilbert damping α and resonance frequency f_0 can be extracted.

$$L(x) = \frac{A}{\pi}\frac{0.5w}{(x-f_0)^2 + (0.5w)^2}\ ,\ \ \alpha = \frac{0.5w}{f_0} \tag{4.2}$$

$$f_0 = \frac{\gamma}{2\pi}\cdot\left(B + \frac{2k_u}{\mu_S}\right) \tag{4.3}$$

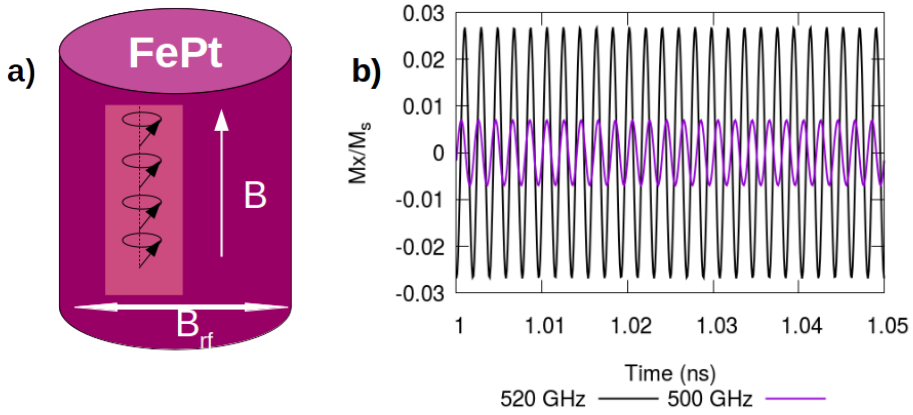

Fig. 4.1 a) Illustration of the setup used for ferromagnetic resonance experiments. An out of plane magnetic field (B) and an in-plane oscillating field, $B_{\mathrm{rf}} = B_0 \sin(2\pi\nu t)$, is applied to the sample; b) Temporal variation of the M_x component of magnetisation for different frequencies of the oscillating field.

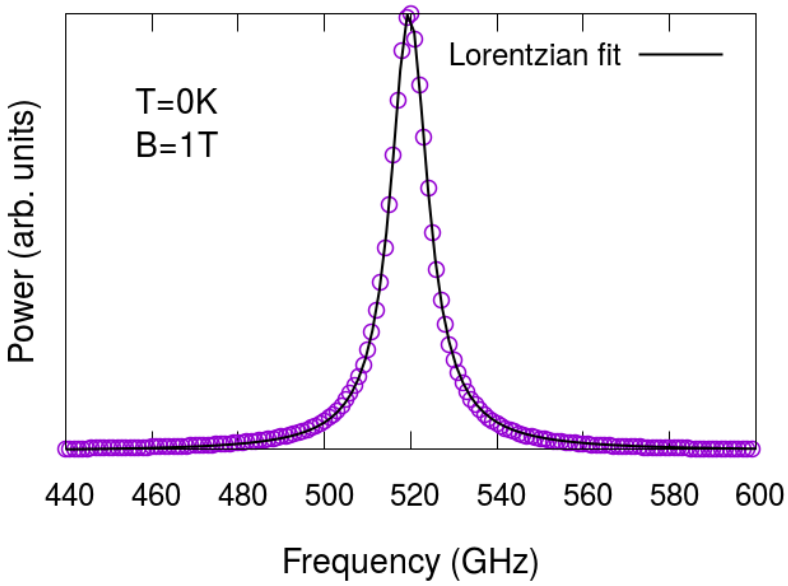

Fig. 4.2 Power spectrum of a single FePt grain at $T = 0$K, with an initial damping of 0.01. The power spectrum is obtained by using the squared amplitude of the Fourier Transformation of the in-plane magnetisation for varying frequencies. By fitting the power spectrum with Eq. 4.2, the input anisotropy and damping can be reproduced. The anisotropy is calculated using the Kittel formula - Eq. 4.3.

We note that there are multiple variations with respect to the fitting function of the FMR spectrum. For example, Ostler *et al.* [108] uses for the power spectrum fit $P(\omega) = P_0\omega^2/[(\omega\alpha_G)^2 + (\omega - \omega_0)^2]$, with the P_0, ω_0 and α_G being the fitting parameters, the power spectrum amplitude, the resonance frequency and damping respectively. Our tests confirmed however that there is a negligible difference in the parameters obtained via different choices of the fitting function.

At $T = 0$K, the damping we extract from the FMR spectrum should correspond to the input coupling λ as no thermal scattering effects are present, hence the effective damping of the system is given by the Gilbert damping which is the coupling to the heat bath. For this simulation, we have used an input heat bath constant of $\lambda = 0.01$, which we then recover by performing FMR calculations at $T = 0$K, method that serves as verification of our model.The damping obtained agrees within 0.1% fitting error. The resonance peak should appear exactly at the resonance frequency given by the Kittel formula - Eq. 4.3, depending on the applied field strength (B) and on the perpendicular anisotropy of our system $(H_K = \frac{2k_u}{\mu_s})$. For an FePt system the resonance frequency we obtain is 520GHz (due to the exceptionally large magnetic anisotropy of the system) within 1% fitting error.

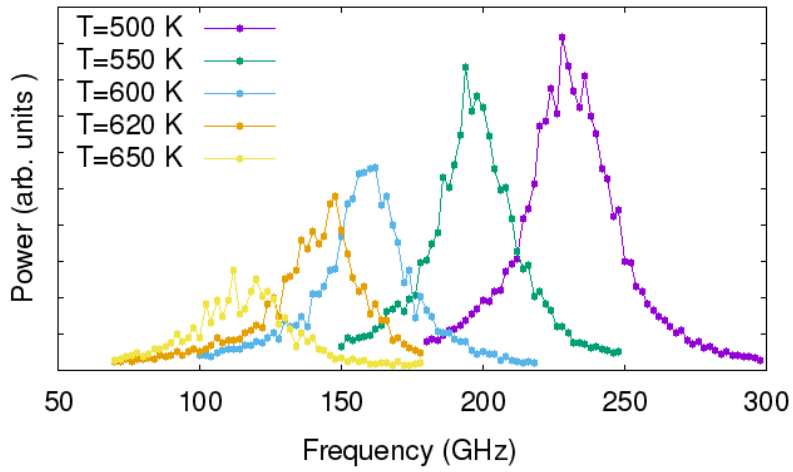

Fig. 4.3 Power spectrum of a FePt grain for different temperatures.

With increasing temperature, the magnetic properties such as anisotropy, total magnetisation and damping vary and this leads to changes in the power spectrum. Fig. 4.3 illustrates the effect of the temperature on the power spectrum. With increasing temperature the power spectra shift to lower frequencies, due to the decreased anisotropy. The amplitude also decreases, as the total magnetisation of the system is reduced for elevated temperatures. This is in agreement with the spectra shown for FMR calculation using the LLB model [108]. In the atomistic spin dynamics package software VAMPIRE [21], the calculated magnetisation

components are divided by the system's total magnetisation. By computing the power spectra using the normalised value of the x component of the magnetisation, an increase in the amplitude of the power spectra with increased temperature is obtained as a sign of increased spin fluctuations with enhanced temperatures. A systematic investigation of the damping and anisotropy for different temperatures and system sizes is presented in the next sections.

4.4 High-temperature FMR: damping and anisotropy calculations for FePt

The model parameters for FePt are listed in Tab. 4.4. $L1_0$ FePt has a face-centred tetragonal structure formed of alternating layers of Fe and Pt, which can be approximated to a body-centered tetragonal structure with the central site occupied by Pt. The *ab initio* calculations by Mryasov *et al.* [110] showed that the Pt spin moment is found to be linearly dependent on the exchange field from the neighbouring Fe moments. This dependence allows the Hamiltonian to be written only considering the Fe degrees of freedom. Under these assumptions, by neglecting the explicit Pt atoms, the system can be modelled as a simple cubic tetragonal structure with each atomic site corresponding to an effective Fe+Pt moment. The model used for the FePt system is restricted only to nearest neighbour interactions to minimise the computational cost of FMR calculations, in contrast with the full Hamiltonian given by Mryasov *et al.* [110]. The nearest-neighbour exchange value is chosen to give a Curie temperature of FePt of 720K, in agreement with reported values for nearest and long-range exchange magnetic Hamiltonian [111]. The damping parameter has been chosen to approximate the experimentally measured value in recording media provided by Advanced Storage Research Consortium (ASRC).

The $L1_0$ phase of FePt has a very large uniaxial anisotropy, hence the increased thermal stability of the grains. The uniaxial anisotropy used in the simulation gives an anisotropy field of $H_K = 2k_u/\mu_s = 17.56$T, slightly larger than the value used by Ostler *et al.* [108] (15.69T). The FMR fields (0.05T) used in our simulations are generally larger than experimental FMR fields to allow more accurate simulations with enhanced temperature. Our tests confirm that no non-linear modes are excited during the FMR simulations for this value of the FMR field.

For initial calculations we model a granular FePt system as a cylinder of 10nm height and 5nm diameter. For comparison, the bulk FePt system is modelled via a system of $32 \times 32 \times 32$ atoms with periodic boundary conditions. Close to T_C, the thermal fluctuations become

Quantity	Symbol	Value	Units
Nearest-neighbors exchange	J_{ij}	6.71×10^{-21}	J
Anisotropy energy	k_u	2.63×10^{-22}	J
Magnetic moment	μ_S	3.23	μ_B
Thermal bath coupling	λ	0.05	
DC perpendicular field	B	1	T
RF in-plane field	B_{rf}	0.05	T

Table 4.1 Parameters used for the initial calculations of the damping constant of FePt.

increasingly large for non-periodic systems and can lead to large errors in the determination of damping and anisotropy. For this reason, to reduce the statistical fluctuations, a system of 15 non-interacting grains is modelled. This significantly reduces the fluctuations in the magnetisation components and leads to statistically improved results. The in-plane magnetisation time series is Fourier transformed, and the damping is extracted as presented in Section 4.3.

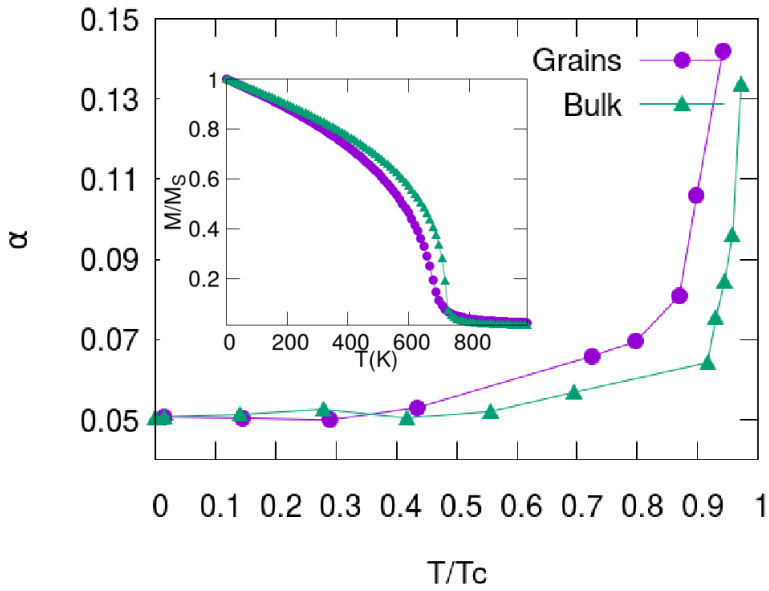

Fig. 4.4 Damping as a function of normalised temperature for bulk and granular FePt system. The granular system shows overall larger damping than the bulk system, due to additional magnon scattering processes at the interface. (inset) Magnetisation curves for granular and bulk FePt. The Curie temperatures for the two systems are: T_C=690K (Grains), T_C=720K (Bulk).

Fig. 4.4 shows the damping as a function of temperature for bulk and granular systems. For comparison the temperature is normalised to the Curie temperature of the systems, which

differs due to finite size effects [112, 111]. The granular system will have a reduced Curie temperature due to the cutoff in the exchange interactions at the surface. This is shown as an inset in Fig. 4.4, where the magnetisation as a function of temperature is computed for the two systems. The magnetisation of the two systems is calculated via Eq. 2.29 for different temperatures via a Monte-Carlo algorithm implemented into the software package VAMPIRE as described in Section 2.7. For each temperature the system has been equilibrated for 100000 Monte Carlo steps, followed by an average over another 100000 Monte Carlo steps. In the case of the granular system, a single grain is used, as the thermal fluctuations in the magnetisation versus temperature curve are reduced by averaging over a large number of Monte Carlo steps after the initial equilibration. In the case of the damping measurements, since the damping is extracted from the Fourier transform of the instantaneous magnetisation, a system of 15 identical non-interacting grains has been used to reduce the thermal noise at high temperatures. The Curie temperatures for the two systems, determined from the susceptibility peak, are: for the grains $T_{\mathrm{C}} = 690\mathrm{K}$, and for the bulk $T_{\mathrm{C}} = 720\mathrm{K}$. The input Gilbert damping parameter is 0.05, this value being reproduced at $T = 0\mathrm{K}$ as expected due to the quenching of magnon excitations.

With increasing temperature, for both bulk and granular systems, the effective damping increases. This can be understood as, with enhanced temperature, there is increasing excitation of magnons which can suffer more complex non-linear scattering processes.

Fig. 4.5 shows the variation of the resonance frequency, from which the anisotropy field can be extracted from the Kittel formula - Eq. 4.3 (plotted on the right axis of Fig. 4.5). Finite size effects are present as well in the temperature dependence of the anisotropy, going from a bulk to a granular system there is a decrease in the anisotropy of the system.

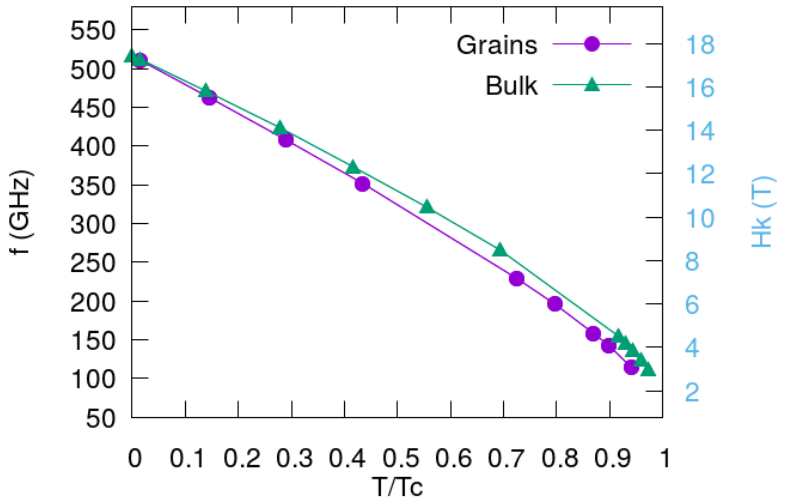

Fig. 4.5 Resonance frequency (left axis) and anisotropy field (right axis) as a function of normalised temperature for bulk and granular FePt.

Moving on to granular systems, the inclusion of surfaces will add extra magnon modes into the system, leading to more scattering effects that will increase the effective damping. In order to have a qualitative illustration of surface effects we use the damping calculated from the Landau-Lifshitz-Bloch equation [109]. An analytical solution to the variation of damping with temperature exists in the LLB description, as given by Garanin [109] and Ostler *et al.* [108]. The effective damping as derived within the LLB description is given by:

$$\alpha(T) = \frac{\lambda}{m(T)}\left(1 - \frac{T}{3T_C}\right), \tag{4.4}$$

where λ is the input coupling to the thermal bath used in atomistic spin dynamics simulations, T_C the Curie temperature of the system, $m(T) = M(T)/M_s V$ the normalised magnetisation. In principle Eq. 4.4 is strictly valid only for an infinite system. However, as a first approximation, finite size effects can be introduced empirically using diameter dependent functions $m(T,D)$ and $T_C(D)$ calculated using the atomistic model. In the damping calculations considered here, the grain surfaces have two effects. Firstly, the loss of coordination at the surfaces drives a reduction in T_C and loss of criticality of the phase transition. This effect can be accounted for by using numerically calculated $m(T,D)$ and $T_C(D)$ for a given diameter D. The second effect is the increased magnon scattering at the surfaces which is a dynamic effect and not included in the parameterization of the static properties. Thus it seems reasonable to associate deviations from the parameterized version of Eq. 4.4 with scattering at the grain surfaces.

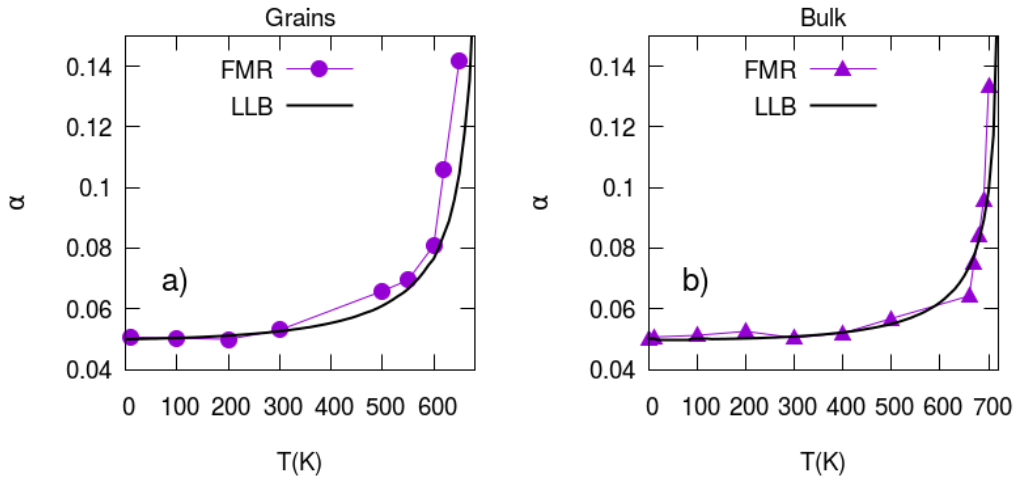

Fig. 4.6 Damping as a function of temperature for granular (5nm×5nm×10nm) (a) and bulk (b) systems. The damping calculated via FMR method is compared against the effective damping from parameterised the LLB formalism - Eq. 4.4, where $m(T,D)$ and $T_C(D)$ are computed numerically from the atomistic model.

Consequently, we compare our numerical results for $\alpha(T,D)$ with the parameterised version of Eq. 4.4 - Fig. 4.6 , where $m(T,D)$ is calculated numerically with the ASD model (shown in Fig. 4.4, inset) and the Curie temperature $T_C(D)$ is calculated from the peak of the susceptibility. For the bulk system, the numerical damping calculated from the FMR curves with the atomistic model agrees well with the damping calculated with the analytical formula given by Eq. 4.4. This is consistent with the first comparison of atomistic and LLB models [113] which showed that the mean-field treatment of [109] agreed quantitatively well with atomistic model calculations for the transverse and longitudinal damping. However, the granular system gives a consistently increased damping compared to the analytical formula. Following the earlier reasoning, this enhancement can be attributed to the scattering effects at the grain surface.

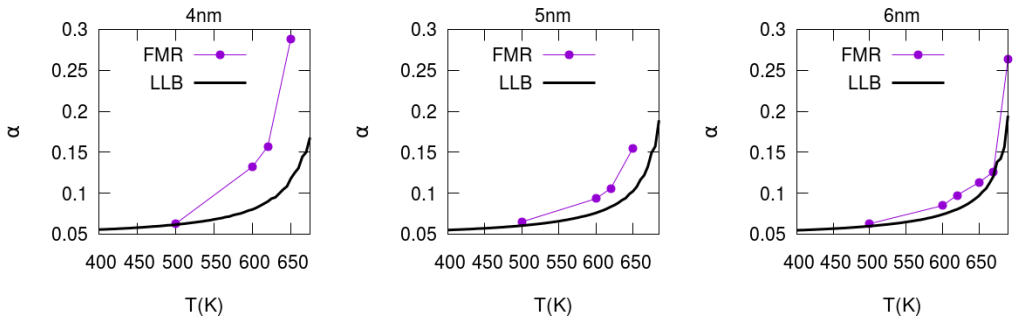

Fig. 4.7 Temperature dependence of the damping constant for cube diameters of 4nm, 5nm and 6nm. Solid lines are calculations using the LLB damping expression. Divergence from the LLB expression for small particle diameter is indicative of surface effects.

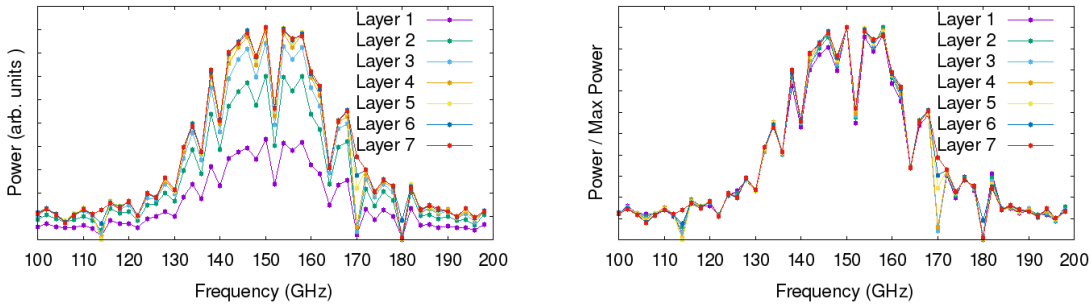

Fig. 4.8 (left) Layer resolved power spectra for a cube of size 4nm at $T = 600$K; (right) Layer resolved power spectra normalised to the maximum amplitude per each mono-atomic layer.

To systematically study the effect of the scattering at the surface, we have calculated the damping as a function of the system size. For simplicity, we consider cubic grains with a volume varying from 4nm×4nm×4nm, 5nm×5nm×5nm and 6nm×6nm×6nm. Fig. 4.7 shows the damping as a function of the temperature for the different system sizes. With decreasing grain size, the damping is enhanced, and systematically diverges further from the LLB analytical damping. The separation of the effects of the finite size on the static and dynamic properties through comparison with the parameterised version of Eq. 4.4 strongly suggests that this is due to surface scattering of magnons. Clearly, the magnon contributions to the damping give rise to an increase of the damping with increasing temperature, which is inconsistent with the results of Richardson *et al.* [103].

The results by Richardson *et al.* [103] suggest that the decrease in the damping is associated with two magnon scattering processes in very small grain sizes which become predominant with enhanced temperatures. ASD simulations enable higher order magnon processes which are more important with elevated temperatures. Interfacial magnon modes could be responsible for magnon scattering. To understand if additional resonance modes

are present at the interface we analyse next the FMR spectra of individual mono-atomic layers of a cubic system of size 4nm - Fig. 4.8. Each layer corresponds to an xy plane of atoms for varying z coordinate, the interfacial layer being numbered as Layer 1. In Fig. 4.8 (left), the power spectra shows a decreased amplitude for the interface, and by going further away from the interface, the power spectra saturates at a constant amplitude. The decreased amplitude at the interface (for Layer 1) appears as a consequence of a decreased value of the magnetisation that is a result of a decreased coordination of the exchange interaction. By normalising the power spectra by the maximum amplitude for each individual layer, we observe that all power spectra collapse into a single curve - Fig. 4.8 (left), characterised by the same damping and resonance frequency. This is an evidence that the system behaves as a macrospin and the ferromagnetic mode $k = 0$ is excited throughout all the system, including at the interface.

The ASD calculations show unequivocally that the damping value increases with increasing temperature due to magnon processes in granular materials. The question remains: how to resolve the apparent disagreement with the experiments. The experiments described in Ref. [103] give the temperature dependence of the linewidth which likely has contributions from inhomogeneous line broadening arising from dispersion of magnetic properties. In Section 4.7 we develop a model accounting for the inhomogeneous line broadening which gives good qualitative agreement with the experiments, showing that in terms of the linewidth the increase of intrinsic damping is more than compensated for by the loss of inhomogeneous line broadening at elevated temperatures. This is an important result since it is the intrinsic damping rather than the linewidth per se that is important for HAMR dynamics.

4.5 Thermal FMR

The damping of magnetic systems can be also determined via optical pump-probe techniques. As shown by Becker *et al.* [104] it is possible to calculate the damping from the magnetisation dynamics triggered by the application of a laser pulse - Fig. 4.9. An external field is applied with an angle of 45° which makes the equilibrium magnetisation to rotate to a new equilibrium axis, as shown in the left panel bottom diagram (II) in Fig. 4.9. The laser pulse is afterwards applied and demagnetises the sample as shown in the right panel of Fig. 4.9. During demagnetisation, the out-of-plane uniaxial anisotropy decreases as well as the Zeeman energy term, both effects leading to a change in the effective magnetic field direction and consequently triggering the precession of the magnetisation. Upon remagnetisation, the oscillatory behaviour of the magnetisation can be fitted to a damped cosine function and the damping and anisotropy of the system can be extracted. This method is similar to

extracting the damping from relaxation curves in a magnetic field after a coherent rotation of the magnetic system with an angle that has been used in Ref. [114] and in the damping calculation from Section 5.2. However, we note the following differences. Firstly, the dynamics of the magnetisation will include the effect of the laser pulse, such as heating and induced local magnetisations due to the inverse Faraday effect. Secondly, there is also an in-plane component of the field which makes the task of calculating the damping and anisotropy field from these measurements more difficult, as we will see below.

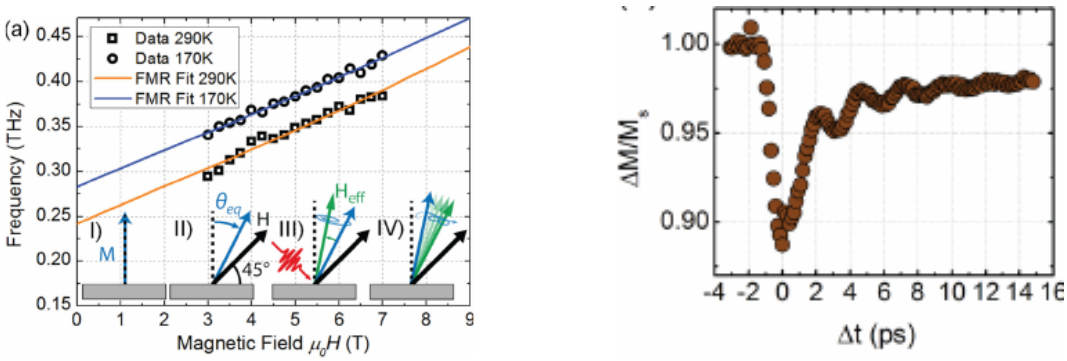

Fig. 4.9 Experimental thermal FMR measurements extracted from [104]; (left panel) Resonance frequency as a function of applied field; (right panel) Magnetisation dynamics after the application of a laser pulse.

Thermal ferromagnetic resonance measurements have been performed for an atomistic spin dynamics simulation for a bulk FePt system. An average over 10 random realisations has been performed to reduce the effect of the thermal noise. The field is applied with an angle of 45° as in the experiments in Ref. [104]. The two temperature model used for including the effect of the laser pulse has been parameterised from John *et al.* [115] for FePt. The pulse width used for the simulation is 100fs and the pulse fluence has been varied in the interval $1-2\text{mJ/cm}^2$. The time-traces of the magnetisation relaxation after the application of the laser pulse have been fitted to:

$$m_x(t) = A\exp(-t/\tau)\cos(2\pi ft+\phi) \tag{4.5}$$

where τ, f, ϕ, A are fitting parameters. From τ the damping parameter can be extracted from the relaxation time τ and this fitting method has been used to extract the damping in granular systems [116].

$$\alpha = 1/(2\pi\tau f) \tag{4.6}$$

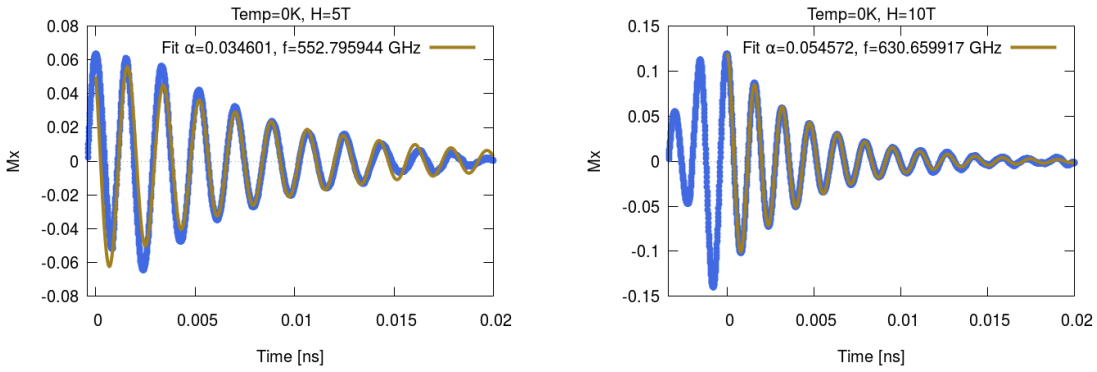

Fig. 4.10 Magnetisation dynamics under the application of a laser pulse of fluence 1 mJ/cm^2 for two magnitudes of the applied field. The gold line shows the fit with Eq. 4.5, the damping being calculated from Eq. 4.6.

Fig.4.10 shows the magnetisation relaxation during the application of a laser pulse of fluence 1 J/cm^2 for two magnitudes of the applied field. The results are fitted just for the decay region, where the amplitude of the magnetisation has a damped oscillation regime. We observe that the damping calculated using Eq. 4.6 is influenced by the value of the applied field. Becker *et al.* [104] provide a complete set of equations that describe the dependence of the resonance frequency during the application of a field H at an angle θ_H for an equilibrium magnetisation characterised by the angle θ_{eq}. The resonance frequency and damping are given by the following set of coupled equations:

$$\frac{\omega}{\gamma} = \sqrt{H_1 H_2} \tag{4.7}$$

$$H_1 = H\cos(\theta_{eq} - \theta_H) + H_K \cos^2(\theta_{eq}) \tag{4.8}$$

$$H_2 = H\cos(\theta_{eq} - \theta_H) + H_K \cos(2\theta_{eq}) \tag{4.9}$$

$$2H\sin(\theta_{eq} - \theta_H) = H_K \sin(2\theta_{eq}) \tag{4.10}$$

$$\alpha = \frac{2}{\tau_L \gamma (H_1 + H_2)} \tag{4.11}$$

The anisotropy field could be determined from the variation of the frequency as a function of the applied field, in the condition when we could determine the equilibrium angle from Eq. 4.10. For particular cases such as $\theta_H = 90°$, the equations are reduced to a much simpler

form, however an analytical general expression could not be found. The equilibrium angle is also dependent on the applied field H, hence a simple fit of Eq. 4.7 as a function of the equilibrium angle and the anisotropy field is not possible. Although we are not able to determine the anisotropy field via a simple fit, the variation of the frequency as a function of initial temperature should reflect the variation of the anisotropy within the system for various temperatures. Fig. 4.11 shows the resonance frequency as a function of temperature for two applied field strengths for a bulk system and a finite size cube of 5nm. With increasing temperature, the resonance frequency decreases due to a reduction of the anisotropy field. Nevertheless, the small system size presents a smaller anisotropy due to the finite size effect associated to the magnetisation.

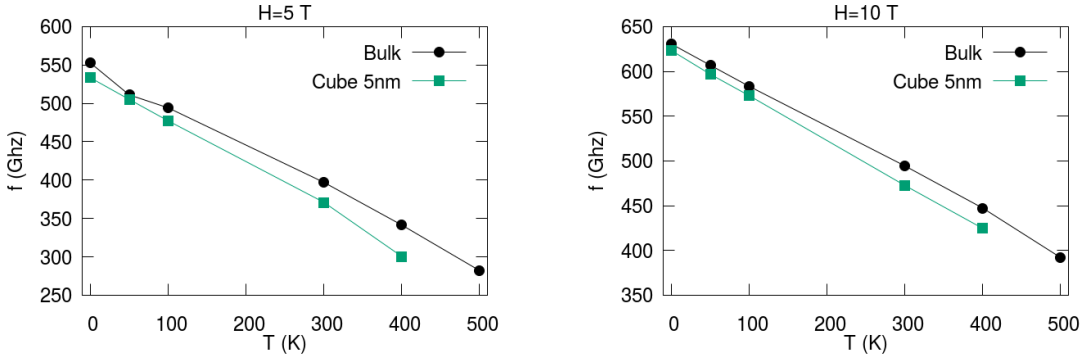

Fig. 4.11 Resonance frequencies for two values of the applied field and a a laser pulse of fluence 1 J/cm^2. The resonance frequencies have been obtained by fitting the magnetisation with Eq. 4.5.

To determine the damping and anisotropy accurately from thermal FMR curves, a more complex fitting approach is necessary. Additionally, the dynamics of the magnetization will include the heating effect from the laser pulse, hence we next describe a more convenient method to calculate the damping and anisotropy of the system. Instead of applying a laser pulse, the system is taken out of equilibrium (by a coherent rotation of the spin system), letting it relax in an applied field, and subsequently recording and fitting the time trace of the magnetization. The calculation of damping and anisotropy is not based on a classical fitting procedure, but rather on a grid search model that compares the time trace of the magnetisation with pre-calculated relaxation curves.

4.6 Grid-search method

The Gilbert damping can be calculated by fitting the time-traces of the magnetisation relaxation obtained via pump-probe experiments [104] as shown in the previous section, however to avoid the contributions from heating, the damping can be calculated by taking the system out of equilibrium, letting it relax and subsequently recording the time-trace of the magnetisation. Ellis *et al.* [117] have numerically studied the damping of rare-earth doped permalloy using the transverse relaxation curves, by fitting them with the analytical solutions of the LLG equations.

In the case of large anisotropy, exchange interaction and applied field, there is no simple general solution to the LLG equation. Pai *et al.* [118] used an applied field much larger than the anisotropy field so that the dynamics closely approximate that of the LLG equation with no anisotropy. However, this approach is unsuitable for FePt due to the very large fields required and also the influence of strong magnetic fields near the Curie temperature. Hence, we adopt a computational grid search method where we pre-calculate single spin solutions for the LLG equation, build a database using these solutions and then build an algorithm that can identify the damping and anisotropy parameters from any transverse relaxation curve. The method we chose simply involves sweeping through the parameter space, the solution being given by minimising the sum of the squared residuals, a method known as grid-search.

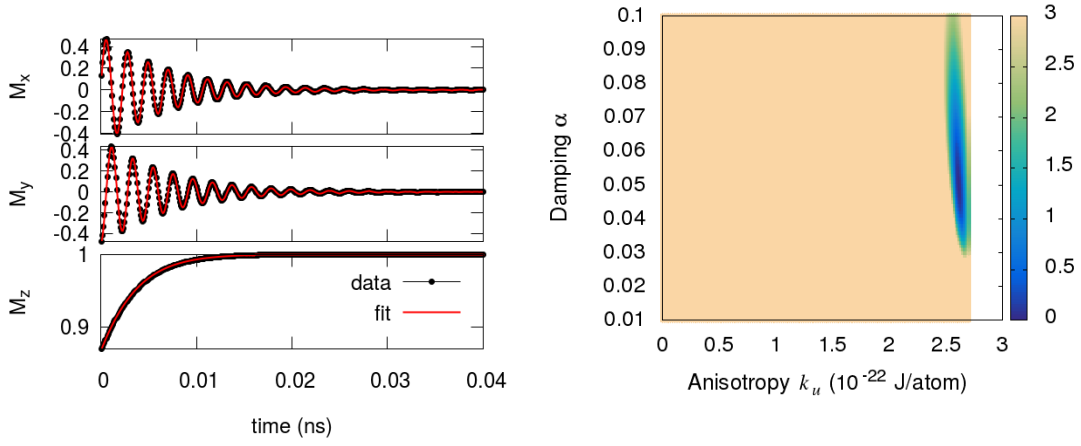

Fig. 4.12 χ^2 map calculated using the grid-search method based on single-spin simulations at $T = 0.1$K. (inset) The input and fitted magnetisation relaxation curves showing the validation of the method.

The grid search method can be used to fit time-dependent $m(t)$ curves in the case where analytical solutions do not exist. The numerical curves that need to be fitted are compared

with each of the pre-calculated numerical curves with the single spin system. The best match will be given by the curve with lowest sum of squared residuals, the χ^2 parameter, where χ^2 is defined as:

$$\chi^2 = \sum_{i=1}^{N} \left[m(t^i) - f(t^i, \mathbf{p}) \right]^2 \tag{4.12}$$

where $m_i(t^i)$ is the value of the magnetisation at each moment in time t^i, $f(t^i, \mathbf{p})$ are the pre-calculated single-spin dependences of the magnetisation at each moment t^i, $\mathbf{p}$ is the list of parameters that have been varied (in our case **p**= (K, α)). The minimum value of χ^2 from all $\mathbf{p}$ parameters is the best-agreement numerical solution.

Figure 4.12 shows the calculated χ^2 as a function of the main parameters, specifically the anisotropy and damping at $T = 0.1$K. In order to construct the single spin simulation database, we chose a resolution of $\Delta k_u = 0.015 \times 10^{-22}$J for the anisotropy and $\Delta\alpha_{\text{step}} = 0.001$ for the damping. It can be seen that the anisotropy is very well resolved: there is a sharp minimum at $k_u = 2.625 \times 10^{-22}$J, which is the closest value to the input anisotropy, $k_u = 2.63 \times 10^{-22}$J taking into account the resolution we use for the database. In the case of damping, the minimum is wider, leading to an error of approximately 0.017 in determination of damping, which is slightly larger than the resolution used in the construction of the database.

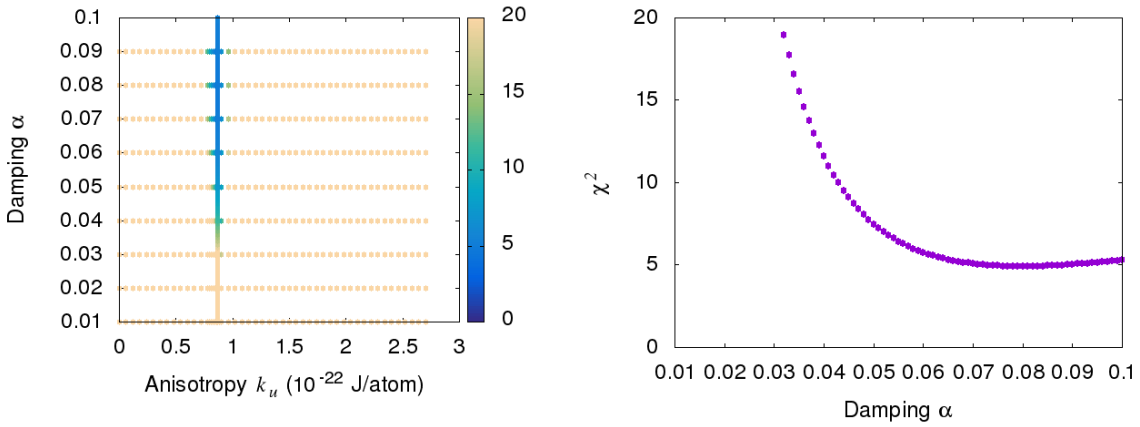

Fig. 4.13 χ^2 map at $T = 550.1$K (left panel) and the variation of χ^2 as a function of damping for the corresponding anisotropy (right panel).

Because of the sharp minimum in the χ^2 map for the anisotropy parameter, the algorithm to calculate the anisotropy and damping can be written more efficiently as follows. Firstly the anisotropy parameter is found, by initially calculating χ^2 with a larger resolution of Δk_u to find an initial interval where the solutions (k_0, α) are found. Then the maximum

resolution is used to calculate accurately the fitting parameters. Fig. 4.13 shows the χ^2 map for a temperature of $T = 550$K, the increased resolution of points being present in the region where the solution k_u is found. Looking at the variation of χ^2 (Fig. 4.13 - right panel) for the solution k_u as a function of damping, we observe the flat region will be responsible for a considerable error of approximately 0.017 in the determination of damping.

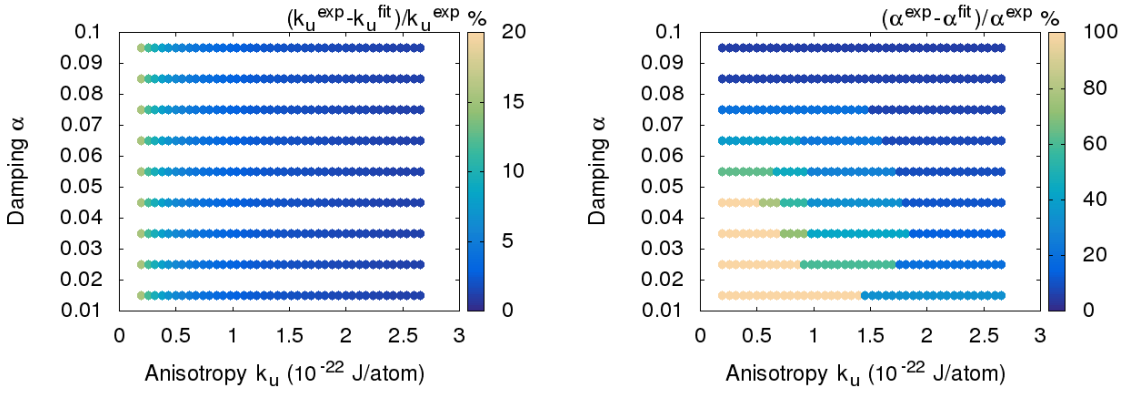

Fig. 4.14 Relative error in the determination of the anisotropy (left panel) and damping (right panel) via the grid search method.

By splitting the database into two datasets, we can further investigate the accuracy to which the damping and anisotropy is calculated via the grid search method. The first dataset is considered the one that we would have access to experimentally (data we try to fit), and the second one will be the database calculated from single spin simulations to which we will fit our results. Fig. 4.14 shows the relative error of the anisotropy and damping. The error in the anisotropy is small, except for the case of low values of anisotropy. For this regime, the frequency of the in-plane oscillation is very small, hence the database and the experimental curves will need to be extended to larger timescales for better fit. For the damping, the errors are much larger, especially in the case of low damping/low anisotropy, where the timescales need to be extended for better results. For FePt we are in the high k_u regime at small temperatures and looking at the right panel in Fig. 4.14 we observe that in this region the error in the damping is reduced. With increased temperature, the anisotropy decreases, however the damping increases (Fig. 4.4) which leads to approximately similar error values as for the large anisotropy case.

Fig. 4.15 shows the comparison between the two methods of calculation of the damping (FMR and grid-search) as a function of temperature for a granular system of 15 non-interacting grains of 5nm diameter and 10nm height. The variations of anisotropy with temperature agree very well between the two methods, however the grid search method is far

more computationally efficient. The enhanced computational efficiency comes from the fact that instead of simulating multiple frequency points to obtain the FMR spectrum, a single transverse relaxation simulation is needed to calculate the same parameters. The time-scales for the two simulations are also different: the frequency dependent FMR spectrum requires around 3 ns for each frequency point to perform the FFT analysis, while the transverse relaxation method requires, depending on the material, less than 1 ns. Extracted damping values agree reasonably well between the two methods, within the error bars. For the grid search method, there will be a damping interval that gives a similar value of χ^2. For the FMR experiment, the error bar is computed as the standard error of groups of 5 non-interacting grains.

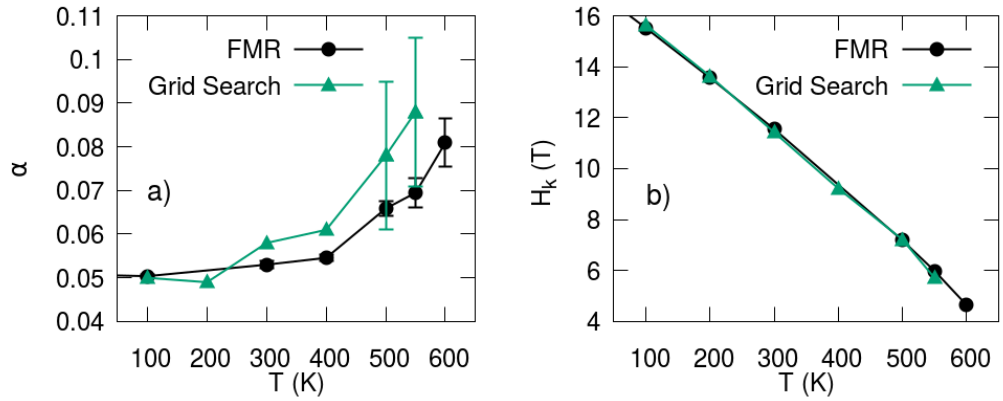

Fig. 4.15 Comparison of FMR and grid-search fitting; a) Damping; b) Anisotropy;

4.7 FMR Model including inhomogeneous line broadening

Realistic granular systems will present a distribution of properties which will affect the FMR spectra of the system. In the presence of a distribution of local resonance fields across the sample, inhomogeneous line broadening will appear in the sample. Fig. 4.16 (left panel) shows the FMR spectra in the absence and presence of a normal distribution of anisotropy fields. The anisotropy field controls the resonance frequency, hence if in the sample there exists a distribution of anisotropy the FMR spectrum will broaden. With temperature, the distribution of anisotropy fields in a granular system will change dynamically, and when a cutoff in the distribution appears (towards T_C), the FMR linewidth can decrease, as shown in Fig. 4.16 (right panel), which can lead to an apparent decreased damping as shown in Ref. [103]. The distribution of magnetic properties can arise from a distribution of the size which can induce a distribution of T_C, m and H_K. At the Curie temperature of the system, the small grains will be already in the superparamagnetic state hence they will not contribute

anymore to the total resonance, leading to a cutoff in the distribution of the anisotropy and consequently a decreased linewidth. In this section, we investigate the effect of the distribution of magnetic properties on the linewidth. Since it is computationally expensive to study a system of grains numerically within the ASD model we can, in the first instance, model the effect of the distributions analytically.

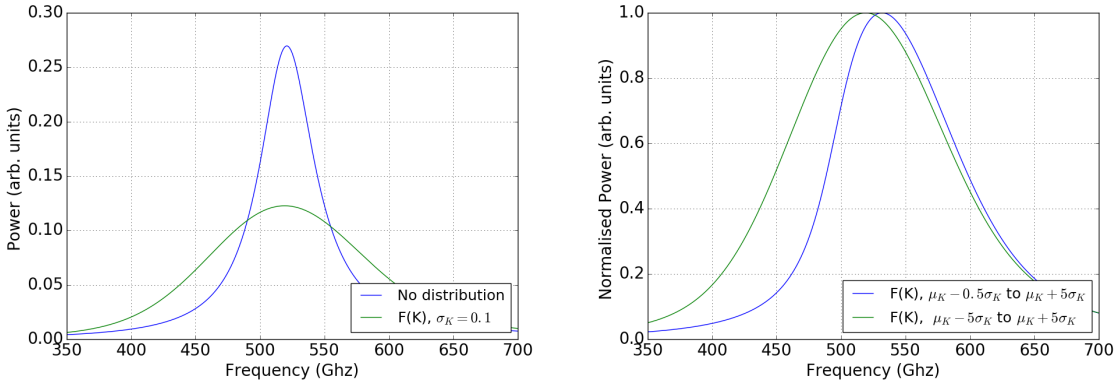

Fig. 4.16 (left panel) Schematics of the inhomogeneous line broadening in the presence of a normal distribution of anisotropy of $\sigma_k = 0.1$ centered around the value of FePt anisotropy; (right panel) FMR spectra in the case when there is a cutoff in the distribution of anisotropy towards the lower values.

The distribution of magnetic properties can arise from a grain size distribution, which can induce a distribution of T_C, m and H_K. In the case of a distribution of grains of diameter D, the power spectrum of the system is expressed by:

$$P^{sys}(f,T) = \int_0^{+\infty} P(f,D,T)F(D)dD \tag{4.13}$$

The distribution of size, $F(D)$, is considered lognormal. The power spectrum of a grain of diameter D can be expressed by [108]:

$$P(f,B_0,D,T) = C\tilde{m}D^2 \frac{f^2\gamma B_0^2\tilde{\alpha}}{(\tilde{\alpha}\tilde{f}_0)^2 + (f-\tilde{f}_0)^2} \tag{4.14}$$

where $\tilde{m} = m(T,D), \tilde{\alpha} = \alpha(T,D), \tilde{f}_0 = f_0(T,D) = \gamma(B_0 + Hk(T,D)), C = \frac{\pi h}{16}$. This allows to model both frequency swept FMR (B_0 =constant) and field swept FMR (f=constant).

We note that a distribution of grain size leads to distributions of further properties, starting, due to finite size effects, with the Curie temperature. Each of these is introduced into the analytical model as follows. Hovorka *et al.* [111] have shown via finite size scaling analysis

that the relation between the size of a grain and its Curie temperature is given by:

$$T_C(D) = T_C^{\infty}\left(1-(d_0/D)^{1/\nu}\right), \tag{4.15}$$

where $d_0 = 0.71$nm and $\nu = 0.79$ [111] parameterised for nearest neighbours exchange systems and $T_C^{\infty} = 720K$. The variation in T_C will introduce a variation in the magnetisation curves given by:

$$m(T,D) = \left(1-\frac{T}{T_C(D)}\right)^{\beta}, \ \beta = 0.33. \tag{4.16}$$

As a further consequence, the anisotropy will be dependent on the diameter. The uniaxial anisotropy energy K has a temperature dependence in the form of $K(T) \sim m(T)^{\gamma}$. For FePt it was found that the exponent is equal to 2.1 by experimental measurements [119][120] in agreement with later *ab initio* calculations [110] . The exponent 2.1 appears for fully ordered $L1_0$ FePt, due to a dominant two-ion anisotropy term, as shown by Mryasov *et al.* [110], in calculations considering a long-range exchange Hamiltonian parameterised from *ab initio*. The granular films presented in [103] are relatively low anisotropy (around 4T coercive field at room temperature) which suggests that the two-ion anisotropy is reduced, possibly because of incomplete $L1_0$ ordering. Hence a scaling exponent of 3 of the uniaxial anisotropy energy ($K(T) \sim m(T)^3$) describes better the films presented in [103]. The anisotropy field can be expressed as:

$$H_K(T,D) = H_K^0 m(T,D)^2 \tag{4.17}$$

Finally the size distribution will produce different variations of damping as a function of grain size, since:

$$\alpha(T,D) = \frac{\lambda}{m(T,D)}\left(1-\frac{T}{3T_C(D)}\right). \tag{4.18}$$

The average magnetisation of distributed grains can be calculated as:

$$M(T) = \frac{\int_0^{\infty} m(T,D)F(D)D^2dD}{\int_0^{\infty} F(D)D^2dD} \tag{4.19}$$

and the anisotropy field is calculated as:

$$H_K(T) = \int_0^{\infty} H_K(T,D)F(D)dD. \tag{4.20}$$

In the presence of distributions of properties, the variation of damping with temperature can have a complex behaviour, especially close to T_C where there is a strong variation of magnetic properties with temperature and size. On reverting to a monodispersed system

by setting the distributions to δ-functions, the damping is given by Eq. 4.18 resulting in an increase of linewidth with temperature consistent with the results shown in Fig. 4.7.

Richardson *et al.* [103] have shown that, in the case of a granular system of FePt, close to T_C a decrease in damping/linewidth is observed - Fig. 4.17. This effect was attributed to the competition between two-magnon scattering and spin-flip magnon electron scattering. We have shown via atomistic spin dynamics simulations that surface effects alone cannot be responsible for a decrease in damping; scattering at the surface leading to increased damping at high temperatures. In our case the distribution of size will lead to a distribution of anisotropy which increases the linewidth. Close to the Curie temperature of the system, some grains will become superparamagnetic and will not contribute further to the FMR spectrum, hence it is possible that close to T_C, the linewidth can decrease.

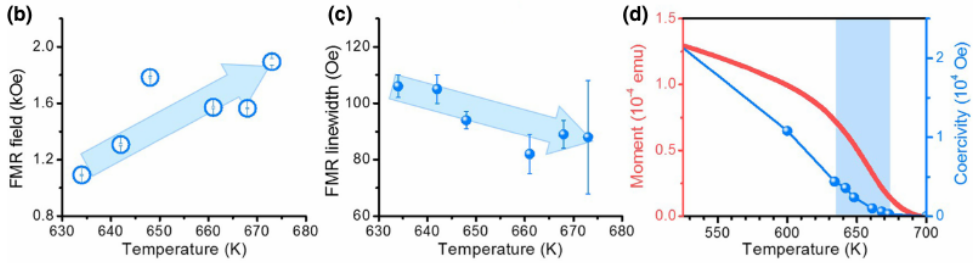

Fig. 4.17 Field swept FMR measurements for granular systems of FePt, extracted from Richardson *et al.* [103] showing a decreased linewidth for elevated temperatures.

Fig. 4.18 presents a case where a decrease in linewidth appears within 30-40K of the Curie temperature of the system, a similar temperature interval as spanned by the experimental measurements [103]- Fig. 4.17. Fig. 4.18 a) and b) show the variation of the FMR field and linewidth as functions of temperature. The FMR spectra are calculated at constant frequency of $f = 13.7$GHz, consistent with the experimental value used in [103]. The decrease in linewidth is associated with the fact that, close to the Curie temperature of the system, the small grains become superparamagnetic and do not contribute to the power spectrum. The loss of the signal from the small grains is especially pronounced due to the enhanced damping of smaller grains.

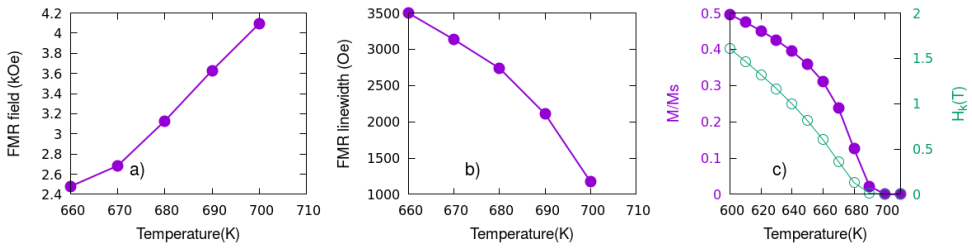

Fig. 4.18 Field swept FMR for a lognormal distribution of grains of average diameter $D = 7$ nm and $\sigma_D = 0.17$. Input damping $\lambda = 0.01$, input $H_K^0 = 6.6$T, $f = 13.7$GHz. The anisotropy is lower than for bulk FePt to allow resonance at a frequency of 13.7GHz corresponding to experiment. The figure shows (a) the variation of the FMR field, (b) FMR linewidth (ΔH) and (c) system magnetisation and anisotropy field as a function of temperature. Close to T_C, the linewidth shows a decrease which translates to a decrease in the damping of the system. No magnetostatic or exchange interaction between grains is considered.

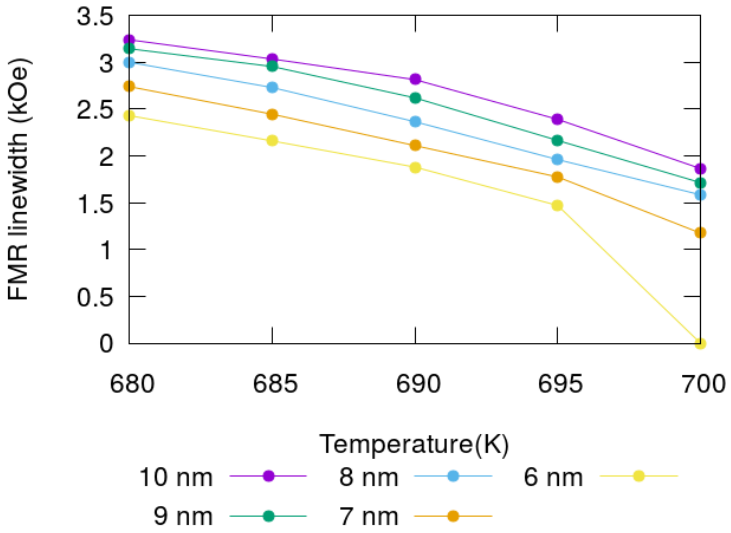

Fig. 4.19 Temperature dependence of the FMR linewidth for different system sizes; A lognormal distribution of grains of $\sigma_D = 0.17$ has been used used with an input damping of $\lambda = 0.01$, input $H_K^0 = 6.6$T, $f = 13.7$GHz.

The decreased linewidth as a function of the system size is shown in Fig. 4.19. We observe that even for average grain sizes of 10 nm there is a decreased linewidth, however the effect is less pronounced that in the case of the smaller dimensions.

To summarize, we have developed a model taking into account inhomogeneous line broadening arising from the size distribution of the grains which gives rise to concomitant dispersions of T_C, m and K. The model has been used to simulate swept field FMR as used in the experiments. Calculations have shown that, under the effect of distribution of

properties, the linewidth can exhibit a decrease towards large temperatures, in accordance with the experiments of Ref. [103]. The decrease is predominantly due to a transition to superparamagnetic behaviour of small grains with increasing temperature. This suggests inhomogeneous line broadening (likely a significant factor in granular films) as an explanation for the unusual decrease in linewidth measured by Richardson *et al.* [103]. The decrease in the inhomogeneous line broadening does not necessary represent a decrease in the effective Gilbert damping, the calculations in Section 4.4 showing an enhanced damping, an important result since a large damping is necessary for good performance of HAMR and MRAM devices.

4.8 FMR in ECC media

Heat-assisted magnetic recording (HAMR) is considered to be the most promising technology for current hard-disk drives. The performance of HAMR media is limited by a number of factors, among those the noise due to the distribution of T_C that arises from the grain size dispersion [6]. The heating of recording media in HAMR is necessary to overcome the writing problem, however other technologies have been proposed to lower the coercive field, these being based on exchange coupled multilayered systems. For example, via the soft ferromagnetic phase of the FeRh metamagnet the coercive field can be lowered in FePt/FeRh bilayer systems [9]. Another promising type of multilayered media is the exchange coupled composite (ECC) [10–12] that uses low-high Tc materials, for example Fe/FePt that show lower switching fields than in the case of FePt systems. The switching in the hard/soft bilayer is via the exchange spring mechanism: firstly the soft layer switches and the exchange coupling at the interface leads to the switching of the hard layer at smaller fields. Bilayered systems are also interesting from a fundamental point of view, as the exchange coupling with a soft layer can largely affect the magnetic properties of the hard layer.

One of the magnetic properties that would be interesting to investigate for ECC media is the damping. Recent experimental studies by Richardson *et al.* [121] shows that the damping in the soft layer is strongly influenced by the coupling at the interface and can be tuned by two order of magnitudes. The temperature dependence of the damping of the soft layer has a complex variation, it can be relatively constant for small interface coupling, however it shows a decrease with increased temperature for large exchange couplings. The discussions presented in Richardson *et al.* [121] are for the soft layer, however the effect of the exchange coupling onto the hard layer damping is also an interesting problem to address. As experimentally it is not possible to investigate the properties of the hard layer over both small and large temperature range, due to necessity to access a large range of frequencies,

employing theoretical models such as atomistic spin dynamics is crucial for the study of damping in bilayer systems.

In the next part of this Section we provide preliminary results of the damping variation as a function of the exchange coupling strength for a simplistic model of ECC media that consists of two macrospins which approximate the soft and hard material in the granular structure. The two macrospins will be coupled by an exchange interaction, which experimentally is difficult to estimate, hence the coupling at the interface is a modelling parameter that is varied. We start with the case corresponding to ECC media where one of the macrospin has lower anisotropy (corresponding to the soft layer) than the macrospin corresponding to the hard layer. The damping and resonance frequency is extracted from the FMR spectrum at $T = 0$K.

a) Soft/Hard bilayers

The soft/hard bilayer system consists of a macrospin S^{hard} having the magnetic parameters corresponding to the FePt system modelled in Section 4.4: input damping - $\alpha = 0.05$, input uniaxial anisotropy constant - $k_u^{hard} = 2.63 \times 10^{-22}$J ($H_K = 17.56$T). The resonance frequency calculated from the Kittel formula (Eq. 4.3) for this value of the anisotropy is 520 GHz. The second macrospin S^{soft} has a decreased anisotropy with one order of magnitude ($k_u^{soft} = 0.1 k_u^{hard} = 2.63 \times 10^{-23}$J, $H_K = 1.756$T), with a corresponding resonance frequency of 77GHz. The exchange coupling constant is expressed in percentage relative to the nearest-neighbours exchange interaction corresponding to FePt ($J_{ij}^{FePt} = 6.71 \times 10^{-21}$J).

An example of the FMR spectra of individual macrospins at $T = 0$K, for a coupling strength of 5% is shown in Fig.4.20, the left and right panels corresponding to the FMR spectra of the individual macrospins and the system respectively. The individual macrospins and the system are excited at the same frequency (228 GHz) which is lower than the one corresponding to the averaged resonance frequencies of individual uncoupled macrospins (298.5 GHz). This can suggest that the magnetic field at the interface given by the exchange coupling of the two macrospins can influence the resonance frequency of the system. By fitting the FMR curves, the damping of the system can be extracted, which in this case gives the same value of 0.05 as the individual damping of the macrospins.

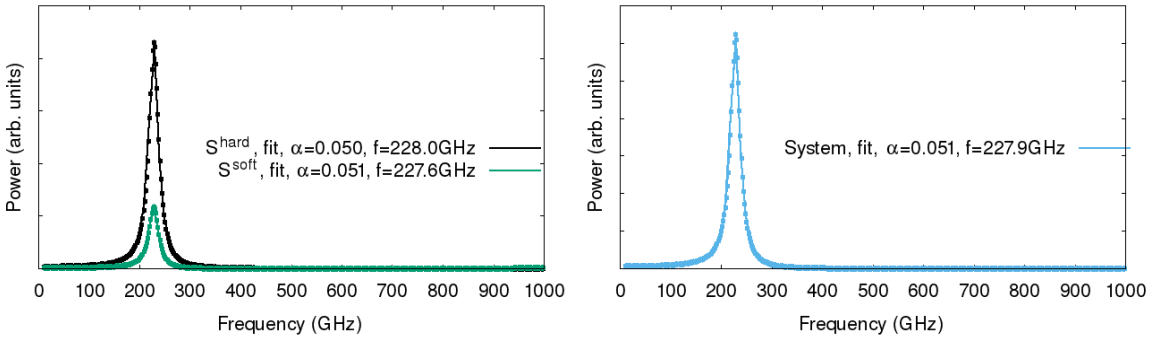

Fig. 4.20 FMR spectra for hard/soft bilayers with a coupling constant of $C = 5\%$. The left panel shows the FMR spectra of individual spins, while the right panel shows the FMR spectra of the system. The input damping and anisotropy for the two macrospins are: $S^{hard}, \alpha^{hard} = 0.05$, $k_u^{hard} = 2.63 \times 10^{-22}$J; $S^{soft}, \alpha^{soft} = \alpha^{hard} = 0.05$, $k_u^{soft} = 0.1 k_u^{hard} = 2.63 \times 10^{-23}$J.

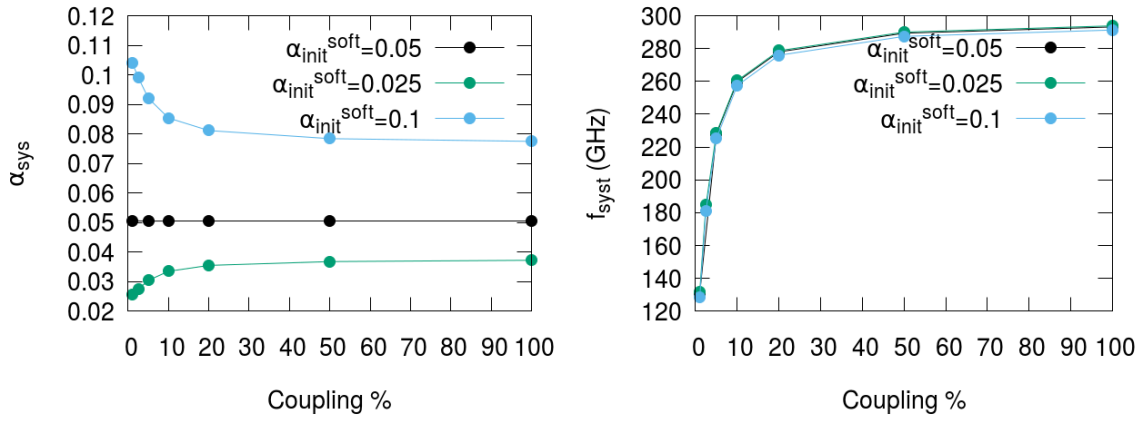

Fig. 4.21 Damping and resonance frequency for a soft/hard system as a function of the coupling strength for different choices of damping for the soft layer. The damping of the system (left panel) is largely affected by the damping of the soft spin. The resonance frequency (right panel) presents the same variation as a function of the coupling strength independent of the soft macrospin input damping.

By modifying the damping of the soft layer, different behaviours of the damping as a function of the exchange coupling can be observed - Fig. 4.21, left panel. For the soft layer we choose three values of the input damping: equal to the damping of the hard layer ($\alpha_{init}^{soft} = \alpha_{init}^{hard} = 0.05$), smaller ($\alpha_{init}^{soft} = 0.5\alpha_{init}^{hard} = 0.025$) or larger ($\alpha_{init}^{soft} = 2\alpha_{init}^{hard} = 0.1$). With increasing coupling the damping saturates to a value given by the average between the damping of the soft and hard macrospin, this leading to either an increase or decrease of the total damping value. Fig. 4.21 (right panel) shows that the resonance frequency increases with increased coupling and saturates at a value given by the average resonance frequency of

the two spins (298.5GHz). The coupling at the interface can hence affect the behaviour of both the damping and resonance frequency.

b) Hard/Hard bilayers

We consider two macrospins of similar uniaxial anisotropy values and the same input damping: the first spin S_1 has magnetic parameters corresponding to FePt ($\alpha = 0.05, k_u^1 = 2.63 \times 10^{-22}$J, $H_K = 17.56$T), while the second spin S_2 has a decreased anisotropy ($k_u^2 = 2 \times 10^{-22}$J, $H_K = 14.68$T). The two values of anisotropy used correspond to a resonance frequency of 520GHz and 440GHz as calculated via the Kittel formula.

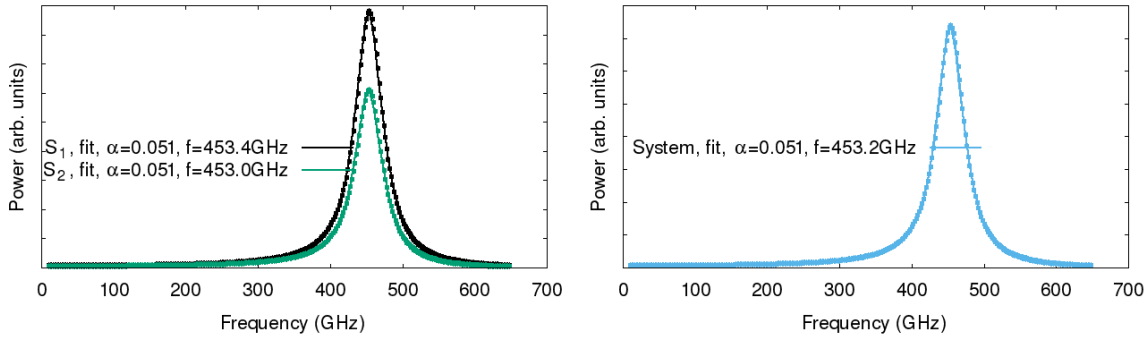

Fig. 4.22 FMR spectra for hard/hard bilayers with a coupling constant of $C = 5\%$. The left panel shows the FMR spectra of individual spins, while the right panel shows the FMR spectra of the system. The input damping and anisotropy for the two macrospins are: $S_1, \alpha = 0.05, k_u = 2.63 \times 10^{-22}$J, $S_2, \alpha = 0.05, k_u = 2 \times 10^{-22}$J.

Fig. 4.22 shows the FMR spectra for a weakly coupled system, together with the variation of the damping and resonance frequency as a function of exchange coupling - Fig. 4.23. By increasing the anisotropy of the second macrospin, the same behaviour of the damping with changing coupling strength can be observed as in the case of the soft/hard bilayers, however the rate of increasing/decreasing of the damping is modified for the hard/hard bilayers. The variation in the resonance frequency - Fig. 4.23 (right panel) is smaller than in the case of the hard/soft layer, due to the similar individual resonance frequencies. We also observe a variation of the resonance frequency with respect to the input damping of the macrospin S_2, variation that is difficult to distinguish in Fig. 4.21 (left panel) due to the large range of the resonance frequency.

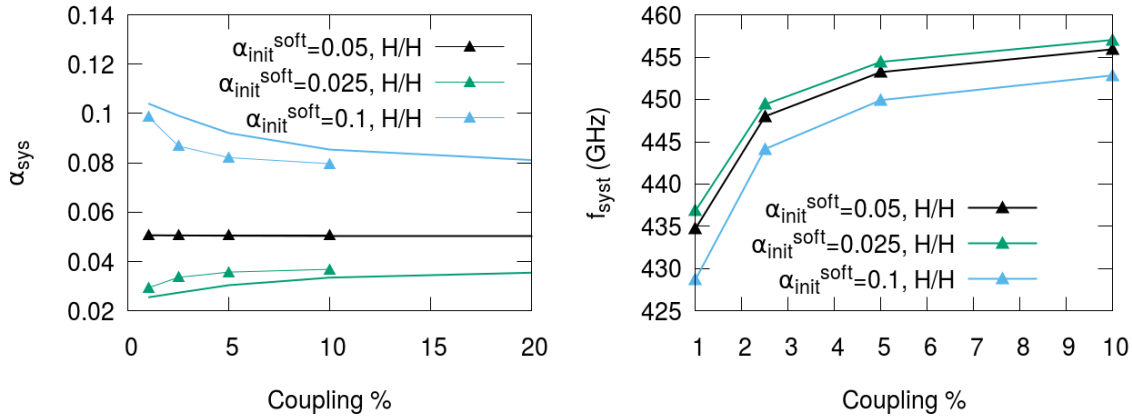

Fig. 4.23 Damping and resonance frequency for a hard/hard system as a function of the coupling strength for different choices of the damping for one of the macrospins. The continuous lines in the left panel show the damping variation for the soft/hard bilayers. The damping of the hard/hard bilayers (linepoints) increases/decreases towards the average of the two macrospins input dampings. The rate of increasing/decreasing of the damping is enhanced for the hard/hard bilayers. The resonance frequency (right panel) presents the same variation as a function of the coupling strength.

Via a simple two macrospin model, we have shown that the behaviour of the damping and anisotropy in the case of coupled bilayers can be complex, depending on both the exchange coupling at the interface, but as well on the damping of the soft layer. The general trend observed is that, with increasing coupling strength, both the system's damping and resonance frequency goes towards the averaged value of the magnetic parameters of individual macrospins, since for strong couplings, the system behaves as a single entity. The rate in the damping variation can also be controlled by the uniaxial anisotropy of one of the macrospins, being larger in the case of hard/hard bilayers. From the preliminary macrospin investigation, it is difficult to correlate back to the experimental results by Richardson *et al.* [121] since we don't include the temperature effects yet. Hence FMR simulations on more realistic ECC media at finite temperature could provide a quantitative description of experimental results.

4.9 Conclusions

We have calculated the temperature dependence of damping and anisotropy for small FePt grain sizes. These parameters were calculated within the ASD framework, via simulations of swept frequency FMR processes and a fitting procedure based on the grid search method. The grid search method offers a much faster determination of damping and anisotropy,

parameters crucial for the development of future generation HAMR drives. The damping calculations at large temperatures showed an increased damping for uncoupled granular systems as expected due to increased magnon excitation at high temperature. Deviations from the parameterised expression for the temperature dependence of damping from the LLB equation with decreasing grain size suggest that scattering events at grain boundaries enhance the damping mechanism. This increase in damping, however, is not consistent with the experimental data of Richardson *et al.* [103] which show a decrease in linewidth at elevated temperatures. By including the distribution of properties that will arise from a distribution of grain sizes, we have shown via an analytical model that the behaviour of small grains with increasing temperature can lead to a decrease in the linewidth in accordance with the experiments. Preliminary investigation of ECC media indicates a complex behaviour of the damping, which can be studied in detail in further work.

5

Spin dynamics under phonon excitation

5.1 Equilibrium M(T)

To gain a better understanding of properties at thermal equilibrium within the spin-lattice dynamics model, we have investigated the temperature dependence of the magnetic order parameter between different frameworks that either enable or disable lattice dynamics, specifically: SLD or ASD. Since reaching joint thermal equilibrium depends strongly on the non-collinearity already present in the magnetic system this process is accelerated by either starting the system from a perfectly magnetised state for $T < 300K$ or from a reduced magnetisation of $M/M_S = 0.9$ for $T > 300K$. For the *ASD* simulation the dynamics is given by integrating the LLG equation connected to a Langevin thermostat.

Fig. 5.1 shows the comparison of the equilibrium magnetisation using either the harmonic potential (HP), Morse potential (MP) or fixed lattice (ASD) simulations. The magnetisation is calculated by averaging for 200ps after an initial equilibration of 800ps (for SLD type simulations) or 100ps (for ASD) simulations. We observe that even without a spin thermostat (SLD model) the magnetisation achieves equilibrium via the thermal fluctuations of the lattice, proving that both energy and angular momentum can be successfully transferred between the spin and the lattice sub-systems. Additionally, both the SLD and ASD methods tend towards the same equilibrium magnetisation over the temperature range considered. This confirms that the equilibrium quantities are independent of the details of the thermostat used, in agreement with the fact that both SLD and ASD obey the fluctuation-dissipation theorem - Appendix B. Additionally, as the equilibrium magnetisation does not substantially differ between the two choices of the potential, this suggests that the harmonic potential, although simplistic, can reproduce the equilibrium properties of the system.

Since the strength of the exchange interaction depends on the relative separation between the atoms, any thermal expansion of the lattice will potentially modify the Curie temperature.

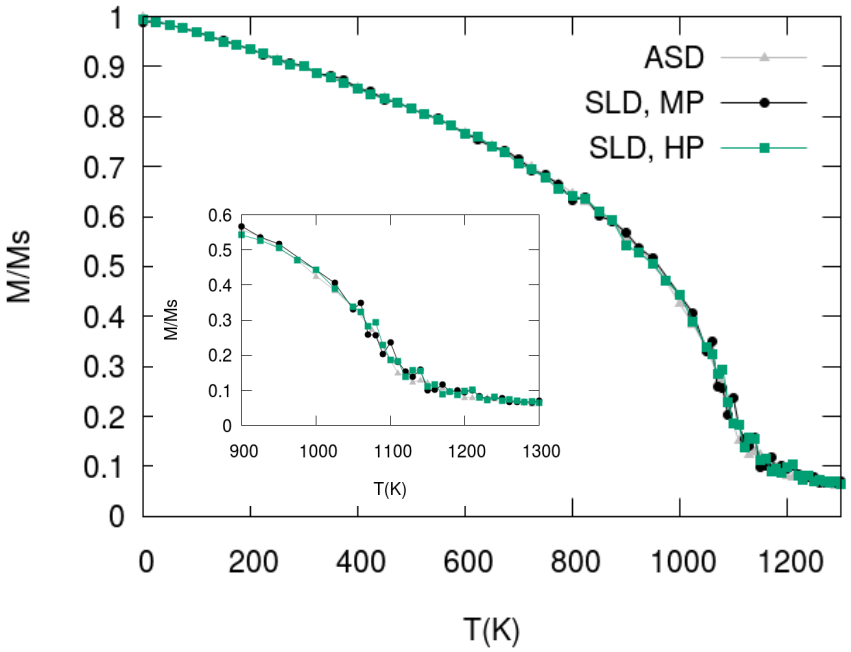

Fig. 5.1 Magnetisation versus temperature curves for the SLD model with different choices of lattice potential: MP-Morse Potential, HP-Harmonic Potential and fixed lattice ASD.

However, as highlighted in the inset of Fig. 5.1, the same Curie temperature is observed in each model. We attribute this to the fact that the thermal lattice expansion is small in the temperature range considered here due to two reasons: i) the Curie temperature of the system is well below the melting point of Fe ($\approx 1800\,\mathrm{K}$) and ii) we model a bulk, constant-volume system that does not present strong lattice displacements due to surfaces. We note that Evans *et al.* [122] found a reduction of T_C in nanoparticles due to a change in structure when removing the boundaries that consequently reduces the exchange interactions. Within periodic systems we anticipate fluctuations in the exchange due to changes in interatomic spacing to be relatively small.

We can approximate a total exchange coupling energy J_{ij}^t by dividing the average exchange field of the final spin configuration of the system by the temporal averaged system's magnetisation M. The exchange fields have been output with large temporal resolution (every 10ps) hence there are not enough points for a good temporal average as the one performed for the magnetisation (every 0.01ps). For this reason, for a first approximation, we use the instantaneous exchange fields calculated for the final configuration of the system, as defined in Eq. 5.1 normalised by the saturation exchange coupling constant J_{ij}^S calculated at $T = 0\mathrm{K}$ for an equilibrium BCC structure.

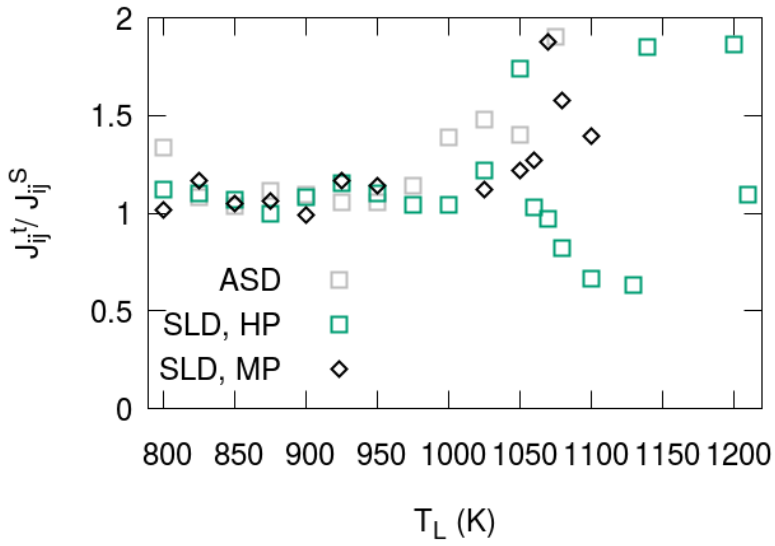

Fig. 5.2 Average exchange coupling versus temperature for the SLD model with different choices of lattice potential: MP-Morse Potential, HP-Harmonic Potential and fixed lattice ASD. The average exchange coupling is normalised to the value corresponding to the total exchange coupling energy calculated for fixed lattice simulations (ASD) $J_{ij}^S = 2703.29$meV.

$$J_{ij}^t = \frac{\sqrt{h_x^2 + h_y^2 + h_z^2}}{M}, \quad h_\alpha = \frac{\sum_i h_{\alpha,i}^{exch}}{N}, \quad \alpha = x,y,z \tag{5.1}$$

Fig. 5.2 shows the average exchange coupling energy normalised by its saturation value as a function of temperature for a static lattice and dynamic lattice simulation. We observe that the inclusion of the dynamic lattice leads to small variations of the effective exchange energy up to 950K, which can motivate the similar Curie temperature observed between the static and dynamic lattice simulations. For larger temperatures, there are strong variations in the average exchange coupling due to the decreased magnetisation and strong thermal effects. Hence an approximation of the exchange constant based on the system's exchange field is not valid anymore. Therefore we introduce a second method to calculate the total exchange coupling energy via a direct summation of the exchange coupling strengths during the simulation time:

$$J_{ij}^t = \frac{1}{N} \sum_{i,j} J_0 \left(1 - r_{ij}/r_c\right)^3 \tag{5.2}$$

Fig. 5.3 shows the normalised effective exchange constant calculated during the simulation time via Eq. 5.2. The normalisation has been done with respect to the total exchange

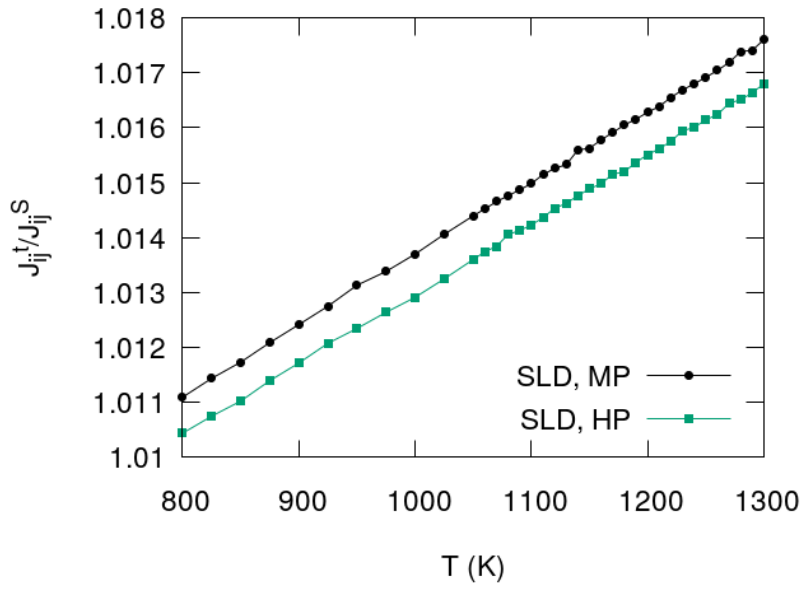

Fig. 5.3 Effective exchange coupling energy calculated during the simulation time for a $10 \times 10 \times 10$ BCC Fe unit cell periodic system. The average exchange coupling is normalised to the value corresponding to the total exchange coupling energy calculated for fixed lattice simulations (ASD) J_{ij}^S =2703.29meV.

constant for a fixed lattice simulation ASD. We observe that the changes in the effective exchange are small $< 2\%$ for periodic systems even at elevated temperature. An increase in the effective exchange constant is observed with increasing temperature, which presumably comes from the symmetric distribution of relative distances of atoms with varying width (equivalent to different temperatures) leading to a small bias of the average exchange constant towards larger values. To understand this, let's assume that the relative distances between the atoms follow a Gaussian distribution $D(r_{ij})$ of width σ around the equilibrium nearest neighbours distance $r_0 = 2.4854$Å:

$$D(r_{ij}) = \frac{1}{\sqrt{2\pi}\sigma} \exp\left(-\frac{1}{2}\frac{(r_{ij}-r_0)^2}{\sigma^2}\right) \tag{5.3}$$

The average exchange $\langle J \rangle$ will be given by the integral between the exchange function and the distribution of relative distances:

$$\langle J \rangle = \int_0^{r_c} J(r_{ij}) D(r_{ij}) dr_{ij} = \int_0^{r_c} J_0 \left(1 - r_{ij}/r_c\right)^3 D(r_{ij}) dr_{ij} \tag{5.4}$$

where $r_c = 3.75$Å is the exchange cutoff distance. Fig. 5.4 shows the variation of the normalised average exchange $\langle J \rangle / J(T = 0K)$ as a function of the width σ of the interatomic

distances for the nearest neighbours interaction. The vertical lines are given by the distribution width of nearest-neighbours interatomic distances calculated for different temperatures for a Morse potential. At $T = 0$K, there is no distribution of distances, as all atoms are positioned around an equilibrium BCC structure with a distance corresponding to the nearest neighbours interaction of $r_0 = 2.4854$Å. With increasing temperature, atoms start to oscillate around the equilibrium position and this leads to the appearance of a distribution of relative distances, which has a Gaussian form. The width of the distribution is proportional to the temperature of the system and can be calculated from the relative distance of the atoms for different temperatures - Fig. 5.5. For $T = 800$K and $T = 1300$K we observe a width of the Gaussian equal to $\sigma = 0.0980$ and $\sigma = 0.1211$ respectively and an increased in the mean displacements due to the small thermal expansion of the system. Moving now to the calculated average exchange Eq. 5.4 we observe that between the widths corresponding to temperatures of 800K and 1300K, the increase of the exchange is 1%. This is in agreement to the exchange energy as a function of temperature observed in Fig. 5.3 where an increase with 0.7% is observed within this temperature range for a Morse potential. The very small difference can be attributed to the fact that in the analytical calculation and numerical fit of the relative distances we include only the distance corresponding to the nearest-neighbours interaction, however the exchange interaction spreads over a larger cutoff.

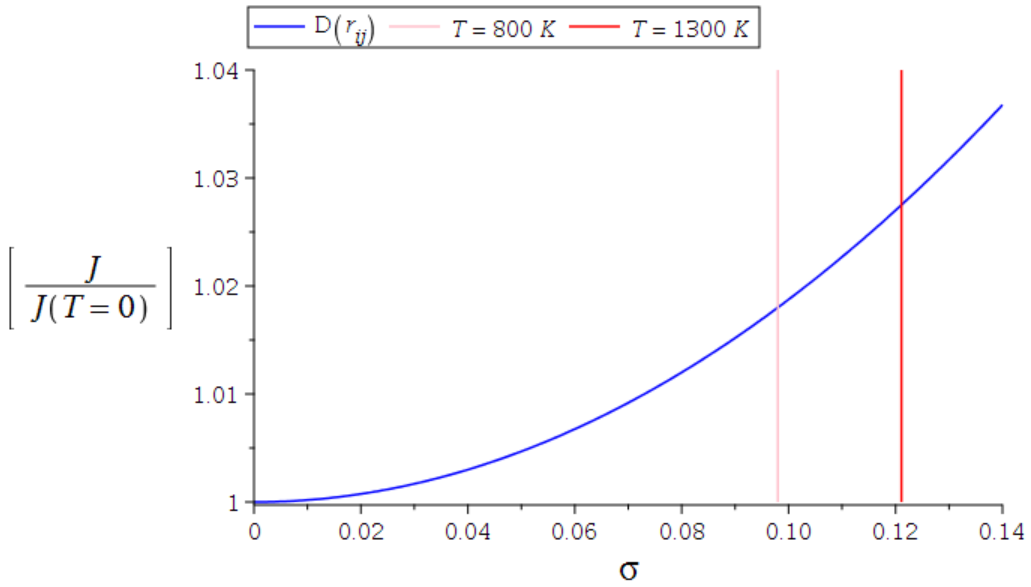

Fig. 5.4 Normalised effective exchange coupling energy as a function of distribution width σ calculated analytically via Eq. 5.4. The vertical lines show the distribution widths corresponding to $T = 800$K and $T = 1300$K calculated from the simulation with a Morse potential for the nearest-neighbours interaction.

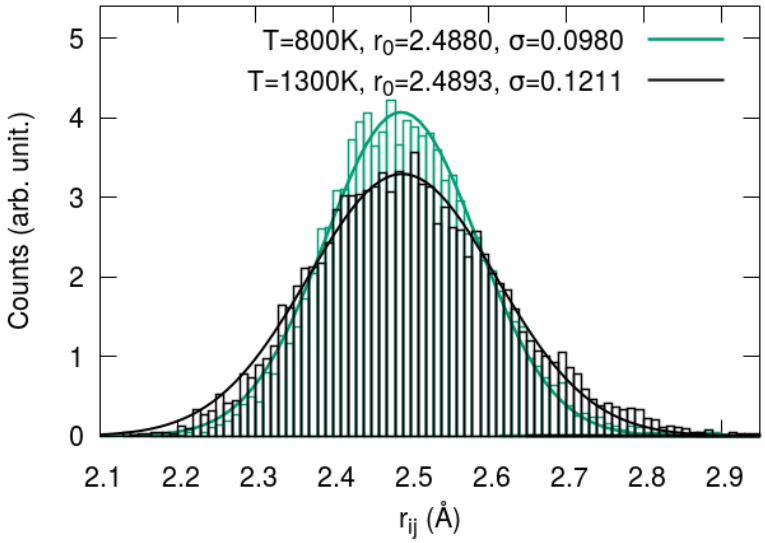

Fig. 5.5 Gaussian distribution of relative distances for nearest-neighbours pairs of atoms for two temperatures. The parameters of the Gaussian obtained by fitting are presented in the key of the plot.

5.1.1 Thin film systems

Removing the periodicity of the system within one direction, the equilibrium magnetisation differs substantially between a fixed and dynamic lattice. Fig. 5.6 shows the equilibrium magnetisation as a function of temperature for a thin film system of $10 \times 10 \times 10$ BCC unit cells system size. Comparing the equilibrium magnetisation for two thin films system sizes of 10 and 16 BCC unit cell size on z direction - Fig. 5.7 we observe that the finite size effects are more pronounced for SLD models. For a fixed lattice simulation (ASD), the difference in the equilibrium magnetisation between a thin film system and a periodic/bulk system is attributed to the loss of coordination at the surface, which affects the exchange energy. For the spin-lattice simulation, the loss of coordination leads as well to an expansion of the surface layers, which further influences the position dependent exchange interaction.

The expansion of the surface layer is shown in the plots of the profile of the relative distance for nearest neighbours interaction for a thin film system of $z = 10$ layers - Fig. 5.8. The horizontal blue line shows the distance corresponding to $T = 0$K neighbor distance. The relative distance r_{ij} is plotted as a function of the z coordinate of the atom i. The profile shows an increase in interatomic distance for the top and bottom layers due to the expansion of the surface in the absence of periodic boundaries. With increased temperature, this effect is more pronounced, as shown by the grey line which represents the averaged interatomic

distance for different r_i^z. Fig. 5.9 confirms that the top layer presents an increase in both the mean value of interatomic distance and distribution width. In this plot the distributions of the relative distances for the middle and top layer of the system are plotted for a temperature of $T = 800$K. For this temperature there is an increase of the averaged distance of about 0.08Å which can lead to a decreased exchange value and hence a smaller Curie temperature.

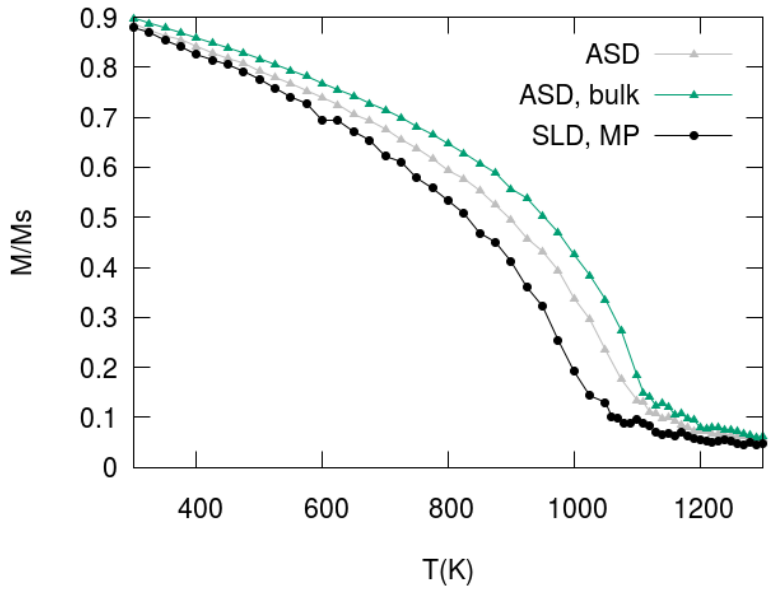

Fig. 5.6 Magnetisation versus temperature curves for a $10 \times 10 \times 10$ BCC Fe unit cell thin film for the ASD model and the SLD, with a Morse Potential.

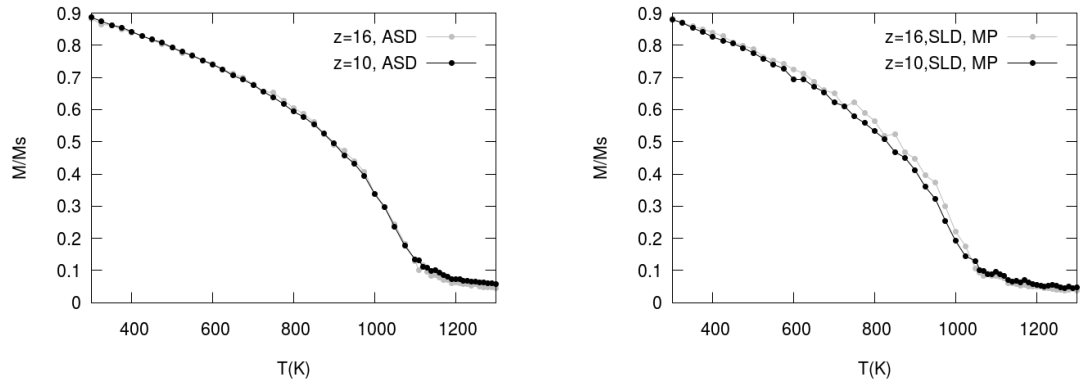

Fig. 5.7 Magnetisation versus temperature curves for a fixed (ASD - left panel) and dynamic lattice simulations (SLD, Morse Potential - right panel). The thin film is periodic in xy and consists of a 10×10 BCC unit cells and consist of 10 respectively 16 unit cells in z.

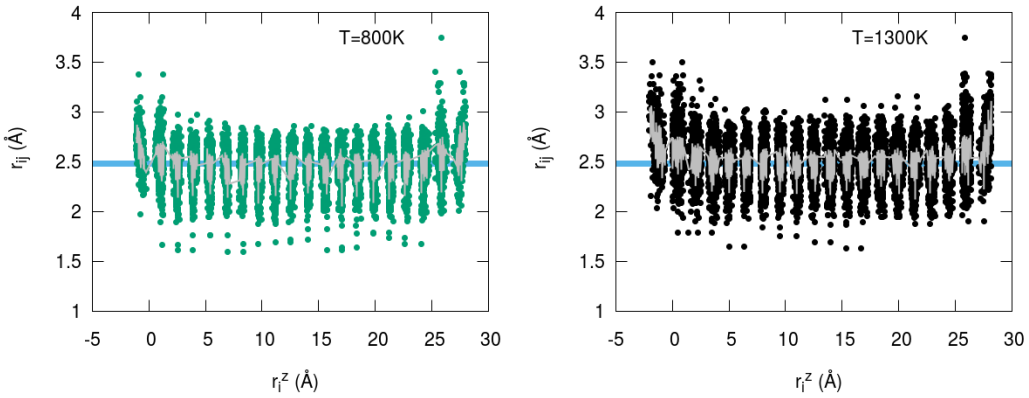

Fig. 5.8 Relative distance profile for nearest neighbours interaction for a thin film system of $z = 10$ layers at two different temperatures; The horizontal blue line shows the distance corresponding to $T = 0$K nearest neighbours interaction; The grey lines correspond to the averaged distances for different r_i^z displacements.

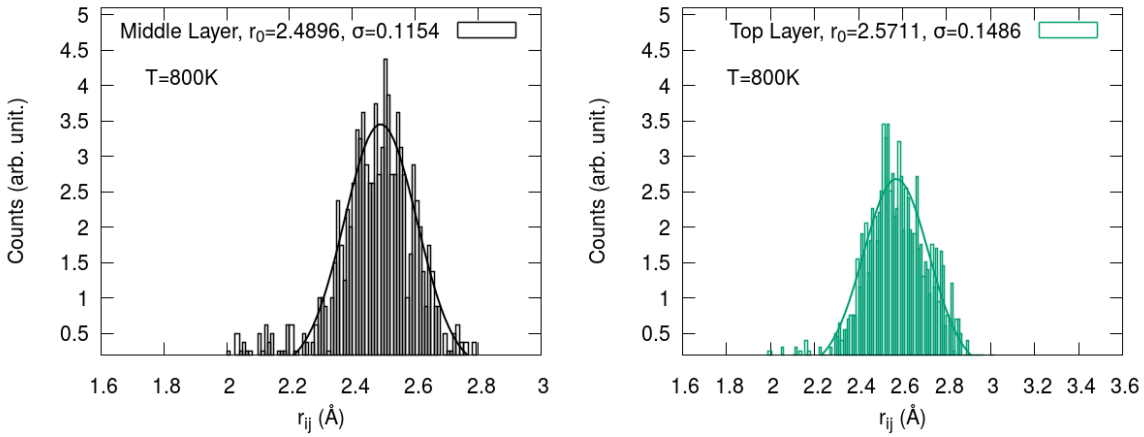

Fig. 5.9 Relative distance distributions for nearest neighbours interaction for the top and middle layer of a thin film system of $z = 10$ layers at a temperature of $T = 800$K.

We next calculate the normalised effective exchange constant during the simulation time via Eq. 5.2. Fig. 5.10 shows that with increased temperature there is a large decrease in the effective exchange (10% for the 16 layers system and 13% for the 10 layers system at 1100K) which explains the pronounced difference in the Curie temperature of the systems with respect to the bulk values. Nevertheless, we observe a change in trend close to the Curie temperature, which can be attributed to a small change in the lattice properties when the system becomes paramagnetic.

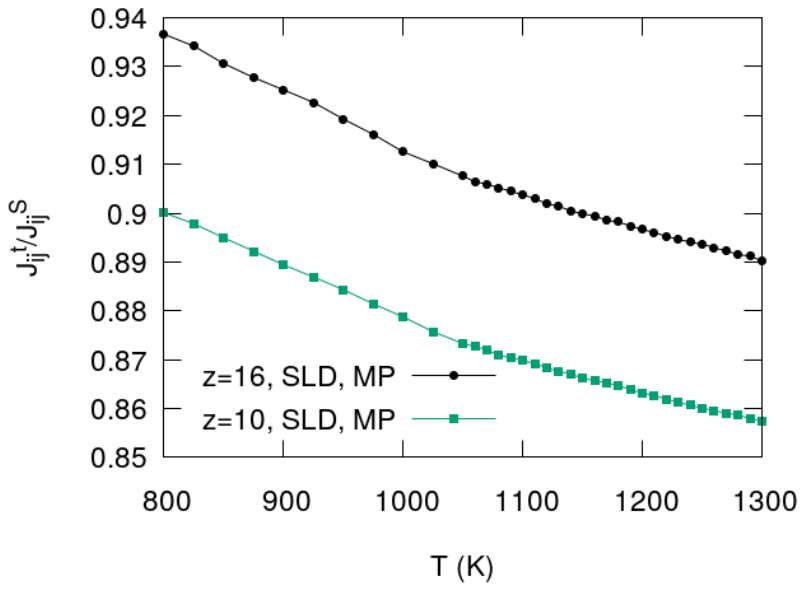

Fig. 5.10 Effective exchange coupling energy calculated during the simulation time for a thin film system. The thin film is periodic in xy and consists of a 10×10 BCC unit cells and consist of 10 respectively 16 unit cells in z; The average exchange coupling is normalised to the value corresponding to the total exchange coupling energy calculated for fixed lattice simulations (ASD) $J_{ij}^S = 2703.29$meV.

Finite size effects in granular systems have been intensively studied for recording media applications using ASD models [111],[123]. Since the SLD model leads to more pronounced finite size effects, a systematic investigation of the effect of the dynamic lattice on the equilibrium parameters for small system size is an important problem to look at.

5.2 Magnon-phonon damping

Using our implementation of the SLD model, in this section we evaluate the magnon-phonon damping for a periodic BCC system. The system is first equilibrated at a non-zero temperature in an external field of $\mu_0 H = 50$T applied on the z direction, then the magnetisation is rotated coherently through an angle of 30°. The system then relaxes back to equilibrium [114]. The z component of magnetisation is then fitted to $mz(t) = \tanh(\frac{\alpha\gamma H}{1+\alpha^2}t + d)$ where α represents the damping, γ the gyromagnetic ratio and d a constant related to the initial conditions. The model system consists of $10 \times 10 \times 10$ unit cells, the damping value being obtained from fitting $m_z(t)$ over 10 different simulations. Each fit value for individual simulations is plotted, the line showing the average over the damping obtained from the fit.

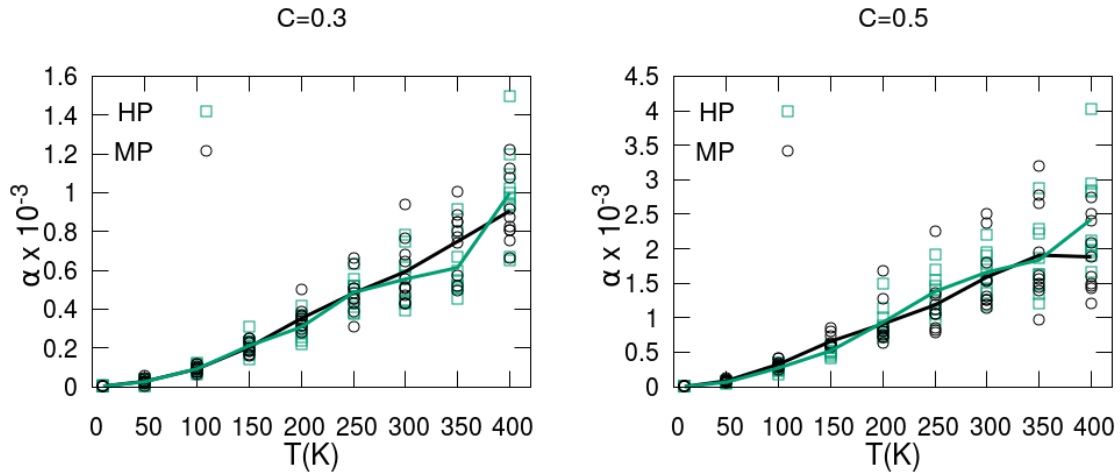

Fig. 5.11 Temperature dependence of the damping parameter extracted from fitting the z component of the magnetisation for two choices of atomic potential - Morse Potential (MP) and Harmonic Potential (HP). The symbols correspond to individual calculations, whereas lines indicate the average over 10 realisations.

Fig. 5.11 shows the temperature dependence of the damping parameter for two coupling strengths and different choice of mechanical potential. With increasing coupling, the angular momentum transfer is more efficient, hence the damping is enhanced. In our model, the spin system is thermalised by the phonon thermostat, hence no electronic damping is present.

Neglecting the lattice contribution, the temperature dependence of the macroscopic damping can be mapped onto the Landau-Lifshitz-Bloch formalism (LLB)[124, 125] and micromagnetic [108] and ASD simulations [126] have shown it to vary inversely with the equilibrium magnetisation. The LLB theory shows that the macroscopic damping is enhanced for large temperatures due to thermal spin fluctuations. Using the equilibrium magnetisation it is possible to approximate the variation of damping with temperature produced due to thermal fluctuations within the LLB model, as shown in Section 4.4. From 100K to 400K the damping calculated via the LLB model increases within the order of 10^{-5}, which is considerably smaller than the results obtained via the SLD model. This shows that within the SLD model the temperature increase of the damping parameter is predominantly due to magnon-phonon interaction, and not due to thermal magnon scattering, as this process is predominant at larger temperatures. The small temperature damping obtained here (at $T = 50$K, $\alpha = 4.9 \times 10^{-5}$) is consistent with the damping observed in magnetic insulators such as YIG (10^{-4} to 10^{-6} [127, 75]) and for similar SLD simulations (3×10^{-5}, [60]).

The results in Fig. 5.11 show that the damping is not greatly affected by the choice of potential. This happens probably due to the fact that when performing damping simulations,

only the spin modes around Γ are excited and for low k-vectors the inter-atomic distance between neighbouring atoms will not vary significantly.

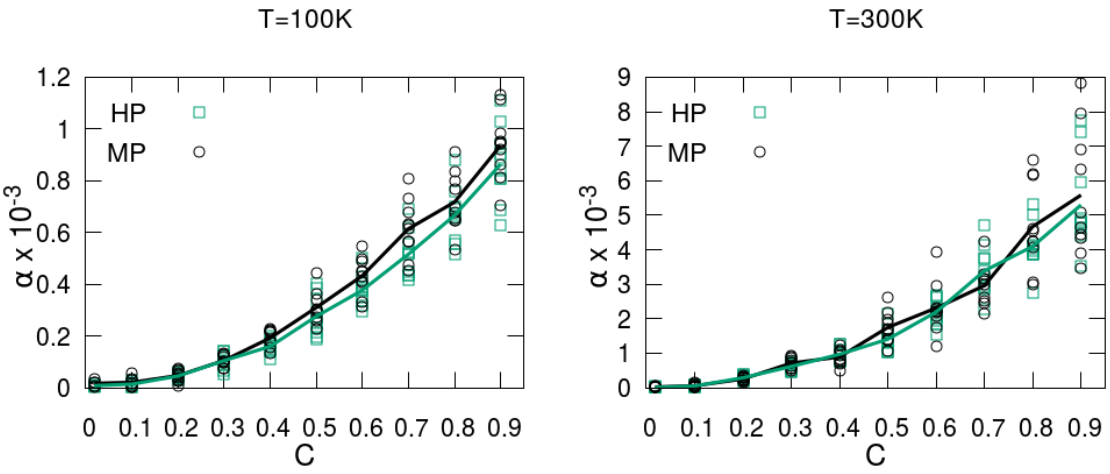

Fig. 5.12 Damping parameter extracted from fitting the z component of the magnetisation for different coupling strength and two choices of atomic potential - Morse Potential (MP) and Harmonic Potential (HP). The symbols correspond to individual calculations, whereas lines indicate the average over 10 realisations.

The extracted magnon-phonon damping as a function of coupling strength is presented in Fig. 5.12. In our simulations the temperature and coupling variation of the damping is quadratic, and we assume that this is due to the form of the pseudodipolar coupling that thermalises the spin system. Measurements of damping on magnetic insulators such as YIG showed a linear increase in the damping with temperature [75] which agrees with the relaxation rates calculated by Kasuya and LeCraw [128] and the relaxation rates calculated in the NVE SLD simulations in [60]. However, Kasuya and LeCraw suggest that the relaxation rate can vary as T^n, where $n = 1-2$, the 2 exponent corresponding to larger temperature regimes. Nevertheless, the difference between the quadratic temperature variation of the damping observed in our simulations and the linear one observed in experiments can suggest that the spin-orbit coupling in YIG should be described better by a linear phenomenological coupling term, such as the one used in [55, 54]. Also, the addition of quantum statistics [129, 130] for Spin Lattice Dynamics models may yield better agreement with experimental data of the temperature dependence of the damping.

Changing the form of the pseudodipolar coupling to an on-site form such as $H_c = -\sum_{i,j} f(r_{ij}) \left((\mathbf{S}_i \cdot \hat{\mathbf{r}}_{ij})^2 - \frac{1}{3}\mathbf{S}_i^2 \right)$ - Néel like anisotropy, leads to a much smaller damping - Fig. 5.13 ($T = 300$K, $\alpha = 5.32 \times 10^{-5}$, average over 10 seeds) making it difficult to calculate accurately the temperature dependence of the damping, especially for large temperatures.

The magnon-phonon damping can have complex behavior depending on the properties of the system, hence no universal behaviour of damping as a function of temperature can be deduced for spin-lattice models.

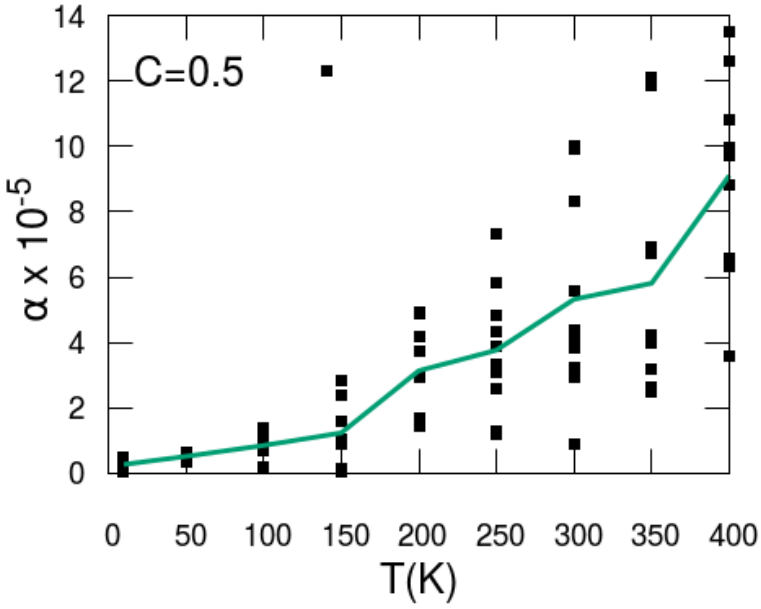

Fig. 5.13 Temperature variation of the damping for Néel-like on-site coupling, $H_c = -\sum_{i,j} f(r_{ij})((\mathbf{S}_i \cdot \hat{\mathbf{r}}_{ij})^2 - \frac{1}{3}\mathbf{S}_i^2)$. Damping is extracted from $m_z(t)$ fittings for 10 realisations.

To summarize, we have calculated the macroscopic damping, showing that it is not greatly influenced by the choice of potential, however it is influenced by the form of the coupling term. This enables the possibility of tailoring the form of the coupling term so it can reproduce experimental dependencies of damping for different materials.

5.3 Magnetisation switching by THz phonons

5.3.1 Introduction: Controlling magnetisation via laser excitation and phonons

The interaction of magnetic materials with fs laser pulses has shown multiple fundamental effects that culminate in the ability to switch the magnetisation by means of purely optical excitation [41]. The current understanding of these processes employs a thermal description, where the optical pulse is absorbed by the electron gas and creates a non-equilibrium distribution that leads to a fast demagnetisation of the spin system and a further relaxation with the lattice. This description can not be applied to dielectrics, as in these systems, there is no free electron gas, hence the optical control of the magnetisation needs to be done by other means. Additionally, thermomagnetic switching increases the temperature of potential devices, hence non-thermal control of magnetisation that can be applied to a large range of magnetic materials needs to be found.

There are several mechanisms that could lead to a magnetic response even in insulating magnetic systems, such as inverse Faraday effect [131], photoinduced magnetic anisotropy [132] and resonant THz pumping [133]. The inverse Faraday effect is based on impulsive stimulated Raman scattering by magnons [131, 134] and represents a non-thermal excitation. An effective magnetic field is generated using a non-resonant circularly polarised light which can lead to switching in a manner similar to a precessional reversal [135] in an applied magnetic field, but at much lower time-scales (100-200fs). Magnetocrystalline anisotropy can be modified by optical induced redistribution of ions in garnets [132] and can lead to changes of the magnetisation associated with a low heating of the material. In antiferromagnets, where characteristic frequencies are much larger than in ferromagnetic materials (in terahertz region), the magnetisation can be excited by terahertz electromagnetic pulses either directly [133] or via phonons. Controlling spins by optical excitation of phonons has been demonstrated in some materials either experimentally [71, 69, 72, 136] or theoretically, showing even the possibility of switching the magnetic order parameter [74, 73]. Switching the magnetisation via phonons can be done non-thermally and can represent a main phenomenon to drive the reversal in insulators.

There are two main mechanisms in which strongly pumped phonons in the THz regime can modulate the magnetisation: via the exchange interaction and via the anisotropy, however in reality there is a combination of both elements. The manipulation of the exchange fields has been shown in the magnetic insulator YIG [68] or in Gd surface [69] - Fig. 5.14 and appears naturally when exciting the phonons in a magnetic system due to the distance

dependence of exchange interaction. In YIG, the exchange between different sublattices is modulated and enables a variation of the sublattice magnetisation, hence a transfer of angular momentum between different sublattices of the material, with the constraint that the total angular momentum of the system remains conserved. The excitation of THz phonons at the surface of the sample at a 3THz frequency leads to a magnetic response with the same frequency in Gd [69] via the exchange modulation phenomena. The similar frequency observed in both magnetic and lattice system proves the necessity of considering the dynamics of both phonons and spins as in the model developed in this thesis.

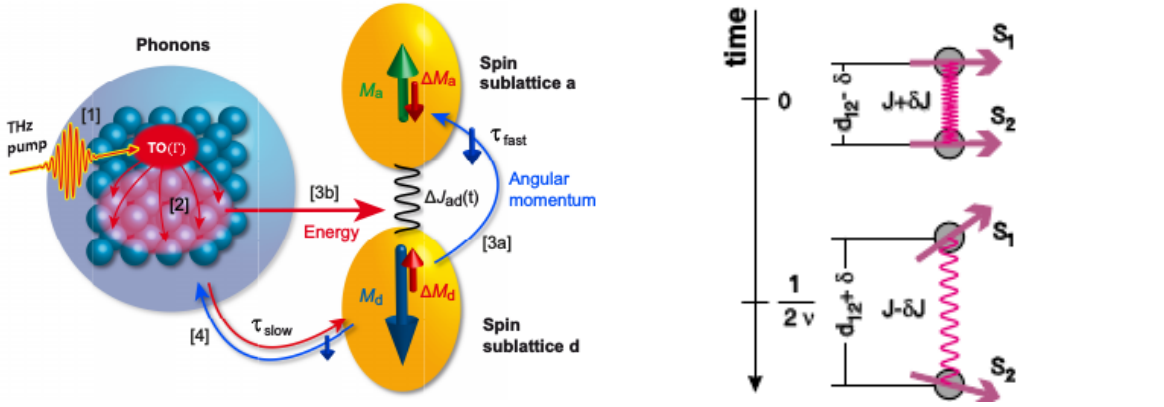

(a) YIG sublattices - extracted from [68].

(b) Gd(0001) surface - extracted from [69].

Fig. 5.14 Modulation of exchange under the application of a laser pulse between two sublattices in YIG and between surface and sub-surface atoms in Gd.

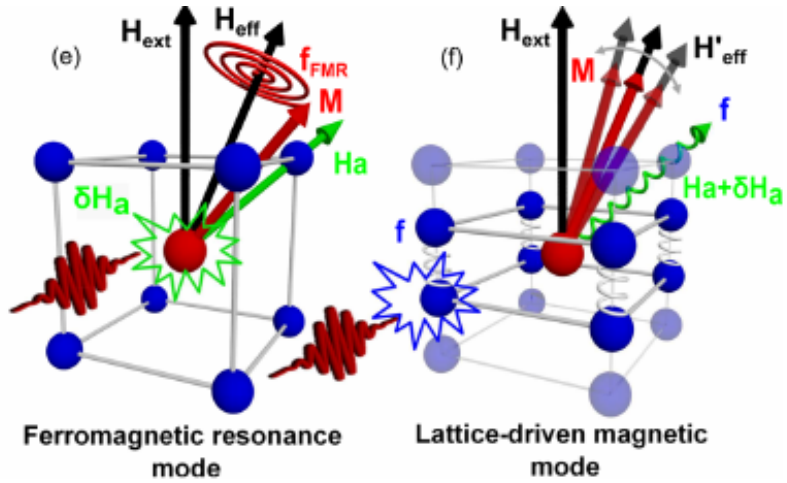

Fig. 5.15 Schematics of light induced FMR and lattice-mediated oscillations of magnetic anisotropy, extracted from [137].

Another mechanism to control the magnetic response by phonon excitation is by modulating the anisotropy via magnetoelastic coupling. Afanasiev *et al.* [137] has shown that in $FeBO_3$ which is an antiferromagnetic dielectric, under the excitation of a fs laser pulse, an acoustic wave is generated into the system that leads to a modulation of anisotropy followed by a magnetic response. Instead of coupling to the magnetic modes as in ferromagnetic experiments, the laser couples to the phonons which will lead to a change in anisotropy, as shown in Fig. 5.15. The modulation of anisotropy pushes the spin system into an anharmonic regime which potentially can lead to switching.

Other scenarios to control magnetisation is by laser induced strain pulses that are either injected into the magnetic system or created at one end of the sample, leading to the propagation of surface acoustic waves (SAW), as illustrated in Fig. 5.16. The theoretical investigations in Ref. [73, 74] show that it is possible to switch the magnetisation by means of acoustic pulses.

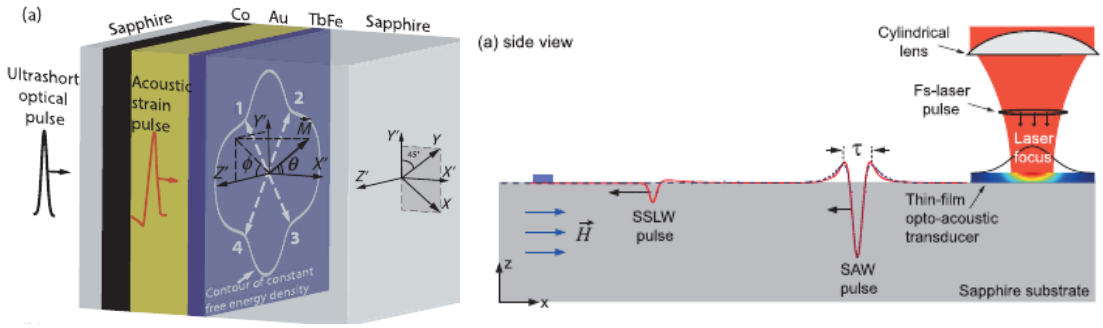

(a) Extracted from [74]

(b) extracted from [73]

Fig. 5.16 Generation of acoustic pulses that can potentially switch the magnetisation.

The examples presented above clearly suggest that there is a strong interaction between the spins and phonons in the magnetic system, which if exploited correctly, can lead to non-dissipative switching of magnetisation which can potentially solve the problem of large energy consumption of data storage centers.

5.3.2 Switching via THz phonons

To model the effect of THz phonons, we apply a periodic external force to each atom in the system (Eq. 5.5) for a finite time. For simplicity, the force is applied only on a single direction $\alpha = (1,0,0)$. In contrast with ferromagnetic resonance experiments, where an external periodic field is applied to lead the spin system into resonance, here the application of an external force with no space-phase factor will only lead to a periodic translation of the system and no excitation of phonons. Hence the introduction of a space-phase factor is

needed, which has been chosen $k = (\pi/a_0, \pi/a_0, \pi/a_0)$, where a_0 is the lattice spacing as shown in Fig. 5.17. This phase factor corresponds to the P point of the Brillouin zone. The periodic force is applied from the beginning of the simulation until a time t_p, that represents the pulse width, as suggested by the Heaviside step function $\Theta(t_p - t)$. We use an amplitude of the THz force $f_0^x = 0.05$. This leads to oscillations of the atoms around their equilibrium position smaller than 7% with respect to the lattice spacing depending on the frequency we excite with, as suggested in Fig. 5.18. The potential used for the following simulations is the Harmonic Potential and the system simulation size is $10 \times 10 \times 10$ BCC unit cells.

$$F_{THz}^{\alpha}(t, \mathbf{r}) = f_0^{\alpha} \cos(2\pi\nu t + \mathbf{k} \cdot \mathbf{r})\Theta(t_p - t) \tag{5.5}$$

Fig. 5.17 Schematics of THz excitation. A periodic THz force given by Eq.5.5 is applied for each atom. A phase factor of $k = (\pi/a_0, \pi/a_0, \pi/a_0)$ is used, where a_0 is the lattice spacing. This phase factor corresponds to the P point of the Brillouin zone.

Fig. 5.18 shows the normalised displacement of an atom in the system for two frequencies (8.3THz and 8.4THz) together with the Fourier Transform of the signal that shows a peak at the frequencies we excite the system with (green dotted lines). To avoid the initial mode that appears at the beginning of the excitation of the system we perform the Fast Fourier Transform (FFT) starting with 20ps. For these frequencies, 8.3THz and 8.4THz, we observe that the response of the lattice is the largest and this correlates to the phonon spectrum of the system. By analysing the phonon spectrum at low temperatures - Fig. 5.19 we observe two aspects: firstly, the 8.3THz and 8.4THz frequencies intersect with the P point of the system, which corresponds to the k vector we use for the THz force and secondly, there are multiple phonon modes available in the system to couple to these frequencies. Because of the strong coupling of the phonon modes with the THz excitation at these precise frequencies given by the multiple k points at this frequency, the excitation of the lattice leads to a strong magnetic response that can even switch the magnetisation as shown in Fig. 5.20. In the next part of this Section we will systematically analyse the switching mechanism via THz phonon and show the window of parameters where switching can be obtained with very small heating of the system.

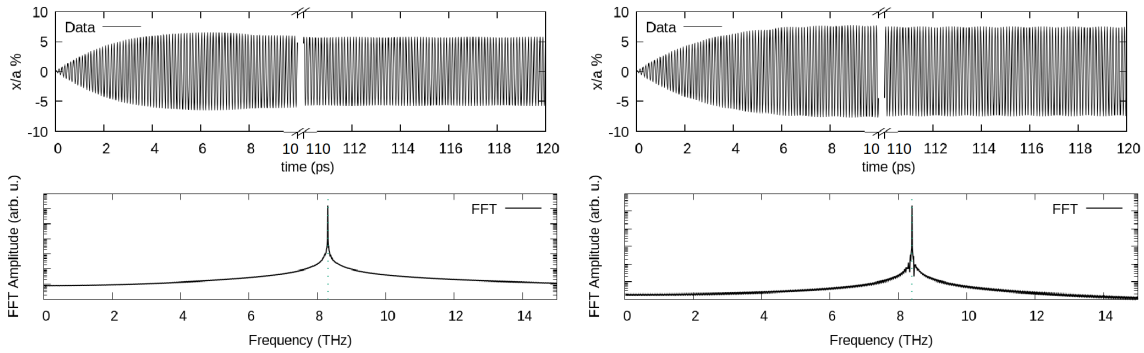

Fig. 5.18 Temporal evolution and the Fourier Transform of the x coordinate of the atom at position (0,0,0) normalised to the lattice constant (a) for a Harmonic potential: left panel - for a frequency of 8.3THz and right panel - for a frequency of 8.4THz. The THz pulse is applied continuously during the simulation. The dotted vertical line shows the frequency of the THz pulse. From the peak of the FFT we observe that the lattice excitation corresponds to the same frequency as the THz pulse.

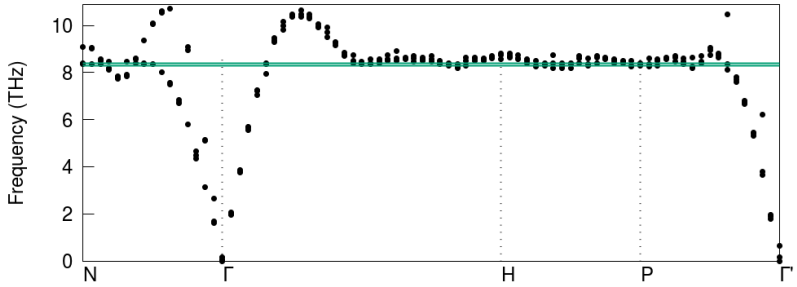

Fig. 5.19 Phonon spectra of the x component of velocities at $T = 10$K for a Harmonic potential; The horizontal green lines show the 8.3THz and 8.4THz frequencies where we observe the largest magnetic response.

Fig. 5.20 shows the behaviour of the magnetisation for different pulse widths (5ps to 125ps) for two frequencies: 8.3THz (left plot) and 8.4THz (right plot). For small pulse widths ($<$ 25ps) the change in the magnetisation is very small. With increasing pulse width, the magnetic system can take more energy from the lattice and switching can occur at 115ps for a frequency of 8.3THz. For longer pulse widths, the magnetisation oscillates back to the initial position, suggesting that the mechanism behind switching is similar to a precessional switching where a small in-plane component of external field is applied to a magnetic system. The magnetic response is observed only for frequencies in the range $8.3 - 8.5$THz which correlates to the phonon spectra - Fig. 5.19, where we observe multiple phonon modes available at this frequency range, especially at the P point in the Brillouin zone, which corresponds to the k point we excite the system with. When the application of the THz pulse

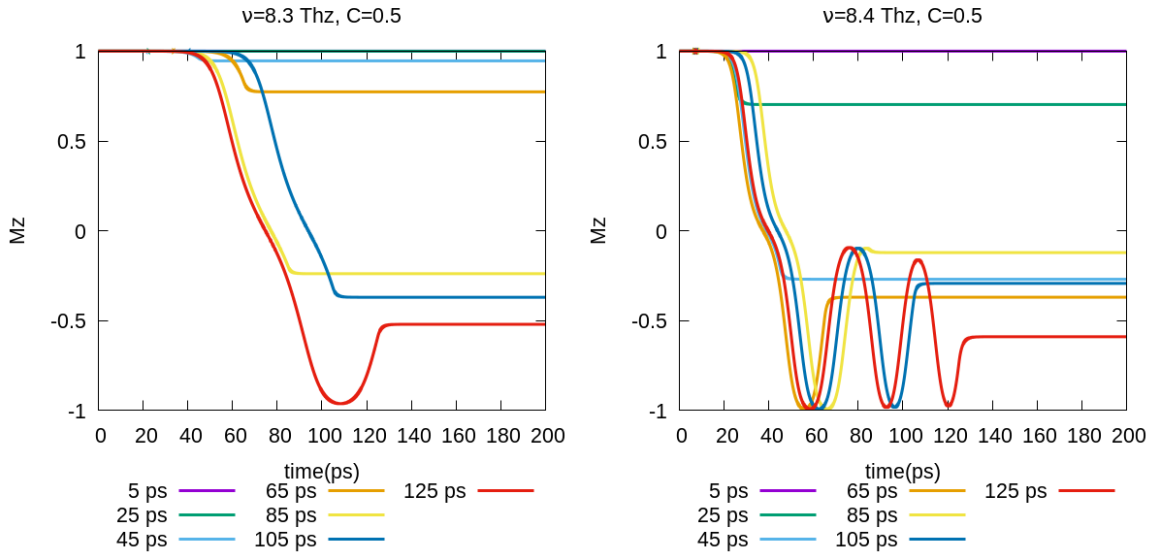

Fig. 5.20 Magnetisation behaviour under the application of different THz pulse widths ranging from 5ps to 125ps at $T = 0$K. For these calculations, a Harmonic potential and a coupling strength of $C = 0.5$ is used. The largest magnetic response is observed for frequencies in the range $8.3 - 8.5$THz correlated with the region where multiple phonon modes are accessible.

has stopped ($t > t_p$), there are very small changes in the magnetisation. This can be explained by the fact that the dynamics of the magnetisation is very slow due to: i) the small magnon-phonon damping, ii) there is no external applied field in the system, the only effective field that can lead the magnetic system returning to +z direction is a small uniaxial anisotropy, $H_K = 0.05$T. Assuming that H_K will play the role of an out-of-plane field that restores the +z direction of magnetisation, in the presence of such a small field and low values of damping (only due to magnon-phonon contribution), the relaxation of magnetisation from an in-plane to an out-of-plane direction can be described analytically by $m_z(t) = \tanh\left(\alpha\gamma Ht/(1.0+\alpha^2)\right)$ and happens at timescales much larger than the ones accessible via this code ($>$ 30ns). Hence the apparent constant magnetisation is in accordance with the small timescale presented here. We have performed additional tests and showed that in the presence of larger anisotropy field and larger damping (by the inclusion of intrinsic electronic contributions), the magnetisation shows a recovery to the z direction at the timescale of a few nanoseconds.

We analyse now the switching results in the case of an applied THz pulse of frequency 8.3THz for a pulse width of $t_p = 115$ps - Fig. 5.21 to Fig. 5.25. Fig. 5.21 shows the magnetisation components during switching, together with the spin temperature of the system. The system is initialised at $T = 0$K, with a z component of magnetisation $M_z = 0.999$ which gives a spin temperature of 10^{-6}K. During the switching, the change in the magnetisation

length is less than 0.04%, suggesting that the mechanism behind switching is non-thermal. Indeed, analysing the spin temperature during switching - Fig. 5.22, we observe that the increase of temperature is in the mK range, proving the lack of heating during this process. After the removal of the THz pulse (white region) the magnetisation remains in the switched state.

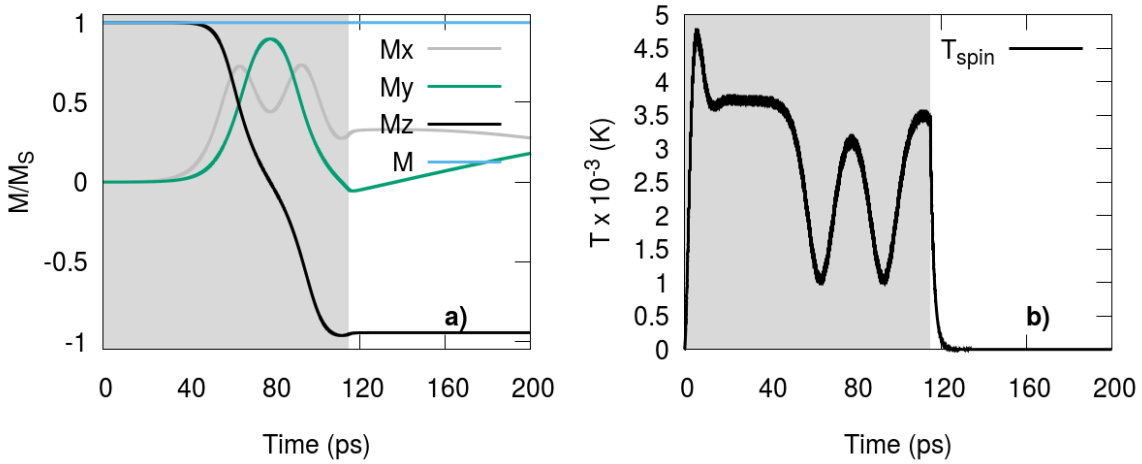

Fig. 5.21 Magnetisation dynamics under the application of a THz pulse of frequency 8.3THz for 115ps. The temporal region where the THz pulse is applied is emphasized by the grey region. a) Magnetisation dynamics showing a switched state after the application of a THz pulse; b) Spin temperature during and after the application of a THz pulse.

Under the application of a THz pulse, the lattice temperature does not have a physical meaning anymore. The THz pulse pumps energy into the lattice and drags the system out of equilibrium, hence no equilibrium Boltzmann distribution is established for the temperature to be defined. To check if the lattice is not affected by the application of the THz pulse, we calculate the average velocities and average displacements during and after the application of the THz pulse. Fig. 5.22, a) shows that all average components of velocity are very small, with a dominant x component in the direction where the THz pulse is applied. By calculating the average displacements with respect to the equilibrium BCC structure Fig. 5.22, b) we observe that these are very small (about 10^{-14}Å), within machine precision, proving that the lattice structure is not affected by the THz pulse.

Going now to the magnetic system, we can calculate the average forces produced by the magnetic subsystem and the average effective fields during the switching process. Fig. 5.23 presents the average exchange and pseudo-dipolar coupling during the application of a THz pulse and shows that the forces are centered around zero, hence no drift effects will be present in the lattice due to the magnetic system. The histogram of magnetic forces is shown in Fig.

5.24 and shows that the distribution is symmetric and centered around 0, which furthermore proves that no drift in the lattice will occur due to the switching of the magnetisation.

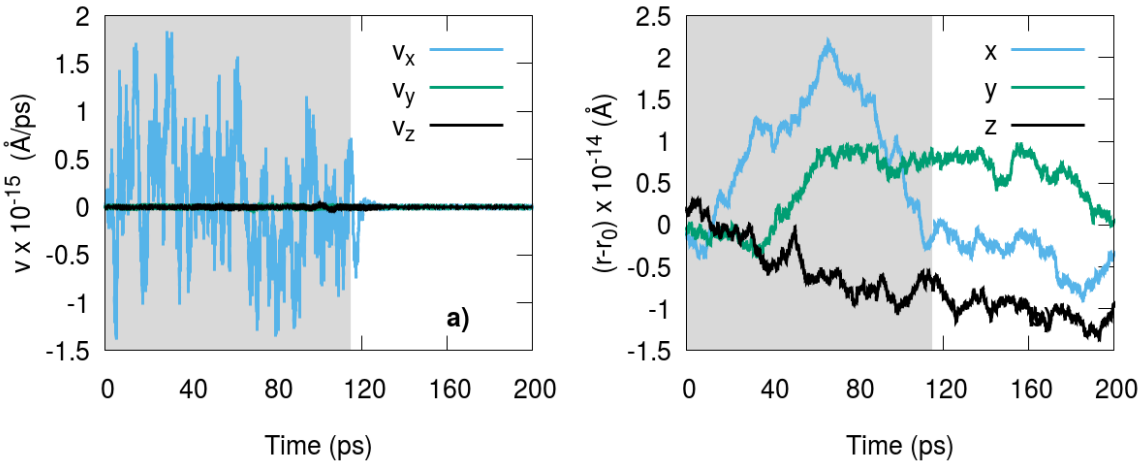

Fig. 5.22 Average velocities (a) and displacements (b) during the application of a THz pulse of frequency 8.3THz for 115ps (grey region).

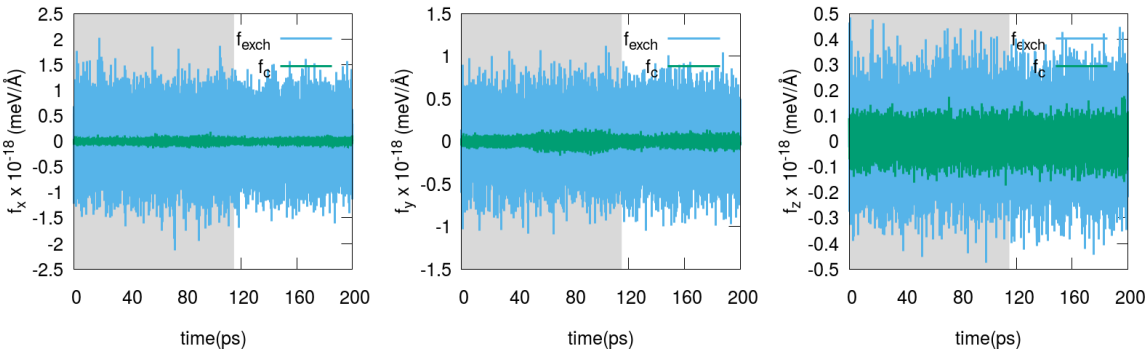

Fig. 5.23 Average forces (exchange force - f_{exch} and pseudo-dipolar force - f_c) produced by the magnetic system during the application of a THz pulse of frequency 8.3THz for 115ps (grey region).

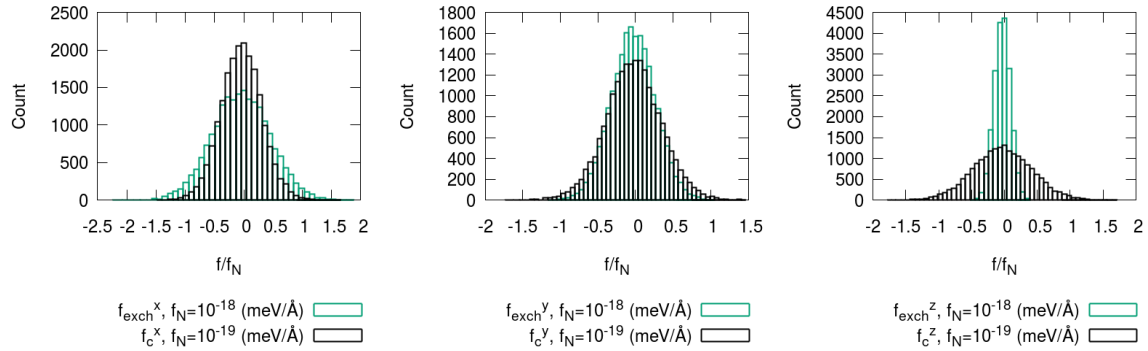

Fig. 5.24 Histogram of average forces (plotted in Fig. 5.22, exchange force - f_{exch} and pseudo-dipolar force - f_c) produced by the magnetic system during the application of a THz pulse of frequency 8.3THz for 115ps.

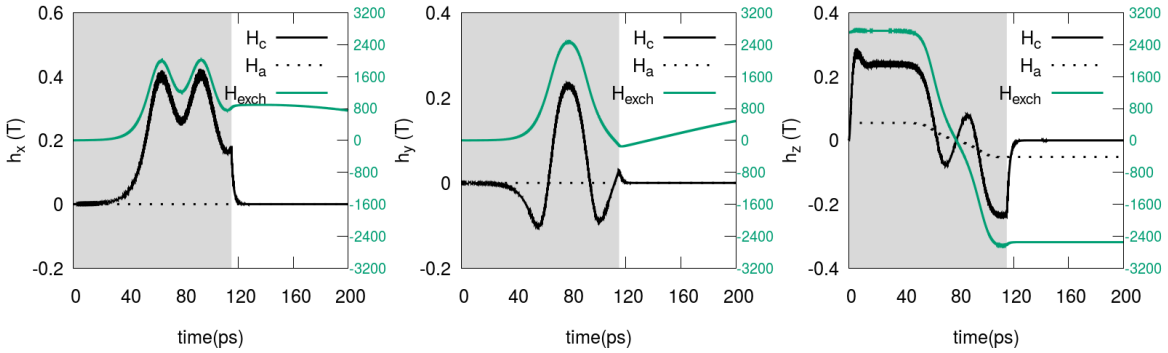

Fig. 5.25 Average magnetic fields during the application of a THz pulse of frequency 8.3THz for 115ps (grey region). The exchange fields are much larger in amplitude, hence they are plotted on a different scale at the right side of the plot (green axis).

The average magnetic fields are plotted in Fig. 5.25. A different scale is used for the exchange field (H_{exch} green lines, right axis) than for the pseudo-dipolar and anisotropy field (H_C, H_a - black lines, left axis) as the atomistic exchange is in general much larger than other magnetic fields (2700T in equilibrium). Initially the coupling field H_C shows a large out of plane component, $h_z = 0.27$T due to the fact that the initial state of the system is $Sz = 0.999$, hence the exchange correction term that enters into the definition of the coupling field will lead to an out of plane spin component. Under THz excitation, the lattice is distorted and this can lead to the creation of local in-plane anisotropy, since the force is applied only on the x direction, hence the coupling field increases to values of about 0.4T in the x component which can trigger the switching. Variations in the M_z component of the magnetisation - Fig. 5.21 happen at about 40ps, and at this point in time, the in-plane components of the coupling field reached a value of 0.05T which competes with the uniaxial out-of-plane anisotropy -

Fig. 5.26. The M_z component of the magnetisation becomes negative at around 80ps and this correlates to the point where the z component of the coupling field is zero, however the in-plane components are very strong. The variations of the uniaxial anisotropy field and exchange follow the form of the variation of the magnetisation. As the system goes in plane, the uniaxial anisotropy field decreases from 0.05T to -0.05T.

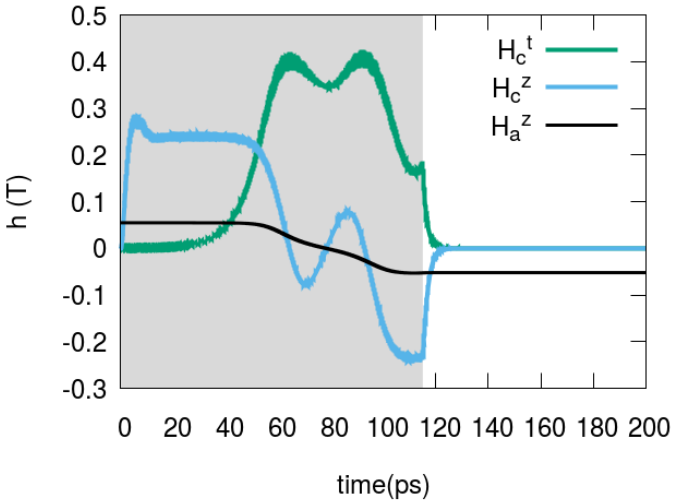

Fig. 5.26 Average coupling and anisotropy fields during the application of a THz pulse of frequency 8.3THz for 115ps (grey region). The transverse component of the coupling field $H_c^t = \sqrt{(H_c^x)^2 + (H_c^y)^2}$ is plotted together with the out-of-plane components of the coupling field and anisotropy.

During the application of the THz pulse, not only the coupling term is modified, but also the exchange field. As the variation in the exchange field overlaps with the variation in the magnetisation, it is difficult to understand if the exchange modulation triggers the change in the magnetisation or whether it is the other way around. A better description of the dynamics of the magnetic system can be understood by looking at the effective coupling constants, rather than the effective fields - Fig. 5.27. The effective constants are calculated as an average over the pairs of exchange energies and coupling energies in the systems:

$$J = \frac{1}{N}\sum_{i,j} J_0 \left(1 - r_{ij}/r_c\right)^3 \tag{5.6}$$

$$C = \frac{1}{N}\sum_{i,j} C_0 J_0 / r_{ij}^4 \tag{5.7}$$

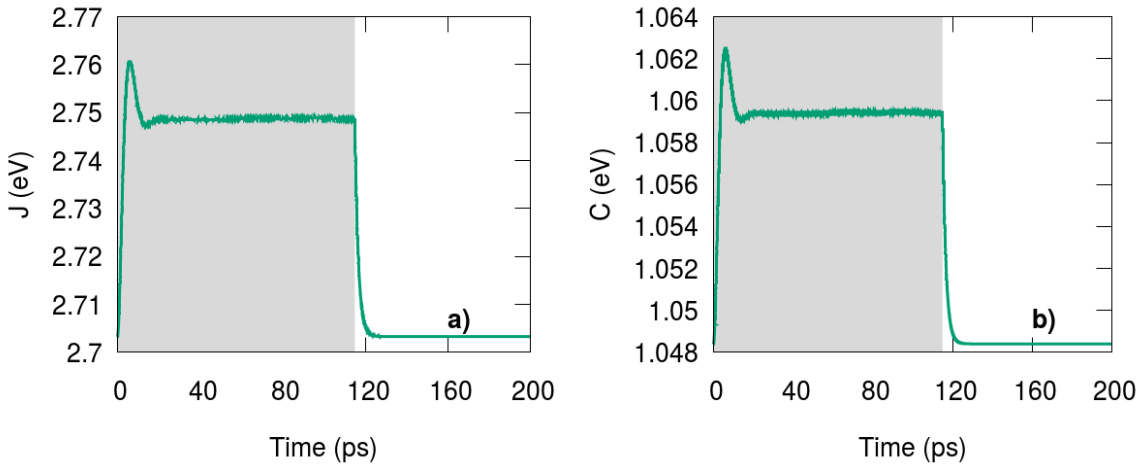

Fig. 5.27 Effective exchange (panel a) and pseudo-dipolar coupling (panel b) under the effect of a THz pulse of frequency 8.3THz for 115ps (grey region) for a pseudo-dipolar coupling constant $C_0 = 0.5$. The effective couplings are calculated via Eq. 5.6 and 5.7. Both energy contributions exhibit a variation during the application of the THz pulse.

Fig. 5.27 shows the variation of the effective exchange coupling (a) and effective pseudo-dipolar coupling (b) during the application of a THz pulse. We observe that both effective couplings exhibit a variation during the time of application of the THz pulse. To test which of the coupling is responsible for the switching of the magnetisation, we consider the case where the exchange coupling is constant and given by the equilibrium positions r_{ij}^0 corresponding to a BCC structure. The same test cannot be applied to the coupling term as this is responsible for the thermalisation of the spin system in the absence of a spin thermostat. We observe that by considering a constant exchange corresponding to an equilibrium BCC structure we still can obtain switching - as shown in Fig. 5.28. The switching appears at larger frequencies 8.5THz and longer pulse widths. The possibility of switching in the absence of a modulated exchange energy proves that the pseudo-dipolar coupling is responsible for the switching via THz phonons. We elucidate that the mechanism behind switching relies on the development of a local in-plane anisotropy created via the pseudo-dipolar coupling field that triggers a precessional switching of the system.

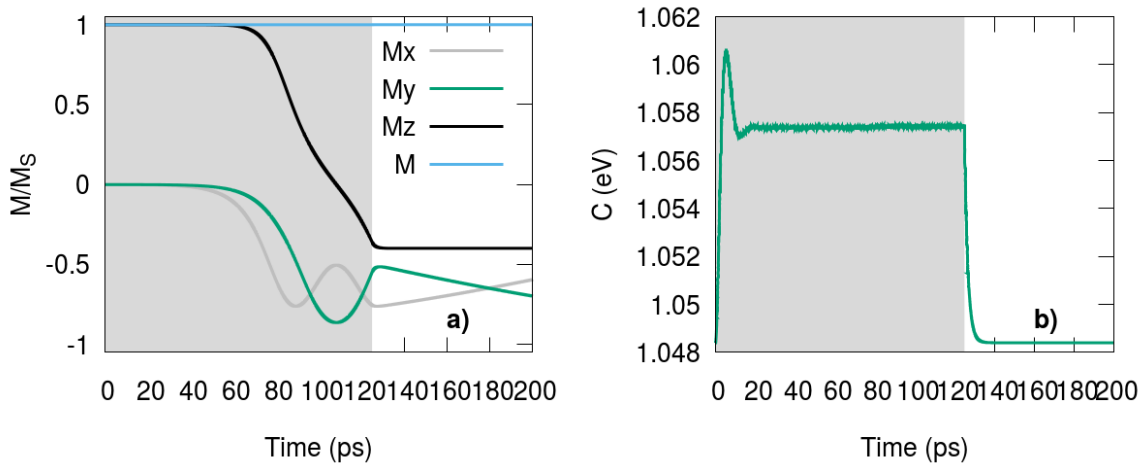

Fig. 5.28 Magnetisation (a) and effective pseudo-dipolar coupling (b) under the effect of a THz pulse of frequency 8.4THz for 125ps (grey region) for a pseudo-dipolar coupling constant $C_0 = 0.5$ and a position independent effective exchange interaction.

5.3.3 Switching phase diagram $T \geq 0$K

In this section, the switching phase diagram for different THz pulse widths and frequencies is presented for two temperatures: $T = 0$K and $T = 10$K. The system size used in the simulations is $10 \times 10 \times 10$ BCC unit cells. The colorbar is given by the final value of the M_z component of the magnetisation, taken at $t = 300$ps - Fig. 5.29. If the final magnetisation after the THz pulse is negative, we can consider the system in a switched state, as if let long enough to evolve, the system will go towards the negative value of saturation. Hence the phase diagrams in terms of switched/not-switched state are presented in Fig. 5.30.

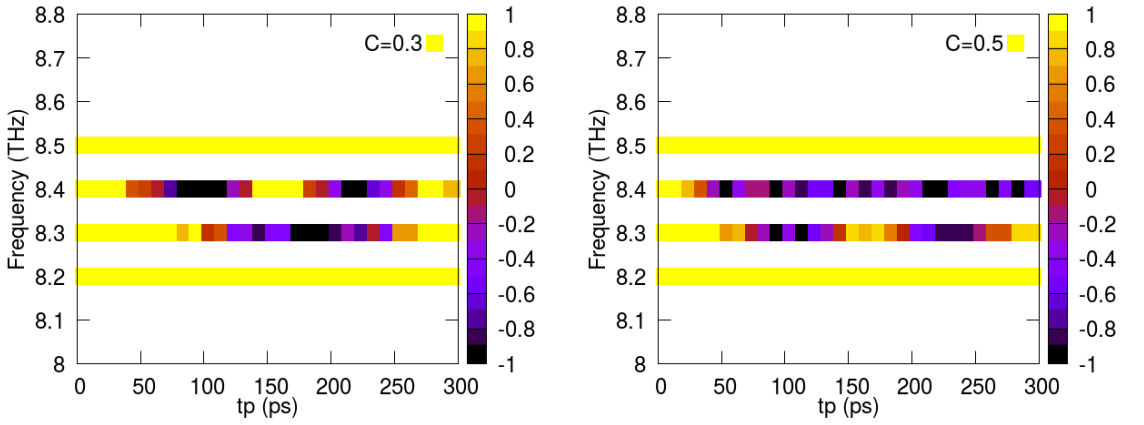

Fig. 5.29 Switching phase diagram at $T = 0$K for two coupling values: $C = 0.3$ and $C = 0.5$; The color bar is given by the final value of the z component of the magnetisation.

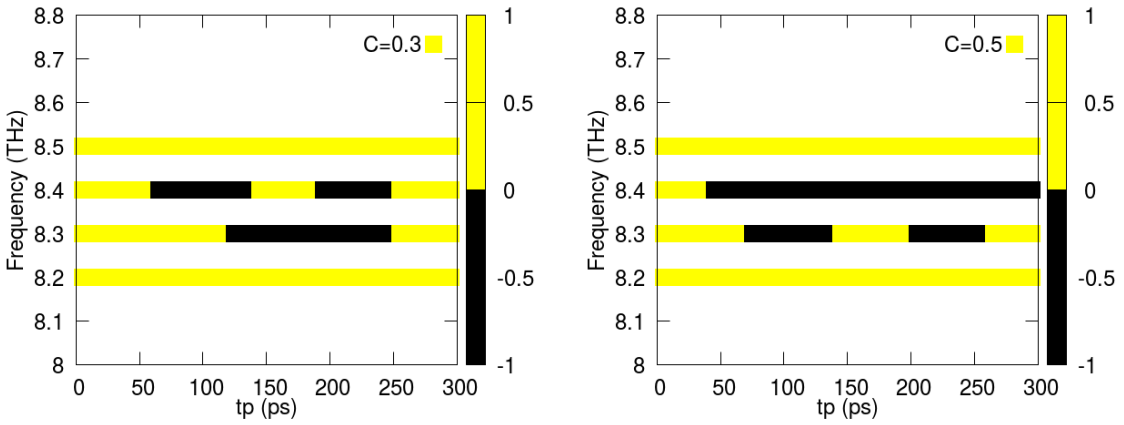

Fig. 5.30 Simplified switching phase diagram at $T = 0$K for two coupling values: $C = 0.3$ and $C = 0.5$; The switched state is given by the black colour which represent negative value of final z component of magnetisation.

Fig. 5.29 shows the phase diagram at $T = 0$K for a coupling constant $C = 0.5$ and $C = 0.3$. We observe that only frequencies in the range $8.3 - 8.4$ THz present variations in the Mz component of the magnetisation and these frequencies relate directly to the accessible phonon modes at the H point of the Brillouin zone for a Harmonic potential. We observe that for longer pulse widths, there is an oscillatory behavior of the magnetisation which correlates to the precessional nature of the switching. The simplified switching phase diagram is shown in Fig. 5.30 for two values of the coupling constant. We observe that with decreasing coupling, the initial switching region moves to longer pulse widths. This happens due to the fact that, for decreasing value of the coupling, the spins are more weakly coupled to the lattice so it is needed more time to transfer the energy from the phonons to the spins and for switching to occur.

We next analyse the behaviour of the magnetic system for 8.4THz - Fig. 5.31 and 8.3THz - Fig. 5.32 for a coupling strength of $C = 0.5$. The top graphs show the magnetisation components for the final state of the system (blue points) as a function of pulse width t_p, during the $t_p = 295$ps simulation (black line) and switching profile extracted from the phase diagram (green line). The bottom graphs show the minimum, maximum and averaged coupling fields developed during the simulation time of 300ps. The left panels show the in-plane transverse components of both magnetisation and coupling field calculated as $M_t = \sqrt{M_x^2 + M_y^2}$, $h_c^t = \sqrt{(h_c^x)^2 + (h_c^y)^2}$. Each point is corresponding to a different realisation, hence the variation of the magnetisation for arbitrary cutoffs of the THz pulse with respect to the $t_p = 295$ps corresponds to the usage of different random seed. In Fig. 5.31 (top), the Mz component of the magnetisation clearly shows a transitory oscillation regime, with switching appearing in the first 40ps of excitation and then oscillations towards the negative

saturation. This suggests that after 40ps, the THz pulse does not excite the magnetic system strongly enough, hence after switching the magnetisation oscillates around the new energy minimum corresponding to the switched state. As the mechanism behind switching is given by the pseudodipolar coupling that acts as a local in-plane anisotropy, we next analyse the components of the developed coupling fields. At 40ps we observe the development of a transverse component of the coupling field that has a maximum absolute value of 0.75T, Fig. 5.31 (bottom), the development of this field being correlated to the region where we observe the system being in a switched state. We also observe that the average coupling field is non-zero both in plane and out-of-plane and this can be attributed to the non-linearity of the coupling field: although the displacements are symmetric around the equilibrium position (due to the form of the harmonic potential and the form of the THz force), the form of the coupling field can lead to a non-zero average.

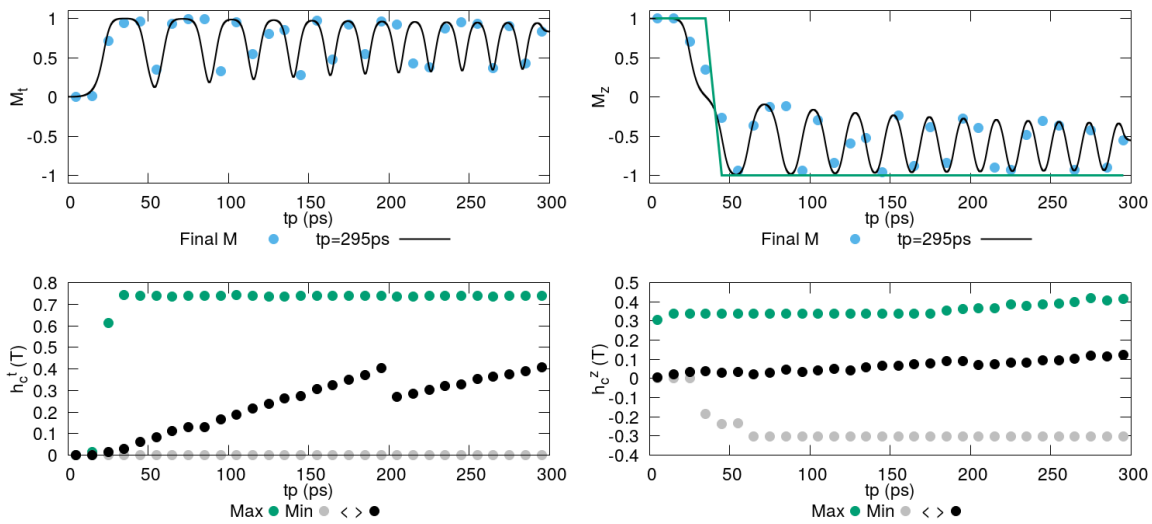

Fig. 5.31 Behaviour of magnetisation and coupling field for different pulse widths of frequency 8.4THz. Top panel - magnetisation components for the final state of the system (blue points), during the $t_p = 295$ps simulation (black line) and switching profile extracted from the phase diagram (green line). Bottom panel - minimum, maximum and average coupling field components. The left panels show the in-plane (transverse) components of both magnetisation and coupling field calculated as $M_t = \sqrt{M_x^2 + M_y^2}$, $h_c^t = \sqrt{(h_c^x)^2 + (h_c^y)^2}$.

In Fig. 5.32 (top right panel), the Mz component of the magnetisation shows oscillations between positive and negative saturation. The maximum in-plane coupling field in Fig. 5.32 (bottom left panel) is comparable with the z component and indicates a weaker excitation of the phonon mode that leads to magnetisation switching.

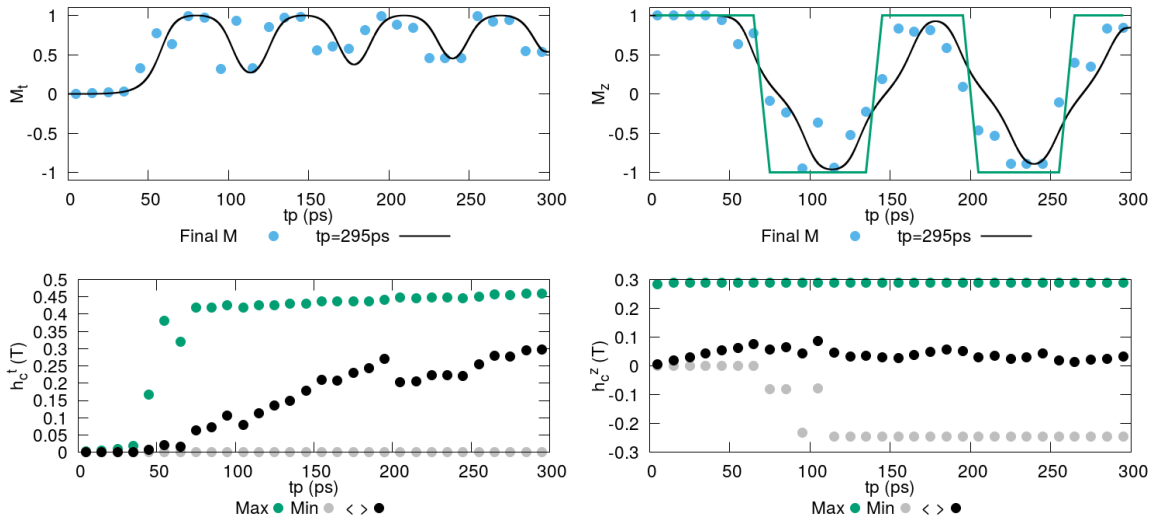

Fig. 5.32 Behaviour of magnetisation and coupling field for different pulse widths of frequency 8.3THz. Top panel - magnetisation components for the final state of the system (blue points), during the $t_p = 295$ps simulation (black line) and switching profile extracted from the phase diagram (green line). Bottom panel - minimum, maximum and average coupling field components. The left panels show the in-plane transverse components of both magnetisation and coupling field calculated as $M_t = \sqrt{M_x^2 + M_y^2}, h_c^t = \sqrt{(h_c^x)^2 + (h_c^y)^2}$.

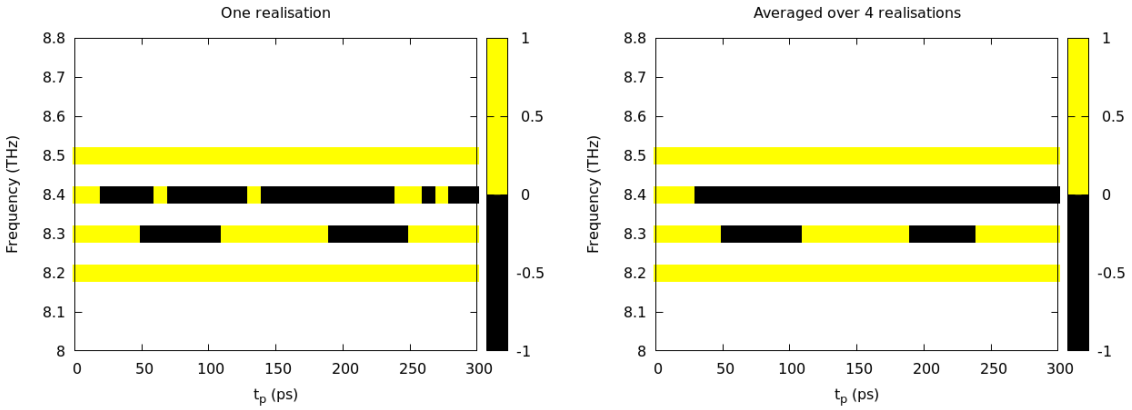

Fig. 5.33 Simplified switching phase diagram at $T = 10$K for a single realisation and averaged over 4 realisations for a coupling constant of $C = 0.5$.

At finite temperature, we expect the switching diagram to be affected by the thermal fields. To reduce the thermal noise, the switching phase diagram is averaged over multiple realisations. Fig. 5.33 presents the switching phase diagram for a finite temperature of $T = 10$K for a single realisation and for an average over 4 realisations. We observe that switching occurs in the same frequency range as for the $T = 0$K case (Fig. 5.29), however the

initial pulse width necessary for switching decreases with approximately 10ps. The decrease can be due to the fact that phase diagram is averaged only for 4 realisation, hence a small change like this of the pulse width can still exhibit an effect of the thermal fluctuations.

5.3.4 Phase diagram for a Morse Potential

Up to this section we investigate the switching mechanism under the application of a THz pulse for a spin-lattice model where the phonons were characterised by a Harmonic potential. In this section we replaced the Harmonic potential by a Morse potential as parameterised in Section 3.9. The switching phase diagram is presented in Fig. 5.34 for an initial temperature $T = 0$K. We observe that the temporal regions that present switching are short in comparison to the results obtained with a Harmonic potential - Fig. 5.30 and the excitation frequencies are larger. The larger frequencies can be correlated to the fact that the Morse phonon dispersion presents multiple modes accessible around the P point in this frequency range. For frequencies larger than 10.3THz no excitations of the magnetic system can be observed in the simulations, as in order to excite at this frequency we need to use a k-point corresponding to this frequency range, such as H.

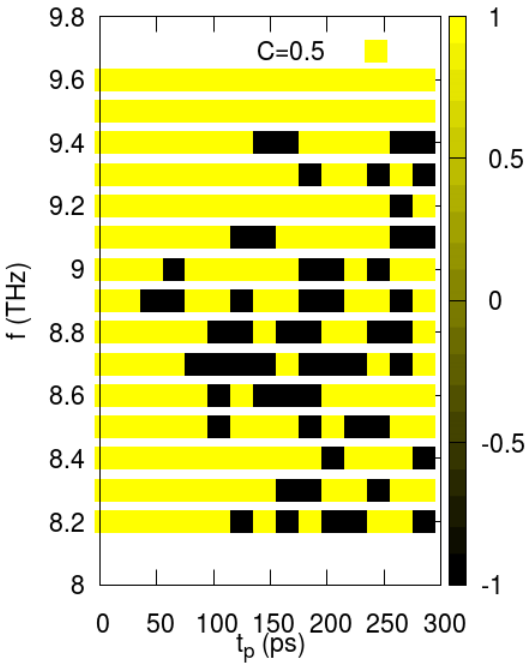

Fig. 5.34 Switching phase diagram at $T = 0$K for a Morse Potential.

Looking at the lattice displacement on the x direction under a continuous application of a THz pulse for the atom situated at position (0,0,0) for the Morse potential - Fig. 5.35 (left) we

observe that the behaviour is very different than in the case of the Harmonic potential. For the Harmonic potential (Fig. 5.35 - left) after an initial transient regime, the atom oscillates with a constant frequency around the equilibrium position due to the simplicity of the potential. For the Morse potential (Fig. 5.35 - left), an initial transient regime (up to 10ps) is followed by an oscillation regime with a constant frequency (up to 20ps) and then an non-linear regime. The Fourier Transform (FFT) of the lattice displacement is presented below. While a single mode is excited in the case of an Harmonic potential, at a frequency corresponding to the THz excitation, for the Morse potential the initial mode (at 8.6THz, corresponding to the frequency of the THz pulse) scatters into multiple lower frequency modes. This can explain the more complicated switching phase diagram, where the switching regions are not anymore so closely grouped for different cutoffs of the pulse widths. By extracting the main peaks from the Fourier transform of the x component of the displacement we can correlate these frequencies to the phonon dispersion curve (Fig. 5.35 - right). In this figure, the black horizontal line is represented by the frequency of the THz excitation which corresponds to the P point in the Brillouin zone that has the same k vectors corresponding to the THz excitation. The green horizontal lines are given by the smaller peaks that appear in the Fourier Transform and we observe that these correspond to phonon modes around the $P-\Gamma'$ path.

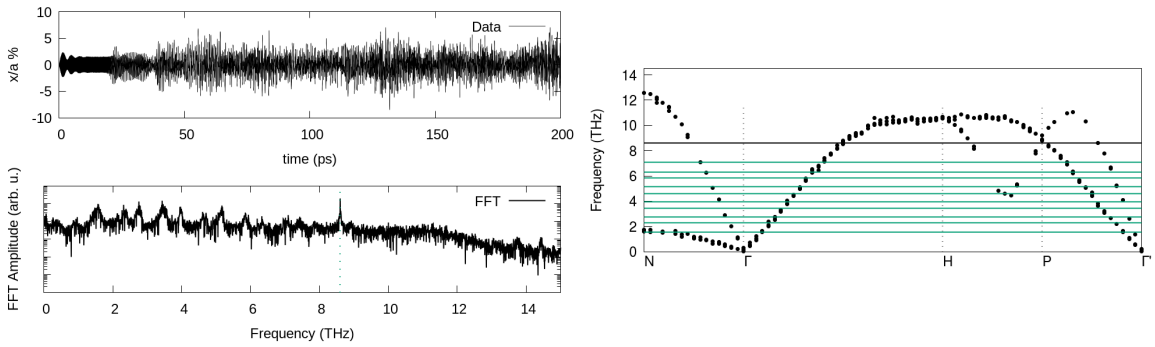

Fig. 5.35 (left panel) Temporal evolution and the Fourier Transform of the x coordinate of the atom at position (0,0,0) normalised to the lattice constant for a Morse Potential for a frequency of 8.6THz. (right panel) Phonon spectra of the x component of velocities at $T = 10$K for a Morse potential together with horizontal lines that show the frequency of the THz excitation (black line) and the frequencies where we observe a peak in the amplitude of the Fourier Transform presented on the left panel (green lines).

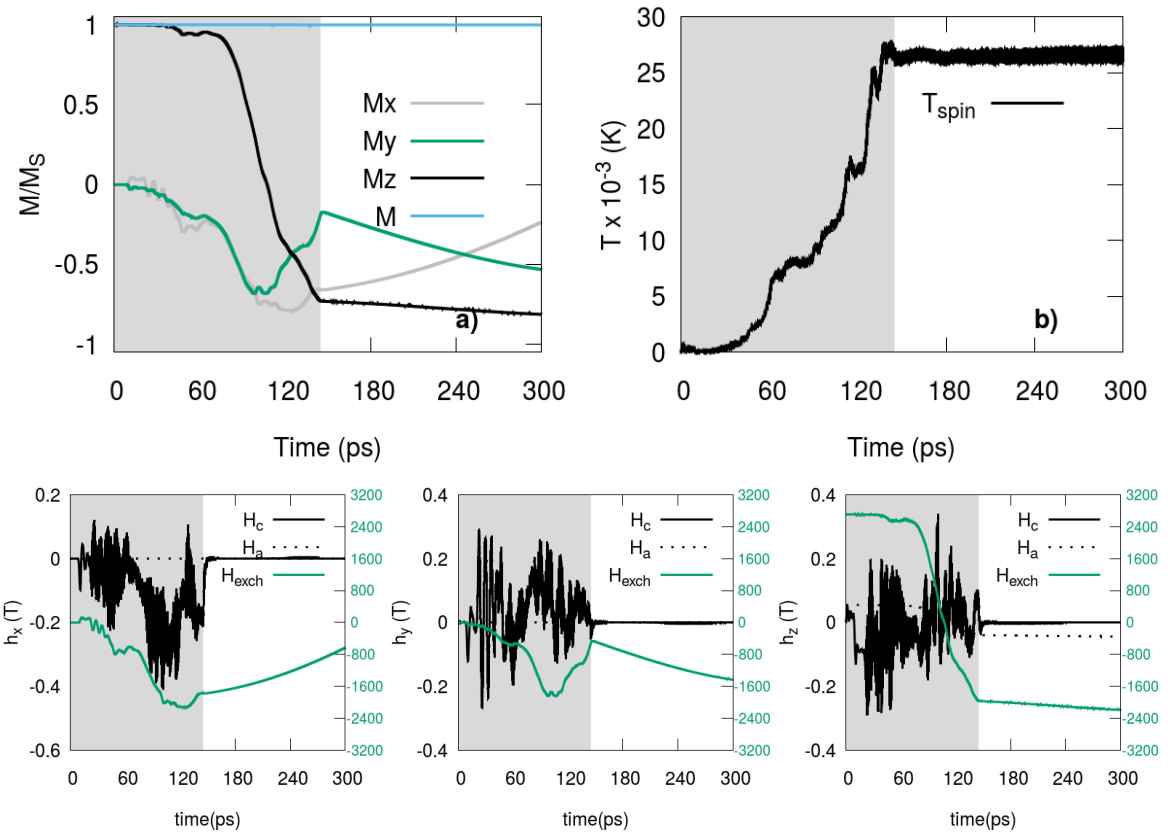

Fig. 5.36 Switching dynamics for a pulse width of 145ps and a frequency of 8.6THz for a Morse potential. Top right panel (a) - magnetisation components, top left panel (b) - spin temperature, bottom - field components during the application of the THz pulse.

In comparison with the Harmonic potential, there is a larger increase in the spin temperature - (Fig. 5.36, top right) presumably due to the scattered phonon modes in the system. The magnetisation also presents additional small peaks during switching proving the rich dynamics of the phonons in this case (Fig. 5.36, top left). This can be further observed in the bottom panel of Fig. 5.36 where the magnetic field components are presented, where the coupling field presents additional high frequency modes with large amplitude. We also observe a large variation in the magnetisation behaviour and coupling field for different random seeds in comparison to $t_p = 285$ps simulation - Fig. 5.37. This correlates to the scattering of the excited phonon mode to lower frequency phonon modes which can give different magnetisation dynamics for different random seeds. The region where switching is observed is reduced by 40ps (145 to 185ps). We also observe for $t_p = 225$ps the development of a very large transverse field.

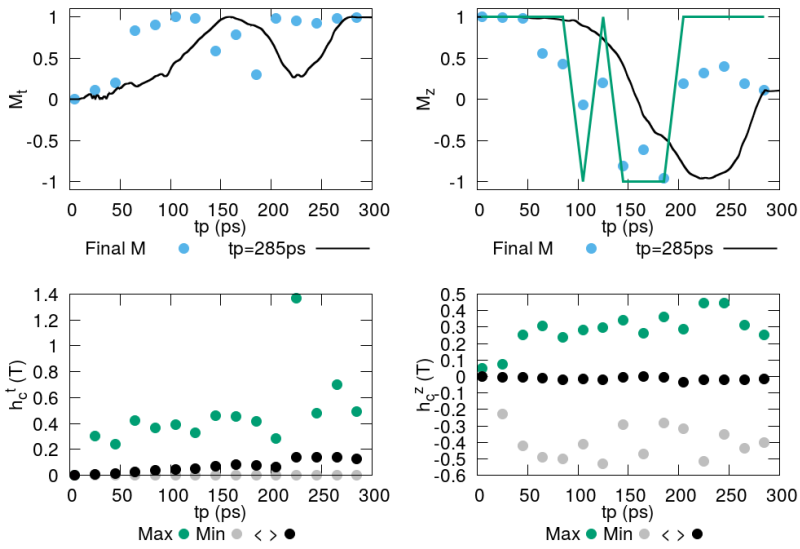

Fig. 5.37 Behaviour of magnetisation and coupling field for a Morse Potential for different pulse widths of frequency 8.6THz. Top panel - magnetisation components for the final state of the system (blue points), during the $t_p = 285$ps simulation (black line) and switching profile extracted from the phase diagram (green line). Bottom panel - minimum, maximum and average coupling field components. The left panels show the in-plane transverse components of both magnetisation and coupling field calculated as $M_t = \sqrt{M_x^2 + M_y^2}, h_c^t = \sqrt{(h_c^x)^2 + (h_c^y)^2}$.

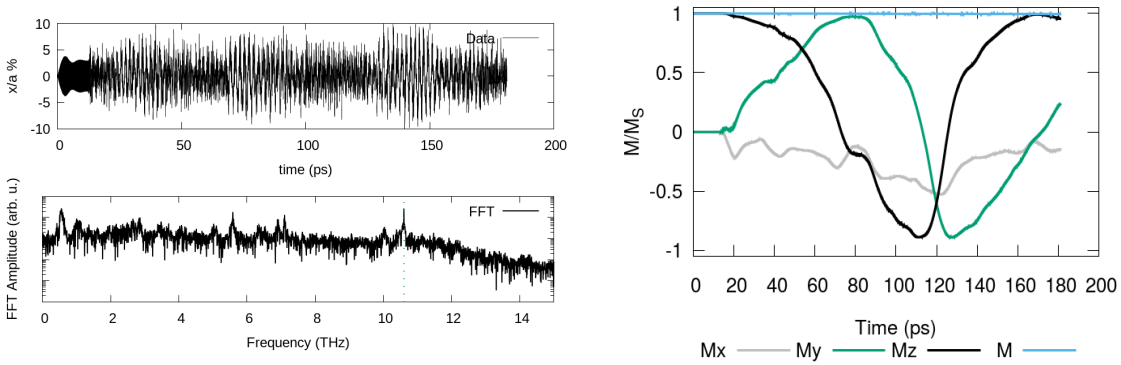

Fig. 5.38 Lattice and spin dynamics for a continuous THz pulse of frequency of 10.6THz for a Morse potential. Left panel - Temporal evolution and the Fourier Transform of the x coordinate of the atom at position (0,0,0) normalised to the lattice constant; Right panel - Magnetisation dynamics.

To access higher frequencies we can change the k vector of the THz force in accordance with the phonon dispersion. The H point is located at a frequency of 10.65THz, hence by changing the k vector to $k = (2\pi/a_0, 0, 0)$ we can access the phonon mode corresponding to

this vector and frequency. The Fourier Transform of the x coordinate of the atom- Fig. 5.38, left, shows a peak at the frequency of the THz force, proving that the THz excitation couples to the phonon modes in the system. The low frequency phonon modes are still present, due to some scattering of the phonon mode corresponding to the H point. On the right panel of Fig. 5.38 we observe that the z component of the magnetisation becomes negative after about 80ps, and the region where we observe a switched state of the magnetisation is increased. By computing the switching phase diagram it is possible to obtain the switching conditions and characteristics for every k point from the phonon dispersion. Nevertheless, we show that it is possible to study rich magnetisation dynamics under phonon excitation for different parametrisation of the potential.

5.4 Conclusions

This chapter presents the equilibrium and dynamical properties of a magnetic material under phonon coupling. Since BCC Fe has been intensively studied within literature for SLD simulations, in the results presented here we use material parameters for bcc Fe with the single exception that it is treated as a magnetic insulator, hence no electronic damping is present. In the case of bulk systems, the equilibrium magnetisation does not depend on the choice of the mechanical potential and the Curie temperature is not significantly affected by a dynamic lattice. This is not the case for a thin film system, where a decreased Curie temperature and stronger finite size effects are present by coupling the magnetic system to a dynamic lattice. Since the magnetic damping presented in the framework is given only by magnon-phonon interaction we calculated the magnon-phonon damping for different temperatures and coupling strengths and we showed that the functional form of the damping depends on the spin-lattice coupling term.

Since the switching of magnetic material with the smallest dissipative effect is crucial for next-generation eco-friendly storage devices, we analysed the effect of phonon excitations onto the switching of magnetic materials. The SLD models are crucial for the investigation of the switching of the magnetic materials via THz phonons, as via the method developed here, we are able to access the magnetisation dynamics corresponding to the excitation of individual or collective phonon modes. Our results suggest that materials that present a flat phonon spectra (such as in the case of the Harmonic potential) have more defined switching diagrams, while for the case of the Morse potential, the excited phonon modes can decay to lower frequency modes and affect the switching region of the material. The results presented here are important in understanding which phonon modes need to be accessed

experimentally in order to lead to the highest magnetic response and eventually switching of the magnetization.

6

Advanced recording media applications

6.1 Heated dot magnetic recording media

Heated dot magnetic recording media (HDMR) represents the ultimate technology that can allow ultrahigh density of stored information, as shown in the ASTC Roadmap- Fig. 1.2, Chapter 1. Heated dot magnetic recording media is a combination between Bit Patterned Media (one single grain used per one single bit) and the Heat Assisted Magnetic Recording (highly anisotropic media heated up via a laser pulse during the writing process). One important quantity that needs to be investigated in the case of HDMR is the bit error rate (BER), which is given by the probability of bits that have not reached the desired orientation of the magnetisation due to thermal fluctuations. Ultimately, as shown in the magnetic quadrilemma - Fig. 1.1 the maximum areal density possible to obtain via HDMR technology will be governed by the minimum BER that can possibly be achieved during reversal.

In this Section the switching probability and the subsequent bit error rate is explored for the FePt system, which is already the main candidate for HAMR. A possible alternative to FePt is NdFeB due to its large anisotropy. NdFeB is a permanent magnet used extensively due to its wide range of applications in the automotive and electronic industry or even in the medical sector [138], with the potential to target the global climate crisis by enabling its utilisation in electric vehicles and low carbon methods of power generation. The employment of NdFeB in HAMR applications is limited by the capacity of the mass-production of this media. Experimental investigation on how NdFeB can be produced for HAMR applications have been recently shown [139]. These studies suggest that NdFeB can be potentially used as an alternative for FePt based HAMR. NdFeB is also a good candidate to tackle the magnetic quadrilemma, since the BER is affected by the saturation magnetisation, which is larger for NdFeB than FePt.

6.1.1 Heated Dot Recording Media: FePt and NdFeB

To model the heated dot experiments we apply a temperature pulse that is Gaussian in time and a negative out-of-plane magnetic field of $B = -1$T (Fig. 6.1, left panel). Under the effect of thermal fluctuations, the system will be demagnetised (Fig. 6.1, centre panel), hence the anisotropy field of the system will decrease. This will allow the magnetisation to reverse in a smaller magnetic field, such as $B = -1$T. By repeating the experiment for an ensemble of 50 identical grains with different thermal field random seeds, we observe that there are grains for which the magnetisation is not switched, even in a negative field of 1T (Fig. 6.1, right panel). The grains that have not switched lead to a non-zero bit error rate.

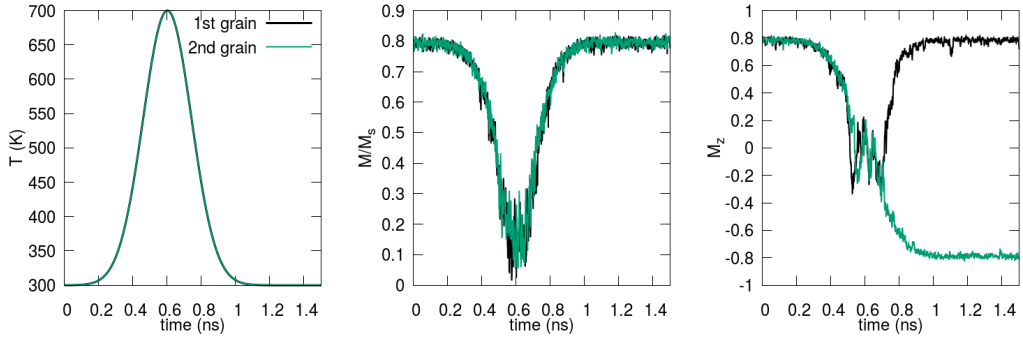

Fig. 6.1 Example of heated dot magnetic simulations for a temperature pulse width of 200ps and a maximum temperature of $T_{max} = 700$K in an out-of-plane magnetic field of $B = -1$T for two FePt cylindrical grain of 3nm×3nm×5nm; The left panel shows the temperature profile during the simulation, followed by the total and the z component of the magnetisation. For the same simulation conditions, with a different sequence of pseudo-random numbers, either a switched or not-switched state can be obtained - right panel.

The switching mechanism at high temperatures can be understood by analysing the energy barrier schematics in Fig. 6.2. In the absence of an applied field, for an uniaxial anisotropy there are two equal energy minima, as shown in Fig. 6.2, left panel. In this case, under the influence of large thermal excitation, the magnetisation can be in either positive or negative orientation, as the thermal energy is sufficient for the system to cross from one energy minimum to another. Under the application of a negative field, Fig. 6.2, right panel, the energy barrier from the positive to the negative magnetisation is lowered hence the system's magnetisation can cross to the negative magnetisation energy minimum. This minimum corresponding to the negative magnetisation has the lowest energy, hence the system's magnetisation will prefer to stay in this orientation. However for high temperature pulses, the thermal energy can be sufficiently high for the system to make a crossing of the energy barrier back to the positive magnetisation energy minimum, even if the energy difference

from the negative to the positive orientation is larger than in the opposite direction. If the system is then cooled sufficiently fast (as in the case corresponding to narrow temperature pulse widths) the system will remain blocked in the energy minimum corresponding to the positive orientation of the magnetisation, anti-parallel to the direction of the applied field; this can lead to a non-zero bit error rate.

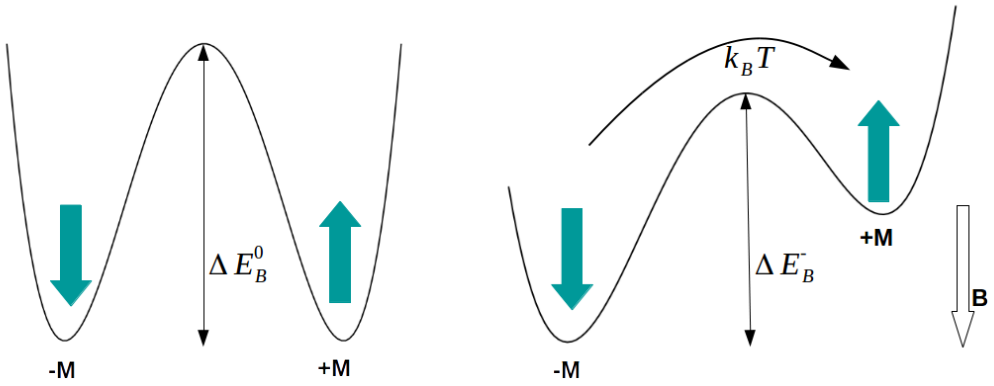

Fig. 6.2 Schematics of energy barrier without an applied field (left panel) and with an applied field (right panel).

We next calculate via atomistic simulations of HDMR the switching probability (defined as the ratio between how many grains have reversed against the total number of grains) for different temperature pulses. By varying the maximum temperature of the pulse (T_{max}) we can obtain the switching probability curves for specific pulse widths. The systems we model are represented by cylindrical grains of 5nm height and varying diameter (3 to 5nm). The model used for FePt has been discussed in Chapter 4, the model parameters being presented in Table 4.4. The FePt Hamiltonian includes just nearest neighbours exchange interaction that lead to a Curie temperature of about 720K for a bulk system as shown in inset Fig. 4.4. The atomistic model of NdFeB (the phase $Nd_2Fe_{14}B$) has been parameterised by Dr. Richard Evans and similar model parameters have been used in Ref. [140], where the temperature dependence of the magnetic properties has been investigated. Since NdFeB has been thoroughly investigated in the group by Dr. Samuel Westmoreland, more details regarding its modelling can also be found in Ref. [141, 142]. The magnetic Hamiltonian used for NdFeB contains exchange interactions between the Fe-Fe and Fe-Nd sites, the B atoms being considered non-magnetic and the interaction between Nd sites being negligible. The very large anisotropy of NdFeB ($\approx$ 17T) comes mainly from the Nd sites [143] and considers second and fourth order uniaxial anisotropy contributions, the Fe sites contributing only weakly to the overall anisotropy. The saturation magnetisation of NdFeB is higher than the one of FePt ($M_S^{NdFeB} = 1610$ emu/cm^3 compared to $M_S^{FePt} = 1043$ emu/cm^3). The Curie temperature is lower in the case of NdFeB $\approx$ 585K.

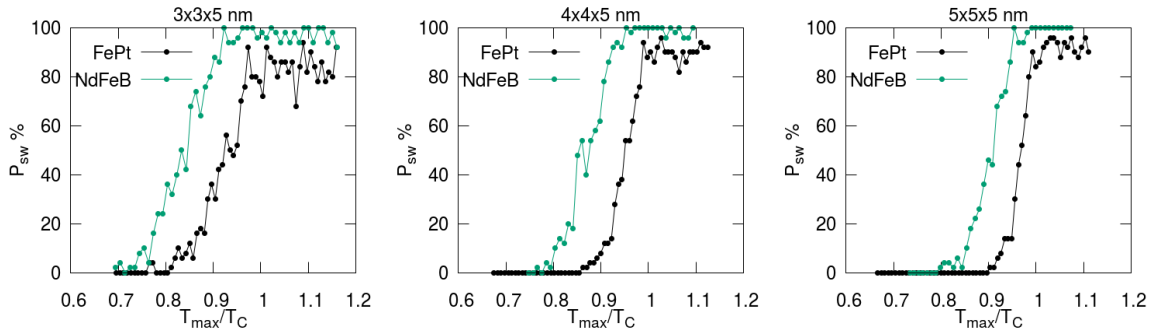

Fig. 6.3 Switching probability calculations for FePt (black points) and NdFeB (green points) for 50 cylindrical grains of 5nm height. The switching probability is calculated for varying maximum temperature of the heat pulse T_{max} normalised by the Curie temperature T_C of individual materials and system size. The temperature pulse width is 200ps.

Fig. 6.3 shows the switching probability for both FePt and NdFeB HDMR, calculated for 50 non-interacting grains. The bit error rate can be calculated from the switching probability plots. The dimensions of the grain varies from 3nm to 5nm in diameter. The height of the grain is kept constant at 5nm size. Since NdFeB and FePt have different Curie temperatures, to be able to compare the switching probabilities of the two materials, the maximum temperature of the pulse width has been normalised by the Curie temperature T_C of individual materials and system size, shown in Table 6.1.1. The Curie temperature has been extracted from the equilibrium susceptibility calculated numerically via Monte-Carlo simulations with a temperature resolution of 10K. The susceptibility has been interpolated via a quadratic function, that takes into account in total 9 points for the interpolation [1]. The interpolation increases the temperature resolution of the susceptibility, without the necessity to compute numerically the intermediate temperature points. We observe in Fig. 6.3 that in the case of FePt, the switching probability is always lower than 100% and its saturation value decreases with decreasing diameters. However, NdFeB has an increased switching probability even for small system sizes, suggesting that it could be more suitable for HDMR.

Figure 6.4 shows the variation of the Curie temperature as a function of the grain diameter D extracted from the interpolation of the equilibrium magnetic susceptibility. The curves have been fitted to the finite size scaling law $T_C(D) = T_C^{\infty}\left[1-(d_0/D)^{1/a}\right]$ from Ref. [111], where T_C^{∞} represents the Curie temperature that would be obtained for $D \to \infty$ (in this case a thin film system of thickness 5nm), d_0 is related to the unit cell size and a represents the critical scaling exponent. A more accurate determination of the finite size scaling exponents

[1] Discussion with PhD student Thanh Binh Nguyen (Tim) who investigates the finite size effects in FePt media as part of his research project is gratefully acknowledged.

would involve increasing the number of convergence steps for each simulated temperature and as well the temperature resolution. For FePt, the scaling exponent $a = 0.7$ obtained from the fit is comparable to Ref. [111] ($a = 0.79$), slightly lower in value presumably due to the 5nm thickness of the systems modelled here. Interestingly, we observe that in the case of FePt the exponent a is larger than in the case of NdFeB, suggesting stronger finite size effects in both the magnetisation and the BER.

D (nm)	$T_C(K)$, FePt	$T_C(K)$, NdFeB
3	647	504
4	667	535
5	675	545

Table 6.1 The Curie temperature of FePt and NdFeB for different grain diameters.

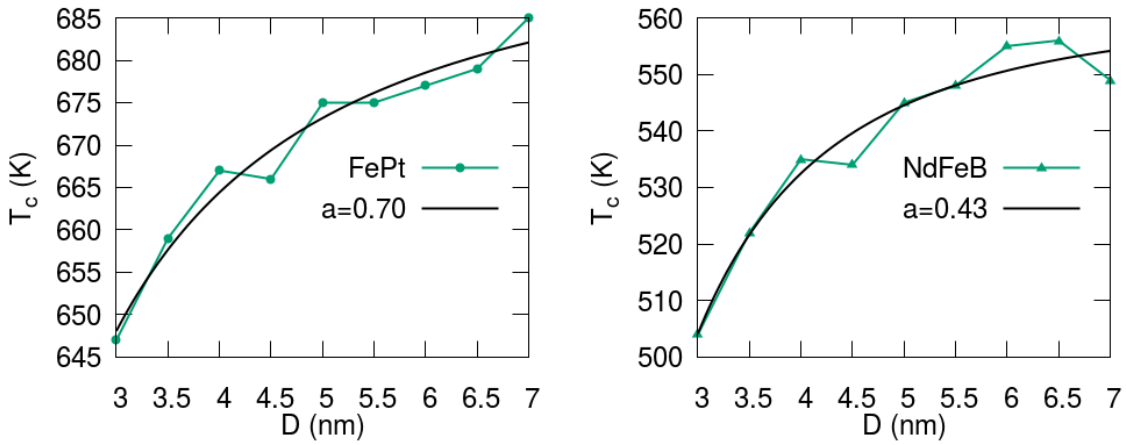

Fig. 6.4 Curie temperature as a function of grain diameter for FePt (left panel) and NdFeB (right panel). The black line shows the fit to the finite size scaling law $T_C(D) = T_C^\infty \left[1 - (d_0/D)^{1/a}\right]$ from Ref. [111]. The fitting parameters are $T_C^\infty = 696.5$K, $d_0 = 0.46$nm, $a = 0.7$ for FePt and $T_C^\infty = 562.2$K, $d_0 = 1.13$nm, $a = 0.43$ for NdFeB.

To systematically analyse the BER, we can fit the switching probabilities plots to a cumulative distribution function (CDF) defined as:

$$f(x) = \frac{P_0}{2}\left(1 + \mathrm{erf}\left(\frac{x-\mu}{\sigma\sqrt{2}}\right)\right) \tag{6.1}$$

$$\mathrm{erf}(x) = \frac{2}{\pi}\int_0^z \exp(-t^2)dt \tag{6.2}$$

where P_0 is the maximum switching probability, σ defines the width of the transition and μ the mean transition temperature. In the ideal case, the maximum switching probability parameter should be $P_0 = 1(100\%)$ and the transition should be abrupt, hence $\sigma = 0$K. In reality, thermal and finite size effects lead to a relatively wide transition 15K-30K and switching probability less than unity. An example of fitting the switching probability calculations via the cumulative distribution function is shown in Fig. 6.5 (left panel). After the fit, the BER can be then calculated as:

$$BER = 1 - P_0 \tag{6.3}$$

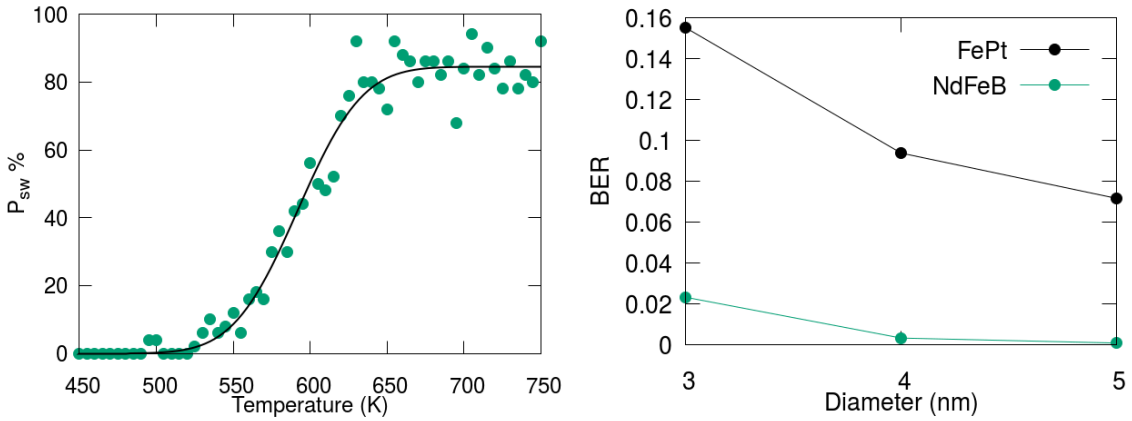

Fig. 6.5 BER calculation for FePt and NdFeB; (left panel) Example of fitting of the switching probability of FePt grains of dimension 3nm×3nm×5nm via the cumulative distribution function in Eq. 6.1. (right panel) The variation of the bit error rate (BER) as function of the system size for FePt and NdFeB systems.

Fig. 6.5 (right panel) shows the BER as function of the system diameter for both FePt and NdFeB. The BER for NdFeB is considerably smaller than in the case of FePt suggesting that NdFeB could be more successfully used in HDMR. Since NdFeB has higher saturation magnetisation and lower Curie temperature than FePt, we can expect that these magnetic properties might influence the switching.

6.1.2 Improved switching probability in FePt

Evans *et al.* [4] has suggested that the BER can be expressed in terms of the equilibrium magnetisation $BER = 0.5(1 - m_e)$. Via the Master equation, the BER for a system with perfectly aligned easy axis is given by:

$$BER = \exp\left(-2\frac{M_S V \mu_0 H_{wr}}{k_B T}\right) \tag{6.4}$$

The equation is derived in thermal equilibrium, which is not the case of HDMR calculations, however in the first instance, can be used as an approximation to understand what magnetic parameters control the BER. We observe that a decreased BER can be obtained by either increasing the writing field H_{wr} or the magnetisation of the system $\mu = M_S V$. We distinguish that an increase in the volume of the system leads to smaller BER, this being confirmed by the numerical results in Fig. 6.3, right panel that describes the dependence of BER on the diameter. For ultrahigh areal densities it is necessary to keep a reduced diameter of the grains, hence a possibility to increase the volume is by an increased height of the grains. The height is limited by the requirement that the grains need to act as mono-domains for a coherent reversal of the grain. Thus in reality, there is not much space to alter the volume of the grains. The writing field H_{wr} is also limited technological accessible values, this suggesting that the BER could be controlled in the first instance more effectively via the saturation magnetisation of the material. Since NdFeB showed a considerably improved BER and its saturation magnetisation is higher than in the case of FePt, we next investigate the effect of the saturation magnetisation on the BER.

Influence of M_S on the BER

The saturation magnetisation of FePt has been varied by artificially changing the magnetic moment of Fe atoms in the material. The magnetic moment used for FePt is $\mu = 3.23\mu_B$ which gives a saturation magnetisation of $M_S = 10.43 \times 10^5$A/m= 1043 emu/cm^3. We have calculated the switching probabilities and the BER for 2 more values of the saturation magnetisation corresponding to $M_S = 5.21 \times 10^5$ A/m (for $\mu = 1.61\mu_B$) and $M_S = 20.86 \times 10^5$ A/m (for $\mu = 1.61\mu_B$). Fig. 6.6 (left panel) shows that with increasing magnetic moment there is an increase in the maximum switching probabilities, which leads to decreased values of BER - Fig. 6.6 (right panel). The dependence of BER on the saturation magnetisation can be explained by the improved switching of NdFeB grains. Hence one alternative for the performance of HDMR is to find materials with increased M_S.

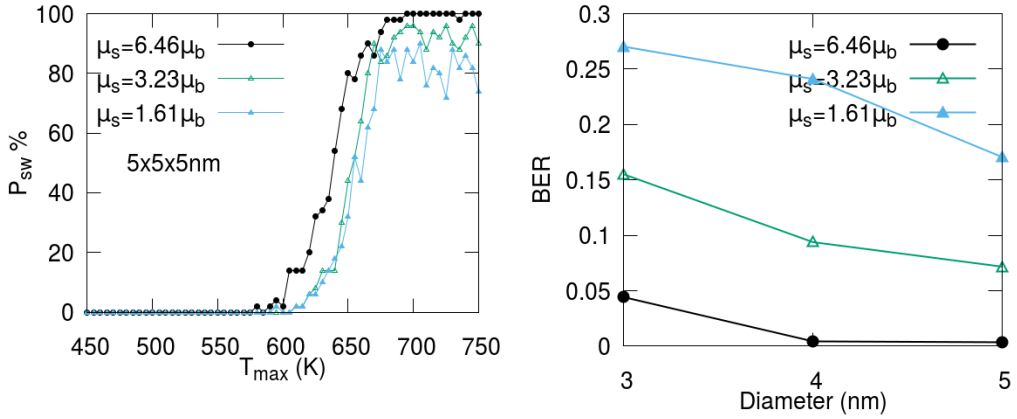

Fig. 6.6 (left panel) Example of switching probability of FePt grains calculated for $t_p = 200$ps and varying magnetic moment for a cylindrical grain size of 5nm×5nm×5nm; (right panel) BER as function of grain diameter calculated for different values of the magnetic moment.

Influence of T_C on the BER

Another difference between NdFeB and FePt is given by the Curie temperatures. NdFeB has a lower Curie temperature than FePt (585K compared to 720K for bulk systems). A decreased Curie temperature for the FePt system can be obtained by scaling the exchange interaction to a value that will correspond to the Curie temperature of NdFeB (since the Curie temperature varies linearly with the nearest-neighbours exchange interaction [21][144]). The decreased Curie temperature in FePt leads to a small decrease in the values of BER, but not sufficiently to favour the 3nm grains for their usage in HDMR; this suggests that M_S is more important.

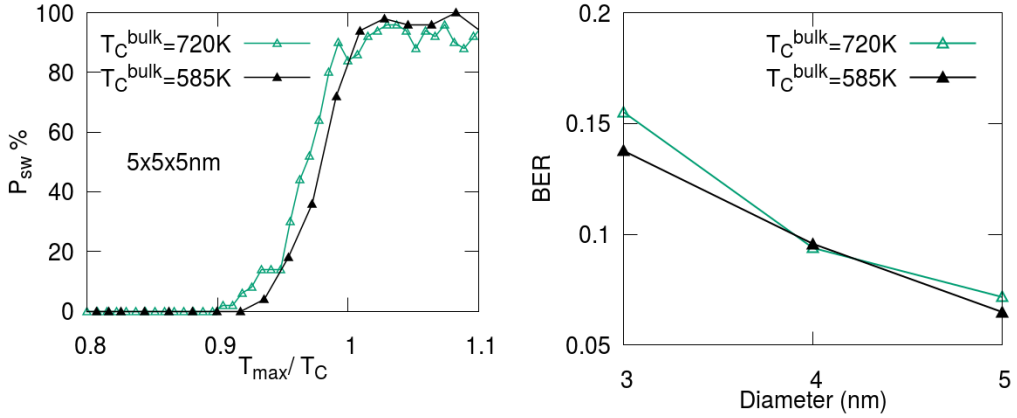

Fig. 6.7 (left panel) Example of switching probability of FePt grains calculated for $t_p = 200$ps and varying Curie temperature for a cylindrical grain size of 5nm×5nm×5nm; (right panel) BER as function of grain diameter calculated for varying Curie temperature.

Influence of the magnetic damping and pulse width on the BER

The BER is calculated for a dynamic evolution of the magnetisation; since the magnetic damping controls the speed of magnetisation dynamics, it is important to understand the effect of the damping on the BER. Fig. 6.8 (left panel) shows that with increased damping, there is a decrease in the BER, the same effect happening with increased pulse widths (right panel). With increasing damping, the magnetisation can evolve more quickly towards equilibrium, hence the probability of the particle to remain blocked in a positive magnetisation minimum due to the fast cooling of the system is reduced. The same happens with increased pulse widths, the magnetisation will have more time to evolve and follow the temporal evolution of the temperature pulse width. This effect has also been shown in Ref. [145] where the influence of the Gilbert damping on the signal-to-noise ratio has been analysed for HAMR. The effect of increased magnetic damping and pulse widths will lead to a behaviour of magnetisation closer to the thermal equilibrium and hence will reduce drastically the BER.

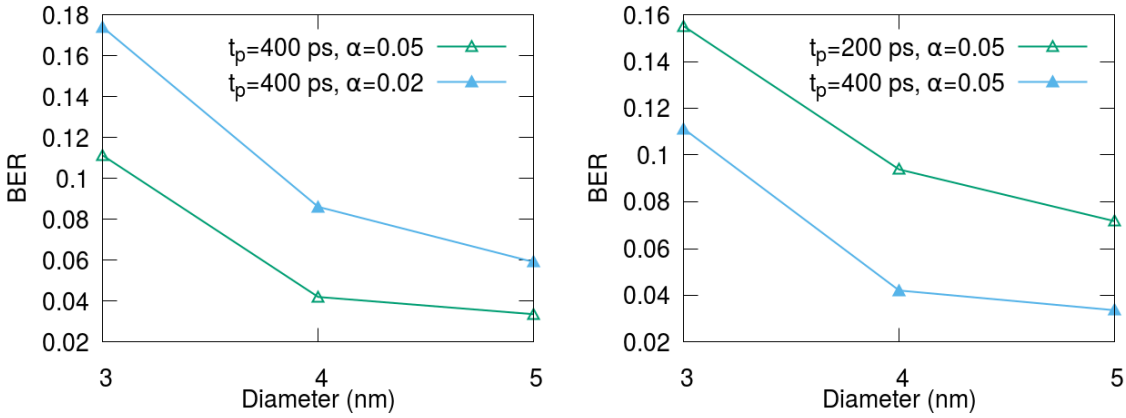

Fig. 6.8 BER as function of grain diameter calculated for varying damping (left panel) and temperature pulse widths (right panel).

The influence of the magnetic field on BER is also investigated below - Fig. 6.9. Indeed, with increasing applied field the BER is drastically reduced, as suggested by Eq. 6.4, however such large values of applied magnetic field are not yet accessible experimentally for recording media applications. The development of all-optical-switching technologies [41] and the subsequent high internal magnetic fields developed during the process either by non-polarised or circularly polarised light (as in the Inverse Faraday effect) might lead to materials that exhibit low BER due to development of such large internal fields.

The systematic investigation performed above suggests that in order to obtain ultrahigh areal densities via HDMR technologies for small grain sizes it is crucial to accurately control the BER of the system. The control of BER can be achieved by searching for magnetic

materials that are characterised by an increased saturation magnetisation and damping, in addition to the high anisotropy which is necessary for the thermal stability of the grains. The large BER appears in HDMR systems due to the magnetisation following a non-equilibrium path that arises from the application of short high temperature pulses. Increasing the pulse width leads to a decreased BER, however, from the technological point of view, also leads to a much lower writing speed. The interplay between all these parameters that control the BER needs to be taken into account while exploring the limits of areal densities of the recording media technologies.

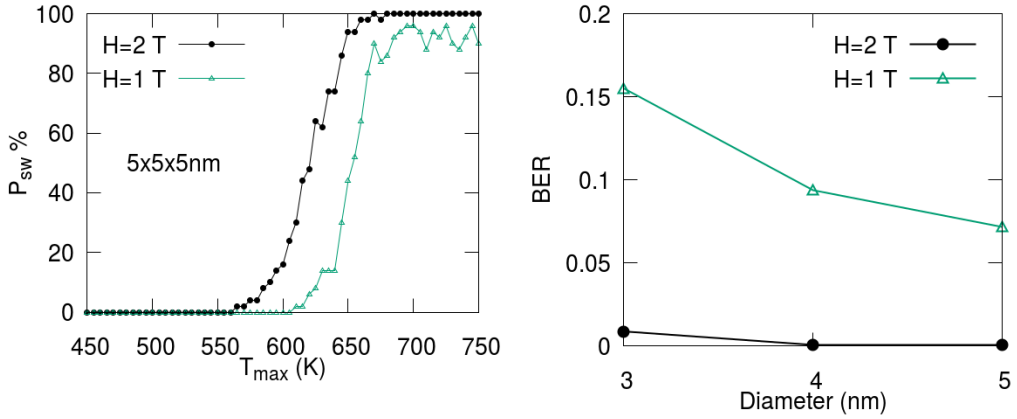

Fig. 6.9 (left panel) Example of switching probability of FePt grains calculated for $t_p = 200$ps and varying applied field for a cylindrical grain size of 5nm$\times$5nm$\times$5nm; (right panel) BER as function of grain diameter calculated for different values of the applied field.

The ultimate limit of the areal density has been explored via analytical means in Ref. [4]. The numerical calculations developed in this section help us reassess the maximum areal density that can be obtained in HDMR via the calculation of BER. This aspect is explored in the following section.

6.1.3 Maximum areal densities for HDMR

Evans *et al.* [4] investigated via analytical means the thermal writability of the magnetic grains, the maximum areal density that could be possibly be achieved via HDMR being controlled by the BER. The calculations were done by assuming a thermal equilibrium, which is not the case in HDMR, since a time-dependence of temperature pulse is used. The BER calculations in the previous section can be used in reassessing the maximum areal density via numerical calculation of BER for small system sizes.

The analytical areal density calculations (AD) in Ref. [4] are given by $V^{-2/3}\varepsilon$, where $\varepsilon = 0.5$ is the areal packing fraction and the volume is expressed from Eq. 6.4:

$$AD = \left(\frac{2M_S(T)\mu_0 H_{wr}}{k_B T \ln[(BER)^{-1}]}\right)^{2/3} \varepsilon \tag{6.5}$$

In Eq. 6.5, the writing temperature T is considered as being 10K lower than the Curie temperature of the system, which is a rough approximation and can lead to higher areal densities. A better description is given by the usage of the blocking temperature T_B, which is the temperature at which the transition towards the superparamagnetic state happens. An initial estimation of the blocking temperature can be deduced from the Arhenius-Néel relaxation equation, where $T_B = KV/(k_B \ln(\tau f_0))$, τ being the relaxation time in a constant temperature and f_0 the attempt frequency ($f_0 = 10^9 - 10^{12}$ s^{-1}). For systems where the temperature is not constant, such as in HAMR, the following rate dependent estimation of the blocking temperature needs to be used, as suggested by Chantrell *et al.* [146]:

$$\frac{KV}{k_B T_B}(1 - H/H_K)^2 = \ln\left[\frac{f_0 \dot{T}^{-1}(KV/k_B)}{(\frac{KV}{k_B T_B})^2(1 - H/H_K)^2}\right] \tag{6.6}$$

In Eq. 6.6, $\dot{T}^{-1}$ is the rate of temperature variation which we approximate as constant. We can calculate numerically the blocking temperature from Eq. 6.6 using the temperature variation of the anisotropy as $K(T) \sim m(T)^3$ for uniaxial anisotropy of FePt in the absence of two-ion anisotropy. The temperature dependence of the magnetisation is considered $m(T) = \left(1 - \frac{T}{T_C(D)}\right)^{\beta}$, $\beta = 0.33$ and a Curie temperature of $T_C(3\text{nm}) = 653$K for a 3nm size grain. Additionally we consider an attempt frequency of $f_0 = 10^{12}$ s^{-1} and a linear cooling of the system from 750K to 300K in 0.3 ns in a field of $H = 1$T. The solution of Eq. 6.6 will be given by the intersection between the temporal variation of the blocking temperature calculated via Eq. 6.7, where the temperature T depends on the time - $T(t)$ and the anisotropy constant and field depend on the temperature of the system, with the temporal variation of the temperature pulse T_P. Fig. 6.10 shows that the blocking temperature of the FePt granular system of 3nm diameter is $T_B = 550$K. For diameters of 4nm and 5nm, blocking temperatures of $T_B = 605$K and $T_B = 640$K were extracted.

$$T_B = \frac{KV(1 - H/H_K)^2}{k_B \ln\left[\frac{f_0 \dot{T}^{-1}(KV/k_B)}{(\frac{KV}{k_B T})^2(1 - H/H_K)^2}\right]} \tag{6.7}$$

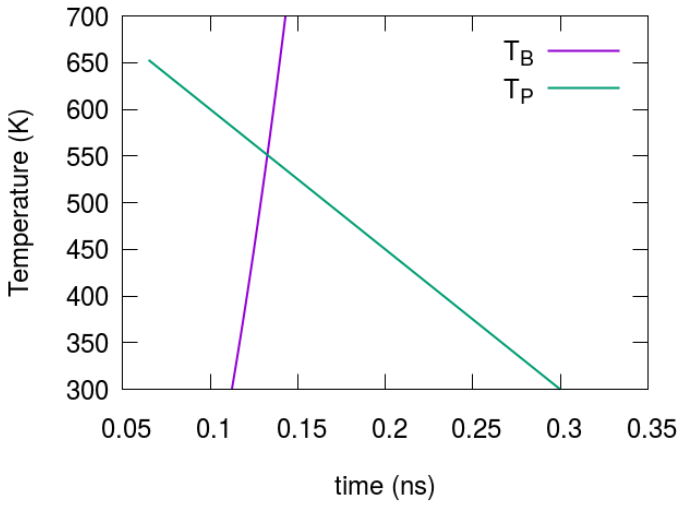

Fig. 6.10 Blocking temperature (T_B) calculations for FePt grains of 3 nm diameter; The intersection with the temperature pulse variation (T_P) shows that the blocking temperature of the system is $T_B = 550$K.

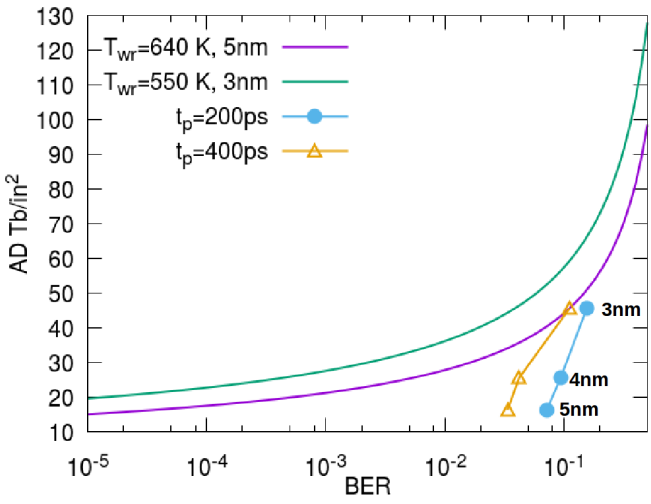

Fig. 6.11 Analytical and numerical areal density calculations for HDMR; The writing temperature is given by the blocking temperature calculated via Eq. 6.7 for two diameters of the grains (3 and 5 nm). Smaller areal densities are obtained numerically for the same values of BER, due to the dynamic variation of the temperature and magnetic properties.

We note that, for realistic systems there is a distribution of blocking temperatures that arises from the variation of anisotropy with temperature, and the value of blocking temperature we calculate in Fig. 6.10 is corresponding to the blocking temperature at the edge of the distribution. Returning now to the areal density calculations, using the blocking temperature

calculated above, we can compare the analytical variation of the areal density as function of BER given by Eq. 6.5 to the BER values calculated numerically for different grain diameters. Fig. 6.11 shows that the BER obtained via numerical calculations corresponds to AD about 50% lower than in the case of the analytical calculations, for temperature pulse widths of $t_p = 200$ps. This is due to the fact that, in the analytical calculations thermal equilibrium is assumed, which is not the case of HDMR systems. The dynamic behaviour of the magnetic properties will strongly influence the maximum areal density that can be achieved.

6.2 Ultrafast dynamics in FePt/FeRh structures

FePt/FeRh has been proposed for use in heat-assisted magnetic recording (HAMR) in order to lower the coercivity of highly anisotropic FePt via the exchange spring mechanism [9]. FeRh is a metamagnet that shows a first order phase transition from antiferromagnetic to ferromagnetic phase at about 350K. It has been shown by Barker and Chantrell [30] that the phase transition appears due to different temperature scalings of the bilinear and four-spin exchange interaction in this material. The FeRh model has been implemented in the atomistic spin dynamics package VAMPIRE and has been used in spin-wave resonance experiments to look at the exchange energies of the system during the mixed-phase region, showing a decreased exchange stiffness due to the effect of the antiferromagnetic phase on the ferromagnetic regions [32]. In this section, the model presented in [32, 31] is used in the investigation of recording media technologies based on these structures.

The recording media technologies based on FePt/FeRh bilayers [9] works as follows: in the antiferromagnetic phase of FeRh, the stability of the stored data is assured by the large anisotropy of FePt and the coupling to the anti-ferromagnetic phase of FeRh does not influence the stored information. By heating up the system, FeRh will undergo a phase transition and will become ferromagnetic. The anisotropy of FeRh is low and hence the magnetisation of FeRh will reverse at lower fields and this will lead to a switching in FePt via the exchange-spring mechanism. The first order phase transition of FeRh will act as an on/off switch to the exchange spring mechanism that potentially could drive the magnetisation reversal. Zhou *et al.* [147] proposed a trilayer of FePt/FeRh/FeCo for HAMR, where the high moment of FeCo leads to three times lower switching fields. At room temperature FePt and FeCo are isolated due to the antiferromagnetic layer of FeRh, however in the ferromagnetic phase, FeRh will couple FePt and FeCo and will act as an exchange switch.

It has been shown experimentally that the ferromagnetic phase of FeRh can be generated at ultrafast timescales by the application of a laser pulse [148], an effect observed as well in the atomistic model of FeRh [30, 31]. This opens the possibility of the usage of FeRh in

optical recording media, where the magnetisation is controlled by femtosecond laser pulses. However, the ultrafast dynamics of exchange spring systems such as FePt/FeRh bilayers has not been investigated, this being interesting from both a fundamental and application point of view. The next section presents the equilibrium magnetic properties of FePt/FeRh bilayers followed by the investigation of the ultrafast magnetisation dynamics in these structures.

6.2.1 Model of FePt/FeRh structures

The structure of FeRh is body-centered cubic (BCC), with the central site occupied by the Rh atoms. In the antiferromagnetic phase, no magnetic moment is associated to Rh, however a small magnetic moment of $1\mu_B$ appears on the Rh site in the ferromagnetic phase. It has been suggested that the Rh moment is induced by the Fe sites [149], hence in the first instance, FeRh can be modelled only in terms of Fe degrees of freedom and a further approximation of a simple cubic lattice. The induced moment of Rh will be however incorporated in the higher-order exchange terms. A four-spin exchange term needs to be considered in order to drive the antiferromagnetic to ferromagnetic phase transition. By modelling only the Fe atoms, FePt has also a simple cubic symmetry. Since both materials have the same crystal structure, the bilayers can be modeled by a simple cubic structure of Fe sites with different properties, corresponding to FePt and FeRh. The Hamiltonian of FeRh consists of bilinear exchange J_{ij}, four-spin exchange D_{ijkl} and a small uniaxial anisotropy k_u as shown below:

$$\mathscr{H} = -\frac{1}{2}\sum_{ij} J_{ij}\,(\mathbf{S}_i \cdot \mathbf{S}_j\,) - \frac{1}{3}\sum_{ijkl} D_{ijkl}(\mathbf{S}_i \cdot \mathbf{S}_j)(\mathbf{S}_k \cdot \mathbf{S}_l) - k_u \sum_i (\mathbf{S}_i \cdot \mathbf{e})^2 \tag{6.8}$$

The coupling between FeRh and FePt is assumed ferromagnetic and limited to nearest-neighbours interaction. The coupling is expressed in terms of the Fe-Fe exchange interactions in FePt. The system modelled is approximately 7nm$\times$7nm$\times$14nm, non-periodic in all three directions, corresponding to 24 layers of FePt and 24 layers of FeRh. The model parameters are shown in Table 6.2. The equilibrium magnetisation as a function of temperature - Fig. 6.12 (left panel) shows that there is an increased magnetisation with increased coupling. The ferromagnetic coupling between the two materials leads to a frustrated spin state, in the region of temperatures where FeRh is antiferromagnetic, as shown in the left inset, yellow squares of Fig. 6.12 (left panel). With increasing coupling strength, a canted spin state appears at the interface with FePt in order to decrease the spin frustration and minimise the energy, as shown in Fig. 6.12 (right panel), thus increasing the total magnetisation of the system. The antiferromagnetic to ferromagnetic phase transition temperature shows a small decrease with increased coupling, since more ferromagnetism appears at the system due to the large coupling.

Quantity	Symbol	Value	Units
FeRh NN exchange	J^1_{FeRh}	4×10^{-22}	J
FeRh NNN exchange	J^2_{FeRh}	2.75×10^{-21}	J
FeRh fourspin	D^{ijkl}_{FeRh}	-0.23×10^{-21}	J
FeRh anisotropy	K_{FeRh}	1.404^{-23}	J
FeRh moment	μ_{FeRh}	3.15	μ_B
Electron-heat capacity	C_{e0}	3.5×10^{-3}	J mol^{-1} K^{-2}
Phonon specific heat	C_p	4.54×10^{1}	J mol^{-1} K^{-1}
Electron-phonon coupling	G_{ep}	1.05×10^{12}	J mol^{-1} K^{-1} s^{-1}
Damping	α	0.05	
Laser power fluence	F	1.7	mJ cm^{-2}
Laser pulse time	τ	100	fs

Table 6.2 Parameters used for the FePt/FeRh simulations, extracted from Ref. [30].

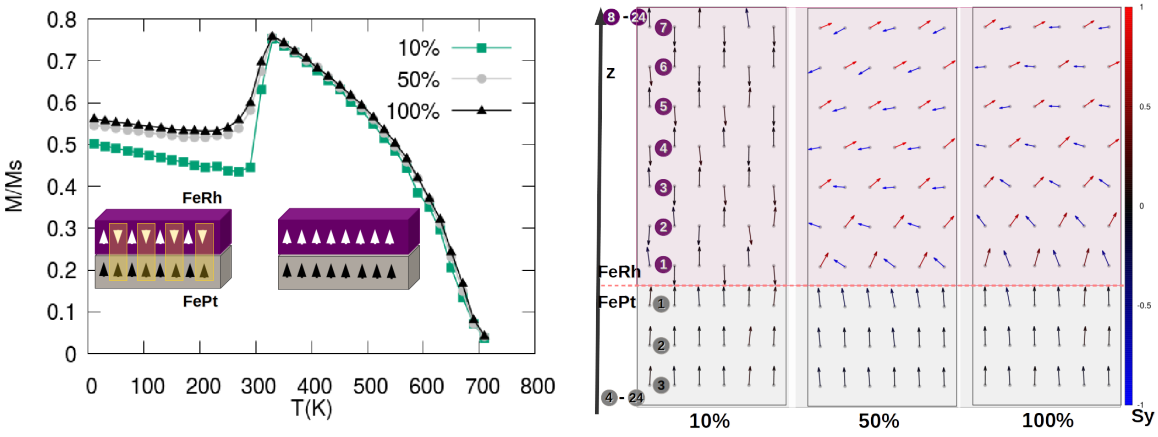

Fig. 6.12 Equilibrium magnetisation (left panel) and spin configuration at $T = 10$K (right panel) for different coupling strengths between FePt and FeRh bilayers. With increasing coupling, there is an increased ferromagnetic ordering, due to the spin canting of the antiferromagnetic phase of FeRh that appears due to the ferromagnetic coupling with FePt.

6.2.2 The two-temperature model

Since the discovery of utrafast demagnetisation [56], the excitation of the magnetic systems via optical means has gained a huge interest, both fundamentally and from the application point of view, since it can lead to the switching of magnetisation in the absence of applied fields [41]. In ultrafast experiments, the laser pulse interacts with the conduction electrons in the system, creating some highly non-equilibrium states which then equilibrate

thermodynamically with the phonons and the spin system, as illustrated in Fig. 6.13 (left panel).

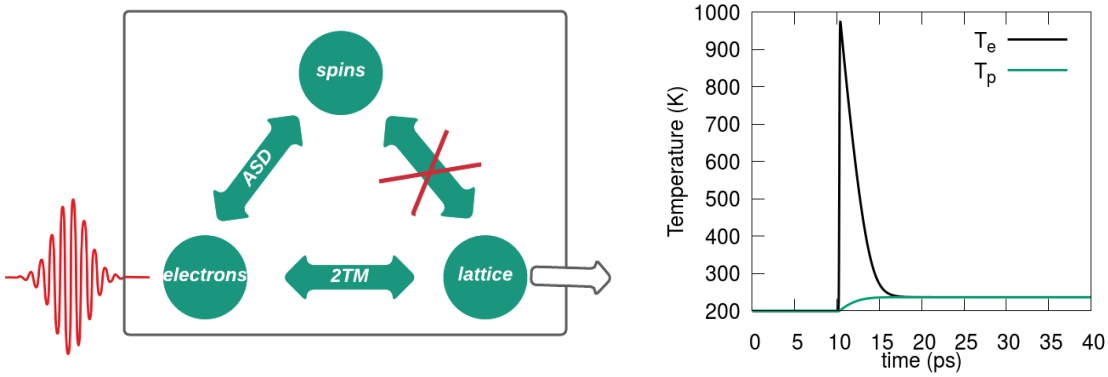

Fig. 6.13 (left panel) Diagram of energy flow in the two temperature model; The laser pulse excites the electrons in the system, which will then thermalise with the spins (via the atomistic spin dynamics model) and lattice (via the two-temperature model). Schematics adapted from Ref. [150]. (right panel) Example of evolution of the electron and phonon temperatures. The laser pulse is applied at $t = 10$ps.

The spin system is treated within the atomistic spin dynamics, while the electron and phonon heat bath are described phenomenologically by the two-temperature model (2TM) [151] in the form of the following coupled equations:

$$C_{e0}T_e\frac{dT_e}{dt} = -G_{ep}(T_e - T_p) + P(t) \tag{6.9}$$

$$C_p\frac{dT_p}{dt} = G_{ep}(T_e - T_p) - \kappa_e(T_p - T_{room})/\tau \tag{6.10}$$

where C_{e0}, C_p are the electron and phonon heat capacity, G_{ep} represents the electron-phonon coupling factor, T_p, T_e the phonon and electron temperatures and $P(t)$ is the time dependent laser pulse power. The laser power density is treated as a Gaussian form $P(t) = [2F_0/(\delta t_p\sqrt{\pi/\ln 2})]\exp[(-4\ln 2)(\frac{t}{t_p})^2]$ where F_0 is the laser fluence (in units of energy density), t_p the pulse temporal width and δ the optical penetration depth, assumed to be $\delta = 10$ nm. The term κ_e represents the diffusion coefficient (heat dissipation to the environment) which usually has large timescales and hence is neglected. The evolution of the electronic and phonon temperature given by the 2TM is illustrated in Fig. 6.13, (right panel).

The electronic system represents the thermostat for the spins and hence the temperature that enters into the LLG equation. As illustrated in Fig. 6.13, there is no coupling between the spin and lattice, since the system is considered fixed. By enabling the diffusion term $\kappa_e(T_p - T_{room})/\tau$, the energy deposited into the system by the laser pulse can dissipate to

the environment via the lattice. The two temperature model can be extended into the three temperature model (3TM), that adds another differential equation for the spin system. The 3TM model is not used for ASD simulations as it has been previously shown that the spin system is not necessarily in equilibrium for the ps timescales presented here [152], the spin temperature being directly calculated from the magnetisation dynamics under the laser excitation via Eq. 3.39.

6.2.3 Switching in FePt/FeRh bilayers

We move now to the investigation of the effect of the laser pulse on the magnetisation dynamics of FePt/FeRh bilayers. The laser pulse is modelled via the two temperature model presented in Section 6.2.2 and the specific parameters are given in Table 6.2. We note that the same parameters of the 2TM are used for both FePt and FeRh, hence the development of 2TM models that can deal with multiple materials might significantly change the switching conditions of the bilayer. The system size is approximately 7nm×7nm×14nm and is non-periodic in all three directions. The FePt/FeRh coupling is 50% of the Fe-Fe interaction and an applied field of $H_z = -4$T is applied to the system in order to drive the switching.

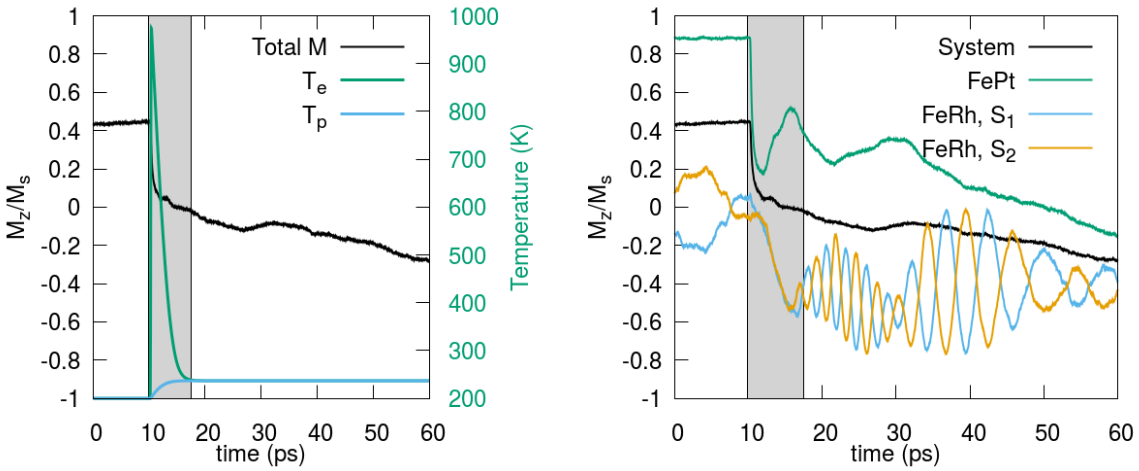

Fig. 6.14 Example of ultrafast switching in FePt/FeRh bilayers; The FePt/FeRh coupling is 50% of the Fe-Fe interaction. An applied field of $H_z = -4$T is applied to the system. Left panel shows the dynamics of the total z component of the magnetisation of the system on the left axis and the evolution of electronic and phononic temperature. The grey area emphasises the region where the electronic and phononic temperature are not equilibrated. Right panel shows the dynamics of the z component of magnetisation for the system, FePt and the two magnetic sublattices of FeRh.

Fig. 6.14 shows the temporal evolution of FePt/FeRh bilayers during the ultrafast switching. The left panel shows the temporal evolution of electronic and phononic temperatures on the right axis, together with the evolution of the total magnetisation of the system, left axis. The right panel shows the dynamics of the z component of magnetisation of FePt and the two magnetic sublattices of FeRh, S_1 and S_2 defined for the type-II antiferromagnetic configuration of FeRh. A representation of the type-II antiferromagnetic configuration is illustrated in Fig. 2.1, c), where the S_1 and S_2 sub-lattices of Fe in FeRh are given by the red and blue spins. The initial temperature of the system is 200K, which corresponds to the region where the FeRh system is in an antiferromagnetic state. This can be confirmed by looking at the z component of the two antiferromagnetic sub-lattices of FeRh, S_1 and S_2 - Fig. 6.14, right panel. The laser pulse is applied at $t = 10$ps, the grey area emphasizing the region where the electronic and phononic temperature are out-of-equilibrium. During the application of the laser pulse, the electronic temperature rises up to about 1000K leading to a demagnetisation of the system, as shown by the total magnetisation of the system. The temperature is sufficient to induce the transition to the ferromagnetic phase in FeRh, as we observe that after 13ps the magnetisations of the two sub-lattices become equal, in the region emphasized by the grey area. During this region, the z component of FePt (green line) shows an initial increase, due to the recovery of its ferromagnetic order after the laser pulse. However, the initial increase is followed by a decrease, at about 16ps, presumably due to the exchange spring mechanism, as in this region FeRh is ferromagnetic and has a negative magnetisation. After the grey area, the electronic and phononic temperatures have reached 240K, and in this region, FeRh is in the antiferromagnetic state, confirmed by the magnetisation plots of the two sub-lattices. After 20ps, we observe that the system is in a switched state and the system's magnetisation slowly relaxing towards a negative value.

The laser pulse triggers complex antiferromagnetic dynamics in FeRh as shown in Fig. 6.14, right panel, close to THz frequencies. By interfacing FeRh with a non-magnet, such as Pt, this complex dynamics can be used for the generation of spin currents and subsequent charge currents via the inverse spin-hall effect [153], which produces THz radiation that can be used in technological applications [154, 155]. Future work involves calculating the spin current induced in FePt due to ultrafast spin-pumping and understand if it additionally contributes to the switching.

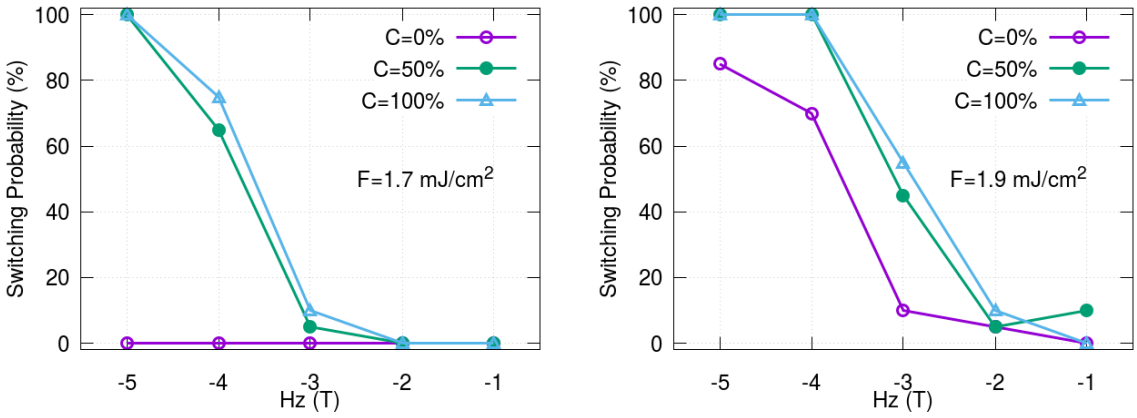

Fig. 6.15 Switching probability of FePt as function of coupling strength calculated for 20 grains of FePt/FeRh of approximately 7nm $\times$ 7nm $\times$ 14nm.

The switching probability of FePt is calculated for varying applied fields, in the uncoupled and strongly coupled case with the FeRh system - Fig. 6.15, for two laser fluences. In the uncoupled case, for a fluence of $F = 1.7\text{mJ/cm}^2$, no switching is observed in the region of fields showed here. This suggests that the large anisotropy of FePt has not decreased enough under the influence of the laser pulse to lead to the switching of the system. By increasing the laser fluence, some switching for the uncoupled systems can be obtained, since more energy is deposited in the system. By coupling the FePt system with the FeRh metamagnet, the switching probability is drastically improved. Even for the higher fluence - Fig. 6.15, right panel, where switching of FePt occurs in the absence of coupling, the coupling of the system with FeRh leads to 100% switching at lower fields. Interestingly, the strength of the coupling to FeRh seems to not strongly influence the switching curve, which is promising since the coupling at the interface is probably difficult to accurately control experimentally. This investigation shows that it is possible to obtain improved switching in FePt by coupling to the FeRh metamagnet, the switching window moving to lower fields and lower fluences than in the uncoupled case.

6.3 Conclusions

The ultimate limit of the areal density has been explored both analytically and numerically. Via numerical calculations of switching probabilities for heated dot magnetic recording, the bit error rate can be assessed, the results showing a decreased areal density due to dynamic evolution of the temperature and magnetic parameters. We have shown that NdFeB presents a lower bit error rate than FePt, hence potentially could be used in recording media applications.

A systematic investigation has shown that it is possible to obtain better switching probabilities in FePt by increasing the saturation magnetisation or the magnetic damping. Increasing the temperature pulse width brings the bit error rates to lower values, since it will bring the magnetic system closer to the equilibrium case.

We have shown that the switching in FePt is enhanced by the coupling with the FeRh metamagnet. Since FePt/FeRh structures have been proposed for HAMR application to lower the switching field via the exchange spring mechanism, we have shown that the exchange spring mechanism can happen at ultrafast time-scales. This results in the switching of FePt at much lower field, proving that FePt/FeRh bilayers could be employed in optical recording media.

7

Conclusions

In this final chapter, the main conclusions are emphasized with respect to the different aspects presented in this thesis. The chapter ends with possible paths to follow starting with the research presented in this thesis.

Damping and anisotropy calculations at elevated temperatures

The damping calculations from ferromagnetic resonance simulations at large temperatures showed an increased damping for uncoupled granular films. With decreasing grain size, this effect is more pronounced, and comparison with the analytical LLB equations suggests that scattering events at grain boundaries enhance the damping parameter. Interestingly, a reduction in the linewidth is observed at high temperatures in systems where there exists a distribution of properties that arises from a distribution of grain size. This result is in agreement with experimental investigation shown in Ref. [103] and proposes the inhomogeneous line broadening mechanism to explain the experimental results. This is an important finding since it suggests that the damping constant itself, relevant for dynamical properties and switching, increases with temperature due to magnon scattering. The fitting procedure based on the grid search method can offer a much faster determination of damping and anisotropy, parameters which are crucial for future generations of HAMR drives. The simple simulations of ferromagnetic resonance in two spin-systems coupled via exchange interaction show that the damping and resonance frequency can have complex behaviour depending on the exchange coupling and the properties of the two systems.

Spin-lattice dynamics and magnetisation switching by THz phonons

The development of spin-lattice simulations allows the explicit inclusion of phonons for spin dynamics calculations. The coupling term, that needs to be formulated in this way to not induce an additional energy drift in the system, mediates the energy and angular momentum

transfer between the phonons and magnons and is responsible for the thermalisation of the spin system in the absence of a phenomenological spin damping term. Within this model, both equilibrium and dynamical properties of the spin system are investigated for two choices of potentials. In the case of bulk systems, the equilibrium magnetisation does not depend on the choice of the mechanical potential and the Curie temperature is not significantly affected by the dynamic lattice. However, this is not the case for a thin film system, where a decreased Curie temperature is present due to the inclusion of surface effects and the dynamic lattice leads to stronger finite size effects. The magnon-phonon damping is calculated for different temperatures and coupling strengths and shows a functional form similar to the spin-lattice coupling term.

By exciting phonons at THz frequencies, it is shown that it is possible to access the magnetisation dynamics corresponding to various phonon modes. The phonon excitation leads to the development of an in-plane magnetic field that can trigger a precessional switching with a very low increase in the spin temperature. One important conclusion is that materials that present a flat phonon spectrum (such as in the case of the Harmonic potential) have more defined switching diagrams, while for the case of the Morse potential, the excited phonon modes can decay to lower frequency modes and affect the switching phase diagram (leading to shorter temporal regions of switching).

Heated dot magnetic recording media

The switching probability and the bit error rate are calculated for FePt systems and NdFeB systems. NdFeB presents a lower bit error rate than FePt, hence potentially could be used in recording media applications. The bit error rate in FePt can be improved by increasing the saturation magnetisation, the magnetic damping or the temperature pulse width, which leads the system to a behaviour closer to the equilibrium case. The calculations of the ultimate limit of recording media addressed by the quadrilemma can be updated by the numerical calculations, which showed a smaller areal density due to the dynamic processes associated with the temperature pulse.

Ultrafast dynamics in FePt/FeRh bilayers

The usage of FeRh has been proposed for recording media applications, where its soft ferromagnetic phase can lead to smaller coercive fields in FePt/FeRh bilayers. Since the phase transition in FeRh can be triggered by an ultrafast laser pulse, we investigate the switching in the FePt/FeRh under the effect of the laser excitation. The numerical simulations showed that the exchange spring mechanism appears at ultrafast time-scales and FePt can switch at lower fields due to this mechanism.

7.1 Further work

Further developments can be included to the research presented in this thesis. These are listed below and discussed in the following section:

1. Further damping calculations for realistic exchange coupled composite (ECC) media;
2. Micromagnetic modelling of linewidth and damping at elevated temperatures for distribution of grain sizes;
3. Development of improved potentials for spin-lattice dynamics simulations;
4. Parametrisation of magnetic insulators for spin-lattice dynamics;
5. Further investigations of NdFeB permanent magnet for heated dot recording media;
6. Two-temperature model for FePt/FeRh bilayer;

1) The ECC system has been treated as a two macrospin approximation, which is rather simplistic. Ferromagnetic resonance simulations on realistic granular systems at elevated temperatures would be interesting to perform since the damping has been shown to have a complex behaviour for the simple two macrospin approximation. The investigation of the damping for large driving fields is also of interest from the reversal perspective, since during the switching process, large spin excitations are present.

2) The semi-analytical investigation of the linewidth in the presence of distribution of magnetic properties that appears due to the variation of the grain size showed that the linewidth can decrease with increasing temperature due to the transition of small grains to the superparamagnetic state. Ferromagnetic resonance calculations at finite temperature for a system of grains via atomistic modelling is computationally expensive, hence for this investigation micromagnetic modelling based on the LLB equation can be performed for HAMR systems. A software package capable of dealing with granular systems at finite temperature for recording media applications (acronym MARS) is currently being developed by Ewan Rannala at The University of York.

3) The spin-lattice model uses a long-range pair-wise potential, either a Harmonic or Morse expression. This is a simplistic approximation, however it can reproduce the phonon spectra of BCC Fe (in the case of Morse potential and with improved parameterisation of the Harmonic potential). Since the magnon properties were not influenced by the choice of potential, the simple pair-wise implementation represents a reasonable first approximation. However, there are many improved mechanical potentials based on many-body formulations

(such as the Embedded Atom Potential) that can predict better the elastic properties hence the implementation of such potential is the next step to be followed. Ultimately, one of the main challenges of the spin-lattice framework would be to develop many-body spin dependent potential from first principles methods [156].

4) The spin-lattice model developed in this work is crucial for the study of magnetic insulators. Further work includes parameterising the model for such a magnetic system, which can include multiple magnetic sub-lattices and complex magnon and phonon dispersion curves. Investigating the switching of the magnetisation via THz phonons within these systems is interesting, since there are experimental results [157] suggesting that switching occurs via a mechanism similar to what is presented in Chapter 5.

5) It has been shown in this work that NdFeB can exhibit lower bit error rates for heated dot recording media applications presumably due to the high saturation magnetisation. Interestingly, the Curie temperature showed a different finite-size scaling exponent than in the case of FePt, which might contribute to the improved behaviour of the BER for different system sizes for NdFeB. Further calculations of the finite-size scaling exponents for the Curie temperature needs to be performed with increased resolution and number of integration steps for more accurate determination of the scaling exponents. It is also interesting to further explore if it exists a correlation between the BER and the critical exponents of the materials proposed for HDMR.

6) For the investigation of ultrafast switching in FePt/FeRh bilayers, the same set of parameters for the two-temperature model has been used for both FePt and FeRh. Further work involves developing and implementing a two-temperature model that ideally could deal with multiple types of materials in layered structures.

A

Conservation properties of the precessional equation

In the absence of a damping term, the total energy of a magnetic system is conserved, the magnetic moments following a conservative dynamics, described by the precessional equation:

$$\frac{\partial \mathbf{S}_i}{\partial t} = -\gamma \mathbf{S}_i \times \mathbf{H}_i \tag{A.1}$$

To analyse the conservative properties of the precessional equation of motion, we start from a simple magnetic Hamiltonian that contains only exchange interaction. The exchange constant depends on the atomic positions which, within SLD dynamics, are dynamically treated. The total energy of the system will vary as [76]:

$$E(t) = \sum_k \frac{m_k \mathbf{v}_k^2}{2} + U\left(\mathbf{r}_1(t), ..., \mathbf{r}_N(t)\right) - \sum_{i,j} J_{ij}\left(\mathbf{r}_1(t), .., \mathbf{r}_N(t)\right) \mathbf{S}_i(t) \cdot \mathbf{S}_j(t) \tag{A.2}$$

Now considering the time derivative of the energy:

$$\frac{dE(t)}{dt} = \sum_k m_k \mathbf{v}_k \frac{d\mathbf{v}_k}{dt} + \sum_l \frac{\partial U}{\partial \mathbf{r}_l}\frac{d\mathbf{r}_l}{dt} - \sum_{i,j}\sum_l \frac{\partial J_{ij}}{\partial \mathbf{r}_l}\frac{d\mathbf{r}_l}{dt}\mathbf{S}_i(t) \cdot \mathbf{S}_j(t) - \sum_{i,j} J_{ij}\frac{d}{dt}\left[\mathbf{S}_i(t) \cdot \mathbf{S}_j(t)\right] \tag{A.3}$$

In the absence of a lattice thermostat and no dissipation terms, the EOM of motion become:

$$\frac{\partial \mathbf{r}_k}{\partial t} = \mathbf{v}_k \tag{A.4}$$

$$\frac{m_k \partial \mathbf{v}_k}{\partial t} = -\frac{\partial U}{\partial \mathbf{r}_k} + \frac{\partial}{\partial \mathbf{r}_k} \sum_{i,j} J_{ij}\left(\mathbf{r}_1(t), .., \mathbf{r}_N(t)\right) \mathbf{S}_i(t) \cdot \mathbf{S}_j(t) \tag{A.5}$$

$$\tag{A.6}$$

The first three terms will cancel in the time derivative of the energy. The last term can be expressed by considering $\frac{d\mathbf{S}_i}{dt} = -\gamma \mathbf{S}_i \times \mathbf{H}_i = -\gamma \mathbf{S}_i \times \sum_l J_{il} \mathbf{S}_l$ and $J_{il} = J_{li}$:

$$\frac{dE(t)}{dt} = -\sum_{i,j} J_{ij} \frac{d}{dt}\left[\mathbf{S}_i(t) \cdot \mathbf{S}_j(t)\right] \tag{A.7}$$

$$= \gamma \sum_{i,j} J_{ij} \left[\sum_l J_{li} (\mathbf{S}_i \times \mathbf{S}_l) \cdot \mathbf{S}_j + \sum_l J_{lj} \mathbf{S}_i \cdot (\mathbf{S}_j \times \mathbf{S}_l)\right] \tag{A.8}$$

$$= \gamma \left[\sum_{i,j} J_{ij} \sum_l J_{li} (\mathbf{S}_i \times \mathbf{S}_l) \cdot \mathbf{S}_j + \sum_{i,j} J_{ij} \sum_l J_{lj} \mathbf{S}_i \cdot (\mathbf{S}_j \times \mathbf{S}_l)\right] \tag{A.9}$$

$$= \gamma \left[\sum_{i,j} J_{ij} \sum_l J_{li} (\mathbf{S}_i \times \mathbf{S}_l) \cdot \mathbf{S}_j + \sum_{i,j} J_{ij} \sum_l J_{li} \mathbf{S}_j \cdot (\mathbf{S}_i \times \mathbf{S}_l)\right] \tag{A.10}$$

$$= 2\gamma \sum_{i,j,l} J_{il} J_{ij} (\mathbf{S}_i \times \mathbf{S}_l) \cdot \mathbf{S}_j = 2\gamma \sum_i \left(\mathbf{S}_i \times \left[\sum_l J_{il} \mathbf{S}_l\right] \cdot \left[\sum_j J_{ij} \mathbf{S}_j\right]\right) \tag{A.11}$$

$$= 2\gamma (\mathbf{S}_i \times \mathbf{H}_i) \cdot \mathbf{H}_i = 0 \tag{A.12}$$

$$\tag{A.13}$$

Hence, the total energy of the system remains constant, even if, the lattice and spin energies can vary as function of time. Similarly, the time derivative of total angular momentum can be expressed as:

$$\frac{d\mathbf{S}}{dt} = \sum_i \frac{d\mathbf{S}_i}{dt} = -\gamma \sum_{i,l} J_{li} \mathbf{S}_i \times \mathbf{S}_l = -\gamma \sum_{i,l} J_{il} \mathbf{S}_l \times \mathbf{S}_i = \gamma \sum_{i,l} J_{il} \mathbf{S}_i \times \mathbf{S}_l = \gamma \sum_{i,l} J_{li} \mathbf{S}_i \times \mathbf{S}_l = 0 \tag{A.14}$$

or

$$\frac{d\mathbf{S}}{dt} = \sum_i \frac{d\mathbf{S}_i}{dt} = -\gamma \sum_{i,l} J_{li} \mathbf{S}_i \times \mathbf{S}_l = -\gamma \sum_{i<l} (J_{il} \mathbf{S}_l \times \mathbf{S}_i + J_{li} \mathbf{S}_i \times \mathbf{S}_l) = 0 \tag{A.15}$$

Hence the total spin angular momentum is conserved. The conservation laws can prevent the spin system from approaching thermodynamical equilibrium, such as in the results by

[61], where the spin and lattice temperature do not equilibrate to the same value due to the conservation of angular momentum in the presence of only exchange energy. The lattice subsystem can exchange only energy with the thermal reservoir, however, the spin can exchange both energy and angular momentum with the lattice or its thermal reservoir. To allow transfer of angular momentum between the lattice and spin system an additional energy term is necessary. Considering the simplest case of an uniaxial anisotropy energy with an easy axis $\mathbf{e}_i$, $E_u = -k_u \sum_i (\mathbf{S}_i \cdot \mathbf{e}_i)^2$:

$$\frac{d\mathbf{S}}{dt} = \sum_i \frac{d\mathbf{S}_i}{dt} = -\gamma k_u \sum_i \mathbf{S}_i \times [2(\mathbf{S}_i \cdot \mathbf{e}_i)\mathbf{e}_i] = -2\gamma k_u \sum_i (\mathbf{S}_i \times \mathbf{e}_i)(\mathbf{S}_i \cdot \mathbf{e}_i) \neq 0 \tag{A.16}$$

Energy terms like a magneto-crystalline anisotropy will allow angular momentum transfer between spin and lattice, the mechanism responsible for this being the spin-orbit coupling.

B

Fluctuation dissipation theorem

To obtain the correct equilibrium distributions of magnetic parameters, the SLD model needs to obey the fluctuation-dissipation theorem. Following the protocol described in [158], we are able to prove that the SLD model employed in this thesis obeys the fluctuation-dissipation theorem. The derivation is firstly for the LLG equation, and then is extended for the SLD model.

The linear response Langevin equation of motion is written in the form:

$$\frac{dx_i}{dt} = -\sum_j \gamma_{ij} X_j + f_i \tag{B.1}$$

where γ_{ij} are the kinetic coefficients and X_j are variables thermodynamically conjugated to x_j, $X_j = \frac{S}{x_j}$, where S is the entropy of the system. For a closed system in an external medium:

$$X_j = \frac{1}{k_B T} \frac{\partial E}{\partial x_j} \tag{B.2}$$

For a magnetic system the total energy can be written as:

$$E = V_i M_s \sum_i (-\vec{M}_i \cdot \vec{H}_i) \tag{B.3}$$

Close to equilibrium, the LLG equation can be linearised using small deviations $\vec{m}_i = \vec{M}_i - \vec{M}_i^0$, $\vec{h}_i = (\vec{H}_i - \vec{H}_i^0)/M_s$

Thus, the LLG equation should be re-written as:

$$\frac{dm_i}{dt} = \frac{M_s^2 V_i}{k_B T} \sum_j^3 N \gamma_{ij} h_j \tag{B.4}$$

Now we expand the LLG equation in its components:

$$\frac{d\vec{M}_i}{d\tau} = -\vec{M}_i \times \vec{H}_i - \alpha \vec{M}_i \times (\vec{M}_i \times \vec{H}_i) \tag{B.5}$$

$$\frac{dM_i^x}{d\tau} = (H_i^y M_i^z - H_i^z M_i^y) - \alpha \left[M_i^x (H_i^y M_i^y + H_i^z M_i^z) - H_i^x \left((M_i^y)^2 + (M_i^z)^2 \right) \right] \tag{B.6}$$

$$\frac{dM_i^y}{d\tau} = (H_i^z M_i^x - H_i^x M_i^z) - \alpha \left[M_i^y (H_i^x M_i^x + H_i^z M_i^z) - H_i^y \left((M_i^x)^2 + (M_i^y)^2 \right) \right] \tag{B.7}$$

$$\frac{dM_i^z}{d\tau} = (H_i^x M_i^y - H_i^y M_i^x) - \alpha \left[M_i^z (H_i^x M_i^x + H_i^y M_i^y) - H_i^z ((M_i^x)^2) + (M_i^y)^2) \right] \tag{B.8}$$

By substituting $\vec{M}_i = \vec{m}_i + \vec{M}_i^0$, $\vec{H}_i = \vec{h}_i M_s + \vec{H}_i^0$ into the components of the LLG equation we can calculate the γ_{ij} components. For example, to calculate the γ_{ij}^{xx} component, we expand the coefficient in $\frac{dM_i^x}{d\tau}$ corresponding to H_i^x:

$$H_i^x \left((M_i^y)^2 + (M_i^z)^2 \right) = (h_i^x M_s + \vec{H}_i^{(x,0)}) \left((m_i^y)^2 + (M_i^{0,y})^2 + 2 m_i^y M_i^y + (m_i^z)^2 + (M_i^{0,z})^2 + 2 m_i^z M_i^z \right) \tag{B.9}$$

Since $\vec{m}_i$, $\vec{h}_i$ are small deviations of the magnetisation and effective field around the equilibrium position, their squared value $\left((m_i^y)^2, (m_i^z)^2 \right)$ and the product between the two $(2 m_i^y h_i^x M_s,\ 2 m_i^z h_i^x M_s)$ can be approximated to zero. Similarly the time derivative of the equilibrium magnetisation $M_i^{x,0}$ is zero. This leads to the coefficient of h_i^x having the following expression:

$$\frac{dm_i^x}{dt} = \cdots + \alpha h_i^x M_s [(M_i^{0,y})^2 + (M_i^{0,z})^2] + \ldots \tag{B.10}$$

From Eq. B.4, we can show that γ_{ij}^{xx} has the following expression [158]:

$$\gamma_{ij}^{xx} = \frac{\alpha k_B T}{M_s V_i} [(M_i^{0,y})^2 + (M_i^{0,z})^2] \partial_{ij} \tag{B.11}$$

Similarly, for the rest of the coefficients can be expressed:

$$\gamma_{ij}^{xy} = \frac{k_B T}{M_s V_i} [(-M_i^{0,z}) + \alpha M_i^{0,x} M_i^{0,y}] \partial_{ij} \tag{B.12}$$

$$\gamma_{ij}^{yx} = \frac{k_B T}{M_s V_i}[(M_i^{0,z}) + \alpha M_i^{0,x} M_i^{0,y}]\partial_{ij} \tag{B.13}$$

$$\gamma_{ij}^{yy} = \frac{\alpha k_B T}{M_s V_i}[(M_i^{0,x})^2 + (M_i^{0,z})^2]\partial_{ij} \tag{B.14}$$

The thermal field coefficients from the Onsager principle [158] are given by:

$$\mu_{ij}^{xx} = \gamma_{ij}^{xx} + \gamma_{ji}^{xx} \tag{B.15}$$

$$\mu_{ij}^{xx} = \frac{2\alpha k_B T}{M_S V_i}[(M_i^{0,y})^2 + (M_i^{0,z})^2]\partial_{ij} \tag{B.16}$$

$$\mu_{ij}^{xy} = \frac{2\alpha k_B T}{M_S V_i} M_i^{0,x} M_i^{0,y} \partial_{ij} \tag{B.17}$$

In equilibrium, $M_i^{0,x} = 0$, $M_i^{0,y} = 0$, $M_i^{0,z} = 1$, hence we obtain the result for the stationary solution:

$$\mu_{ij}^{xx} = \mu_{ij}^{yy} = \frac{2\alpha k_B T}{M_s V_i}\partial_{ij}, \mu_{ij}^{zz} = 0 \tag{B.18}$$

In the absence of a damping term, we need to linearise $\frac{d\vec{M}_i}{dt} = -\gamma(\vec{M}_i \times \vec{H}_i)$. As magnetisation and field are variables thermodynamically conjugated, the fluctuation dissipation theorem does not need to be written anymore. Hence we need to look at the lattice equations: $\dot{v}_i = F_i/m_i$, which obey the fluctuation dissipation theorem.

References

[1] Elena Yu Vedmedenko, Roland Kenji Kawakami, Denis D Sheka, Pietro Gambardella, Andrei Kirilyuk, Atsufumi Hirohata, Christian Binek, Oksana Chubykalo-Fesenko, Stefano Sanvito, Brian J Kirby, et al. The 2020 magnetism roadmap. *Journal of Physics D: Applied Physics*, 53(45):453001, 2020.

[2] H J Richter. The transition from longitudinal to perpendicular recording. *Journal of Physics D: Applied Physics*, 40(9):R149–R177, 2007.

[3] HJ Richter, Andreas Lyberatos, Ulrich Nowak, Richard Francis L Evans, and Roy W Chantrell. The thermodynamic limits of magnetic recording. *Journal of Applied Physics*, 111(3):033909, 2012.

[4] RFL Evans, Roy W Chantrell, Ulrich Nowak, Andreas Lyberatos, and H-J Richter. Thermally induced error: Density limit for magnetic data storage. *Applied Physics Letters*, 100(10):102402, 2012.

[5] http://idema.org/?page_id=416. Accessed: 2020-11-03.

[6] Dieter Weller, Gregory Parker, Oleksandr Mosendz, Eric Champion, Barry Stipe, Xiaobin Wang, Timothy Klemmer, Ganping Ju, and Antony Ajan. A HAMR Media Technology Roadmap to an Areal Density of 4 Tb/in^2. $IEEE\ TransactionsonMagnetics, 50(1), 2014$.

[7] https://blog.seagate.com, Accessed: 2020-11-03.

[8] R. E. Rottmayer, S. Batra, D. Buechel, W. A. Challener, J. Hohlfeld, Y. Kubota, L. Li, B. Lu, C. Mihalcea, K. Mountfield, K. Pelhos, C. Peng, T. Rausch, M. A. Seigler, D. Weller, and X. . Yang. Heat-assisted magnetic recording. *IEEE Transactions on Magnetics*, 42(10):2417–2421, 2006.

[9] Jan-Ulrich Thiele, Stefan Maat, and Eric E. Fullerton. FeRh/FePt exchange spring films for thermally assisted magnetic recording media. *Applied Physics Letters*, 82(17):2859–2861, 2003.

[10] Randall H Victora and Xiao Shen. Composite media for perpendicular magnetic recording. *IEEE Transactions on Magnetics*, 41(2):537–542, 2005.

[11] Randall H Victora and X Shen. Exchange coupled composite media for perpendicular magnetic recording. *IEEE Transactions on Magnetics*, 41(10):2828–2833, 2005.

[12] Dieter Suess, Thomas Schrefl, S Fähler, Markus Kirschner, Gino Hrkac, Florian Dorfbauer, and Josef Fidler. Exchange spring media for perpendicular recording. *Applied Physics Letters*, 87(1):012504, 2005.

[13] Thomas R Albrecht, Hitesh Arora, Vipin Ayanoor-Vitikkate, Jean-Marc Beaujour, Daniel Bedau, David Berman, Alexei L Bogdanov, Yves-Andre Chapuis, Julia Cushen, Elizabeth E Dobisz, et al. Bit-patterned magnetic recording: Theory, media fabrication, and recording performance. *IEEE Transactions on Magnetics*, 51(5):1–42, 2015.

[14] John C Slonczewski et al. Current-driven excitation of magnetic multilayers. *Journal of Magnetism and Magnetic Materials*, 159(1):L1, 1996.

[15] Unai Atxitia, Tom A Ostler, Roy W Chantrell, and Oksana Chubykalo-Fesenko. Optimal electron, phonon, and magnetic characteristics for low energy thermally induced magnetization switching. *Applied Physics Letters*, 107(19):192402, 2015.

[16] HY Yuan, Zhe Yuan, Ke Xia, and XR Wang. Influence of nonlocal damping on the field-driven domain wall motion. *Physical Review B*, 94(6):064415, 2016.

[17] Alexander G Gurevich and Gennadii A Melkov. *Magnetization oscillations and waves*. CRC press, 1996.

[18] Tomohiro Taniguchi and Hiroshi Imamura. Enhancement of the gilbert damping constant due to spin pumping in noncollinear ferromagnet/nonmagnet/ferromagnet trilayer systems. *Phys. Rev. B*, 76:092402, Sep 2007.

[19] Andrei Kirilyuk, Alexey V Kimel, and Theo Rasing. Ultrafast optical manipulation of magnetic order. *Reviews of Modern Physics*, 82(3):2731, 2010.

[20] Joseph Barker. *Atomistic Models of Magnetic Systems with Combined Ferromagnetic and Antiferromagnetic Order*. PhD thesis, University of York, 2013.

[21] Richard FL Evans, Weijia J Fan, Phanwadee Chureemart, Thomas A Ostler, Matthew OA Ellis, and Roy W Chantrell. Atomistic spin model simulations of magnetic nanomaterials. *Journal of Physics: Condensed Matter*, 26(10):103202, 2014.

[22] Björn Skubic, Johan Hellsvik, Lars Nordström, and Olle Eriksson. A method for atomistic spin dynamics simulations: implementation and examples. *Journal of physics: condensed matter*, 20(31):315203, 2008.

[23] Werner Heisenberg. Zur Theorie des Ferromagnetismus. *Zeitschrift für Physik*, 49(9-10):619–636, 1928.

[24] IE Dzialoshinskii. Thermodynamic theory of weak ferromagnetism in antiferromagnetic substances. *Soviet Physics JETP-USSR*, 5(6):1259–1272, 1957.

[25] Tôru Moriya. Anisotropic superexchange interaction and weak ferromagnetism. *Physical Review*, 120(1):91, 1960.

[26] Hongxin Yang, André Thiaville, Stanislas Rohart, Albert Fert, and Mairbek Chshiev. Anatomy of Dzyaloshinskii-Moriya interaction at Co/Pt interfaces. *Physical Review Letters*, 115(26):267210, 2015.

[27] UK Rößler, AN Bogdanov, and C Pfleiderer. Spontaneous skyrmion ground states in magnetic metals. *arXiv preprint cond-mat/0603103*, 2006.

[28] GT Herring C. in Rado and H Suhl. Magnetism, vol. iib. *Suhl and Rado, Academie Press, New York*, 1966.

[29] Minoru Takahashi. Half-filled hubbard model at low temperature. *Journal of Physics C: Solid State Physics*, 10(8):1289, 1977.

[30] Joseph Barker and Roy W Chantrell. Higher-order exchange interactions leading to metamagnetism in FeRh. *Physical Review B*, 92(9):094402, 2015.

[31] Mara Strungaru. Atomistic modelling of metamagnetic transition in FeRh with four-spin exchange. *MSc by Research Thesis*, University of York, 2017.

[32] J. R. Massey, K. Matsumoto, M. Strungaru, R. C. Temple, T. Higo, K. Kondou, R. F. L. Evans, G. Burnell, R. W. Chantrell, Y. Otani, and C. H. Marrows. Phase boundary exchange coupling in the mixed magnetic phase regime of a Pd-doped FeRh epilayer. *Physical Review Materials*, 4:024403, 2020.

[33] Charles Kittel. *Introduction to solid state physics*. Wiley, 8th edition, 2014.

[34] Olle Eriksson, Anders Bergman, Johan Hellsvik, and Lars Bergqvist. *Atomistic spin dynamics: Foundations and applications*. Oxford University Press, 2017.

[35] Ch Kittel. Excitation of spin waves in a ferromagnet by a uniform rf field. *Physical Review*, 110(6):1295, 1958.

[36] Stephen Blundell. *Magnetism in condensed matter*. Oxford University Press, 2001.

[37] John MD Coey. *Magnetism and magnetic materials*. Cambridge University Press, 2010.

[38] CH Back, D Weller, J Heidmann, D Mauri, D Guarisco, EL Garwin, and HC Siegmann. Magnetization reversal in ultrashort magnetic field pulses. *Physical Review Letters*, 81(15):3251, 1998.

[39] Mark H Kryder, Edward C Gage, Terry W McDaniel, William A Challener, Robert E Rottmayer, Ganping Ju, Yiao-Tee Hsia, and M Fatih Erden. Heat assisted magnetic recording. *Proceedings of the IEEE*, 96(11):1810–1835, 2008.

[40] E Beaurepaire, J-C Merle, A Daunois, and J-Y Bigot. Ultrafast spin dynamics in ferromagnetic nickel. *Physical Review Letters*, 76(22):4250, 1996.

[41] TA Ostler, J Barker, RFL Evans, RW Chantrell, U Atxitia, O Chubykalo-Fesenko, S El Moussaoui, LBPJ Le Guyader, E Mengotti, LJ Heyderman, et al. Ultrafast heating as a sufficient stimulus for magnetization reversal in a ferrimagnet. *Nature communications*, 3(1):1–6, 2012.

[42] J Barker, U Atxitia, TA Ostler, O Hovorka, O Chubykalo-Fesenko, and RW Chantrell. Two-magnon bound state causes ultrafast thermally induced magnetisation switching. *Scientific reports*, 3:3262, 2013.

[43] Lev Davidovich Landau and E Lifshitz. On the theory of the dispersion of magnetic permeability in ferromagnetic bodies. *Phys. Z. Sowjet.*, 8:153, 1935.

[44] Thomas L Gilbert. A phenomenological theory of damping in ferromagnetic materials. *IEEE Transactions on Magnetics*, 40(6):3443–3449, 2004.

[45] Jonathan David Hannay. *Computational simulations of thermally activated magnetisation dynamics at high frequencies*. PhD thesis, University of Wales, Bangor, 2001.

[46] Karl Blum. *Density matrix theory and applications*. Plenum Press, New York and London, 1981.

[47] William Fuller Brown Jr. Thermal fluctuations of a single-domain particle. *Physical Review*, 130(5):1677, 1963.

[48] Ph Depondt and FG Mertens. Spin dynamics simulations of two-dimensional clusters with heisenberg and dipole–dipole interactions. *Journal of Physics: Condensed Matter*, 21(33):336005, 2009.

[49] J H Mentink, M V Tretyakov, A Fasolino, M I Katsnelson, and Th Rasing. Stable and fast semi-implicit integration of the stochastic Landau–Lifshitz equation. *Journal of Physics: Condensed Matter*, 22(17):176001, 2010.

[50] Nicholas Metropolis, Arianna W Rosenbluth, Marshall N Rosenbluth, Augusta H Teller, and Edward Teller. Equation of state calculations by fast computing machines. *The journal of chemical physics*, 21(6):1087–1092, 1953.

[51] D. Hinzke and U. Nowak. Monte carlo simulation of magnetization switching in a heisenberg model for small ferromagnetic particles. *Computer Physics Communications*, 121-122:334 – 337, 1999. Proceedings of the Europhysics Conference on Computational Physics CCP 1998.

[52] JD Alzate-Cardona, D Sabogal-Suárez, RFL Evans, and E Restrepo-Parra. Optimal phase space sampling for monte carlo simulations of heisenberg spin systems. *Journal of Physics: Condensed Matter*, 31(9):095802, 2019.

[53] HB Callen and Earl Callen. The present status of the temperature dependence of magnetocrystalline anisotropy, and the l (l+ 1) 2 power law. *Journal of Physics and Chemistry of Solids*, 27(8):1271–1285, 1966.

[54] Serdal Karakurt, Roy W Chantrell, and Ulrich Nowak. A model of damping due to spin–lattice interaction. *Journal of Magnetism and Magnetic Materials*, 316(2):e280–e282, 2007.

[55] Dilina Perera, Markus Eisenbach, Don M. Nicholson, G. Malcolm Stocks, and David P. Landau. Reinventing atomistic magnetic simulations with spin-orbit coupling. *Physical Review B*, 93(6):1–5, 2016.

[56] David Beaujouan, Pascal Thibaudeau, and Cyrille Barreteau. Anisotropic magnetic molecular dynamics of cobalt nanowires. *Physical Review B - Condensed Matter and Materials Physics*, 86(17):1–11, 2012.

[57] Pui-Wai Ma, CH Woo, and SL Dudarev. Large-scale simulation of the spin-lattice dynamics in ferromagnetic iron. *Physical Review B*, 78(2):024434, 2008.

[58] Pui Wai Ma and C. H. Woo. Parallel algorithm for spin and spin-lattice dynamics simulations. *Physical Review E - Statistical, Nonlinear, and Soft Matter Physics*, 79(4):1–8, 2009.

[59] J. Tranchida, S. J. Plimpton, P. Thibaudeau, and A. P. Thompson. Massively parallel symplectic algorithm for coupled magnetic spin dynamics and molecular dynamics. *Journal of Computational Physics*, 372:406–425, 2018.

[60] Matthias Aßmann and Ulrich Nowak. Spin-lattice relaxation beyond Gilbert damping. *Journal of Magnetism and Magnetic Materials*, 469:217–223, 2019.

[61] Johan Hellsvik, Danny Thonig, Klas Modin, Diana Iuşan, Anders Bergman, Olle Eriksson, Lars Bergqvist, and Anna Delin. General method for atomistic spin-lattice dynamics with first-principles accuracy. *Physical Review B*, 99(10):1–19, 2019.

[62] C. Dornes, Y. Acremann, M. Savoini, M. Kubli, M. J. Neugebauer, E. Abreu, L. Huber, G. Lantz, C. A.F. Vaz, H. Lemke, E. M. Bothschafter, M. Porer, V. Esposito, L. Rettig, M. Buzzi, A. Alberca, Y. W. Windsor, P. Beaud, U. Staub, Diling Zhu, Sanghoon Song, J. M. Glownia, and S. L. Johnson. The ultrafast Einstein–de Haas effect. *Nature*, 565(7738):209–212, 2019.

[63] Jakob Walowski and Markus Münzenberg. Perspective: Ultrafast magnetism and THz spintronics. *Journal of Applied Physics*, 120(14), 2016.

[64] I. Radu, C. Stamm, A. Eschenlohr, F. Radu, R. Abrudan, K. Vahaplar, T. Kachel, N. Pontius, R. Mitzner, K. Holldack, A. Föhlisch, T. A. Ostler, J. H. Mentink, R. F.L. Evans, R. W. Chantrell, A. Tsukamoto, A. Itoh, A. Kirilyuk, A. V. Kimel, and Th Rasing. Ultrafast and Distinct Spin Dynamics in Magnetic Alloys. *Spin*, 5(3):1–10, 2015.

[65] Martin Hennecke, Ilie Radu, Radu Abrudan, Torsten Kachel, Karsten Holldack, Rolf Mitzner, Arata Tsukamoto, and Stefan Eisebitt. Angular Momentum Flow during Ultrafast Demagnetization of a Ferrimagnet. *Physical Review Letters*, 122(15):157202, 2019.

[66] Albert Einstein. Experimenteller nachweis der ampereschen molekularstrome. *Verh. d. Deutsch. Phy. Ges.*, (2):152–170, 1915.

[67] Andreas Rückriegel, Simon Streib, Gerrit E. W. Bauer, and Rembert A. Duine. Angular momentum conservation and phonon spin in magnetic insulators. *Physical Review B*, 101:104402, 2020.

[68] Sebastian F Maehrlein, Ilie Radu, Pablo Maldonado, Alexander Paarmann, Michael Gensch, Alexandra M Kalashnikova, Roman V Pisarev, Martin Wolf, Peter M Oppeneer, Joseph Barker, et al. Dissecting spin-phonon equilibration in ferrimagnetic insulators by ultrafast lattice excitation. *Science advances*, 4(7):eaar5164, 2018.

[69] A. Melnikov, I. Radu, U. Bovensiepen, O. Krupin, K. Starke, E. Matthias, and M. Wolf. Coherent Optical Phonons and Parametrically Coupled Magnons Induced by Femtosecond Laser Excitation of the Gd(0001) Surface. *Physical Review Letters*, 91:227403, 2003.

[70] Ji-Wan Kim, Mircea Vomir, and Jean-Yves Bigot. Controlling the spins angular momentum in ferromagnets with sequences of picosecond acoustic pulses. *Scientific reports*, 5:8511, 2015.

[71] Ji Wan Kim, Mircea Vomir, and Jean Yves Bigot. Ultrafast magnetoacoustics in nickel films. *Physical Review Letters*, 109(16):1–5, 2012.

[72] A. V. Scherbakov, A. S. Salasyuk, A. V. Akimov, X. Liu, M. Bombeck, C. Brüggemann, D. R. Yakovlev, V. F. Sapega, J. K. Furdyna, and M. Bayer. Coherent magnetization precession in ferromagnetic (Ga,Mn)As induced by picosecond acoustic pulses. *Physical Review Letters*, 105(11):1–4, 2010.

[73] Vladimir S. Vlasov, Alexey M. Lomonosov, Anton V. Golov, Leonid N. Kotov, Valentin Besse, Alexandr Alekhin, Dmitry A. Kuzmin, Igor V. Bychkov, and Vasily V. Temnov. Magnetization switching in bistable nanomagnets by picosecond pulses of surface acoustic waves. *Physical Review B*, 101(2):1–9, 2020.

[74] Oleksandr Kovalenko, Thomas Pezeril, and Vasily V. Temnov. New concept for magnetization switching by ultrafast acoustic pulses. *Physical Review Letters*, 110(26):1–5, 2013.

[75] H. Maier-Flaig, S. Klingler, C. Dubs, O. Surzhenko, R. Gross, M. Weiler, H. Huebl, and S. T.B. Goennenwein. Temperature-dependent magnetic damping of yttrium iron garnet spheres. *Physical Review B*, 95(21):1–8, 2017.

[76] Pui Wai Ma, C. H. Woo, and S. L. Dudarev. Spin-lattice dynamics simulations of ferromagnetic iron. *AIP Conference Proceedings*, 999:134–145, 2008.

[77] IP Omelyan, IM Mryglod, and R Folk. Conservation-laws-preserving algorithms for spin dynamics simulations. *EPL (Europhysics Letters)*, 52(6):603, 2000.

[78] Pui-wai Ma and S L Dudarev. Spin-lattice-electron dynamics simulations of magnetic materials. *Physical Review B*, 184301:30–37, 2012.

[79] Louis A Girifalco and Victor G Weizer. Application of the morse potential function to cubic metals. *Physical Review*, 114(3):687, 1959.

[80] SL Dudarev and PM Derlet. A 'magnetic'interatomic potential for molecular dynamics simulations. *Journal of Physics: Condensed Matter*, 17(44):7097, 2005.

[81] Peter M Derlet and SL Dudarev. Million-atom molecular dynamics simulations of magnetic iron. *Progress in materials science*, 52(2-3):299–318, 2007.

[82] Masuo Suzuki. Generalized Trotter's formula and systematic approximants of exponential operators and inner derivations with applications to many-body problems. *Communications in Mathematical Physics*, 51(2):183–190, 1976.

[83] Shan-Ho Tsai, H. K. Lee, and D. P. Landau. Molecular and spin dynamics simulations using modern integration methods. *American Journal of Physics*, 73(7):615–624, 2005.

[84] Shan-Ho Tsai, M. Krech, and D.P. Landau. Symplectic integration methods in molecular and spin dynamics simulations. *Brazilian Journal of Physics*, 34(2a):384–391, 2004.

[85] Matthew Ellis. *Simulations of magnetic reversal properties in granular recording media*. PhD thesis, University of York, 2015.

[86] Aleksandr I Akhiezer, SV Peletminskii, and Victor G Baryakhtar. *Spin waves*. North-Holland, 1968.

[87] J. H. Van Vleck. On the anisotropy of cubic ferromagnetic crystals. *Physical Review*, 52(11):1178–1198, 1937.

[88] Charles Kittel. Physical theory of ferromagnetic domains. *Reviews of modern Physics*, 21(4):541, 1949.

[89] Akashdeep Kamra, Hedyeh Keshtgar, Peng Yan, and Gerrit EW Bauer. Coherent elastic excitation of spin waves. *Physical Review B*, 91(10):104409, 2015.

[90] D. Sander. The correlation between mechanical stress and magnetic anisotropy in ultrathin films. *Reports on Progress in Physics*, 62(5):809–858, 1999.

[91] Pui-Wai Ma, SL Dudarev, AA Semenov, and CH Woo. Temperature for a dynamic spin ensemble. *Physical Review E*, 82(3):031111, 2010.

[92] Wahyu Setyawan and Stefano Curtarolo. High-throughput electronic band structure calculations: Challenges and tools. *Computational materials science*, 49(2):299–312, 2010.

[93] NI Papanicolaou, IE Lagaris, and GA Evangelakis. Modification of phonon spectral densities of the (001) copper surface due to copper adatoms by molecular dynamics simulation. *Surface science*, 337(1-2):L819–L824, 1995.

[94] VJ Minkiewicz, G Shirane, and R Nathans. Phonon dispersion relation for iron. *Physical Review*, 162(3):528, 1967.

[95] M Krech, Alex Bunker, and DP Landau. Fast spin dynamics algorithms for classical spin systems. *Computer physics communications*, 111(1-3):1–13, 1998.

[96] C-K Loong, JM Carpenter, JW Lynn, RA Robinson, and HA Mook. Neutron scattering study of the magnetic excitations in ferromagnetic iron at high energy transfers. *Journal of applied physics*, 55(6):1895–1897, 1984.

[97] Dilina Perera, Don M Nicholson, Markus Eisenbach, G Malcolm Stocks, and David P Landau. Collective dynamics in atomistic models with coupled translational and spin degrees of freedom. *Physical Review B*, 95(1):014431, 2017.

[98] U Atxitia, D Hinzke, O Chubykalo-Fesenko, U Nowak, H Kachkachi, O.N. Mryasov, R.F. Evans, and Chantrell R.W. Multiscale modeling of magnetic materials: Temperature dependence of the exchange stiffness. *Physical Review B*, 82:13440, 2010.

[99] A Lyberatos and K Yu Guslienko. Thermal stability of the magnetization following thermomagnetic writing in perpendicular media. *Journal of applied physics*, 94(2):1119–1129, 2003.

[100] T Kobayashi, Y Nakatani, F Inukai, K Enomoto, and Y Fujiwara. Impact of damping constant on bit error rate in heat-assisted magnetic recording. *Journal of the Magnetics Society of Japan*, 41(3):52–57, 2017.

[101] Dieter Weller, Gregory Parker, Oleksandr Mosendz, Andreas Lyberatos, Dmitriy Mitin, Nataliia Y. Safonova, and Manfred Albrecht. Review Article: FePt heat assisted magnetic recording media. *Journal of Vacuum Science & Technology B, Nanotechnology and Microelectronics: Materials, Processing, Measurement, and Phenomena*, 34(6):060801, 2016.

[102] J. F. Hu, T. J. Zhou, W. L. Phyoe, Kelvin Cher, and J. Z. Shi. Microstructure control of L10 ordered FePt granular film for HAMR application. *IEEE Transactions on Magnetics*, 49(7):3737–3740, 2013.

[103] Daniel Richardson, Sidney Katz, J Wang, YK Takahashi, Kumar Srinivasan, Alan Kalitsov, K Hono, Antony Ajan, and Mingzhong Wu. Near-t c ferromagnetic resonance and damping in fe pt-based heat-assisted magnetic recording media. *Physical Review Applied*, 10(5):054046, 2018.

[104] J. Becker, O. Mosendz, D. Weller, A. Kirilyuk, J. C. Maan, P. C.M. Christianen, Th Rasing, and A. Kimel. Laser induced spin precession in highly anisotropic granular L10 FePt. *Applied Physics Letters*, 104(15), 2014.

[105] Lee Kyeong-Dong, Song Hyon-Seok, Kim Ji-Wan, Ko Hyun Seok, Sohn Jeong-Woo, Park Byong-Guk, and Shin Sung-Chul. Gilbert damping and critical real-space trajectory of L10 -ordered FePt films investigated by magnetic-field-induction and all-optical methods. *Applied Physics Express*, 7(11):113004, 2014.

[106] S. Mizukami, S. Iihama, N. Inami, T. Hiratsuka, G. Kim, H. Naganuma, M. Oogane, and Y. Ando. Fast magnetization precession observed in L10-FePt epitaxial thin film. *Applied Physics Letters*, 98(5), 2011.

[107] Nan Mo, Julius Hohlfeld, Misbah ul Islam, C Scott Brown, Erol Girt, Pavol Krivosik, Wei Tong, Adnan Rebei, and Carl E Patton. Origins of the damping in perpendicular media: Three component ferromagnetic resonance linewidth in co–cr–pt alloy films. *Applied Physics Letters*, 92(2):022506, 2008.

[108] T. A. Ostler, M. O.A. Ellis, D. Hinzke, and U. Nowak. Temperature-dependent ferromagnetic resonance via the Landau-Lifshitz-Bloch equation: Application to FePt. *Physical Review B - Condensed Matter and Materials Physics*, 90(9):1–11, 2014.

[109] Dmitry A Garanin. Fokker-Planck and Landau-Lifshitz-Bloch equations for classical ferromagnets. *Physical Review B*, 55(5):3050, 1997.

[110] Oleg N Mryasov, Ulrich Nowak, K Yu Guslienko, and Roy W Chantrell. Temperature-dependent magnetic properties of fept: Effective spin hamiltonian model. *EPL (Europhysics Letters)*, 69(5):805, 2005.

[111] O Hovorka, S Devos, Q Coopman, WJ Fan, CJ Aas, RFL Evans, Xi Chen, G Ju, and RW Chantrell. The curie temperature distribution of fept granular magnetic recording media. *Applied Physics Letters*, 101(5):052406, 2012.

[112] A Lyberatos, D Weller, GJ Parker, and BC Stipe. Size dependence of the curie temperature of l 1 o-fept nanoparticles. *Journal of Applied Physics*, 112(11):113915, 2012.

[113] Oksana Chubykalo-Fesenko, Ulrich Nowak, Roy W Chantrell, and D Garanin. Dynamic approach for micromagnetics close to the curie temperature. *Physical Review B*, 74(9):094436, 2006.

[114] MOA Ellis, TA Ostler, and RW Chantrell. Classical spin model of the relaxation dynamics of rare-earth doped permalloy. *Physical Review B*, 86(17):174418, 2012.

[115] Robin John, Marco Berritta, Denise Hinzke, C Müller, Tiffany Santos, Henning Ulrichs, Pablo Nieves, Jakob Walowski, Ritwik Mondal, Oksana Chubykalo-Fesenko, et al. Magnetisation switching of fept nanoparticle recording medium by femtosecond laser pulses. *Scientific reports*, 7(1):1–8, 2017.

[116] Lewis J Atkinson, Thomas A Ostler, O Hovorka, KK Wang, B Lu, GP Ju, J Hohlfeld, B Bergman, B Koopmans, and Roy W Chantrell. Effects of interactions on the relaxation processes in magnetic nanostructures. *Physical Review B*, 94(13):134431, 2016.

[117] M. O. A. Ellis, T. A. Ostler, and R. W. Chantrell. Classical spin model of the relaxation dynamics of rare-earth doped permalloy. *Physical Review B - Condensed Matter and Materials Physics*, 86(17):1–9, 2012.

[118] Sutee Sampan-A-Pai, Jessada Chureemart, Roy W Chantrell, Roman Chepulskyy, Shuxia Wang, Dmytro Apalkov, Richard FL Evans, and Phanwadee Chureemart. Temperature and thickness dependence of statistical fluctuations of the gilbert damping in co-fe-b/mg o bilayers. *Physical Review Applied*, 2019.

[119] J-U Thiele, Kevin R Coffey, MF Toney, JA Hedstrom, and AJ Kellock. Temperature dependent magnetic properties of highly chemically ordered fe 55- x ni x pt 45 l1 0 films. *Journal of applied physics*, 91(10):6595–6600, 2002.

[120] S Okamoto, N Kikuchi, O Kitakami, T Miyazaki, Y Shimada, and K Fukamichi. Chemical-order-dependent magnetic anisotropy and exchange stiffness constant of fept (001) epitaxial films. *Physical Review B*, 66(2):024413, 2002.

[121] Daniel Richardson, Kumar Srinivasan, Alan Kalitsov, Antony Ajan, Shikha Jain, Sidney Katz, and Mingzhong Wu. Interlayer exchange coupling in magnetic hard-soft bilayered structures. *Physiscal Review Applied*, 11:044016, 2019.

[122] Richard Evans, Ulrich Nowak, Florian Dorfbauer, T Shrefl, Oleg Mryasov, Roy W Chantrell, and Gregory Grochola. The influence of shape and structure on the curie temperature of fe and co nanoparticles. *Journal of applied physics*, 99(8):08G703, 2006.

[123] MOA Ellis and RW Chantrell. Switching times of nanoscale fept: Finite size effects on the linear reversal mechanism. *Applied Physics Letters*, 106(16):162407, 2015.

[124] O Chubykalo-Fesenko, U Nowak, Chantrell R.W, and D. Garanin. Dynamic approach for micromagnetics close to the curie temperature. *Physical Review B*, 74:094436, 2006.

[125] P Nieves, D Serantes, U Atxitia, and O Chubykalo-Fesenko. Quantum Landau-Lifshitz-Bloch equation and its comparison with the classical case. *Physical Review B*, 90:104428, 2014.

[126] Matthew O A Ellis, Mario Galante, and Stefano Sanvito. Role of longitudinal fluctuations in L10 FePt. *Physical Review B*, 100(21):214434, 2019.

[127] CL Jermain, SV Aradhya, ND Reynolds, RA Buhrman, JT Brangham, MR Page, PC Hammel, FY Yang, and DC Ralph. Increased low-temperature damping in yttrium iron garnet thin films. *Physical Review B*, 95(17):174411, 2017.

[128] T Kasuya and RC LeCraw. Relaxation mechanisms in ferromagnetic resonance. *Physical Review Letters*, 6(5):223, 1961.

[129] R. F. L. Evans, U. Atxitia, and R. W. Chantrell. Quantitative simulation of temperature-dependent magnetization dynamics and equilibrium properties of elemental ferromagnets. *Physical Review B*, 91:144425, 2015.

[130] Joseph Barker and Gerrit E. W. Bauer. Semiquantum thermodynamics of complex ferrimagnets. *Physical Review B*, 100:140401, 2019.

[131] AV Kimel, A Kirilyuk, PA Usachev, RV Pisarev, AM Balbashov, and Th Rasing. Ultrafast non-thermal control of magnetization by instantaneous photomagnetic pulses. *Nature*, 435(7042):655–657, 2005.

[132] Fredrik Hansteen, Alexey Kimel, Andrei Kirilyuk, and Theo Rasing. Femtosecond photomagnetic switching of spins in ferrimagnetic garnet films. *Physical Review Letters*, 95:047402, 2005.

[133] Tobias Kampfrath, Alexander Sell, Gregor Klatt, Alexej Pashkin, Sebastian Mährlein, Thomas Dekorsy, Martin Wolf, Manfred Fiebig, Alfred Leitenstorfer, and Rupert Huber. Coherent terahertz control of antiferromagnetic spin waves. *Nature Photonics*, 5(1):31–34, 2011.

[134] SR Woodford. Conservation of angular momentum and the inverse faraday effect. *Physical Review B*, 79(21):212412, 2009.

[135] CH Back, R Allenspach, W Weber, SSP Parkin, D Weller, Edward L Garwin, and HC Siegmann. Minimum field strength in precessional magnetization reversal. *Science*, 285(5429):864–867, 1999.

[136] JV Jäger, AV Scherbakov, TL Linnik, DR Yakovlev, M Wang, P Wadley, V Holy, SA Cavill, AV Akimov, AW Rushforth, et al. Picosecond inverse magnetostriction in galfenol thin films. *Applied Physics Letters*, 103(3):032409, 2013.

[137] D. Afanasiev, I. Razdolski, K. M. Skibinsky, D. Bolotin, S. V. Yagupov, M. B. Strugatsky, A. Kirilyuk, Th. Rasing, and A. V. Kimel. Laser Excitation of Lattice-Driven Anharmonic Magnetization Dynamics in Dielectric $FeBO_3$. *Physical Review Letters*, 112:147403, 2014.

[138] David Brown, Bao-Min Ma, and Zhongmin Chen. Developments in the processing and properties of NdFeb-type permanent magnets. *Journal of magnetism and magnetic materials*, 248(3):432–440, 2002.

[139] Takayuki Tsuchida, Jun Fukushima, Shintaro Hinata, Yamato Hayashi, Shin Saito, and Hirotsugu Takizawa. Fabrication and growth of c-axis textured Nd2Fe14B thin films by high-rate sputtering. *Journal of Applied Physics*, 127(10):103901, 2020.

[140] Qihua Gong, Min Yi, Richard F. L. Evans, Bai-Xiang Xu, and Oliver Gutfleisch. Calculating temperature-dependent properties of $Nd_2Fe_{14}B$ permanent magnets by atomistic spin model simulations. *Physical Review B*, 99:214409, 2019.

[141] Samuel Westmoreland. *Atomistic calculations of magnetic properties of rare-earth transition-metal permanent magnets*. PhD thesis, University of York, 2018.

[142] SC Westmoreland, RFL Evans, G Hrkac, Thomas Schrefl, GT Zimanyi, M Winklhofer, N Sakuma, M Yano, A Kato, T Shoji, et al. Multiscale model approaches to the design of advanced permanent magnets. *Scripta Materialia*, 148:56–62, 2018.

[143] D Haskel, JC Lang, Z Islam, A Cady, G Srajer, M Van Veenendaal, and PC Canfield. Atomic origin of magnetocrystalline anisotropy in $Nd_2Fe_{14}B$. *Physical Review Letters*, 95(21):217207, 2005.

[144] DA Garanin. Self-consistent gaussian approximation for classical spin systems: Thermodynamics. *Physical Review B*, 53(17):11593, 1996.

[145] Olivia Muthsam, Florian Slanovc, Christoph Vogler, and Dieter Suess. The superior role of the gilbert damping on the signal-to-noise ratio in heat-assisted magnetic recording. *Journal of Magnetism and Magnetic Materials*, page 167125, 2020.

[146] RW Chantrell and EP Wohlfarth. Rate dependence of the field-cooled magnetisation of a fine particle system. *Physica Status Solidi (a)*, 91(2):619–626, 1985.

[147] TJ Zhou, K Cher, JF Hu, ZM Yuan, and B Liu. The concept and fabrication of exchange switchable trilayer of FePt/FeRh/FeCo with reduced switching field. *Journal of Applied Physics*, 111(7):07C116, 2012.

[148] Ganping Ju, Julius Hohlfeld, Bastiaan Bergman, René J. M. van de Veerdonk, Oleg N. Mryasov, Jai-Young Kim, Xiaowei Wu, Dieter Weller, and Bert Koopmans. Ultrafast Generation of Ferromagnetic Order via a Laser-Induced Phase Transformation in FeRh Thin Films. *Physical Review Letters*, 93(19):197403, 2004.

[149] Oleg N Mryasov. Magnetic interactions and phase transformations in fem, m=(pt, rh) ordered alloys. *Phase Transitions*, 78(1-3):197–208, 2005.

[150] Natalia Kazantseva. *Dynamic response of the magnetisation to picosecond heat pulses*. PhD thesis, The University of York, 2008.

[151] JK Chen, DY Tzou, and JE Beraun. A semiclassical two-temperature model for ultrafast laser heating. *International Journal of Heat and Mass Transfer*, 49(1):307–316, 2006.

[152] Natalia Kazantseva, Ulrich Nowak, Roy W Chantrell, Julius Hohlfeld, and Adnan Rebei. Slow recovery of the magnetisation after a sub-picosecond heat pulse. *EPL (Europhysics Letters)*, 81(2):27004, 2007.

[153] Tom Seifert, Uwe Martens, S Günther, MAW Schoen, F Radu, XZ Chen, I Lucas, R Ramos, Myriam H Aguirre, Pedro A Algarabel, et al. Terahertz spin currents and inverse spin hall effect in thin-film heterostructures containing complex magnetic compounds. In *Spin*, volume 7, page 1740010. World Scientific, 2017.

[154] Marco Menarini, Rajasekhar Medapalli, Eric E Fullerton, and Vitaliy Lomakin. Micromagnetic simulation of THz signals in antiferromagnetic FeRh by sub-picosecond thermal pulses. *AIP Advances*, 9(3):035040, 2019.

[155] R Medapalli, G Li, Sheena KK Patel, RV Mikhaylovskiy, Th Rasing, AV Kimel, and EE Fullerton. Femtosecond photocurrents at the FeRh/Pt interface. *Applied Physics Letters*, 117(14):142406, 2020.

[156] Pui-Wai Ma and SL Dudarev. Atomistic spin-lattice dynamics. *Handbook of Materials Modeling: Methods: Theory and Modeling*, pages 1017–1035, 2020.

[157] A Stupakiewicz, CS Davies, K Szerenos, D Afanasiev, KS Rabinovich, AV Boris, A Caviglia, AV Kimel, and A Kirilyuk. Ultrafast phononic switching of magnetization. *arXiv preprint arXiv:2010.13671, Accepted for a Nature publication, as mentioned during the workshop COST Action MAGNETOFON, 23rd of November 2020*, 2020.

[158] O. Chubykalo, R. Smirnov-Rueda, J. M. Gonzalez, M. A. Wongsam, R. W. Chantrell, and U. Nowak. Brownian dynamics approach to interacting magnetic moments. *Journal of Magnetism and Magnetic Materials*, 266(1-2):28–35, 2003.